HIGH POWER RF PROCESSING STUDIES OF 3 GHz NIOBIUM SUPERCONDUCTING ACCELERATOR CAVITIES

A Dissertation
Presented to the Faculty of the Graduate School
of Cornell University
in Partial Fulfillment of the Requirements for the Degree of
Doctor of Philosophy

by
Joel Henry Graber
May 1993

HIGH POWER RF PROCESSING STUDIES OF 3 GHz NIOBIUM SUPERCONDUCTING ACCELERATOR CAVITIES

Joel Henry Graber, Ph.D.

Cornell University 1993

Superconducting radio-frequency (SRF) cavities are a promising technology for future high energy particle accelerators. SRF technology is presently limited by field emission (FE), a quantum mechanical tunneling effect wherein electrons are emitted from a metal surface into vacuum in the presence of a strong electric field.

A systematic study is presented of the effects of pulsed high power RF processing (HPP) as a method of understanding and reducing field emission in SRF cavities. The HPP experimental apparatus was built to provide up to 200 kW peak RF power to 3 GHz cavities, for pulse lengths of hundreds of microseconds. Single-cell, two-cell, and nine-cell cavities were tested extensively.

HPP proved to be a highly successful method of reducing FE loading in SRF cavities. Attainable continuous wave (CW) fields are increased by as much as 80% from their pre-HPP limits. Analysis of HPP results and data increases our understanding of the nature of RF processing.

Clear correlations are obtained linking FE reduction with the maximum electric field attained during processing. Analysis of the pulsed behavior of the cavities indicates that thermal breakdown, initiated by high surface magnetic fields, is a dominant limitation on the attainable fields. A thermal model is developed which accurately predicts the limitations.

A special two-cell cavity with a reduced magnetic to electric field ratio is successfully tested. During HPP, pulsed fields reach E_{peak} = 113 MV/m (H_{peak} = 1600 Oe), and subsequent low power measurement reaches

E_{peak} = 100 MV/m (H_{peak} = 1420 Oe), the highest CW field ever measured in a superconducting accelerator cavity.

Additional studies improve our understanding of the microscopic effect of HPP. Thermometry measurements of the outer wall of single-cell cavities reveal that processing gains are made by reduction in emission from localized sites. Scanning electron microscope examination of RF surfaces reveals craters and other phenomena which indicate that processing occurs through a violent melting/vaporization phenomenon. A "model" for RF processing is presented based upon the experimental evidence, both from this study and from other related experiments.

BIOGRAPHICAL SKETCH

Joel Henry Graber was born on March 9, 1964, in the town of Munising, in the U.P. (Upper Peninsula) of Michigan. At the age of eighteen months, he visited upstate New York with his parents. This view of New York apparently imprinted deeply upon his mind, a fact that did not become obvious until twenty years later, when it came time to choose a graduate school. He graduated from Munising High School in June of 1982.

He enrolled at Michigan Technological University in September, 1982, majoring in Applied Physics. After two years in the Applied Physics progam, with a minor in Computer Science, he decided that he enjoyed the computers enough to make a full degree of it. He therefore switched to a double major, Physics and Computer Science. He graduated from Michigan Tech in May 1987, with Bachelor of Science degrees in Physics and Computer Science, both degrees Summa Cum Laude. It is also worth noting that while in his third year at Michigan Tech, he took up his true avocation in life, ice hockey goaltending.

In August 1987, he enrolled at Cornell University with the intention of obtaining a Ph.D. in Physics. Following two rather disastrous oral examinations in the fall of 1988, it was decided that he should pursue a Master of Science degree to verify that he was, in fact, capable of doing scientific work. He obtained the M.S. in December, 1989, and has since gone on to sail through yet a fourth oral examination, and now is finishing his Ph.D.

His future plans are to continue working in the field of Superconducting RF Cavities as Post-doctoral Researcher, unless the Detroit Red Wings call.

This dissertation is dedicated to my grandparents:
My school teacher grandmothers Ingrid Rundquist Carmody and Marie Barton Graber, who helped give me my love of learning, and my grandfathers, Ronald Carmody and Walter Graber, who helped to show me the value of hard work.

ACKNOWLEDGMENTS

The completion of this dissertation is a testament to the work and support of many people.

First, and foremost, my thanks go to my advisor, Hasan Padamsee, for essentially teaching me to think like a scientist. His faith in me early on, his calm in the face of my panic attacks, his pushing and urging for more effort when I needed to be pushed, and his general availability have made him the ideal advisor. I simply state that I would not have wanted to obtain my Ph.D. under anyone else's supervision.

Special thanks also go to Dave Rubin for acting as Chair of my Special Committee. Dave was also instrumental in obtaining another chance for me when I needed it, and I am grateful for that. In addition, he has put up with me occasionally walking into his office, plopping down and unloading everthing I've been thinking about recently. Don Hartill and Henry Tye acted as the other members of my Special Committee, and I thank them for their efforts.

Maury Tigner has lent his vast expertise in SRF matters, as well as his knowledge of possible future employers.

The rest of the SRF group at the Laboratory of Nuclear Studies has provided physical help, scientific inspirations, good conversation, an occasional clambake, and friendship over the last five and a half years. They include Joe Kirchgessner, Dave Moffat, James Sears, Phil Barnes, Henry Muller, Don Metzger, Walter Hartung, Jens Knobloch, Tom Hays, Curtis Crawford, Michael Pekeler, Peter Schmüser, Q.S. Shu, Kazunori Akai, Will Fox, Vadim Vescherevich, and probably several more people that I missed.

The construction of the HPP apparatus was primarily the work of the machine shop at Newman Lab, under the able command of Dick Mitstifer

and Chuck Firenze. In addition, they have been my friends, they have mended broken skates, and they've put up with running updates on my hockey career. Thanks to Captain Randy, Roger, Phil, Seth, Big John, Gerhard, Bill, Neil, Terri, Ron, and any one else I forgot.

The thermometry apparatus and analysis package for the HPP set-up was a result of a great deal of help performed by Will Dickinson, Karen Sauer, and Adam Leibovich.

The SRF community world-wide (CERN, DESY, KEK, CEBAF, Saclay, etc.) is a remarkably friendly, collegial group. My education as a physicist has been greatly enhanced by the biannual gatherings of this community. It has also provided me with wonderful travel opportunities.

I also thank Jim Sethna for a well-timed conversation on the nature of an expanding normal conducting region on a superconducting surface.

I extend a special thanks to D. Dasbach and M. Peiniger at Interatom/Siemens for their assistance in fabrication of the two-cell cavity used in these experiments.

Many of the figures in this dissertation, as well as various papers over the last few years, are the work of the LNS drafting room, primarily Don Miller. In addition, the drafting room also provided needed diversions in the day to day drudgery. My thanks go to Tim, Dawn, Jim, and Tom. Further thanks go to Chuck, Monica, Mary, Pam, and Dusty for mainly putting up with the fact that when I don't want to work, I'm going to find someone to talk to!

This work was funded by the National Science Foundation, with supplementary support from the U.S.-Japan Collaboration.

Now on to the personal. In the dedication to my Master's Thesis, I said that if it weren't for my parents, Ken and Tina Graber, I wouldn't be

here in more ways than one, and it's only more true now. Their unswerving love and support is one of the driving forces in my life, and I can never repay it, except for maybe what Dad said- to pass it on.

The rest of my immediate family has been there through dark and light, and I thank them as well- Jon, Jay, Serene, Grandpa, and Toby!

To Lindsay- what do you say to someone who brightens a day by just being there? You have made my last few months a constant joy and adventure, and I can't wait to see what comes next! I don't think that I could have dreamed up a companion more wonderfully suited to my life than you.

My years with the Physics department have been brightened incredibly by two of the best friends anyone could ask for: Debby Hatfield and Vince Kotmel. Thank you seems inadequate, but it'll have to do.

To Buck, Jun, and Tammy, who were there at the darkest times, when I needed help, thank you always. Thank you Tammy, Jim, and Hana for showing me how to laugh and smile again.

Finally, I started a list in the acknowledgments of my M.S. Thesis, which as it turns out was incomplete, even for then. I also now have three and a half more years to add to it, so here we go again, probably with duplication, and maybe this time without omission (not likely!)- Thanks in no particular order goes out to: Mom, Dad, Jon, Serene, Jay, Holly, Lindsay, Toby, Grandpa, Abby, Hershey, Curt, Jean, and Alan, the rest of the Kansas Grabers, Bill, Molly, and Willow, the Carolina Carmodys, the California Reitzes, H.P., Don Paajanen, Kon and Ethel, the Shoplands of New Jersey, Lottie, Dr. Bob Weidman, the Doctor and companions, Tim, Dave D., Dan, Kris (Barbie!), Anne and Brian (the Badgers), Bruce, Town & Country Inn: the 1992-93 Cass Park Adult Hockey League Champions!!!, Rita, Jeff, Joy, Dr. Carol, Andres (if for no other reason than the look when you realized it

was my parents in the Chapter House), Ernie and Bert, Underdog, Meers and Yvonne, Kyle and Linda, Buck, Greg, Jun, Adrian, Brian, Beth, Jake, Dave P., Crash Davis and Annie (Oh My!), Thursday nights at the Chapter House, Rick Blaine and Ilsa Lund, the Ithaca Hash House Harriers, Mu Beta Psi, Grad Science Hockey, Curtis and Donna, Ted Time Hockey, Kiwanis Baseball, Vince, Janet, Sara, and Danny, Z, Russ and Tricia, Dan and Amy, Jack and Carole Zurawka, Heidi, Carol, Sandy, Julie, Jack and Rita Dwyer, Craig, Nicole, Alan George, Bryan Suits, Luke Skywalker, Han Solo, George Lucas, Albert Einstein, Gene Roddenberry, Jennifer, Mike and Patti Kelley, Hans Bethe, Stephen Youngs, the residents of Cicely, Alaska, Thurgood Marshall, Kurt Vonnegut, Sting, Riley Sisson, Suzanne, Maynard, Laura, Dorothy Diggs (goalie coach supreme), Chris, Eldora, Jim Kirk, Jean-Luc Picard, the coffee growers of the world, Alex (you monkey-head!), Gallileo, J.R.R. Tolkien, Ed and Linda, Highway Hockey, Harlan Ellison, Carl Rowan, Mike Royko, HAL, Starfleet, Robin Williams, ...

TABLE OF CONTENTS

TABLE OF CONTENTS (Continued)

TABLE OF CONTENTS (Continued)

LIST OF TABLES

LIST OF FIGURES

LIST OF FIGURES (Continued)

LIST OF FIGURES (Continued)

LIST OF FIGURES (Continued)

LIST OF FIGURES (Continued)

LIST OF FIGURES (Continued)

LIST OF ABBREVIATIONS

HPP	High Power Pulsed Processing
RF	Radio-Frequency
SRF	Superconducting Radio-Frequency
NC	Normal Conducting
FE	Field Emission
F-N	Fowler-Nordheim
CW	Continuous Wave
BCS	Bardeen-Cooper-Schrieffer Theory
SEM	Scanning Electron Microscope
BCP	Buffered Chemical Polish (HNO_3, H_3PO_4, HF)
RRR	Residual Resistance Ratio

CHAPTER 1: INTRODUCTION

Advances in particle physics are inextricably linked to advances in particle accelerators. Many parameters affect the performance of the accelerators, and the physics they make accessible. A very important factor is the availability of higher energy particle beams, for higher energy beams allow for increasingly finer measurement of the fundamental nature of particles.

The technology for accelerating particles is dependent on the type of particle being accelerated. Heavy particle (proton) accelerators are generally circular machines, with the technological challenges lying in high field magnet development. The Superconducting Super Collider, currently under construction, is an example of this type of machine. The SSC will accelerate protons both directions in a 52 mile circumference ring, colliding them with a center of mass energy of 43 TeV.

Electron positron colliders have been almost exclusively circular machines up to the present. The synchrotron radiation which results from accelerating charged particles in a circle makes circular machines impractical for further increase in energy. For this reason, the next generation of electron positron colliders will have to be linear. A linear collider with center of mass energy in the 1 TeV range would be a complimentary machine to the previously mentioned SSC. Several proposals have been put forward for the construction of such a machine.[1]-[3]

The work described in this dissertation is part of an attempt to increase the energy available to electron-positron accelerators by extending the accelerating gradients of superconducting radio-frequency (SRF) cavities.

1.1. RF Cavities

An RF cavity is the device through which power is coupled into the particle beam of an accelerator. In electron-positron colliders, RF accelerating cavities are microwave resonators which generally derive from a "pillbox" shape (right circular cylinder), with connecting tubes to allow particle beams to pass through for acceleration. Figure 1.1 shows a typical cylindrically symmetric cavity. The fundamental, or lowest RF frequency, mode (TM 010) of the cavity has fields as shown. The electric field is roughly parallel to the beam axis, and decays to zero radially upon approach to the cavity walls. Boundary conditions demand that the electric surface be normal to the metal surface. The peak surface electric field is located near

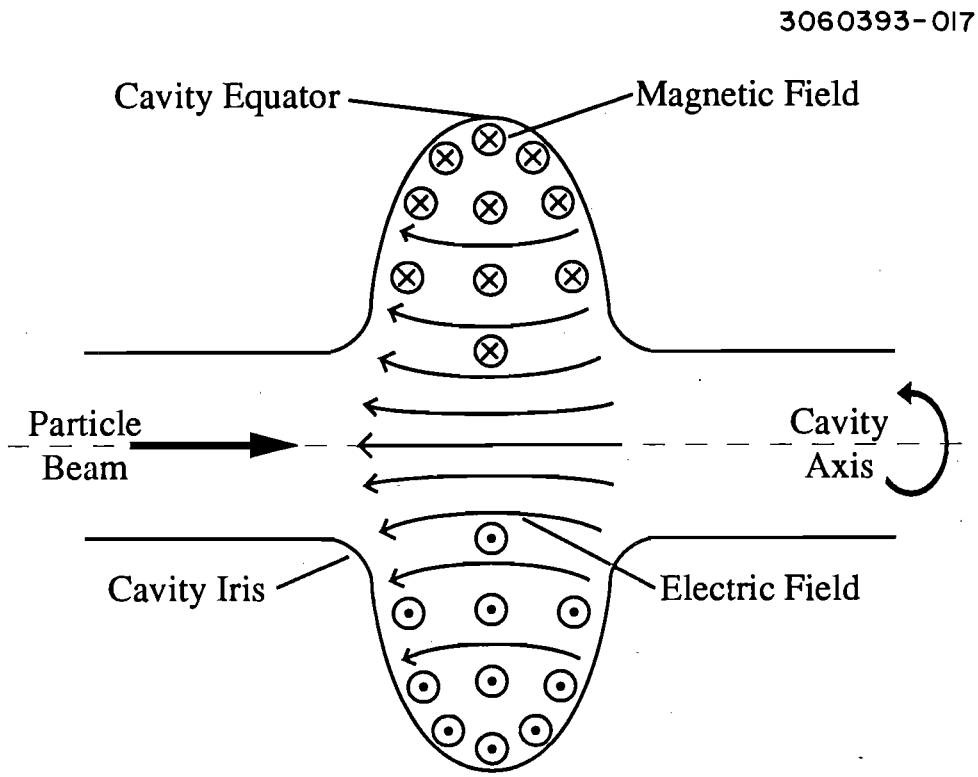

Figure 1.1. A typical accelerating cavity geometry, showing particle beam and fundamental fields of the RF cavity.

the iris, or region where the beam tube joins the cavity. The magnetic field is azimuthal, with the highest magnetic field located near the cavity equator. The magnetic field is zero on the cavity axis.

The particle beam traverses the cavity as shown, experiencing an accelerating force along the axis of the cavity due to the electic field. Since the RF fields alternate in time, the particle beam must, of course, be in the proper phase with respect to the fields in order that the force be accelerating rather than decelerating. In addition, since the particles take a finite time to cross the cavity, the accelerating field is the time average of the electric field along the particles flight. The average gradient is defined in equation 1-1:

$$\langle E_{acc} \rangle = \frac{2}{T_{RF}} \int_0^{\frac{1}{2}T_{RF}} dt\, E(z,t) \qquad (1\text{-}1)$$

T_{RF} is the RF period, and $E(z,t)$ is the electric field at the time and position of the particle.

The Q_0 of an accelerating cavity is defined as the RF angular frequency (ω) times the ratio of the stored energy in the electromagnetic fields (U) to the dissipated power (P_{diss}), as shown in equation 1-2.

$$Q_0 = \frac{\omega U}{P_{diss}} \qquad (1\text{-}2)$$

The relationships between the stored energy and the magnitudes of the electric fields are obtained by numerical solution of Maxwell's Equations for the cavity geometry. Several computer program packages are available to solve the equations for typical cavity geometries, e.g. SUPERFISH[4], URMEL[5] and URMEL-T[6], or MAFIA.[7] Of particular interest in these solutions are the ratios of peak surface electric and magnetic fields

to the square root of the stored energy, and the ratio of peak surface electric electric field to the average accelerating field in the cavity, given by:

$$k_e = \frac{E_{peak}}{\sqrt{U}}, \; k_h = \frac{H_{peak}}{\sqrt{U}}, \text{ and } \alpha = \frac{E_{peak}}{E_{acc}} \tag{1-3}$$

In the situation where all cavity losses are due to surface currents, the Q_0 can alternately be defined as the ratio of the geometry factor G to the microwave surface resistance R_s, as shown in equation 1-4.

$$Q_0 = \frac{G}{R_s} \tag{1-4}$$

The geometry factor is defined in equation 1-5. Geometry factors have units of resistance, and generally have values between 200 and 300 Ohms.

$$G = \frac{\varepsilon_0}{2} \frac{\int_{volume} dV \, E^2}{\oint_{surface} dA \, H^2} \tag{1-5}$$

The microwave surface resistance in a normal conductor is given by equation 1-6, and is approximately 15 mΩ for copper at 3 GHz.

$$R_s = \sqrt{\frac{\mu\omega}{2\sigma}} = \frac{1}{\sigma\delta} \tag{1-6}$$

where δ is the RF skin depth in a normal conductor.

The surface resistance causes power dissipation by the surface currents which arise in order to support the magnetic fields at the RF surface. Wall losses are the primary reason for investigating superconducting cavities, as the RF surface resistance is five to six orders of magnitude lower than that of a normal conduncting surface. Superconducting surface resistance will be discussed in the next section.

1.1.1. Basics of RF Superconductivity

The intention of this section is to provide the basics of RF superconductivity which are necessary to understand the work performed in the HPP project. A more in depth discussion can be found in several of the listed references.[8]-[13] The famous BCS theory of superconductivity was originally worked out for DC conditions by Bardeen, Cooper, and Schrieffer.[14] Extension of BCS theory to RF conditions was made by Mattis and Bardeen[15] and Abrikosov, Gor'kov, and Khalatnikov.[16] In addition, the empirical models of London[17] prove to be useful in understanding the basic nature of RF superconductivity.

It is well known that many materials, known as superconductors, lose all DC electrical resistance when the temperature drops below the critical temperature T_c. The BCS theory has quite successfully described this phenomenon. According to BCS theory, below T_c the electrons of a conductor gain a small net attraction through their interaction with the surrounding lattice. The electrons then condense into "Cooper pairs," which move without resistance through the conductor. The Cooper pairs have binding energy Δ, which is dependent on temperature.

Unlike DC resistance, RF surface resistance is zero only at $T = 0$ K (absolute zero). At temperatures above absolute zero, but below the critical temperature, the surface resistance is greatly reduced, yet non-zero. This can be most easily understood through the "London two-fluid model." The two fluids are paired (superconducting) and unpaired (normal conducting) electrons. The binding energy of the Cooper pairs is comparable to thermal energies, therefore we can express the fraction of unpaired electrons by a Boltzman distribution:

$$\frac{n_{NC}}{n_{SC}} = \exp\left(-\frac{\Delta(T)}{k_B T}\right) \tag{1-7}$$

where k_B is the Boltzman constant.

Cooper pairs move without resistance, and thus dissipate no power. The Cooper pairs do nonetheless have an inertial mass, and thus the electromagnetic fields must extend into the surface of the conductor in order to provide the forces to accelerate the pairs back and forth to sustain the RF surface currents. The EM fields will act on the unpaired electrons as well, therefore causing power dissipation.

For temperatures less than $T_c/2$, the superconducting surface resistance can be well represented as:

$$R_s = A\,\frac{\omega^2}{T}\exp\left(-\frac{\Delta(0)}{k_B T}\right) + R_0 \tag{1-8}$$

The first term on the right hand side of equation 1-8 is the BCS resistance. For temperatures less than $T_c/2$, the binding energy is nearly unchanged from its value at absolute zero, $\Delta(0)$. The coefficient A is a complex function of material parameters such as the superconducting coherence length, the penetration depth, the electron mean free path, and the Fermi velocity. A can be evaluated computationally via programs by Turneaure[18] or Halbritter.[19] The BCS resistance in a typical 3 GHz cavity varies from 3 microOhms at $T = 4.2$ K to less than 1 nanoOhm at $T = 1.4$ K.

The second term on the right hand side of equation 1-8 is the residual, or temperature independent, resistance R_0. Mechanisms for R_0 are not well understood, though several possiblilities have been proposed and investigated.[20],[21] Residual resistance values are generally found to be between 5 and 100 nanoOhms, though values as low as 1 nanoOhm have been measured.[22]

1.1.2. Advantages of SRF Technology

As previously mentioned, the chief advantage in the use of SRF cavities is the reduced dissipation due to wall losses. The wall loss power dissipation is proportional to the surface resistance, which is reduced by a factor of 10^6 in superconducting cavities. The total power usage does not reflect all of this gain, however, due to the need to refrigerate the cavities to liquid helium temperatures. Even including refrigerator power, using typical refrigerator efficiencies, the net power usage drops by a factor of several hundred to a thousand in superconducting cavities. In CW operation this means greatly reduced power and higher accelerating gradients. In pulsed operation, SRF cavities offer long pulse lengths and high duty cycles compared to NC cavities.

Many proposed accelerator projects (e.g. B-factories) require significant improvements in the luminosity, which is a measure of the rate at which particles in counter rotation beams will collide. One factor in the luminosity is the average beam current. The maximum current can be limited by beam-cavity interactions. The beam can be significantly disrupted anytime the surrounding environment is changed, for example cavities, vacuum connections, etc. The typical normal conducting cavity is an extreme change in the surrounding environement. The extreme shape of normal conducting cavities is necessary in order to minimize the power dissipation for a given electric field. SRF cavities avoid the disruptive cavity shapes by instead reducing the power dissipation with superconductivity. Given their smoother shape and larger beam holes, superconducting cavities present less of a disruption to the beam than their normal conducting counterparts.

In addition, in continuous wave operating conditions, the higher accelerating gradient which SC cavities can sustain compared to NC cavities minimizes the required length of accelerating sections, therefore minimizing the overall disruption to the beam quality.

Niobium is currently the material of choice for superconducting cavities. The primary reason for this choice is that niobium has the highest critical temperature of all pure metals (T_c = 9.25 K), and in addition is relatively simple to use in terms of fabrication. Many compounds (including the new high-T_c ceramic materials) have shown higher critical temperatures than niobium. None of these materials can match niobium, however, either in terms of its ease of use, or in terms of its performance with increasing RF fields.

1.1.3. Theoretical Potential of SRF Cavities

It is well established that even at T = 0 K, a sufficiently high surface magnetic field can destroy superconductivity. The limiting field is referred to as the critical field. There are two types of classical superconductors, which have the same fundamental mechanism for superconductivity, but differ in their behavior with increasing magnetic fields. The difference in behavior can be traced to differences in the free energy associated with NC/SC boundaries on the RF surface, which are controlled by such parameters as the coherence length and the penetration depth. For a more complete description of these phenomena, see reference 8.

In Type I superconductors, the magnetic field is completely shielded from the superconductor interior for fields up to the critical field H_c. Above this field, the magnetic field penetrates completely, destroying the superconductivity.

In Type II superconductors, the magnetic field is completely expelled up to a first critical field, H_{c1}. Above H_{c1}, the magnetic field penetrates partially, with normal conducting regions isolated on the surface of the superconductor. This behavior persists up to a second critical field, H_{c2}. Above H_{c2}, the field penetrates completely, destroying the superconductivity.

These descriptions are for DC or steady fields at $T = 0$ K. Above absolute zero, the critical fields drop approximately according to equation 1-9.

$$H_c(T) = H_c(0)\left[1 - \left(\frac{T}{T_c}\right)^2\right] \tag{1-9}$$

In RF conditions, the requirements are relaxed somewhat, as the penetration of the magnetic field into the RF surface requires nucleation of a flux line, which requires a finite amount of time. The nucleation time has been determined[23] to be such that the complete shielding of magnetic fields can persist to fields higher than the critical field, up to a limit termed the superheating critical field, H_{sh}. In niobium, the superheating critical field is estimated to be approximately $H_{sh.} = 2300$ Oe.[8]

Experimentation with specially designed SRF non-accelerating cavities[24],[25] has clearly shown that there are no fundamental limits to the peak electric field on a niobium surface up to $E_{peak} = 200$ MV/m. The theoretical limit on accelerating cavity performance is therefore dependent on the cavity magnetic fields.

In typical SRF accelerating cavities, $H_{peak} = 2300$ Oe corresponds to accelerating gradients of 50 to 60 MV/m. Given that accelerators with niobium cavities generally operate at $E_{acc} = 5$-10 MV/m, the need for further work is clear. Accelerating gradients of 20 to 30 MV/m are necessary to make linear colliders with SRF technology economically attractive.[1]

1.2. Historical Limitations on SRF Cavities and Their Solutions

SRF cavities have been in operation for over twenty-five years, and through that time many limitations have been encountered and overcome. We will mention several of the more important limitations here, along with the method in which they were overcome.

1.2.1. Multipacting

Multipacting, or Resonant Field Emission, was an early limitation on SRF cavities. In multipacting, electrons emitted from the RF surface into the cavity follow a trajectory such that they impact back at the surface of the cavity an integral number of RF cycles after emission. The impacting electron then frees further electrons which repeat the cycle causing an avalanche effect, until all available power goes into this process.

Multipacting was overcome by changing the cavity cross section from a rectangular to a spherical or elliptical shape, as was shown in Figure 1.1. In the spherical shape, the fundamental mode has no electrical field at the equator region of the cavity. Furthermore, the nature of the fields are such that emitted electrons will drift towards the equator, eventually ending up in a region with zero surface electric field, thus stopping the avalanche effect.

1.2.2. Thermal Breakdown

Thermal breakdown, or quench, is a phenomenon where the temperature of part or all of the RF surface exceeds the critical temperature, thereby becoming normal conducting and rapidly dissipating all stored energy in the cavity fields. Thermal breakdown is most often a localized effect, where a small "defect" in the RF surface dissipates power more rapidly than the surrounding superconducting walls. Breakdown occurs when the power dissipation overwhelms the ability of the surrounding metal to conduct

away the heat. The field at which breakdown occurs is dependent upon multiple factors, including thermal conductivity of the bulk niobium, heat transfer from the niobium to liquid helium bath, and size and resistance of the defect.

The primary method of bypassing the thermal breakdown limitation has been inproving the thermal conductivity of the niobium. Improved thermal conductivity comes from improved purity of the metal. Material purity, and thus thermal conductivity, are described via the Residual Resistivity Ratio (*RRR*), which is the ratio of the resistivity at room temperature to the normal conducting resistivity at 4.2 K. A more complete description of *RRR* and its measurement can be found in Appendix D. Bulk material purity has improved greatly (from *RRR* of 10-30 to $RRR \geq 250$) in the last twenty years through improved purification methods, e.g. high vacuum electron beam melting.[26]

Niobium can be further purified of interstitial oxygen by solid state gettering.[27]-[29] In gettering the niobium is baked to 1400° C, with exposure to either yttrium or titanium vapor. The vapor adsorbs to the surface of the niobium; the higher affinity of Y or Ti (compared to Nb) to oxygen effectively removes the oxygen from the bulk niobium. Following baking, the oxide layer at the outer surface is removed, leaving purified bulk niobium. Typically, $RRR = 250$ material can be purified to $RRR = 500$ through yttrification.

The earliest niobium SRF cavities were made of reactor grade material, $RRR \approx 25$, and experienced thermal breakdown with suface magnetic fields in the range $H_{surface}$ = 200-400 Oe (corresponding to E_{peak} = 10-20 MV/m in a typical SRF cavity). Improvement to $RRR = 250$ raised breakdown fields to 800-900 Oe (E_{peak} = 35-40 MV/m). Gettering

improvements to RRR = 500 have raised breakdown fields as high as 1200-1300 Oe (E_{peak} = 50-60 MV/m), as we will show below.

In the course of the HPP work, another type of thermal breakdown phenomena was encountered, termed Global Thermal Instability (GTI). In GTI, the heating is nearly uniform over all high surface magnetic field regions. GTI occurs because even without localized defects, the RF surface retains some uniform residual RF resistance. GTI is initiated when the power dissipation due to the residual resistance raises the temperature enough such that the exponentially growing BCS surface resistance becomes dominant, causing a thermal runaway process which leads to a thermal breakdown. An extensive description of the GTI phenomenon and its observation is given in Appendix F.

Each of these types of thermal breakdown are driven by the surface currents, and therefore the surface magnetic fields of the cavity. This is an important consideration which will be encountered again several times in the course of this work.

1.2.3. "Q Virus"

The "Q virus[30][31]" is a recently discovered phenomenon, in which excessive hydrogen in high purity niobium can condense onto the RF surface of the cavity, forming a niobium hydride with poor superconducting characteristics. The Q virus is characterized by an anomalously low cavity Q (high surface resistance) at low electric field, followed by a rapid Q decrease with increasing fields. Once this behavior has been identified, a vacuum bake to 900° C is sufficient to remove the hydrogen from the niobium, while not damaging the cavity.

The hydrogen contamination can be avoided completely, however, by controlling the acid etch which is used to prepare a sufficiently clean

surface for RF testing. Investigation of the Q virus indicated that hydrogen contamination was a danger when the temperature of the niobium/acid region rises above 20-25° C. This condition is avoided by controlling the rate of reaction, through acid temperature, volume of acid, and time of exposure. In extreme geometries, such as 3 GHz nine-cell cavities with a relatively high surface to volume ratio and small beam tube radius, this is not always sufficient, and the 900° C bake is standard procedure.

1.3. Present Limitation: Field Emission

With the problems described in the last section overcome, the primary limitation of the last five to ten years has been field emission (FE) of electrons out of the niobium surface in the presence of high surface electric fields. FE loading is detrimental for several reasons. Emitted electrons impact elsewhere on the cavity surface, heating the surface, and therefore increasing the surface resistance. This increases power dissipation of the cavity, as well as adding to the load on the refrigerator. In extreme cases, FE heating of the cavity walls can lead to thermal breakdown, as described in the last section. Acceleration of emitted electrons absorbs power out of the electromagnetic fields which would otherwise be available for acceleration of the particle beam. Eventually, as fields are raised, the power dissipation into FE related processes limits the attainable fields in the cavity.

1.3.1. Fowler-Nordheim Theory

The emission of electrons from a metal-vacuum interface in the presence of an electric field normal to the surface was intially treated as a quantum mechanical tunneling process by Fowler and Nordheim.[32] Their theory predicted the field emitted current density, in equation 1-10, and the total current, equation 1-11.

$$j_{FN} = \frac{C}{\phi\, t^2(y)} E^2 \exp\left(-\frac{B\,\phi^{\frac{3}{2}}\, v(y)}{E}\right) \tag{1-10}$$

$$I_{FN} = j_{FN}\, A \tag{1-11}$$

where E is the applied electric field, ϕ is the work function of the metal, C and B are constants, A is the emitter area, $y = \sqrt{e^3 E/\phi^2}$, and $v(y)$ and $t(y)$ are functions which arise due the inclusion of image charge effects. $v(y)$ and $t(y)$ are near unity for typical conditions, and therefore standard practice is to omit them. We follow that convention here.

According to these expressions, however, field emission should only reach hundreds of microamps, which is necessary for significant loading of an RF cavity, for fields higher than 10,000 MV/m (assuming an emitter area of 10^{-10} cm^2). Experiments showed that in real systems this level of emission occurs at fields as low as a few MV/m.

In order to explain emission at low fields within the Fowler-Nordheim model, an "enhanced" version of the theory was proposed.[33] In the enhanced Fowler-Nordheim picture, the mechanism is the same (quantum mechanical tunneling), but a local field enhancement factor β is introduced. The emission current density is then given by equation 1-12, and total current is given by equation 1-11.

$$j_{FN} = \frac{C}{\phi} (\beta E)^2 \exp\left(-\frac{B\,\phi^{\frac{3}{2}}}{\beta E}\right) \tag{1-12}$$

Initially β was postulated to arise due to geometrical effects at the surface. The enhancement due to geometrical irregularities on the surface (e.g. hemispheres, cylindrical projections, etc.) can be computed[34]-[36]. Comparison of measured values of β from the field emission current

(which were often several hundred to a thousand), with geometric asperities at the surface failed to produce any features which could result in enhancements of this magnitude.

Local field enhancement has also been predicted due to contaminants and defects on the surface of the metal. Models[37] have been proposed which introduce field enhancement due to semiconducting or insulating materials on the metal surface. In addition, surface contaminants are capable of altering the work function of the surface, thus producing similar effects to a field enhancement.

The present best model of the enhancement allows for both geometrical and material mechanisms of field enhancement. Furthermore, while no definite physical significance can be attributed to β or A, they are still useful quantities for characterizing the nature of emitters, as has been done extensively in previous studies.

1.3.2. DC Emission Studies

A great deal of study has been performed in the area of field emission out of metal surfaces under DC conditions. The investigations generally fall into one of two categories: studies of field emission and studies of vacuum breakdown or explosive emission. These two categories are related in that explosive emission is best explained as field emission extended to conditions such that the emission becomes explosive in nature.

Studies of niobium electrodes under high field DC conditions were performed by Ph. Niedermann.[38],[39] The apparatus was constructed such that it could be examined via field emission measurements, scanning electron microscope, and scanning tunneling microscope without vacuum break. This project has shown a clear link between surface contaminants and field emission. In addition, the studies of heat treated niobium elec-

trodes helped lead to the use of high temperature vacuum baking as a successful method of RF cavity preparation. This will be discussed further below.

Further in depth studies of DC emission have been performed by the group of Latham.[40]-[42] From this work has come several models of non-geometric mechanisms of local field enhancement. In addition, extensive studies of gas conditioning of electrodes were performed.

Vacuum breakdown refers to processes where high DC voltages under vacuum conditions result in an arcing process. We will show later in this dissertation that this phenomenon is analogous to RF processing. Extensive studies have been performed in this area, therefore we will only discuss those phenomena which will prove useful for comparison with the results to be detailed later in this thesis. Comprehensive reviews of this field are available.[34]-[36],[43],[44]

Examination of cathodes which have been exposed to high electric fields and the associated arcs has revealed extensive cratering.[34],[35],[45],[46] The craters have characteristic sizes on the order of microns. Often the craters are overlapping, showing multiple events. The explosive nature of emission processes on cathodes is clearly verified by the detection of craters.

The time required to initiate an arc has been measured[47],[48] to vary from microseconds to less than nanoseconds, with the initiation time decreasing with increasing electric field (or increasing emission current density). Further measurements on niobium surfaces[47] show that superconductivity of the cathode surface does not effect the initiation time for explosive processes.

Modelling of explosive processes and the ensuing plasma[35],[43] predict thermionic emission of electrons from the plasma cloud with velocity on the order of 10^8 cm/s. Nearly all modelling of explosive processes has been of pure metal vacuum interfaces, with field enhancement entirely due to geometric effects. The limitations of modelling only this type of emission have been pointed out,[36],[46] yet only passing reference is made to other sources of emission, such as surface contaminants.

1.3.3. Twenty Years of Knowledge in Avoiding Field Emission

Superconducting RF cavities have been in use since the late 1960's. In that time, as other limitations have been overcome, significant progress has also been made in reducing FE loading of cavities.

The most important gains, both in understanding and improved performances, have been in the area of surface cleanliness. The DC studies described in the last section clearly showed the link between contaminants and emission, therefore great effort has been put forward to reduce sources of contamination to the cavities. Cavities are now assembled in clean rooms in order to minimize atmospheric contaminants. Rinsing of cavities is perfomed with high purity liquids (e.g. deionized water or methanol).

High temperature vacuum baking of the cavity is another method of reducing surface contamination. This procedure was drawn from the DC studies of Niedermann as listed above, and in that work it was clearly shown that the effect of high temperature baking was to reduce the number of surface contaminants. Studies of heat treatment preparation of RF cavities to reduce FE at Cornell[49],[50] and Wuppertal[29] have shown significant gains in achievable surface electric fields.

Low power RF processing (up to 100 watts CW power) has also been used with some success in SRF cavities. Unfortunately, the exponentially

increasing power dissipation due to field emission quickly utilizes all available power. The mechanism of the processing was not well understood until recently.

Helium processing, or RF processing in the presence of a partial pressure of helium (10^{-5} torr), has been shown to be successful in increasing attainable electric fields by ten to twenty percent above their original values. This mechanism is not yet clearly understood. It was originally believed that the helium ions sputter the RF surface, removing condensed gases, or other contaminants. More recently, Latham has postulated that helium becomes embedded in the RF surface[42], creating electron traps, which inhibit emission. The effect of helium processing on individual sites has been shown to be reduction in field enhancement β.[50],[51]

Further gains in attainable accelerating gradient have been achieved through alteration of cavity geometry in order to minimize the ratio of peak surface field to accelerating gradient. In this manner, accelerating gradient is maximized with respect to the maximum surface electric field.

1.3.4. Thermometry as a Tool for SRF Cavity Investigation

As SRF technology has advanced, thermometry has emerged as a valuable tool for investigation of cavity behavior. Many phenomena of interest dissipate sufficient power in the cavity so that a temperature signal may be measured by sensitive thermometers located at the cavity/helium interface. Thermometry studies have been performed at many laboratories,[52]-[55] both with fixed and movable arrays of thermometers.

Field emission phenomena are observable, because emitted electrons are accelerated by the electromagnetic field and then impact elsewhere on the cavity surface. The power deposition from electron impact can cause measureable temperature rises at the outer surface of the cavity. The

thermometry signal can be modelled via solution of the relativistic equations of motion of the emitted electrons in the cavity fields, combined with heat transfer models within the niobium-helium system. Comparison of measured and simulated signals yields further information on the nature of the emission sites. Features of thermometry will be discussed further in Chapters 4 and 5, when the thermometry measurements from the HPP cavities are discussed.

1.4. The Argument for Higher Power

The preceding sections have shown the state of SRF technology at the time when the HPP program was initiated. We now explain why high power RF processing was thought to be worthy of investigation, and specifically what this study was designed to investigate.

1.4.1. Results from Previous RF Processing Studies

High power has, in fact, been used previously in SRF cavities. Campisi and Farkas[56],[57] exposed 3 GHz cavities to megawatt pulses of a few microseconds. Their results indicated the possibility of gains in low power behavior following high power, however their apparatus was not capable of testing cavities at low power without vacuum break. In addition, sustaining high fields for microseconds is not useful for SRF cavities, as the same fields and time can be obtained in copper cavities. The main advantage of SRF cavities is that they offer CW, or long pulse, or high duty cycle operation. It was unclear whether the application of megawatts of power to SRF cavities would yield any benefits to the CW performance.

High power processing with incident powers of a few kilowatts has been used routinely on 100 MHz heavy ion accelerating cavities at Argonne.[58] However, no systematic study of the characteristics and

parameters of the processing has been produced. In addition, the maximum operating fields in these cavities was 3 to 10 MV/m, well below that necessary for obtaining E_{acc} = 20-30 MV/m.

1.4.2. Results from Normal Conducting RF Processing Studies

RF processing is a routine procedure in the commissioning of NC accelerator cavities. Cavities are "conditioned" with high power to reduce the field emission to an acceptable level for cavity operation. Loew and Wang[59],[60] have performed extensive studies which show that high power is an excellent tool for extending the capabilities of NC cavities.

With the common use of high power RF processing normal conducting cavities, it is reasonable to ask why it has not been used previously in SRF cavities. The primary reason for the hesitancy in applying high power to SRF cavities has been fear of damage to the superconducting surfaces. Loew and Wang examined the high field regions of NC cavities following high power processing, and found extensive cratering and surface erosion. The fear for SRF cavities was that surface damage of this nature would result in cavity degradation, both through increased surface resistance (decreased Q) and thermal breakdown due to poor thermal characteristics of the cratered regions. Fortunately, this study showed that these fears appear to have been groundless.

1.4.3. What was Missing from Previous Processing Studies?

The indications were clear that high power had the potential to be a method for field emission reduction. What was missing was an extensive study of the potential and the nature of high power processing in superconducting RF cavities. The normal conducting experiences showed that high power processing was clearly successful in extending the attainable

gradients when field emission was the limiting factor. The limited work on superconducting cavities indicated that processing was worth investigating.

Clearly what was needed was a systematic study of high power processing as a method of reducing field emission in SRF cavities. The HPP project was begun with the intention of performing such a study. The primary questions to be answered by this investigation are:

1) Do the benefits of HPP extend to CW or long pulse operation of SRF cavities?

2) What is the mechanism of processing in SRF cavities?

3) What are the important parameters to control to get the best processing results? Possibilities include pulse length, incident power, input coupling, surface field, etc.

4) How high must the power be to be useful?

5) What are the limitations of the method?

6) Is there any difference between HPP and CW RF processing?

We present the answers to these questions in the remainder of this dissertation. Several specialized apparati were constructed or obtained to facilitate this study. The ability to conduct all of these experiments on a single apparatus, without breaking the vacuum, was a significant step forward, as exposure of the RF surface to contamination is a well documented source of field emission. A thermometry system for single cell cavities was constructed with the intention of investigating the local effects of high power processing. Scanning Electron Microscopy investigation of RF processed surfaces was available to further investigate the nature of processing.

1.4.4. Dissertation Organization

The remainder of this dissertation is organized in the following manner: Chapter 2 describes the apparati and procedures used in the HPP ex-

perimental program. Chapter 3 is a general overview of the results showing the success of the HPP experiments. Chapter 4 describes the microscopic investigation of RF surfaces following experimentation, including correlation of surface features to measurements made during RF testing. Chapter 5 contains analysis of thermometry from single-cell experiments, and a working model of a mechanism for RF processing. Chapter 6 is an analysis of the thermal limitations encountered in HPP experiments. Chapter 7 contains conclusions and remarks.

CHAPTER 2: APPARATUS AND PROCEDURES

2.1. Introduction

In this chapter, we detail the apparatus and procedures of the HPP experimental program. Much of the experimental apparatus was previously described in the Masters Thesis[61] titled "An Apparatus for High Power Processing of Field Emitters in Superconducting RF Cavities," and therefore will not be described as thoroughly here. The experimental procedures and techniques are ever changing, as we learn more about the behavior of the apparatus and cavities. They will be presented in their current form (March 1993), with special note made of techniques which have changed significantly over time, due to new insights.

Many terms and equations will be defined as needed, however a more complete list of definitions and relationships can be found in Appendix A.

2.2. Apparatus

2.2.1. 3 GHz Niobium Accelerator Cavities

The cavities used are 3 GHz niobium accelerator cavities, single-cell and multi-cell. Three different cavities were used in the HPP program. Figure 2.1 shows a diagram of one quarter of a cell in an accelerating cavity. All cavities used are cylindrically symmetric about the beam axis, and the individual cavities are defined by two circular sections connected by a line segment. Defining parameters are shown in Figure 2.1. The values of these parameters for each of the cavity types used are listed in Table 2-1.

The bulk of the experiments were performed with single-cell cavities, termed the S3C1 shape. Nine-cell cavities (shape name S3C9) were also constructed of a similar geometry, though the end cells require a slightly

TABLE 2-1: DEFINING CHARACTERISTICS OF CAVITY SHAPES USED IN THE HPP EXPERIMENTAL PROGRAM (All dimensions in cm)

Shape	R1	R2	x1,z1	x2,z2	x3,z3	x4,z4	α
S3C	1.651	0.602	2.88, 0.0	3.31, 1.60	2.10, 1.92	2.26, 2.50	75°
W3C	2.183	0.320	2.85, 0.0	2.29, 2.18	1.99, 2.18	1.67, 2.50	90°

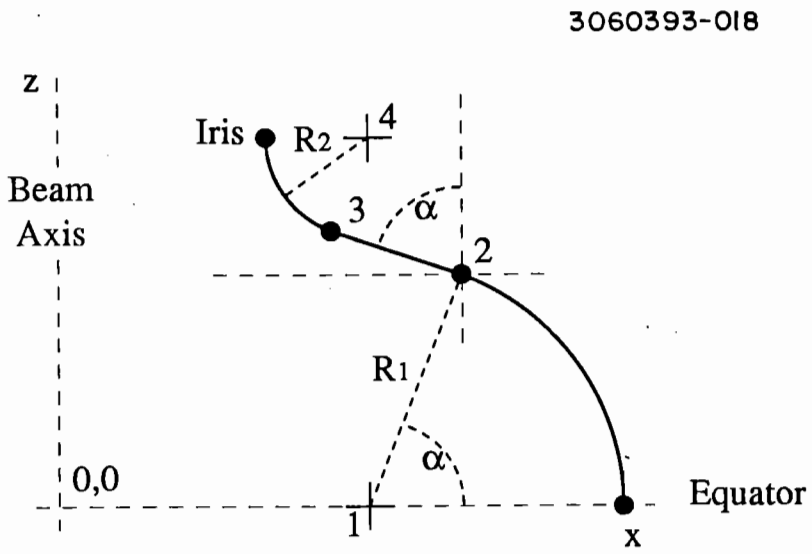

Figure 2.1. Diagram of one quarter cross section of a cell of an accelerating cavity, with defining characteristics shown.

different geometry to insure field flatness (equal field in all cells). Finally, a special two-cell cavity was constructed in the geometry (named the W3C2 shape) used by the SRF group at the University of Wuppertal for a special set of experiments, testing the magnetic/electric field relationship to HPP results (described more fully in Chapters 3 and 6). In all, the HPP experiments used nine single-cell cavities, two nine-cell cavities, and one two-cell cavity. These cavities were tested multiple times, for a total of over twenty single-cell experiments, ten nine-cell experiments, and three two-cell tests. Successive tests of the same cavity were preceded by an acid etch of the RF

surface, removing a minimum of 10 microns. We believe that this is equivalent to testing a new cavity. Past thermometry studies[62] support this conclusion, as the field emission behavior of the repeated test is uncorrelated to the previous history of the cavity.

A diagram of each of these cavities, with beam tubes included is shown in Figure 2.2. Also included in Figure 2.2 are RF characteristics of each cavity as determined by the SUPERFISH[4] program codes.

2.2.2. Low Power RF Circuit

Low power CW RF measurements are necessary to measure the baseline (low field) Q_0, the degree of field emission (and other) loading of the cavity, and the thermal breakdown field (if reached). A diagram of the low power RF circuit used in conjunction with the HPP program is shown in Figure 2.3. In order to keep the RF frequency of the oscillator locked on the cavity's resonant frequency, a feedback mechanism must be used. In this circuit, frequency locking is achieved through a phase lock loop (PLL), where the difference between the forward and transmitted powers (obtained from a mixer) is fed back into the oscillator as the FM input. The PLL is highlighted in Figure 2.3.

The breakpoints shown in Figure 2.3 are for input to the HPP circuit, which is described in Appendix H.

2.2.3 The HPP Experimental Test Stand

The test stand is shown in Figures 2.4 (photograph), and Figures 2.6 and 2.7. (diagrams). Important features are pointed out in Figures 2.6 and 2.7. We will discuss the most important characteristics here.

Coupling variation: The HPP test stand was constructed such that the input coupling to a cavity was smoothly variable between $Q_{ext} = 10^5$ and $Q_{ext} = 10^{10}$, with no break of the vacuum system. The RF input coupler is a

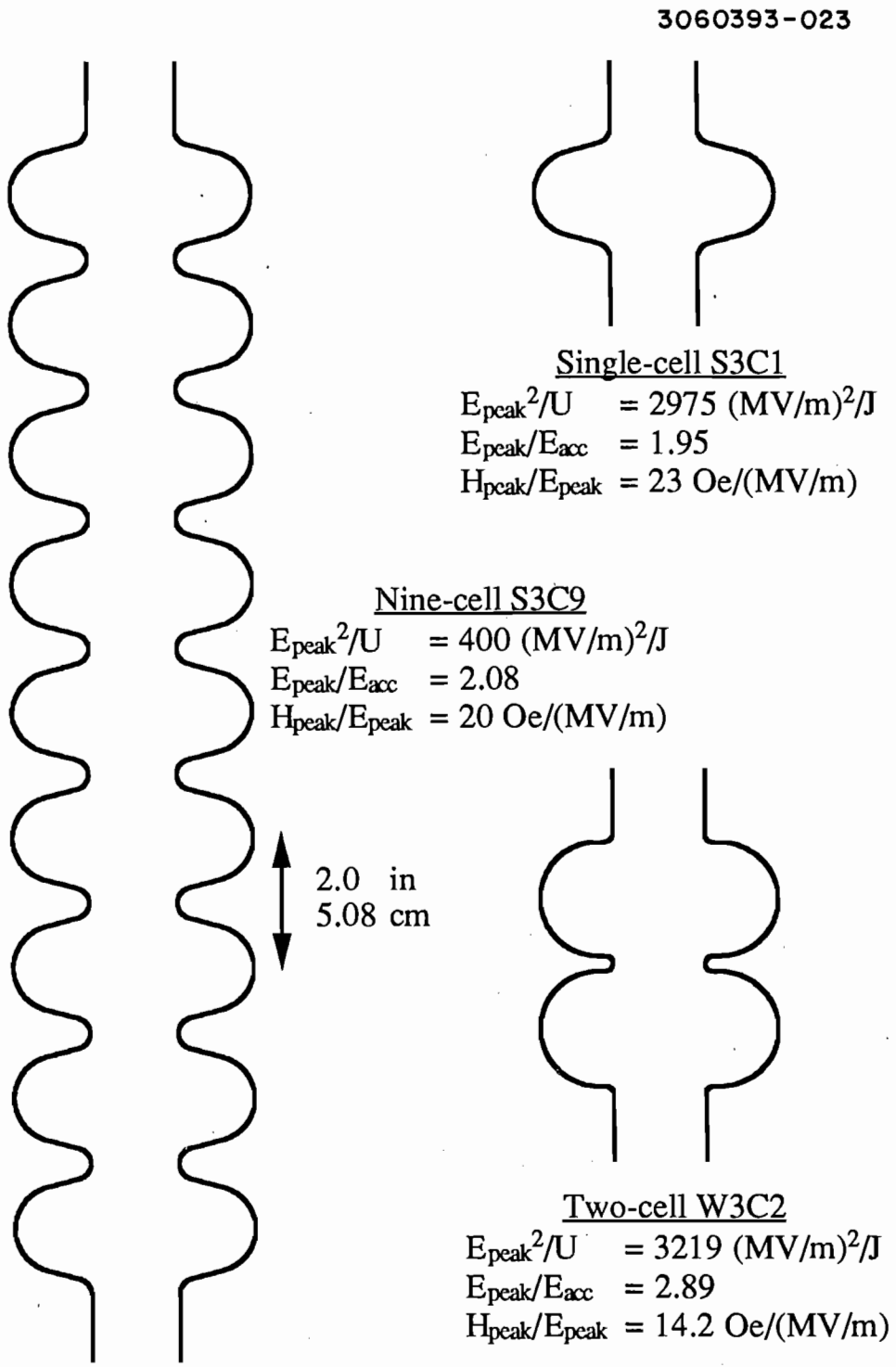

Figure 2.2. Diagrams the cavities used in the HPP program. RF characteristics shown as determined by the SUPER-FISH[4] programs.

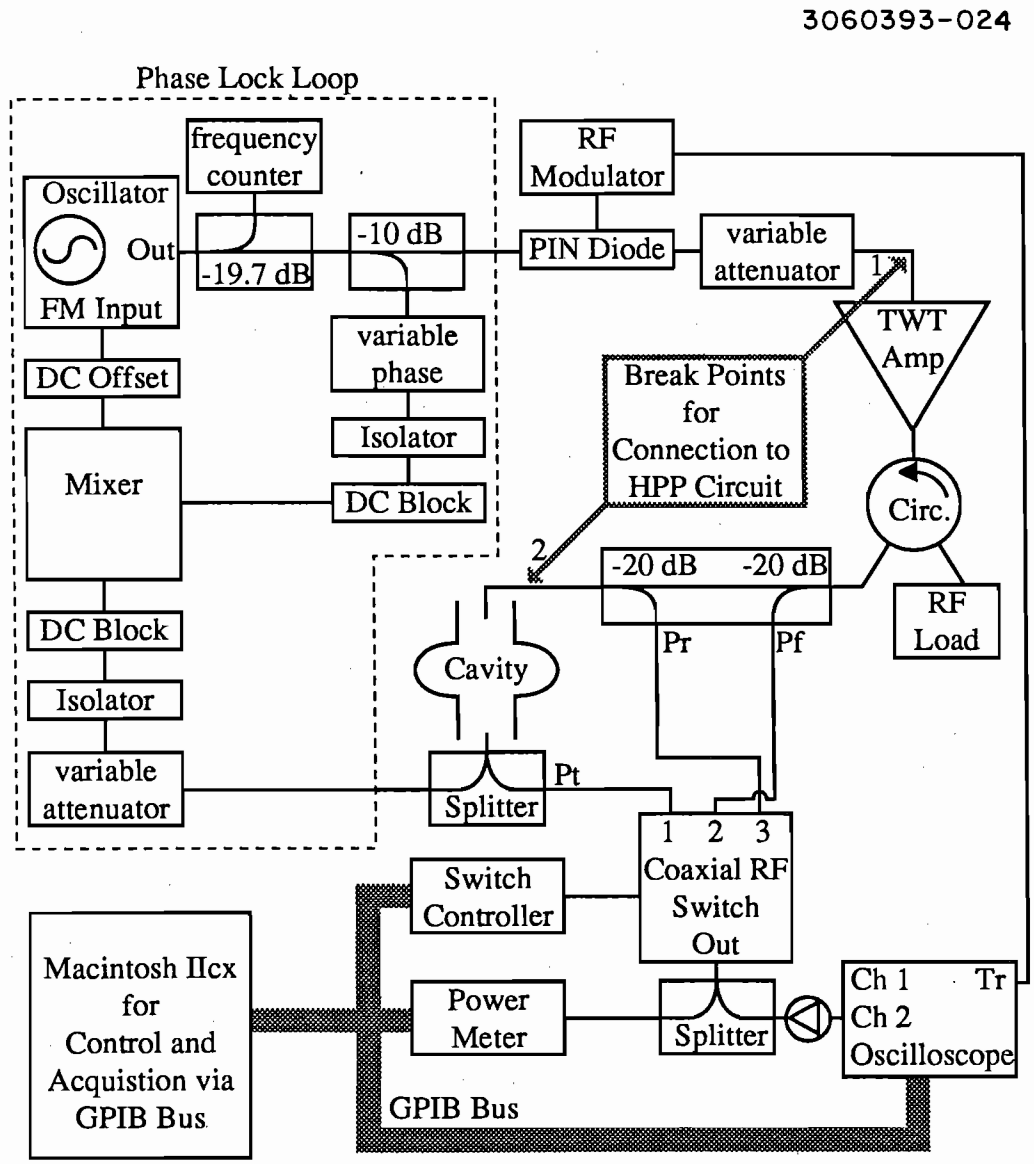

Figure 2.3. Low Power RF measurement circuit used in the HPP Experiments. Breakpoints shown are for connection to the HPP circuit (See Appendix H).

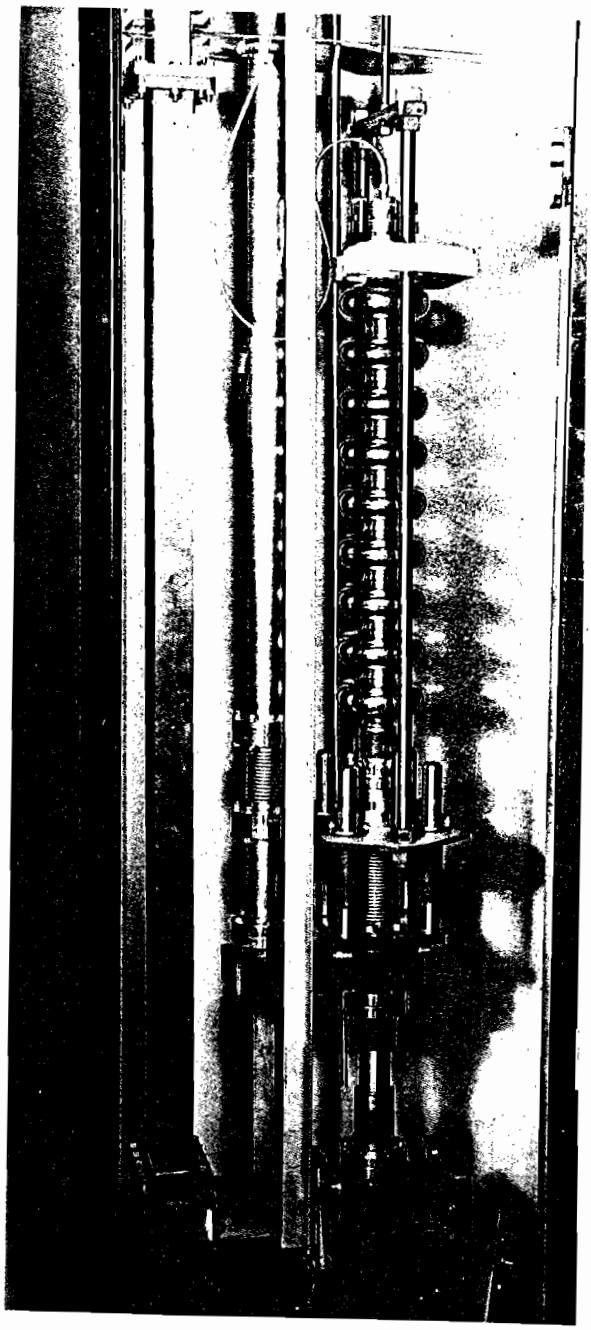

Figure 2.4. Photograph of the HPP Test Apparatus.

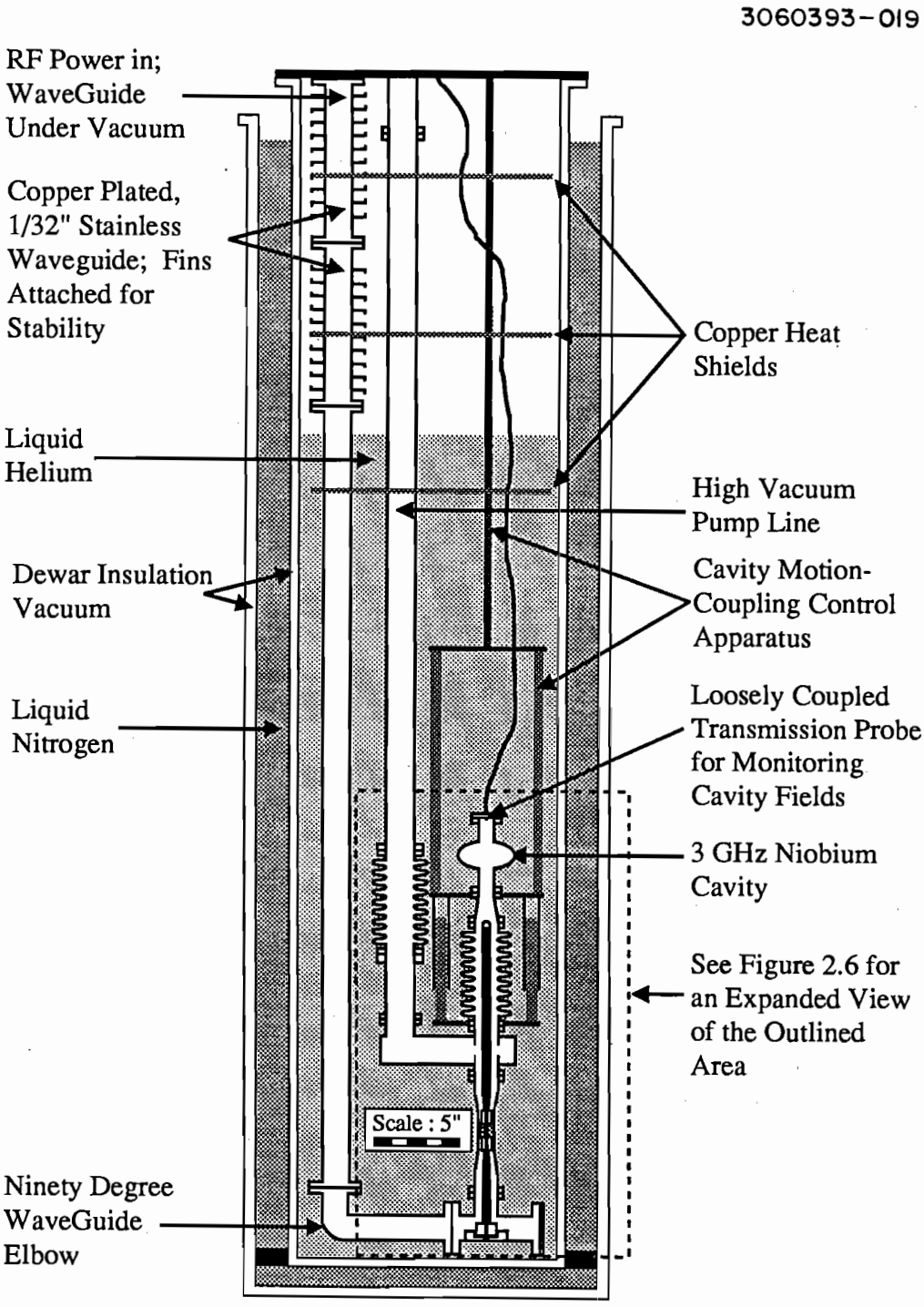

Figure 2.5. Overall diagram of the HPP apparatus.

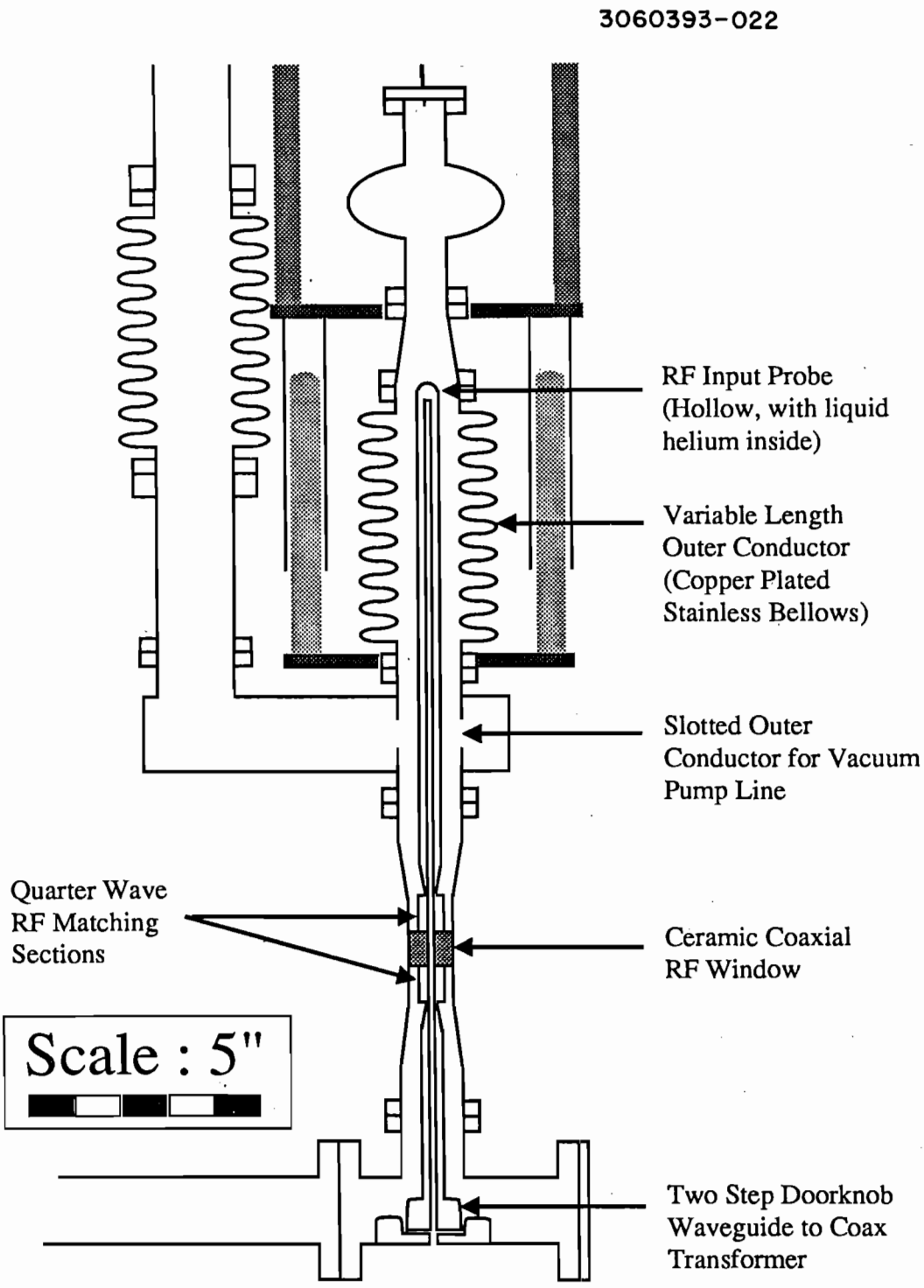

Figure 2.6. Diagram of the HPP test stand, highlighting the cavity/input probe region.

coaxial probe aligned with the beam axis of the cavity. The coupling variation is accomplished through moving the cavity relative to the fixed RF input probe. The wide variation in coupling is required because low power RF testing is done at near unity coupling in order to couple all available power into the cavity for maximum field, and also to minimize error propagation. (See Appendix G for a discussion of error propagation in RF measurements.) Superconducting 3 GHz cavities have Q_0 values in the range 10^9 to 10^{10}, setting the upper limit on Q_{ext}. HPP Processing is done in a highly overcoupled ($Q_{ext} >> Q_0$) condition, for two reasons: (1) The available RF pulse length in the HPP circuit is variable between 100 μsec and 2 msec. This is short compared to the characteristic time of a unity coupled cavity, which is typically hundreds of milliseconds for an SRF cavity. The cavity must therefore be loaded such that the characteristic time is tens or hundreds of microseconds in order to get useful fields during the RF pulse. This requirement stipulates that the input coupler Q_{ext} vary as low as 5 - 10 x 10^5. (2) It will be shown in the analysis of HPP results (Chapter 3), that the Q_0 of the cavity drops as low as 10^6-10^7 during HPP processing. The ability of the test stand to reach $Q_{ext} = 10^5$ makes it possible maintain unity coupling under extreme cavity loading situations, which in turn allows maximum power coupled into the cavity for RF processing. Because of the variable coupling, it was possible to measure the effect of HPP processing, using CW power, without breaking the cavity vacuum.

High Power Transmission Capability: The primary goal of the HPP experimental program has been to investigate high power processing of cavities, therefore it is imperative that the test stand be capable of consistently transmitting up to 200 kW peak power to the cavity without significant reflection.

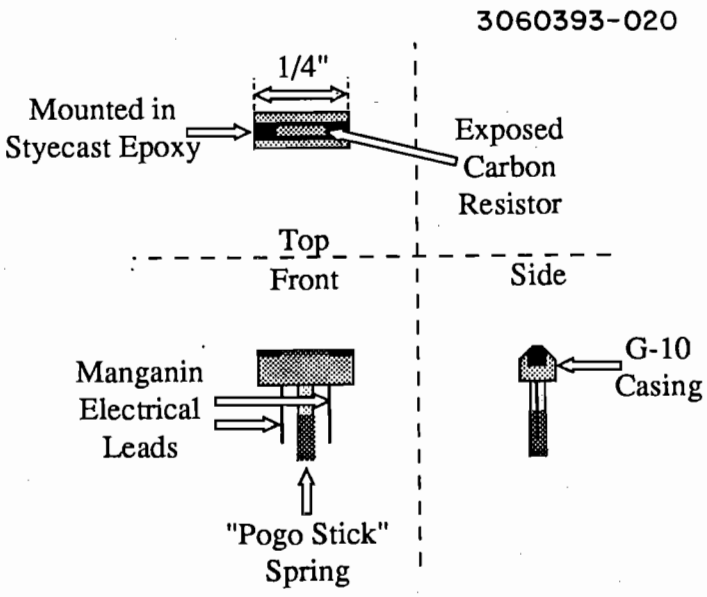

Figure 2.7. Diagram of the thermometers used in the HPP experiments.

2.2.4. Thermometry for Single-cell Cavities

Thermometry is a standard diagnostic technique for superconducting cavities, as discussed in Section 1.3.5. Figure 2.7 shows a diagram of the thermometer device used in this program. This thermometer was developed at Cornell LNS[54].

The sensitive element of the thermometers is a 1/8 W, 100 Ω Allen-Bradley resistor. At cryogenic temperatures (1-5 K), the resistors have a resistance on the order of 10 kΩ, with a temperature gradient of 10 Ω/mK, making them easily sensitive to temperature changes on the order of mK Electrical leads are low thermal conductivity manganin wires, which are spot welded to the resistors copper leads. The thermometers are mounted in G-10 board with Stycast epoxy. One surface is ground down to expose the carbon resistor, with care being taken to not expose the metal leads. Finally, the carbon surface is painted with an electrically insulating varnish.

The thermometers for the HPP experimental program are mounted in a fixed array, with ten mounting boards equally spaced around the azimuth

of the cavity and ten resistors on each of the boards for a total of 100 thermometers. The thermometer positions with respect to the cavity are shown in Figures 2.8(a) (profile), and 2.8(b) (axial cross section). A photograph of the thermometry system is shown in Figure 2.8(c). A thin layer of apiezon N grease is used to glue the thermometers to the outer wall, insuring good thermal contact. A more complete description of the resistors can be found in reference 15.

The measurement apparatus for thermometry is shown in Figure 2.9. Calibration of the thermometers is done individually for each resistor while cooling the helium bath, using a calibrated germanium resistance thermometer (GeRT). The actual measurements are voltage measurements, made with a constant current DC 10 μA source. As is shown in Figure 2.9,

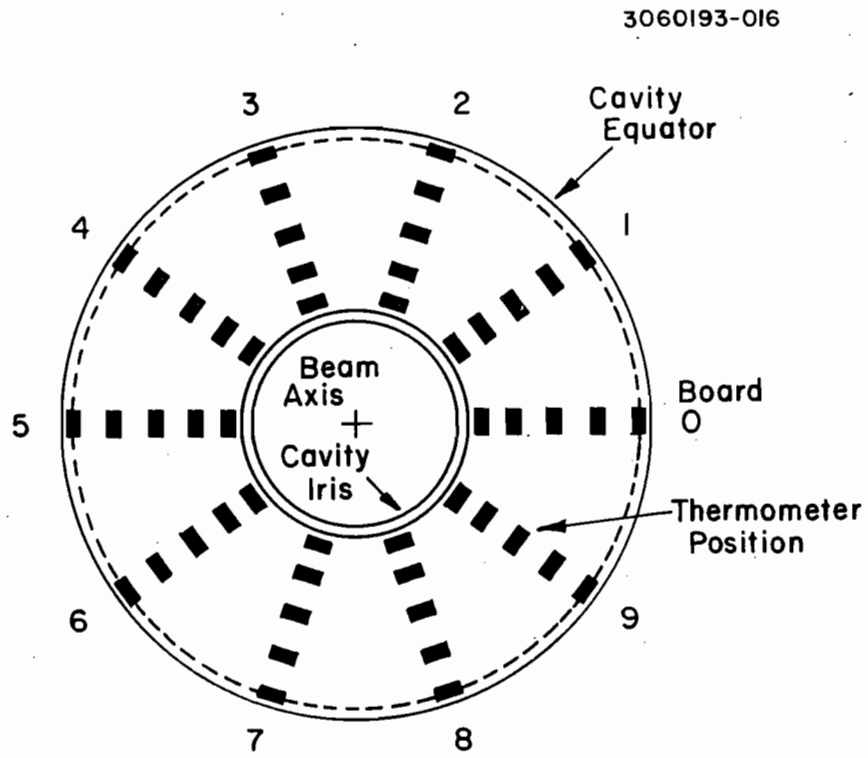

Figure 2.8 (a). Axial view of thermometer positioning on a single cell S3C cavity.

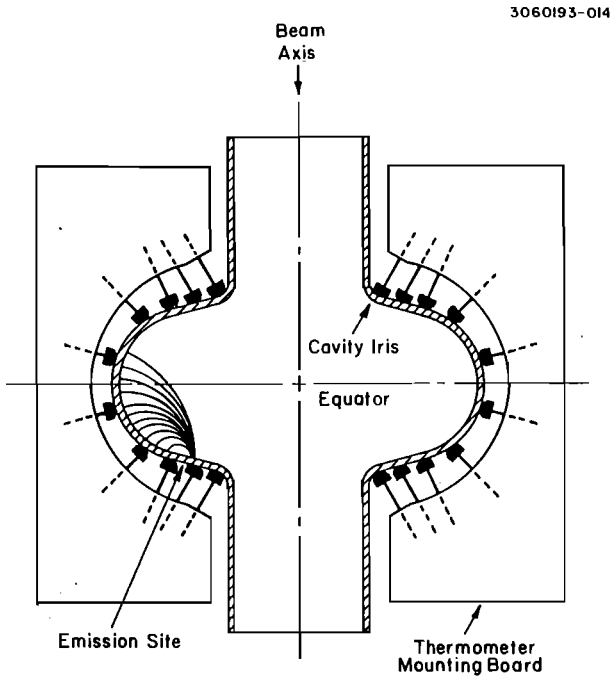

Figure 2.8 (b). Cross section view of thermometer and mounting boards for a single cell S3C cavity.

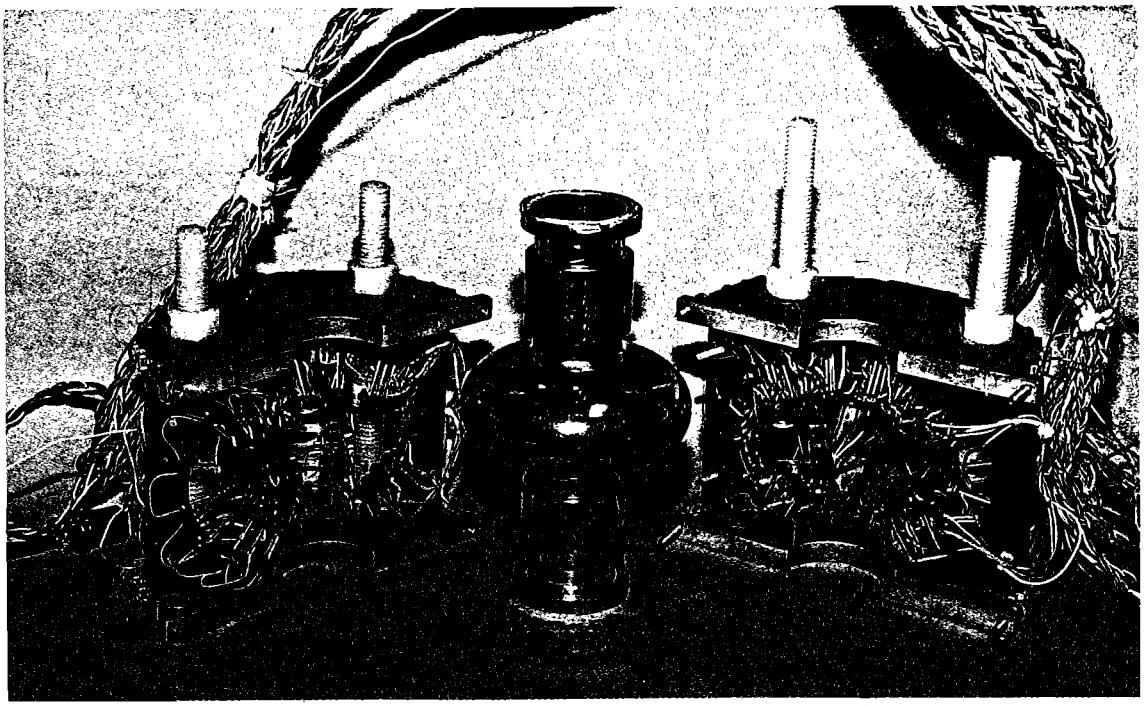

Figure 2.8 (c). The thermometers and mounting apparatus shown with a typical S3C Cavity.

each resistor has its own V+ connection, while all share a common ground. Switching between resistors is controlled by a Keithley 706 Scanner, which is controlled from a Macintosh IIcx via a GPIB connection. The thermometer measurement program, the analysis programs, and the thermometry scanning procedure will discussed in the next section.

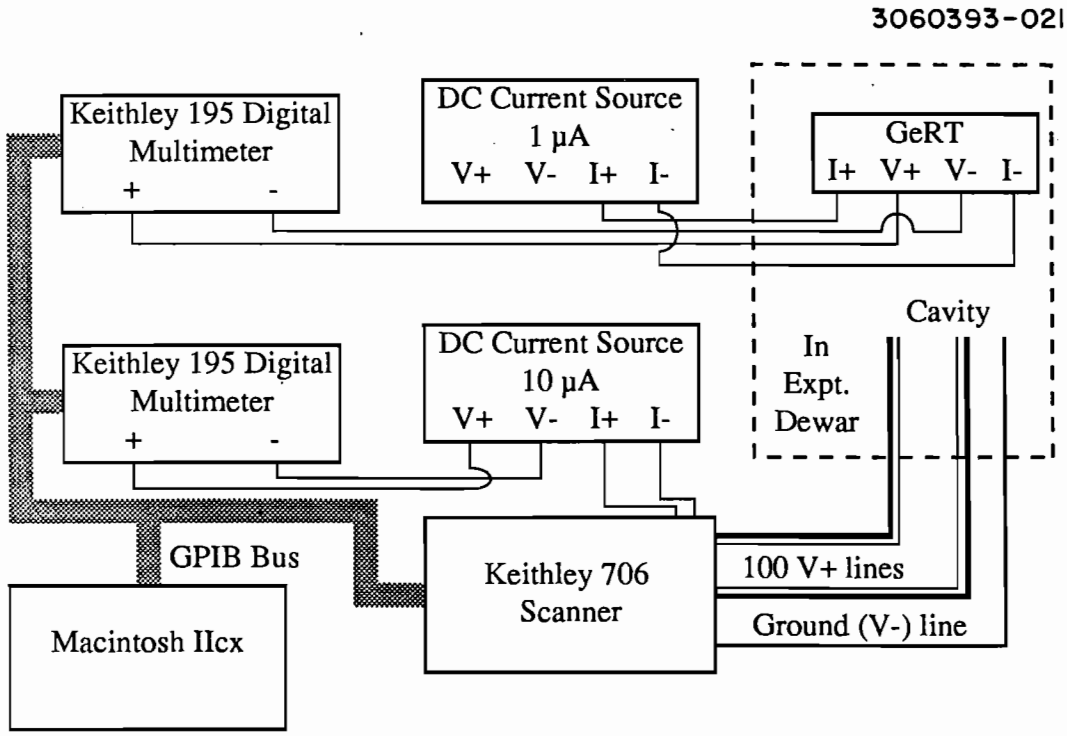

Figure 2.9 Measurement apparatus for thermometry measurements.

2.3. Experimental Techniques and Procedures

2.3.1. Cavity Fabrication

Niobium SRF cavities are fabricated with the following method:

(1) Flat plates of high purity (*RRR* ≈ 250) 1/16" (1.6 mm) niobium are deep drawn into the shape of cavity half cells, and then trimmed. Beam tubes are swaged from medium purity (*RRR* ≈ 25) niobium tubing. Flanges are machined from medium purity bulk niobium.

(2) All parts of the cavity are de-greased, de-rusted (sulfuric acid soak for 24 hours, starting temperature 100° C), and etched (approximately

2 μm removal) with Buffered Chemical Polish (BCP), a mixture of Hydrofluoric Acid, Nitric Acid, and Phosphoric Acid.

(3) At this stage the cavity parts may be further purified (for improved *RRR*, as discussed in Chapter 1) through yttrification.

(4) All welds (equator, irises, and flange to beam tube) are made in a high vacuum (10^{-5} torr) electron beam welder.

(5) Final degreasing, followed by heavy chemistry (approximately 40-50 μm surface removal). The acid reaction must be temperature controlled to prevent hydrogen contamination of the metal during the heavy chemistry, lest the cavity fall victim to the "Q disease", which was described in Section 1.2.3. In multi-cell cavities, such as the nine-cell cavities used in the HPP program, heavy etching is followed by an ultra-high vacuum, 900° C bake out, in order to drive the hydrogen from the niobium RF surface.

(6) [Multi-cell cavities only]. The field flatness must be measured (and corrected if necessary), as described in Appendix C.

2.3.2. Cavity Preparation for Cold RF Test and HPP

The cavities are prepared for cold testing in the following manner:

(1) Clean and de-grease the cavity with hot (60° C) high-purity, deionized (DI) water and detergent.

(2) If the cavity has been previously used in an experiment, soak the cavity in nitric acid for thirty minutes to remove all traces of indium (used as gaskets in vacuum joints). Indium traces have been found associated with many FE sites, making its removal a necessary step in re-use of the cavity. This is more thoroughly discussed in Chapter 4.

(3) Etch the cavity in BCP for two minutes (8-10 microns of surface removal), maintaining roughly constant temperature (T = 15° C) during the

etch. If the temperature is not controlled, the hydrogen contamination previously discussed can be encountered.

(4) Rinse the cavity thoroughly in DI water. For single cell cavities, this is done by submerging the cavity successively in several containers of DI water. For multi-cell cavities, the rinse is performed by connecting the cavity to a closed filtered loop of DI water for two to three hours.

(5) [Multi-cell cavities only] Field flatness is once again measured, and adjusted, if necessary.

From this point onward, all steps are performed in a clean room area (Class 100 at least), with workers dressed in clean room clothing to minimize contamination to the cavity interior.

(6) Rinse the cavity with high purity methanol, pouring two to three liters of the methanol through the cavity while rotating the cavity.

(7) Subject the cavity to ultrasonic vibrations, with high purity methanol inside the cavity. Drain the methanol, and pour two to three more liters of methanol through the cavity.

(8) Allow the cavity to dry horizontally in a Class 10 clean area.

(9) Mount the transmission probe endplate to one end of the cavity while still in the Class 10 clean area. Enclose the cavity in a clean nylon bag.

In order to preserve the high vacuum characteristics of the test stand, the time that the test stand is left open is minimized. While the test stand is open, dry nitrogen is flowed through the apparatus to further minimize contamination.

(10) Mount the cavity to the test stand in a Class 100 clean area, with minimal time between removal from the nylon bag and mounting to the stand.

(11) Slow evacuation of the cavity vacuum via turbo pump.

(12) When the turbo pump vacuum reaches equilibrium, close valves to the turbo pump, and open to triode ion sublimation pump.

(13) Allow two to three days for the cavity to thoroughly evacuate before cold testing. Typically the pump vacuum drops to 4×10^{-8} torr.

(14) One day before cold test, put the test stand into the experimental dewar, evacuate the helium can, and back fill with helium gas. Fill the nitrogen jacket with liquid nitrogen, and allow to cool overnight.

2.3.3. Cavity Test Procedures

The RF cold testing procedure is easily described via flow chart diagram Figure 2.10. We will expand upon those portions of the flow chart which require more explanation here. The data measurement and logging for all parts of the HPP program are controlled by a Macintosh II computer running program **SRF_Cavity**, which is written in the LabVIEW 2™ programming language, from National Instruments. Figure 2.11 shows the display screen of **SRF_Cavity**, with a typical set of measurements displayed.

Initial Check of Q_0 at 4.2 K: The Q_0 of the cavity is checked at 4.2 K, to determine if the Q_0 is acceptable for further experimentation. At 4.2 K, the Q_0 should be dominated by the BCS surface resistance, and thus be greater than 6×10^7. If the 4.2 K Q_0 is lower than 6×10^7, the cavity is unacceptably loaded, and its Q_0 will not improve enough upon cooling to warrant further experimentation.

Power Calibration: Calibration of E_{peak} with P_t is performed as follows: Cavity Q_0 is determined by measuring characteristic decay time of the emitter power with the forward power modulated, as shown in the reflected power trace in Figure 2.12. The emitted power is directly

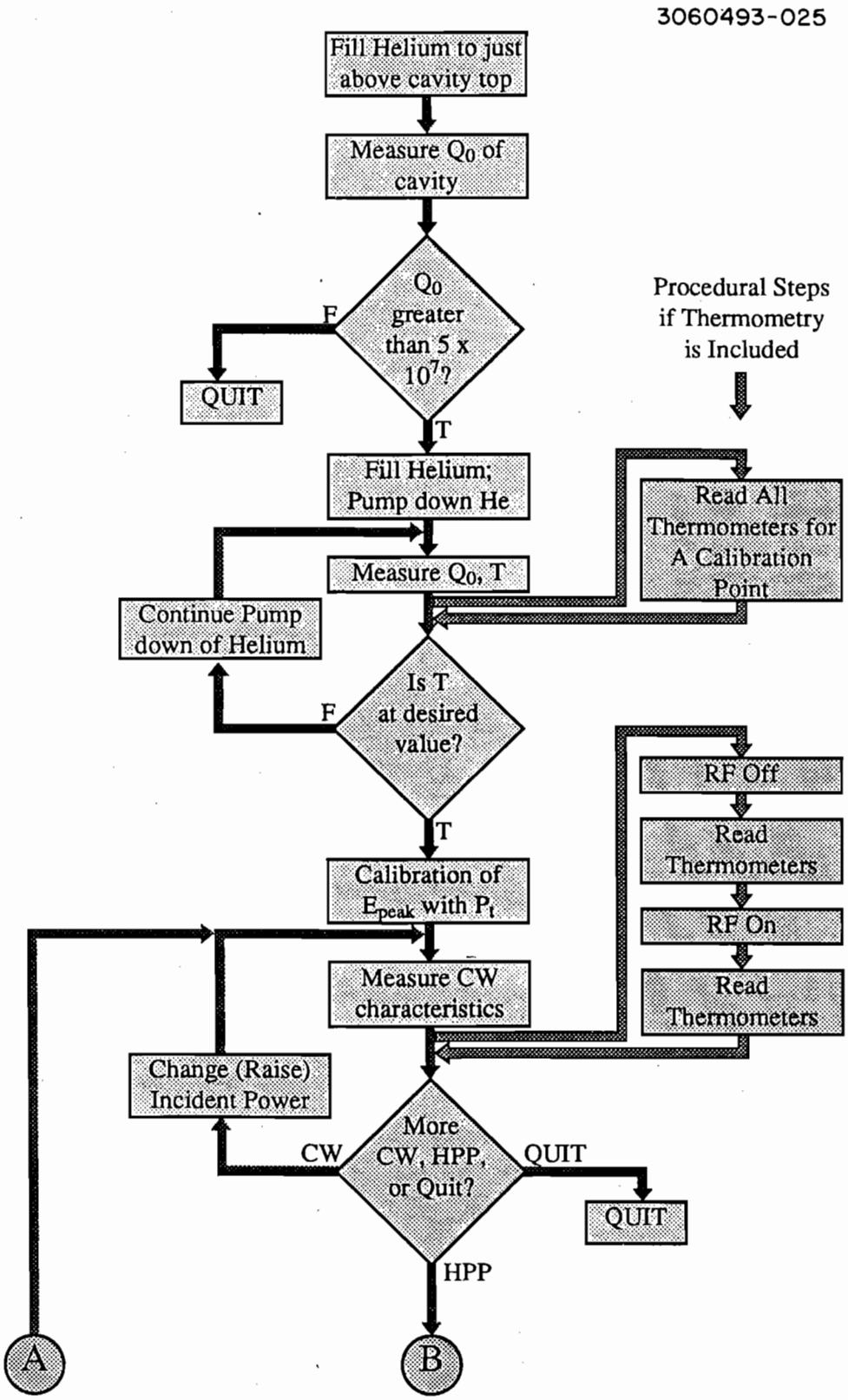

Figure 2.10. Flow chart diagram of the HPP experimental procedure.

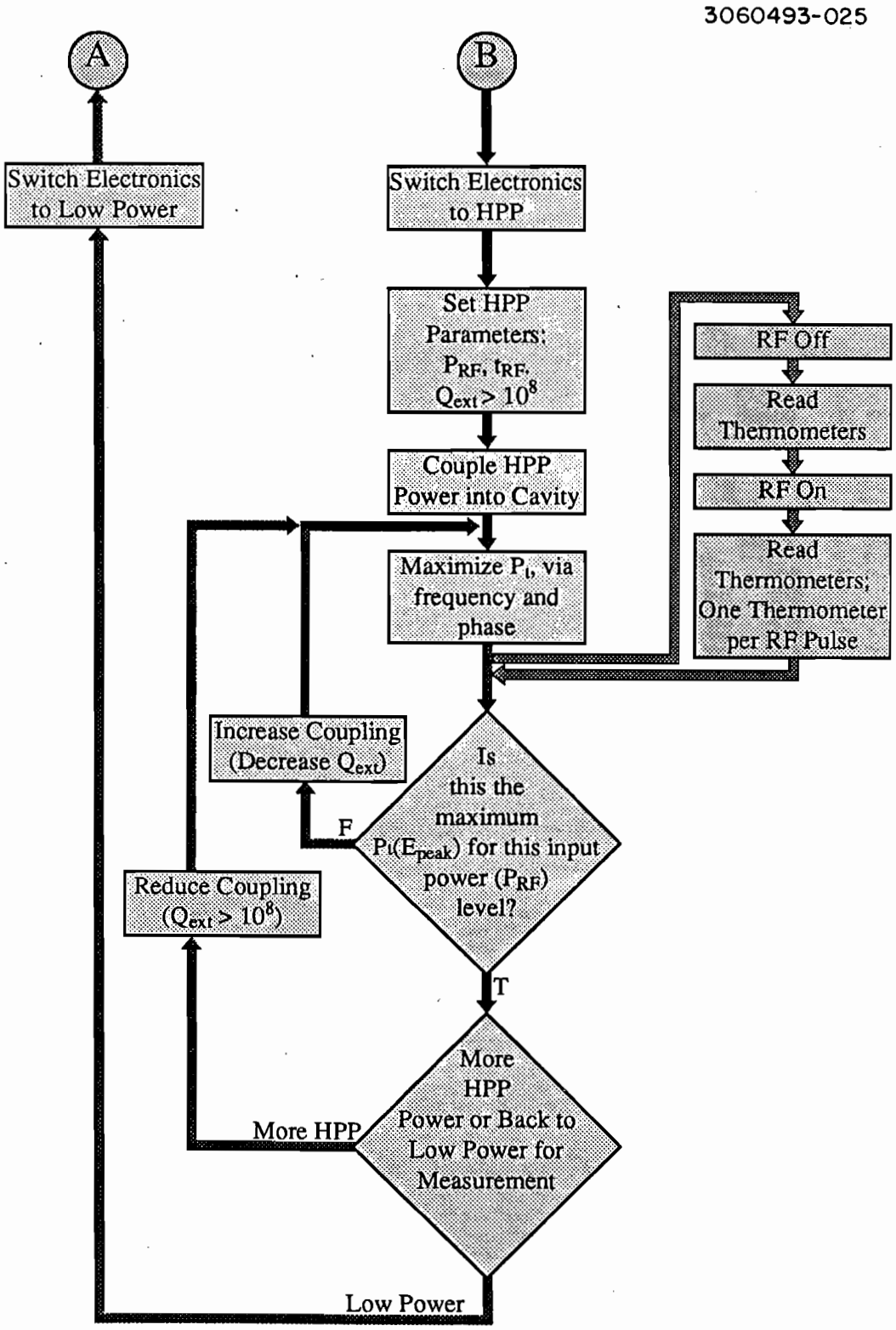

Figure 2.10. (Continued).

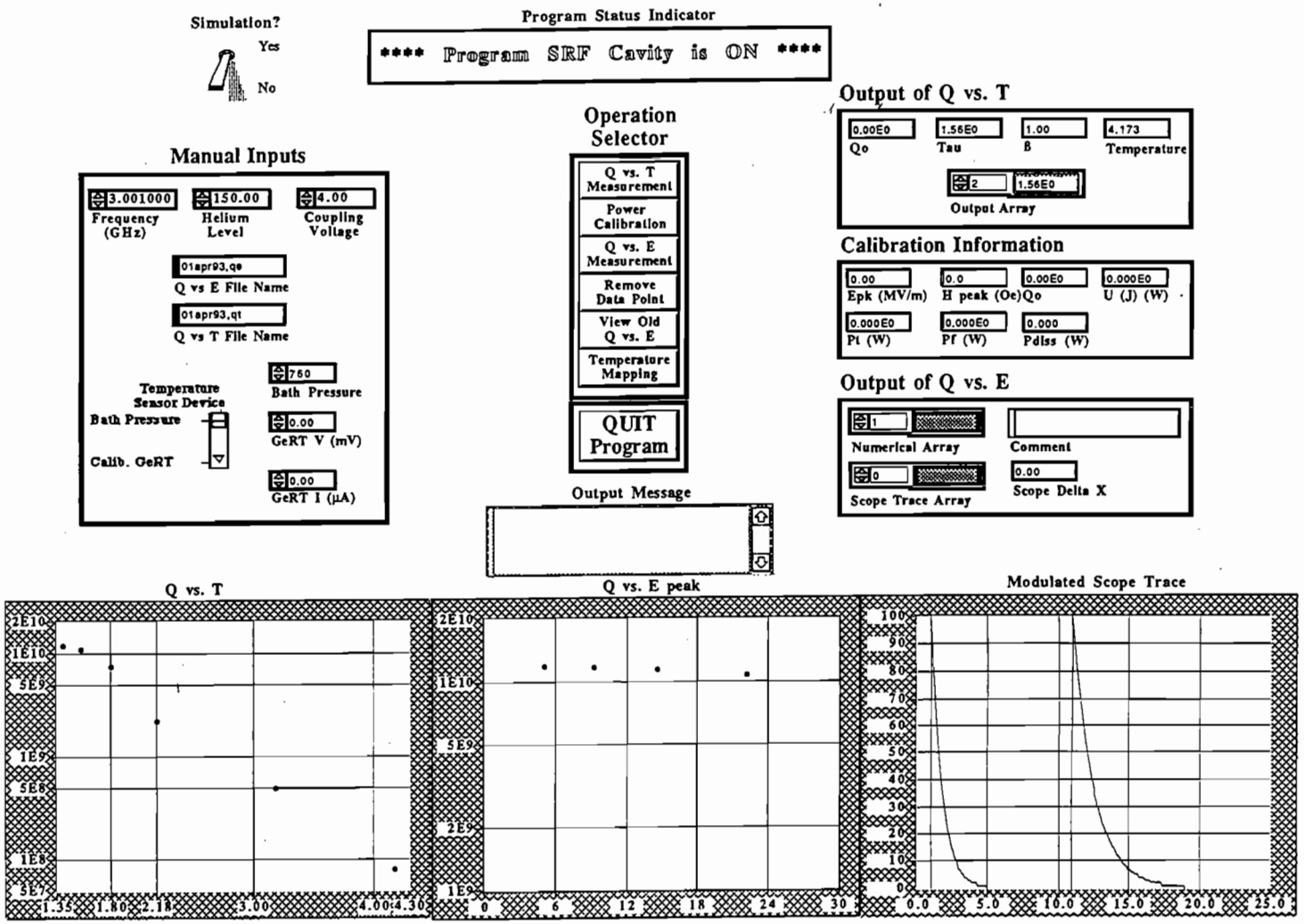

Figure 2.11. Display screen from program **SRF_Cavity**.

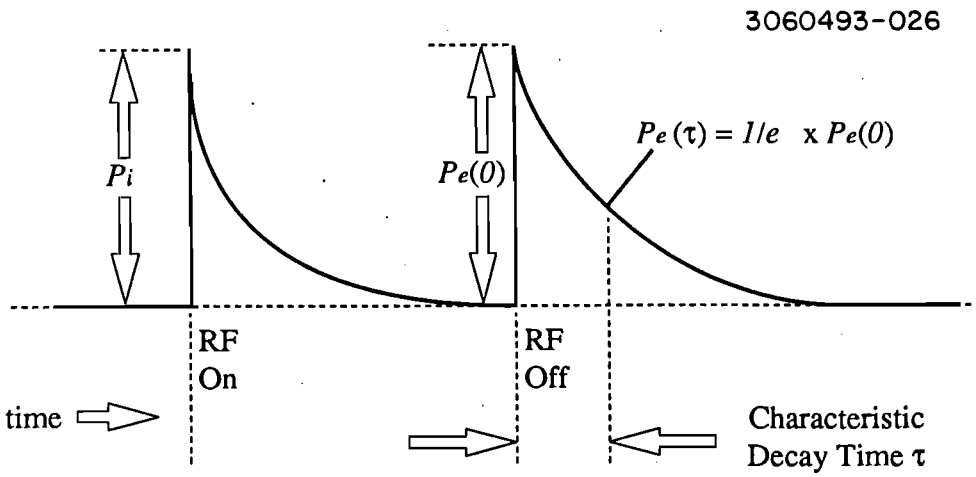

Figure 2.12. Reflected power trace during modulated excitation of a cavity, with pertinent quantities highlighted.

proportional to the stored energy as given by equation 2-1, which comes from equations A-3 and A-20 (in Appendix A):

$$P_e(t) = \frac{\omega U_{t=0}}{Q_{ext}} \exp\left(-\frac{t}{\tau}\right) \tag{2-1}$$

The decay time τ is determined as the time when P_e decays to 1/e = 0.368 of its initial value. β is determined by P_i and P_e (from equation 2-15), which are also shown in Figure 2.12. Then Q_0 is given by equation 2-2, which derives from equations A-1, A-7, and A-10:

$$Q_0 = (1 + \beta)\, Q_L = (1 + \beta)\, \omega\, \tau = (1 + \beta)\, 2\, \pi\, \nu\, \tau \tag{2-2}$$

Incident power on the cavity is then measured, and dissipated power determined by equation A-11. Finally, we get calibration of peak electric

field and stored energy from equation 2-3, which comes from equations A-2 and A-9:

$$E_{peak-cal} = k_e \sqrt{U_{cal}} = k_e \sqrt{\frac{P_{diss} Q_0}{\omega}} \tag{2-3}$$

The relationship between transmitted power to the monitor probe and calibration peak field is given by equation 2-4, which comes from equations A-4 and A-8:

$$E_{peak-cal} = k_e \sqrt{U_{cal}} = k_e \sqrt{\frac{P_{t-cal} Q_t}{\omega}} = k_e \sqrt{\frac{Q_t}{\omega}} \sqrt{P_{t-cal}} \tag{2-4}$$

but everything on the right hand side of equation 2-4, other than $P_{t\text{-}cal}$, is constant, thus we get all subsequent peak electric field values from the following relationship:

$$E_{peak} = E_{peak-cal} \sqrt{\frac{P_t}{P_{t-cal}}} \tag{2-5}$$

Thermometer Calibration: When thermometry is a part of the experiment, the calibration is done individually for each of the 100 thermometers. Data points are taken for each thermometer, at several different temperatures, while cooling from 4.2 K to 1.4 K, and then the resistance vs. temperature is fit according to the following equation:

$$\frac{1}{T} = A_i \ln(R) + \frac{B_i}{\ln(R)} + C_i \text{ for } i = 1, 100 \tag{2-6}$$

Thermometry Measurements: Thermometry measurements are made via the following procedure:

(1) Turn incident RF off.

(2) Measure bath temperature.

(3) Measure the voltage of all 100 thermometers with RF still off.

(4) Turn incident RF on CW.

(5) Measure the voltage of all 100 thermometers with RF on, subtract RF off voltage, to get difference.

(6) Measure bath temperature to determine bath drift while RF is on.

The entire procedure takes approximately 25 seconds; the reading of all 100 thermometers takes 8 seconds. All thermometry measurements are performed by a sub program of **SRF_Cavity**, titled **S_Temp_Scan**. The display from **S_Temp Scan** is shown in Figure 2.13. Detailed analysis of the thermometry data (for F-N characteristics, e.g.) was performed with the **TEMPER** and **HOTS** programs, which were previously developed for use with the 1.5 GHz field emission study program at Cornell LNS.[63]

Decision of whether or not to perform HPP processing: Low power RF is increased until all available power is being dissipated, thermal breakdown is encountered, or field emission becomes severe (Q_0 drop of approximately a factor of ten). The decision of whether or not to utilize HPP processing is primarily a question of whether or not FE loading is dominating the cavity. If FE is the dominant loading mechanism, then HPP processing is the next step. If, however, the cavity experiences a thermal breakdown with little or no FE, then HPP will not produce any significant improvement, and is therefore not useful.

Choice of Initial HPP Parameters: Following early experience with HPP induced cavity damage (see Chapter 3 for explanation), we generally start HPP processing with a moderate incident power level ($P_{RF} \leq 10$ kW). RF pulse shape and power level are fixed while connected to an RF load. When the RF pulse shape is made as close to rectangular as possible, with t_{RF} between 0.5 and 1 msec, the power is switched into the cavity, to begin

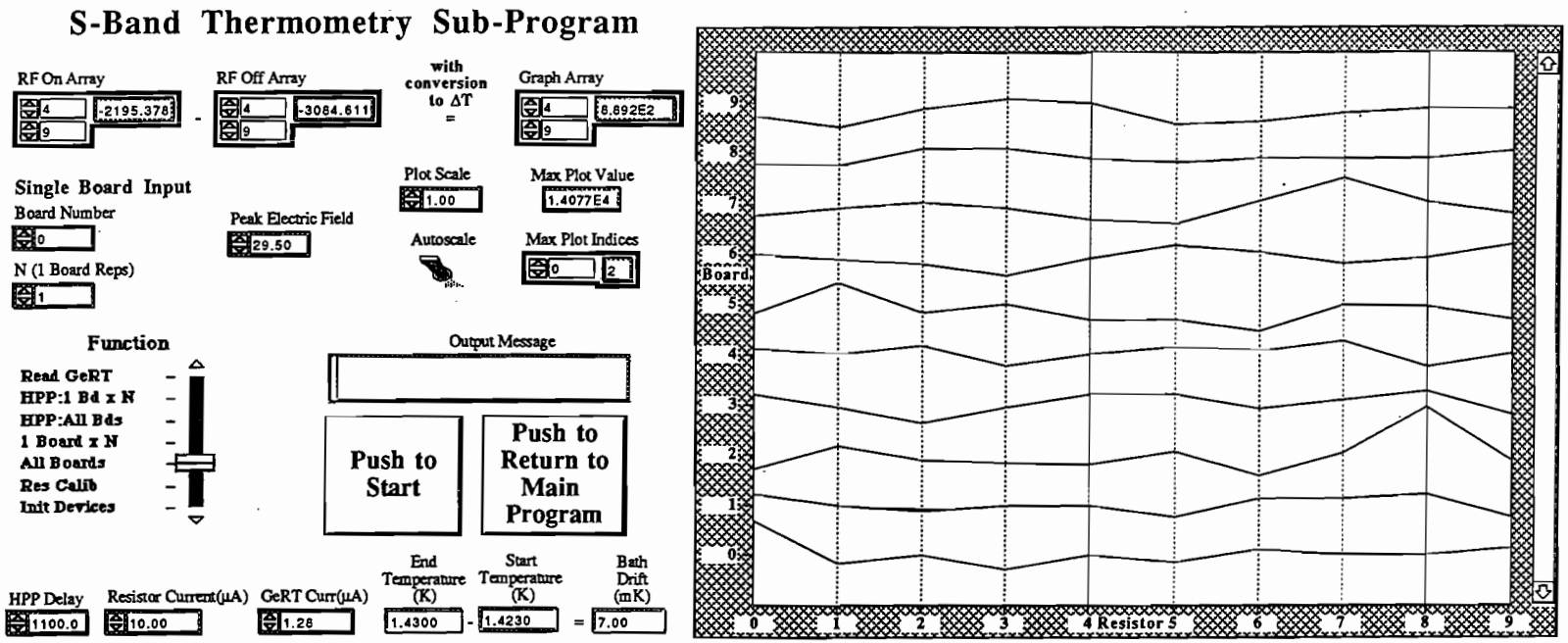

Figure 2.13. Display screen from sub-program **S_Temp_Scan.**

HPP processing. We then begin with $Q_{ext} \geq 10^8$, again to keep the fields and power from rising too quickly and damaging the cavity.

Continuation of HPP: During HPP, the peak electric fields in the cavity are monitored via the transmission probe on an oscilloscope. The short time scale of cavity reaction (tens of microseconds) and low average power transmitted preclude the use of a conventional power meter. Thus the transmitted power is monitored on an oscilloscope, with calibration done in the same manner as for the power meter (equation 2-29).

The input coupling is slowly increased (Q_{ext} reduced), maximizing P_t (and thus E_{peak}) via frequency and feedback adjustments at each value of Q_{ext}. When the maximum value of P_t for a given pulse (defined by P_{RF} and t_{RF}) is reached, another choice must be made: further HPP with higher power or low power measurement to determine gains from HPP processing. If further HPP is to be done, the RF is disconnected from the cavity, and reconnected to the load; when the higher power RF pulse is acceptable (in terms of P_{RF}, t_{RF}, and pulse shape), it is re-connected to the cavity with the coupling again reduced such that $Q_{ext} \approx 10^8$. The process of generally increasing coupling until maximum field is reached is repeated.

When to Quit: The cycle of HPP processing followed by low power measurement is continued until low power measurements show no further gains due to HPP processing.

2.3.4. Post-experimental Analysis

Following all steps of the experiment, the cavity and test stand are removed from the experimental dewar and allowed to warm to room temperature. The possible avenues from there are: (1) removal of cavity from the stand followed by etching and re-testing of the cavity, (2) removal

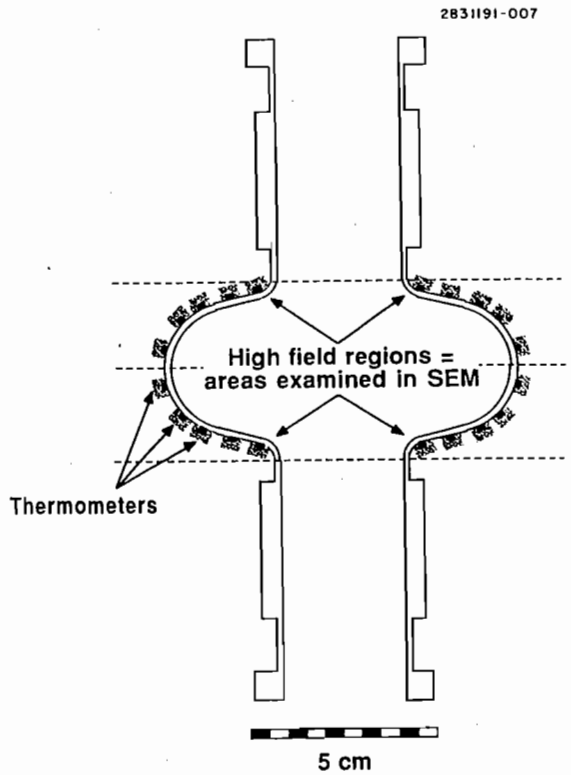

Figure 2.14. Diagram detailing location of dissection cuts for SEM examination of an S3C Cavity.

of the cavity followed by storage, and (3) removal of the cavity, followed by dissection and examination in a Scanning Electron Microscope (SEM).

For multi-cell cavities, the immediate step upon removal from the test stand is to once again test the cavity for field flatness (See Appendix C), to verify cavity behavior during cold tests.

In the case of single-cell cavities which had been provided with thermometry during cold tests, the thermometry data was investigated for possible phenomena which justify destruction and examination in the SEM. The primary selection criteria for SEM examination is large reduction in field emission with HPP, and location of the processed site with thermometry. Observed changes in heating as measured by thermometry are investigated with the FE simulation codes, to determine which regions of the cavity surface should be examined. If SEM examination is warranted, the cavity is

cut apart at the equator and each iris, as shown in Figure 2.14. Five single-cell cavities were examined in this manner. Thermometry and SEM analysis are more thoroughly discussed in Chapter 4.

CHAPTER 3: OVERVIEW OF RESULTS OF THE HPP EXPERIMENTS

3.1. Introduction

As was stated in the introductory chapter, the High Power Processing (HPP) experiment was designed to explore the benefits of high power pulsed radio-frequency (RF) processing as a means of reducing field emission (FE) loading in 3 GHz niobium accelerator cavities. In this chapter, we will show that significant improvements are achieved. To support this conclusion, we report on investigation of cavity performance before and after HPP processing, as well as correlation of the improvements with the characteristics of HPP processing.

Single-cell cavities are convenient for research and development work, and were therefore used for the initial studies in the HPP experimental program. Single-cell cavity results are quoted in terms of peak surface electric field (E_{peak}). Accelerators, however, are constructed of multi-cell cavities. Therefore it is important to verify that the HPP technique can successfully reduce FE loading in multi-cell structures as well as it does in single cavities. To this end, two nine-cell cavities were constructed and tested several times each. All nine-cell cavity electric field values listed below are given in accelerating gradient (average accelerating field experienced by a particle traversing the cavity, E_{acc}) rather than peak surface electric field. The ratio of peak to accelerating field in the nine-cell cavity is $E_{peak}/E_{acc} = 2.08$, as determined by SUPERFISH.[4]

We will also discuss the nature of the limitations on HPP processing, leading directly into the next chapter where we fully investigate the limitations. The primary limitation on HPP processing was thermal. In order to fully investigate (as well as bypass) this limit, a two-cell cavity with a

different geometry (producing a lower H_{peak}/E_{peak} ratio) was tested. This cavity reached a peak surface field of 100 MV/m, and an accelerating gradient of 34 MV/m, both records for CW operation of an accelerating cavity. Geometric profiles and pertinent parameters of each of the three cavities to be discussed were shown in Figures 2.1 and 2.2.

Finally, we close with a discussion of some subsidiary issues related to HPP processing, such as parameters of HPP (e.g. Power, coupling, pulse length), and durability/sustainability of the cavity performance improvement due to processing.

3.2. Cavity Performance Before and After HPP Processing

3.2.1. Typical HPP Improvement of an SRF Cavity

Field emission loading has been the dominant limitation on attainable accelerating gradients in superconducting RF cavities in the last 5-10 years[49]. One of the most easily observed manifestations of FE loading is the degradation of the cavity quality factor (Q_0) as the electromagnetic field magnitude, and thus the stored energy, in the cavity are increased. Recall that the Q_0 of a cavity is defined by equation 3-1, shown below:

$$Q_0 = \frac{\omega U}{P_{diss}} \tag{3-1}$$

where ω is cavity frequency, U is stored energy in the cavity, and P_{diss} is the dissipated power in the cavity due to all mechanisms (FE, wall losses, and other phenomena). If a cavity has only wall losses, Q_0 remains constant with rising fields, since then U and P_{diss} are both proportional to the square of the fields in the cavity. When field emission is present in the cavity, the dissipated power is no longer proportional to E_{peak}^2, but rather rises exponentially with rising E_{peak}, corresponding to the exponential

growth of the field emission current with electric field (See Chapters 5 and 6 for more discussion of the specifics of field emission loading.).

The standard experimental procedure was described in depth in the last chapter. Briefly, it is as follows. The cavity's low power CW performance is measured first, with incident power up to 10-100 watts. The cavity is then subjected to HPP processing, and then the cavity's low power performance is re-measured, to check for HPP induced improvements. The procedure (HPP followed by CW measurement) is repeated until no further gains are observed in low power performance. In both CW and HPP conditions, electric fields are monitored by a fixed transmission probe with coupling factor $\beta_t \ll 1$.

Figure 3.1 shows an example of the benefits of HPP processing. This particular data is from the best test of a nine-cell cavity. The general characteristics have been the same for all types of cavities tested. The solid symbol plot is the Q_0 vs. E_{acc} measurement for the cavity before HPP processing. As can be seen, the cavity was limited by available power to

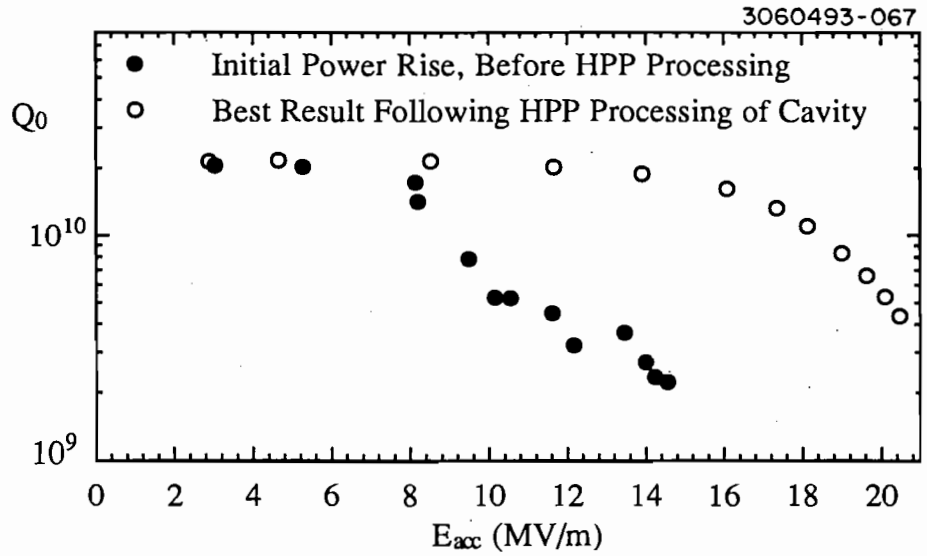

Figure 3.1. Q_0 vs. E_{acc} plot showing typical improvement of a nine-cell cavity due to HPP processing.

an accelerating gradient of E_{acc} = 14 MV/m, with Q_0 degraded to 2 x 10^9 from a low field value of Q_0 = 2 x 10^{10}. X-ray detection indicated heavy FE. The cavity Q_0 remained above 1 x 10^{10} up to E_{acc} = 9 MV/m. The X-ray threshold field was 6 MV/m. The open symbol plot is the measurement for the cavity following HPP processing with incident power up to 100 kW (maximum surface electric field of 68 MV/m). A significant improvement can be seen in the cavity performance, as the cavity now reaches E_{acc} = 20 MV/m, with associated Q_0 = 4.5 x 10^9. In addition, Q_0 remained greater than 1 x 10^{10} for fields as high as E_{acc} = 18 MV/m, and the X-ray threshold increased to 13.5 MV/m.

3.2.2. Overview of All Results of HPP Processing Experiments

In order to compare the general behavior of superconducting cavities before and after HPP processing, we will use three characteristics: (1) maximum attainable field, (2) threshold field for X-ray detection, and (3) field emission loading threshold. Some definition and discussion is necessary for each of these characteristics.

1. Maximum Attainable Field (E_{max}). The maximum attainable field is the highest peak field condition attained under continuous wave (CW), low power measurement conditions. The maximum attainable field is a function of many parameters: available power, field emission loading, low field Q_0 value, and cavity thermal loading are examples. The maximum field is limited by one of two effects: (1) All available power being consumed in dissipative phenomena in the cavity, such as field emission or wall losses, and (2) Thermal breakdown , as defined in Chapter 1.

Since maximum attainable field is not solely dependent on field emission characteristics, it is not always a good indication of processing progress. In many cavities, however, (especially the nine-cell cavities to be

discussed) field emission loading is the primary limitation, and thus examination of the maximum attainable fields for these cavities does show the effectiveness of the HPP procedure.

2. X-ray Threshold Field (E_x). The X-ray threshold field is the field level at which X-rays first are detectable on a low energy gamma ray counter monitor placed outside the experimental test dewar within one meter, aligned approximately along the axis of the test cavity. X-rays are produced when field emitted electrons are accelerated by the cavity fields and then impact elsewhere in the cavity. X-ray detection is therefore a sensitive method of determining whether or not field emission is present, independent of other processes in the cavity.

3. Field Emission Loading Threshold Field (E_{fe}). The field emission (FE) loading threshold field is defined as the field level at which the emission based loading becomes significant in the cavity. The definition of "significant" loading is somewhat arbitrary. We have defined E_{fe} for this work as the field at which emission related dissipation surpasses 0.5 watts in one-cell and two-cell cavities, and 1.0 watt in nine-cell cavities. These threshold power values were chosen such that they be discernible from the remaining cavity dissipation. Lower threshold values could not be reliably separated from the total cavity losses.

For this work, FE loading was defined as any loading not proportional to the square of the cavity fields. This definition has the possible disadvantage of including power loss due to other mechanisms if their power dissipation is not proportional to the square of the fields. In the cavities studied, however, no other significant loading sources (non-proportional to E_{peak}^2) were identified at the fields where field emission became significant.

An alternative, popular method of defining field emission threshold is "Q_0 rollover," or the field level at which a notable degradation of the Q of the cavity (due to field emission) is detected. This method has the disadvantage, however, of being highly dependent on the low field, non-emission related losses of the cavity. We instead use the absolute power into field emission as the threshold field to avoid this disadvantage.

3.2.3. Initial Studies: Single-cell Cavities

Figures 3.2 through 3.4 are histograms of the measurements before and after HPP, of E_{max}, E_x, E_{fe}, respectively. Also included in these plots is the mean value of E_{max}, E_x, E_{fe}, respectively, as well as standard deviations. In each of these plots a clear improvement can be seen in that the distribution of measurements is centered about a higher peak electric field. This is especially apparent in the plots of E_x and E_{fe}, where the distributions barely overlap. The plot of E_{max} also shows a shift to the right, though not as prominent, due to the dependence of E_{max} on factors other than FE loading.

The post-HPP histogram for maximum field (Figure 3.2) has two peaks, centered on 35-40 MV/m and 50-55 MV/m. These peaks can be explained by thermal breakdown limitation of the single-cell cavities under test. The single-cell cavities used in the HPP program were made from niobium with Residual Resistance Ratio (RRR) $\approx$ 250. RRR is a measure of the purity of the niobium, as is further discussed in Appendix D. Several of the cavities, however, were purified, through solid state gettering, to $RRR \approx$ 450-500. Computational simulations of thermal processes in niobium predict that RRR = 250 material will experience thermal breakdown at approximately $H_{surface}$ = 800-900 Oe (corresponding to E_{peak} = 35-39 MV/m in the single-cell cavities), while RRR = 500 material will

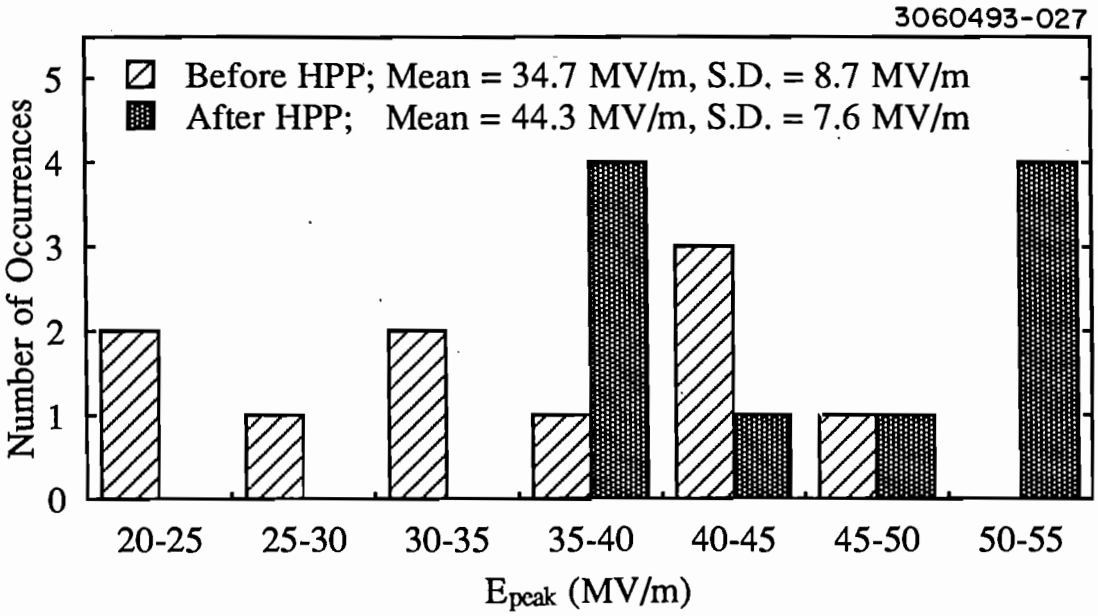

Figure 3.2. Histogram comparison of maximum achieved peak electric field in single-cell cavities before and after HPP processing. This includes the tests of six different cavities.

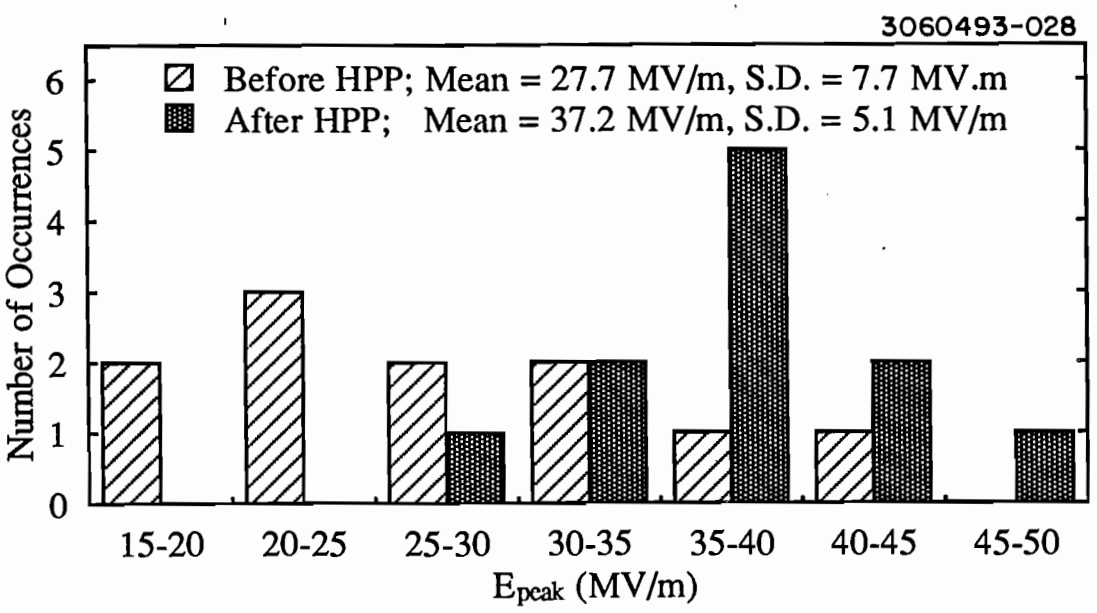

Figure 3.3. Histogram comparison of X-ray threshold electric field in single-cell cavities before and after HPP processing.

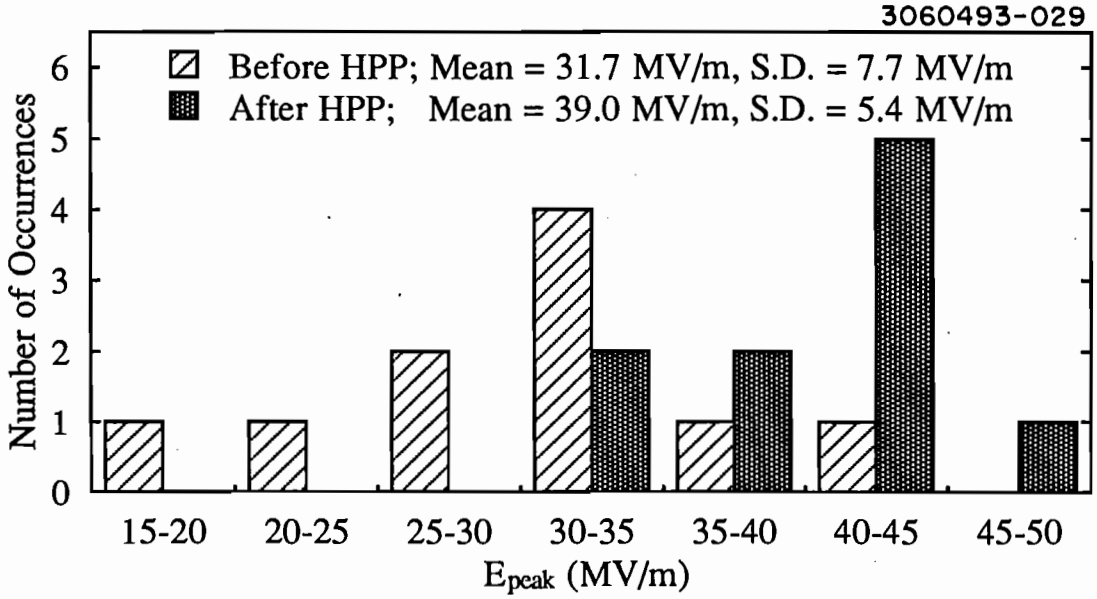

Figure 3.4 Histogram comparison of Field Emission loading (P_{fe} = 0.5 W) threshold electric field in single-cell cavities before and after HPP processing.

experience thermal breakdown at $H_{surface}$ = 1200-1300 Oe (E_{peak} = 52-56 MV/m).

3.2.4. Multi-cell Structures: Nine-cell Cavities

Figures 3.5 through 3.7 show histograms of nine-cell experimental results, similar to those presented for the single cell cavities (Figures 3.2 through 3.4). As stated in the introduction, the quoted electric field values are accelerating gradient, rather than peak electric field. The results clearly show that HPP does significantly reduce field emission loading in nine-cell cavities. Once again, the mean values and standard deviations are included in the plots. Similar to the single-cell results, these plots show a clear shift towards higher fields in the distribution of post-HPP measurements compared with pre-HPP measurements. Furthermore, the post-HPP results are comparable to those obtained by high temperature

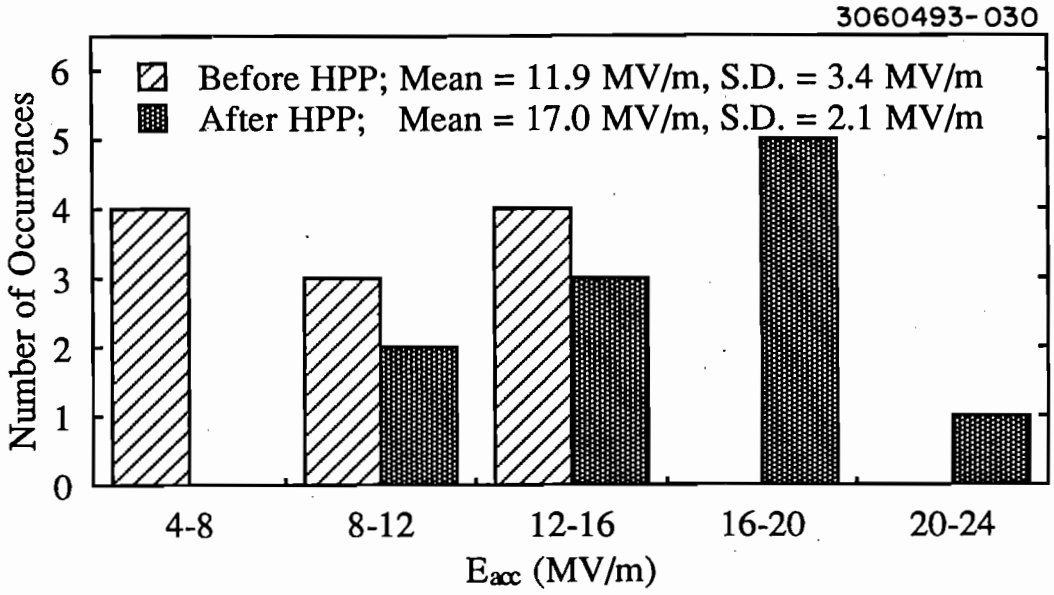

Figure 3.5. Histogram comparison of maximum achieved peak accelerating gradient in nine-cell cavities before and after HPP processing. This includes all tests of two nine-cell cavities.

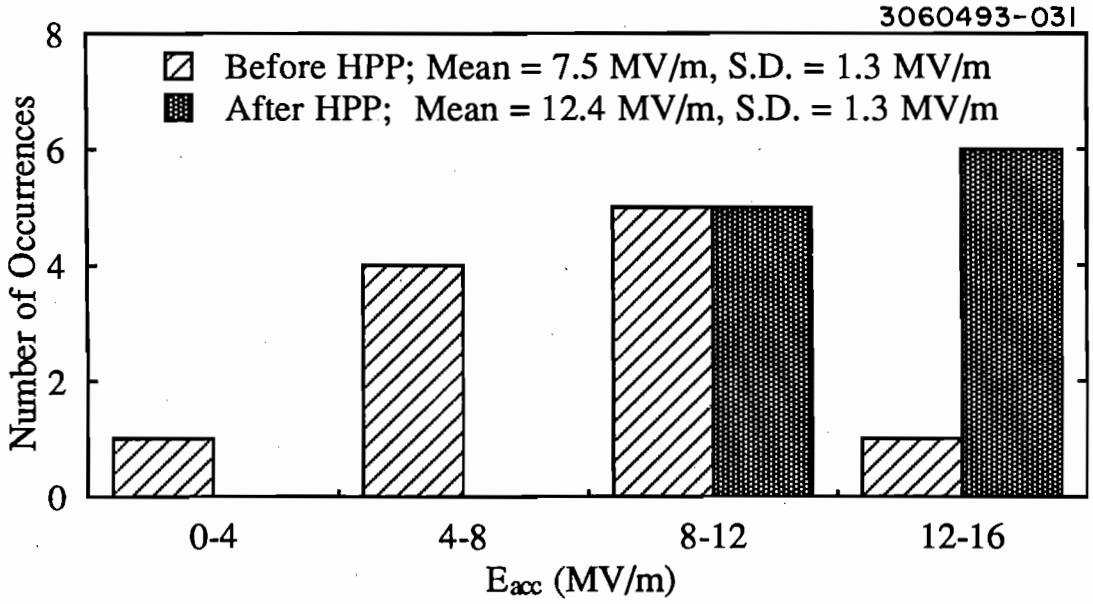

Figure 3.6. Histogram comparison of X-ray threshold accelerating gradient in nine-cell cavities before and after HPP processing.

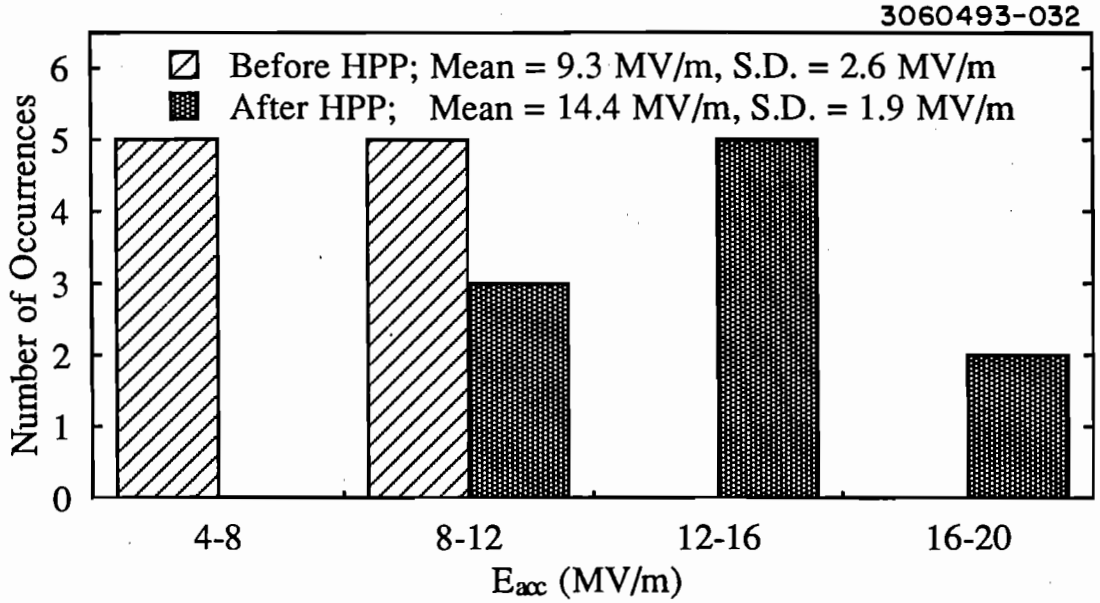

Figure 3.7. Histogram comparison of Field Emission loading (P_{fe} = 1.0 W) threshold accelerating gradient in nine-cell cavities before and after HPP processing.

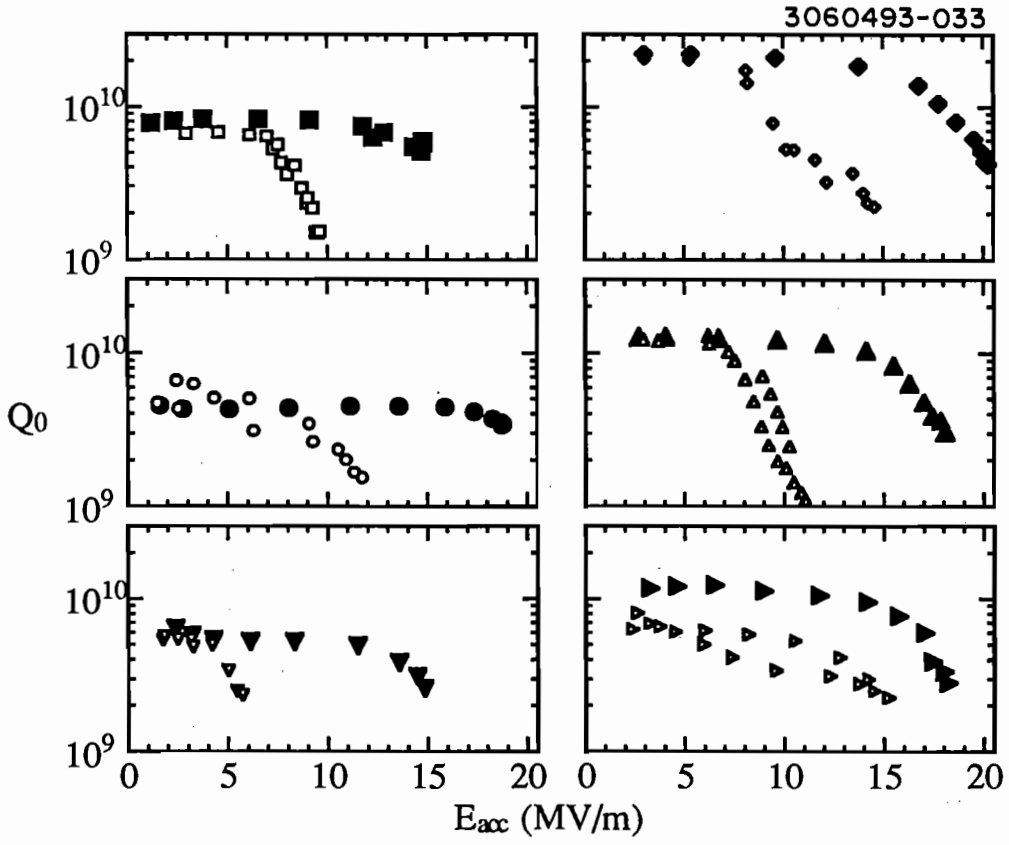

Figure 3.8. Composite Q_0 vs. E_{acc} plots for the best results of HPP processing experiments on nine-cell cavities.

UHV baking (HT). HT treatment produced the best experimental cavity results prior to the HPP technique.[50]

Figure 3.8 is a composite plot of the Q_0 vs. E_{acc} curves for most of the experiments with nine-cell cavities, showing before and after HPP processing for each experiment. The open symbol in each plot is pre-HPP, and the solid symbol is post-HPP. The improvement due to HPP processing is clearly shown in these plots. The information of overall improvement in nine-cell cavities due to HPP processing, shown in Figures 3.5-3.7, is listed in Table 3-1. Also included in Table 3-1 is the maximum pulsed field during processing (E_{HPP}), which will be discussed in the next section. Determination of Q_0 during HPP will be discussed in section 3.4.

TABLE 3-1. TABULATION OF ALL HPP RESULTS ON NINE-CELL CAVITIES, BEFORE AND AFTER HPP, WITH PROCESSING FIELD (E_{HPP}) INFORMATION INCLUDED. (Fields in MV/m)

Max. E_{HPP}		Max. E_{acc}		X-ray TH E_{acc}		1 W FE TH E_{acc}	
E_{peak}	Q_0	pre-HPP	post-HPP	pre-HPP	post-HPP	pre-HPP	post-HPP
46.1	7×10^6	9.2	14.8	6.5	11.8	7.0	13.0
*38.0	NA	3.5	8.8	3.0	8.4	4.8	8.5
61.8	5×10^6	14.5	20.2	8.3	14.8	9.0	16.4
57.4	3×10^6	11.6	18.9	9.2	13.6	9.0	17.0
59.1	1×10^6	11.1	18.4	8.6	12.1	11.6	15.6
*30.2	5×10^6	5.0	9.8	6.1	7.2	5.5	8.0
47.8	3×10^6	8.8	17.9	5.0	11.5	5.4	12.5
58.2	5×10^6	15.2	18.2	7.4	11.8	8.1	14.4
56.2	4×10^6	15.3	16.9	7.5	13.0	13.2	14.0
42.0	6×10^6	8.3	14.4	7.2	10.7	7.8	11.4

* Data set was not used in computing means, standard deviations. Reasons for not including a data set include insufficient chemistry or low quench field due to defects.

3.3. Dependence of Processing Results on Processing Field

The overriding determining factor on success of HPP processing was the peak electric field reached during the HPP processing (E_{HPP}). Table 3-1 shows that the best results in nine-cell cavities were achieved with the highest processing fields. When the maximum value of E_{HPP} was reached, low power performance stopped improving. The dependence of processing success on E_{HPP} is clearly shown in Figures 3.9 through 3.11. These figures show the characteristics listed above (E_{max}, E_x, and E_{fe}) as a function of the peak electric field achieved during the HPP processing session immediately preceding the CW measurement. These plots include all tests of single-cell and nine-cell cavities, as well as the special two-cell

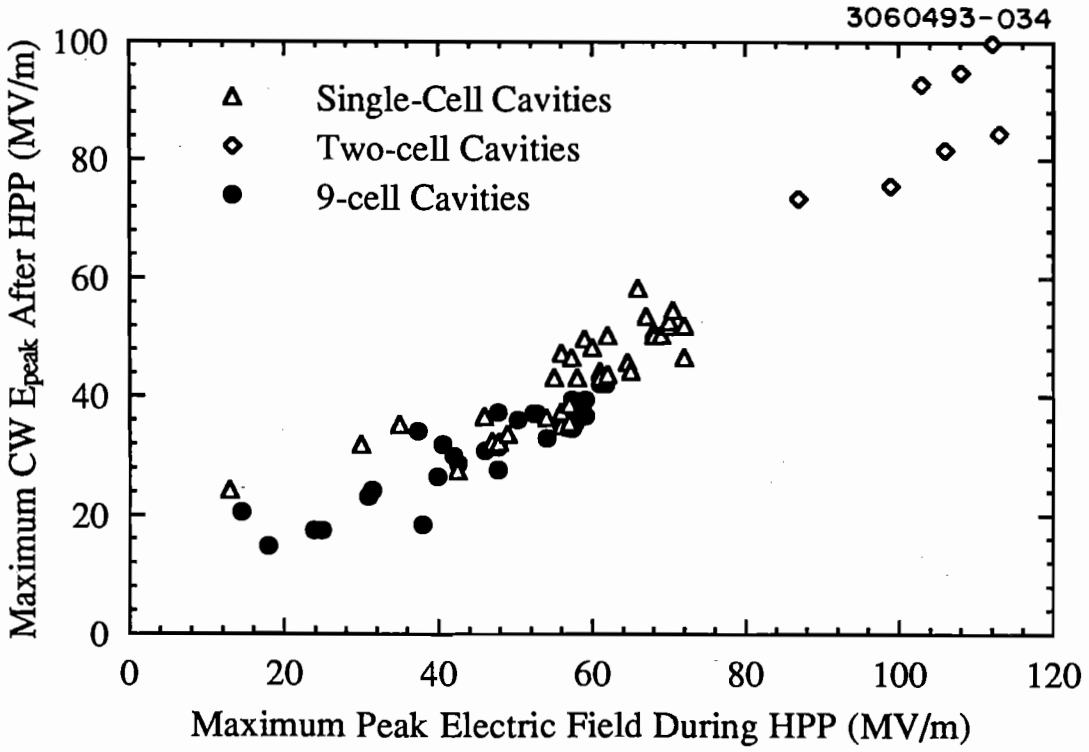

Figure 3.9. Maximum achieved CW peak electric field plotted as a function of the maximum peak electric field during the HPP processing immediately preceding CW measurement. All types of S-band cavities tested are shown.

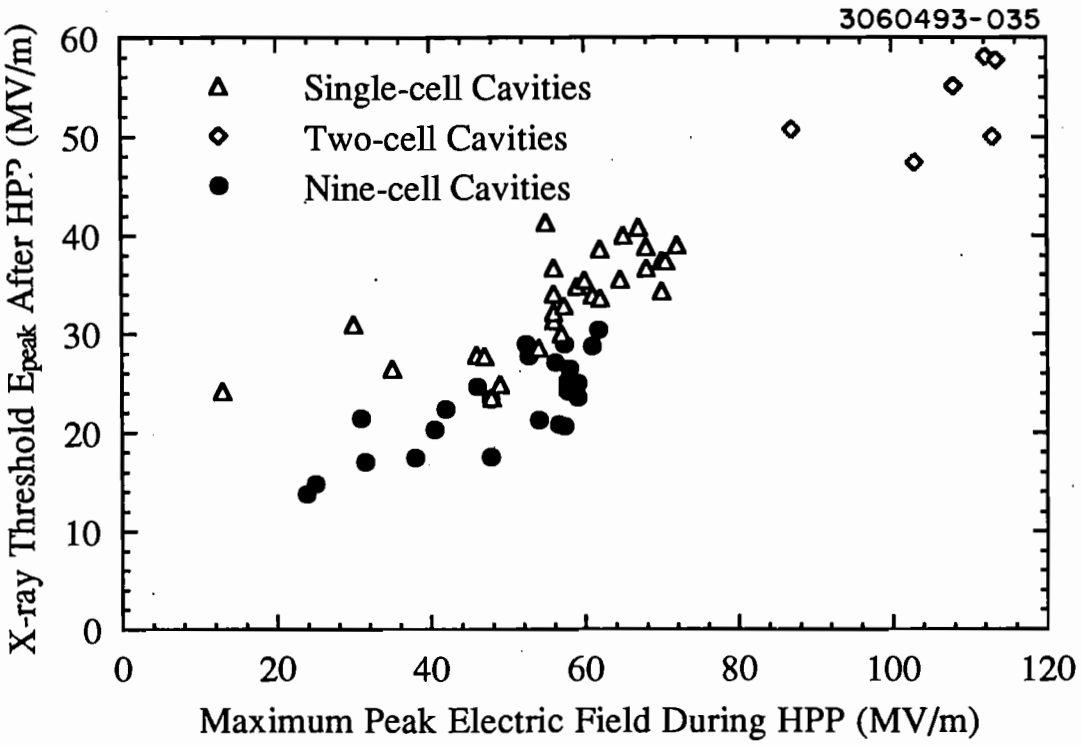

Figure 3.10. X-ray threshold peak electric field plotted as a function of the maximum peak electric field during the HPP processing immediately preceding CW measurement. All types of S-band cavities tested are shown.

cavity to be described later. Allowing for small individual cavity variations, all three plots show a nearly linear relationship between the measured quantity (E_{max}, E_x, and E_{fe}) and E_{HPP}.

The relationships between E_x and E_{HPP} (Figure 3.10) and E_{fe} and E_{HPP} (Figure 3.11) clearly indicate that in order for processing to be successful, E_{HPP} needs to be 1.5 to 2 times higher than the desired operating field. Implications of this ratio will be discussed in detail in chapters 5 and 6. In addition, from Figure 3.9, we see that the maximum CW fields reached are never as high as those reached during HPP processing. Each

of these phenomena proves significant to the analysis of the HPP technique. This will be further discussed below, both later in this chapter, and more extensively in chapter 6.

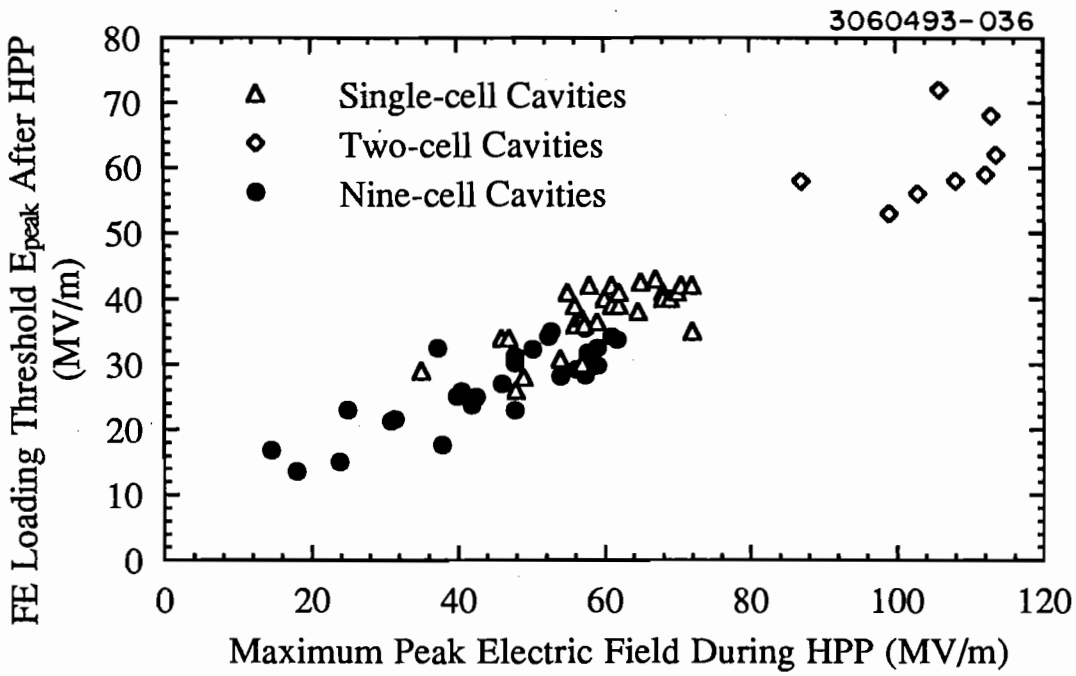

Figure 3.12. Field emission loading threshold peak electric field plotted as a function of the maximum peak electric field during the HPP processing immediately preceding CW measurement. FE loading threshold is defined as 0.5 W for single-cell and two-cell cavities, and 1.0 W for nine-cell cavities.

3.4. Limitations of HPP

The peak electric field during pulsed processing is dependent upon the following parameters: P_{inc}, the incident power at the cavity; t_{RF}, the RF pulse length (assuming a rectangular RF pulse); Q_{ext}, the external Q associated with the input coupler; ω, the angular frequency of the cavity; k_E, the ratio of peak electric field to the square root of the stored energy in

the cavity; Q_0, the unloaded Q of the cavity; β, the coupling factor, defined by $\beta = Q_0/Q_{ext}$; and Q_L the loaded Q of the cavity, defined by $1/Q_L = 1/Q_0 + 1/Q_{ext} = (1+\beta)/Q_0$. The expression for electric field at the end of the RF pulse is developed and shown in equation 3-2.

$$E_{peak}(t_{RF}) = E_{EQM}\left(1 - \exp\left[-\frac{t_{RF}}{2\tau}\right]\right),\ E_{EQM} = k_E\sqrt{U},\ \tau = \frac{Q_L}{\omega} \tag{3-2a}$$

This shows the exponential fill of the cavity fields to some equilibrium value. The equilibrium value is determined by the incident power, coupler Q, and cavity Q:

$$E_{EQM} = k_E\sqrt{\frac{P_{diss}Q_0}{\omega}} = k_E\sqrt{\frac{P_{inc}Q_{ext}}{\omega}}\ \frac{2\beta}{1+\beta} \tag{3-2b}$$

We can combine equations 3-2a and 3-2b to get the following:

$$E_{peak}(t_{RF}) = k_E\sqrt{\frac{P_{inc}Q_{ext}}{\omega}}\ \frac{2\beta}{1+\beta}\left(1 - \exp\left[-\frac{\omega t_{RF}}{2Q_l}\right]\right) \tag{3-2c}$$

Figure 3.12 shows an ideal RF input pulse, and the expected peak field change with time. The peak field also includes the predicted decay of fields when the RF pulse is turned off. Finally, it also shows the transmitted power pulse (see Section 3.2.1), since this is what we monitor during HPP processing.

We get the predicted field during HPP processing by assuming that the Q_0 value remains roughly unchanged from its low field value. Under these conditions, $\beta \gg 1$, and $Q_L \approx Q_{ext}$. Substituting these values into equation 3-2c gives the following relationship for predicted peak electric field:

$$E_{pre}(t_{RF}) = 2k_E\sqrt{\frac{P_{inc}Q_{ext}}{\omega}}\left(1 - \exp\left[-\frac{\omega t_{RF}}{2Q_{ext}}\right]\right) \tag{3-3}$$

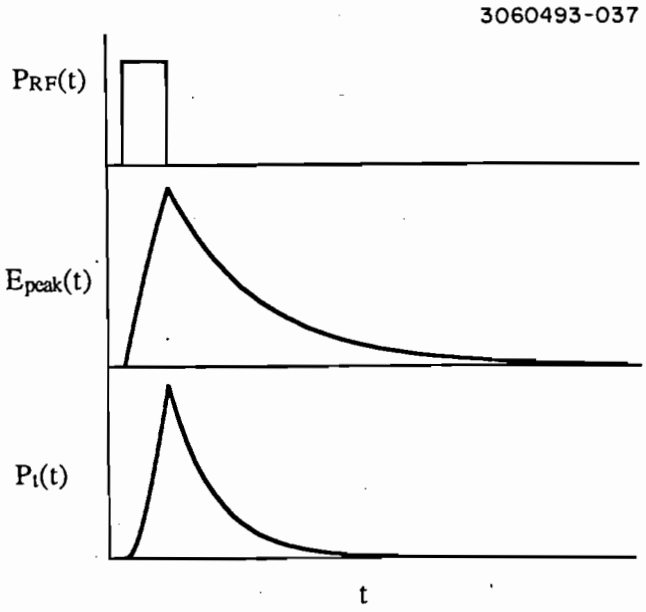

Figure 3.12. Example of a typical HPP P_{inc} pulse, with the corresponding response of E_{peak} and P_t with time.

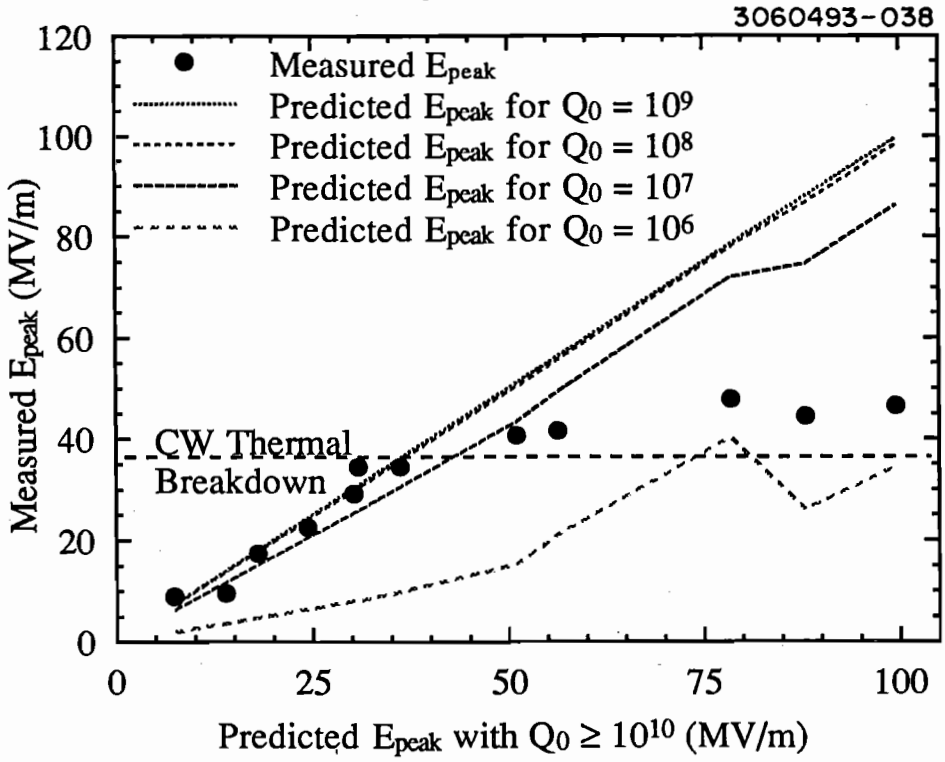

Figure 3.13. Measured peak field during HPP processing plotted against predicted peak field, based on the experimental HPP parameters. "Bumps" in the predicted curves are due to changing HPP parameters (P_{inc}, t_{RF}, Q_{ext}).

In Figure 3.13, we plot the attained peak electric field (y-axis) as a function of predicted peak eletric field (x-axis), for the experimental conditions (P_{inc}, Q_{ext}, t_{RF}, etc.) of a typical HPP processing session on a single-cell cavity. The scatter plot in Figure 3.13 is the measured value of E_{peak} during processing. The line plots are the predicted values for E_{peak} (from equation 3-3) for differing Q_0 values. From this information (measued E_{peak} value compared to predicted E_{peak}) we can extract a Q_0 value for the cavity at the measured electric field. Figure 3.14 shows the low power measurements before and after this high power processing session, along with the extracted Q_0 vs. E_{peak} for the HPP processing.

This analysis suggests that the cavity Q_0 decreases to 10^6-10^7 during HPP processing. This means that dissipated power in the cavity rises to

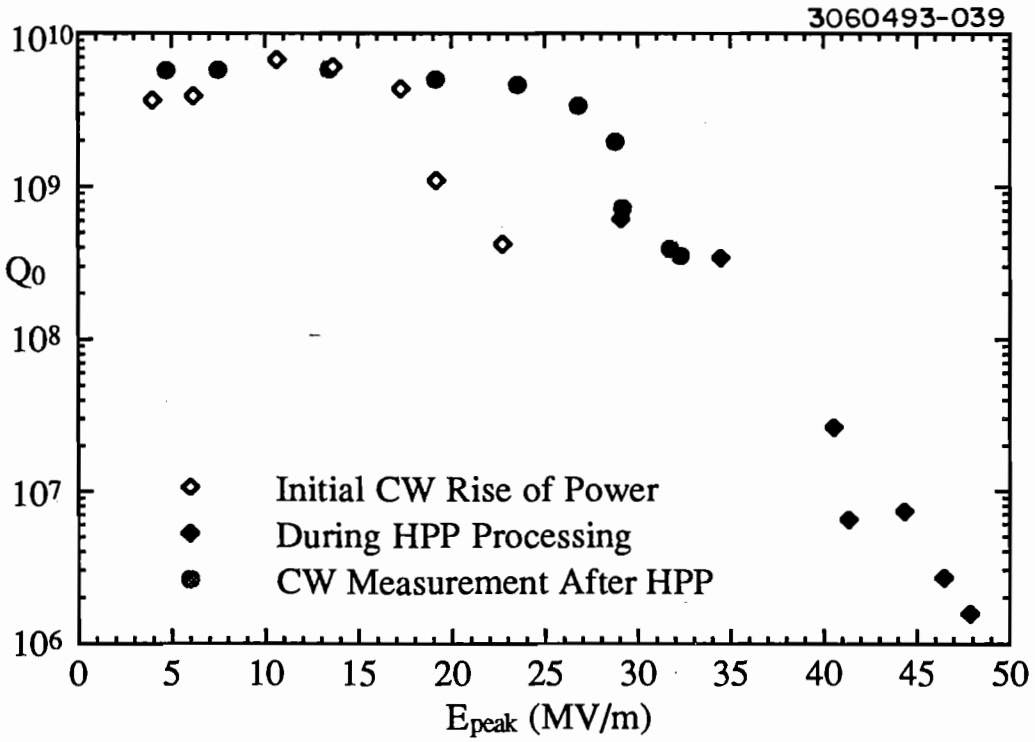

Figure 3.14. Q_0 vs. E_{peak} plots for the HPP session shown in Figure 3.13, along with the CW measurements immediately before and after the HPP processing session.

approximately 10 kW for the highest field shown on this plot. This also indicates that one limitation on achievable fields during HPP (E_{HPP}) is the rapidly falling Q_0 with increasing E_{peak}. All that remains is to identify the mechanisms which cause the decrease in Q_0 with increasing E_{peak}.

3.4.1. Field Emission Intensity

Field emission is an obvious source of Q_0 degradation, since it is the mechanism we are trying to reduce via HPP.

Departures from a smooth curve for Q_0 vs. E_{peak}, as shown in Figure 3.14, are associated with processing gains. These "jumps" indicate that a power dissipation source has been removed, giving a larger increase in E_{peak} than would have been expected from the previous behavior. The jumps are clearly seen in low power processing as will be shown below.

If we compare the plots of Figure 3.14 with the occasional processing event at low power, we find that Q_0 vs. E_{peak} plot is qualitatively similar. Figure 3.15 shows an example of low power processing in a single cell cavity. The lower curve in Figure 3.15 is the initial power rise. As the power was raised from 1.8 to 3.4 watts, the processing event shown occurred. Upon lowering the incident power, the top curve in Figure 3.15 was obtained, indicating a sudden improvement in Q_0 due to the processing of the emitter.

Table 3-2 lists all experiments of single-cell cavities, with performance parameters before and after HPP processing, as well as E_{HPP}, and associated Q_0 value.

Nine-cell cavities show the same behavior as single-cell cavities under HPP processing conditions. Figure 3.16 shows the Q_0 vs. E_{peak} plots for all measurements of a nine-cell cavity, through several CW runs along with the intervening HPP processing sessions. The HPP Q_0 vs. E_{peak} plots

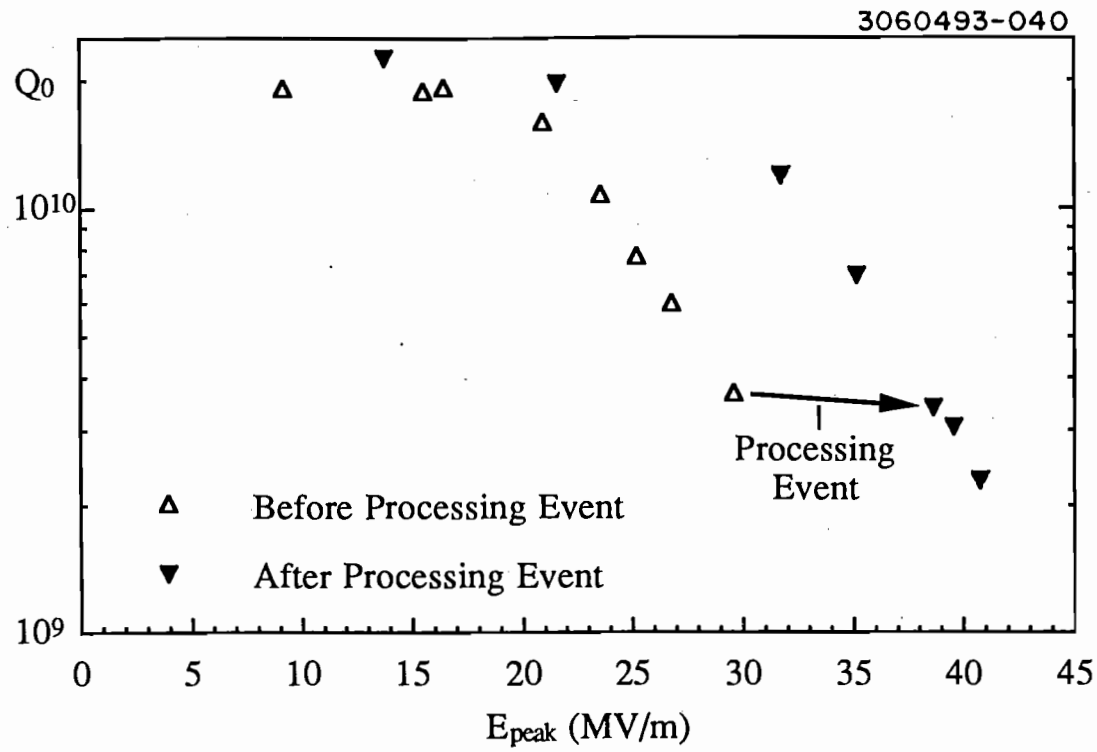

Figure 3.15. Q_0 vs. E_{peak} plot showing a low power RF processing event in a single-cell cavity.

TABLE 3-2. TABULATION OF ALL HPP RESULTS ON SINGLE-CELL CAVITIES, BEFORE AND AFTER HPP, WITH E_{HPP} AND ASSOCIATED Q_0 INFORMATION. (Fields in MV/m.)

Cavity	Before HPP			During HPP		After all HPP		
	E_{max}	E_x	E_{fe}	Max E_{HPP}	Q_0	E_{max}	E_x	E_{fe}
1-5	36.8	25.0	27.0	56.0	3×10^6	37.3	34.0	36.0
1-5	31.7	19.6	22.0	54.0	1×10^7	35.4	28.5	30.8
1-7	40.1	24.5	34.5	70.0	9×10^5	54.6	40.8	43.0
1-7	31.9	30.5	33.0	72.0	2×10^5	52.7	39.0	42.0
1-2	28.2	29.0	32.0	68.0	3×10^6	50.2	36.6	40.0
1-2	44.1	26.4	30.0	62.0	3×10^6	50.2	38.6	41.0
1-4	22.1	20.2	NA	56.0	NA	35.6	36.6	NA
1-6	22.7	17.3	19.0	57.0	7×10^5	35.5	30.0	30.0
1-6	46.0	31.2	35.2	70.0	1×10^6	46.5	35.5	38.0
1-6	59.0	41.2	49.0	66.0	NA	59.0	47.8	47.0
1-8	43.2	39.6	39.0	65.0	NA	44.2	41.3	42.0

were obtained via the same procedure as described for single cell cavities in the last section. Figure 3.17 shows the measured E_{peak} vs. predicted E_{peak} values for all HPP sessions in Figure 3.16. Similar to the single cell results shown above, the measured E_{peak} curve "rolls over" just above the CW thermal breakdown (quench) field. Notice, also, that in each successive HPP session, the measured and predicted fields are nearly equal for higher fields. This is because the field emission loading is being processed at lower fields. The increased agreement between $E_{measured}$ and $E_{predicted}$ is equivalent to "processing" jumps shown in Q_0 vs. E_{peak} plots.

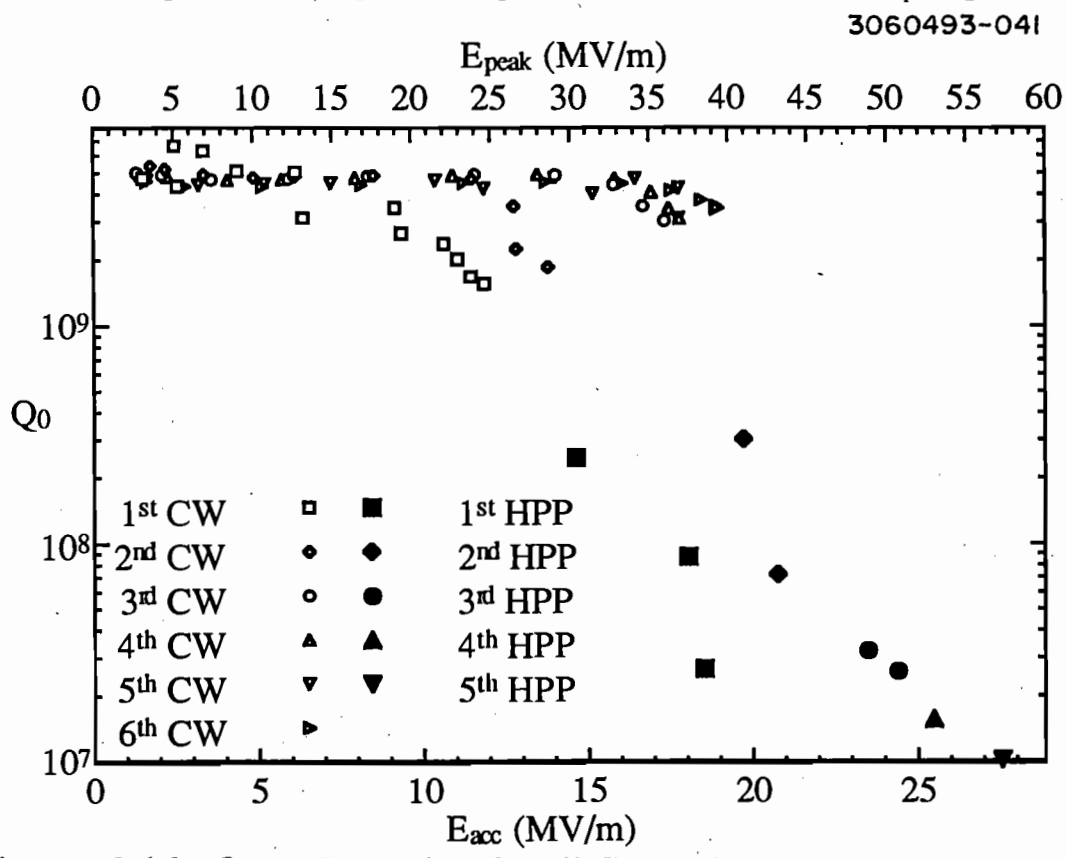

Figure 3.16. Q_0 vs. E_{peak} plots for all CW and HPP sessions in one experiment on a nine-cell cavity. Only the highest field values are shown for the HPP sessions, to clarify the plot. Again we see the "processing" behavior, where driving the fields higher, and the Q_0 lower, produces gains in the subsequent low power measurements.

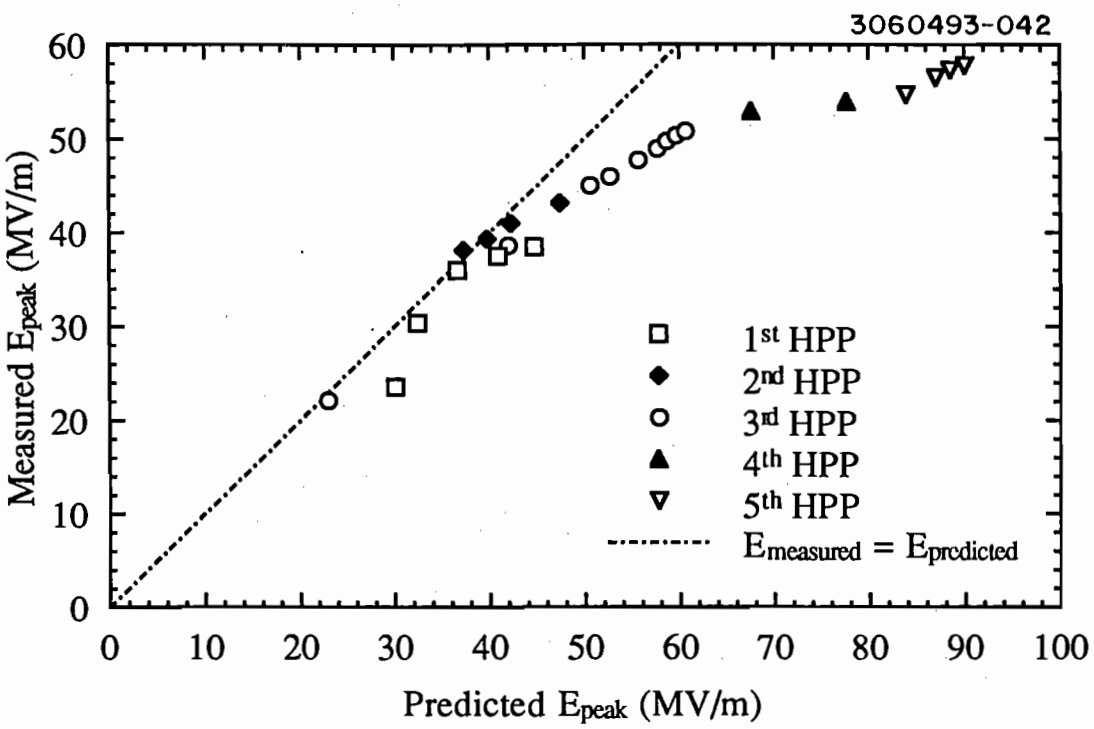

Figure 3.17. Measured fields plotted against predicted fields for all HPP sessions shown in Figure 3.16.

3.4.2. Thermal Breakdown

A limitation on E_{HPP} more severe than field emission loading, is thermal breakdown of the cavity. Thermal breakdown is recognized in CW measurements by a rapid dissipation of the stored energy in the cavity (as monitored by the transmitted power probe). In addition, thermometry can further aid identification of thermal breakdown, by showing hot spots prior to breakdown. Figure 3.13 contains an excellent example of a thermal breakdown limitation on E_{HPP}. The CW measurements of the cavity whose data is shown Figure 3.13 were limited by a thermal breakdown at E_{peak} = 37 MV/m, H_{peak} = 850 Oe. The CW thermal breakdown limit for this cavity is shown by a dashed line in Figure 3.13.

The scatter plot of measured E_{peak} vs. predicted E_{peak} begins to roll over just above the CW breakdown field, supporting the hypothesis that a

new limitation has set in. We generally find that the HPP quench level is slightly higher than the CW quench field. Implications of this relationship will be discussed more thoroughly in the Chapter 6. Furthermore, when the cavity experiences a quench during the processing pulse, the transmitted power (P_t) pulse used to monitor the fields during processing drastically changes its appearance. Figure 3.18 shows oscilloscope traces which show the evolution of the P_t pulse (the lower curve in each trace), while changing only the external coupling (Q_{ext}). As Q_{ext} is decreased, the attained electric field passes through the quench threshold, and the P_t pulse takes on the appearance shown. The change in pulse shape can clearly be seen by comparing parts (d) and (e) of Figure 3.18. The external Q is decreased only slightly, and the achieved electric field rises accordingly, however the pulse shape changes drastically. Parts (a)-(d) are distinguished by an exponential decay in the P_t pulse when the RF pulse is turned off. In part (e), however, the decay is much more rapid. The extreme change in decay shape and time, cannot be explained solely by the change in Q_{ext} (and thus Q_l and τ), but instead we associate this pulse shape change with the crossing of the thermal breakdown threshold. As mentioned, this will be discussed in much greater detail in Chapter 6.

We have found that by choosing the HPP operating conditions suitably, the quench field may be exceeded for short (10's of micro-seconds) periods, and E_{peak} maximized by increasing incident power, and decreasing Q_{ext}, so that the cavity fills more rapidly. In this way, the electric field is able to reach higher values in the time it takes the quench to occur, and thus processing is extended beyond the thermal breakdown limit. Figure 3.18, part (f) shows an excellent example of maximization of E_{peak} while experiencing thermal breakdown.

Figure 3.18. Oscilloscope traces showing the variation in transmitted power pulse as the coupling is increased. The lower trace in each plot is the transmitted power. In parts (a), (b), (d), and (e), the top trace is the reflected power from the cavity. In parts (c) and (f), the top trace is the incident power. Parts (a) through (e) have the same incident power, with continually increasing coupling. The thermal breakdown threshold is passed between parts (d) and (e), which have nearly the same field and coupling, but very different P_t pulse shapes. Part (f) shows an example of a maximized P_t signal, where coupling and power are optimized, so that the fields reach a maximum value in the time that the quench requires to initiate.

3060493-043

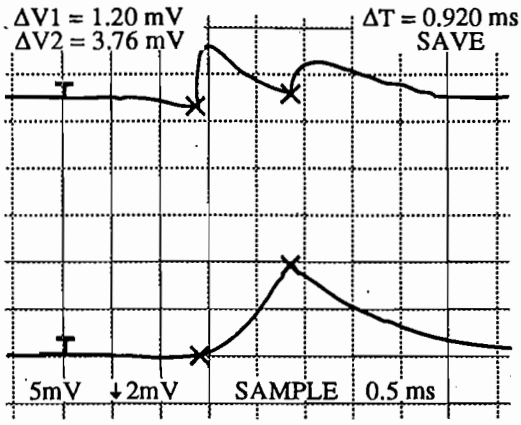

(a).

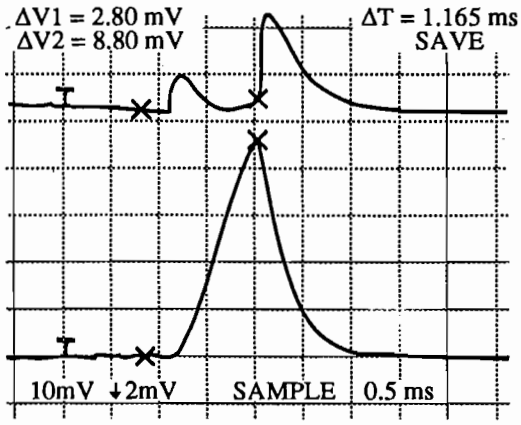

(d).

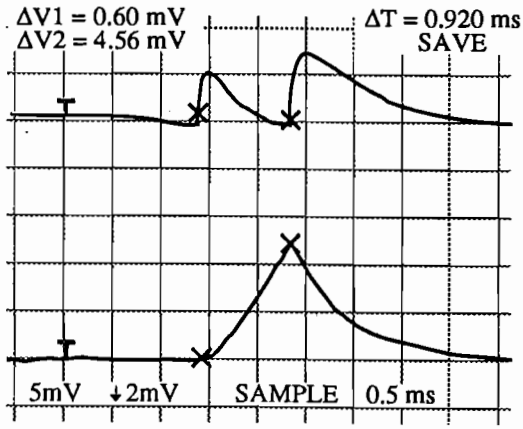

(b).

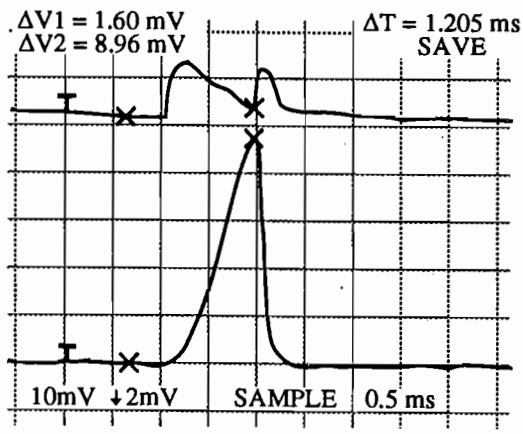

(e).

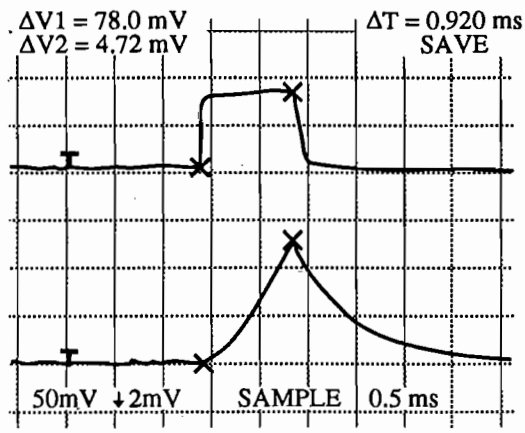

(c).

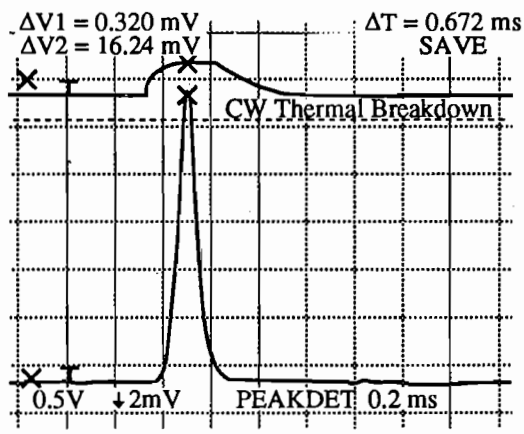

(f).

3.5. Processing

In this section, we discuss events encountered during HPP which we believe are associated with the "processing" effect. These events are characterized by a distinct appearance, as compared with other phenomena.

3.5.1. Processing Events

As E_{HPP} was increased during the processing procedure, the P_t pulse occasionally showed a rapid collapse event, where the transmitted power, and thus the stored energy in the cavity (proportional to E_{peak}^2) decayed to zero in less than 1 μsec. Figure 3.19 shows an oscilloscope trace of an event of this nature. We associate this pulse shape with a "processing event," where during the RF pulse, the emission current becomes large enough so that the emission site "processes". The stored energy in the cavity is apparently absorbed by the processing event. Processing events generally happen once, or possibly on two consecutive pulses, following

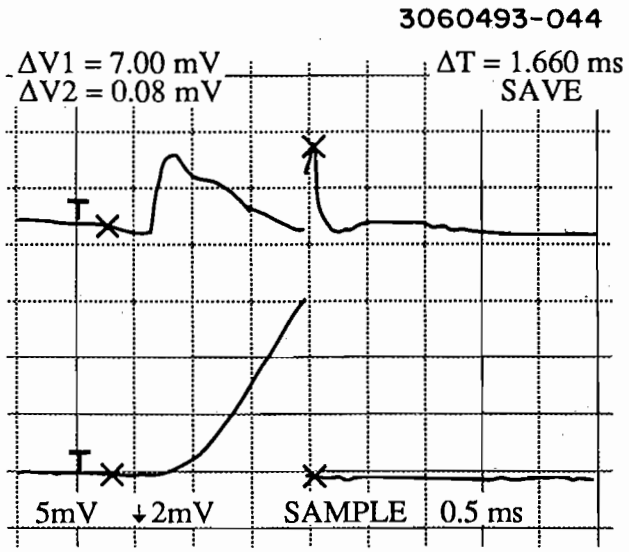

Figure 3.19. Oscilloscope trace showing a processing event. The top trace is reflected power from the cavity, and the bottom trace is transmitted power, showing the nearly instant (less than 1 μsec) collapse of fields in the cavity.

which the P_t pulse returns to its previous shape, though often at a higher maximum field level, supporting our belief that the event is connected with cavity improvement. Processing events can occur even if the cavity is experiencing a thermal breakdown during the RF pulse.

3.5.2. Multiple, Variable-Shaped Events

The CW performance of a cavity always continues to improve as long as the processing field (E_{HPP}) increases. The processing fields in nine-cell cavities could be extended above the thermal breakdown limit by increasing the incident power and lowering the Q_{ext}. Unlike the single cell cavities, however, a new phenomena appeared as the fields were increased. As in the single cells, while the fields were being raised, occasionally a "processing event" would be encountered, but then the P_t pulse would return to it's pre-event shape. In the nine-cell cavities, however, the processing events would eventually give way to a new type of event, which we term "multiple variable-shaped (MVS) events." Unlike the processing events, the MVS events did not have a single characteristic shape of P_t pulse, as viewed on the oscilloscope. Figure 3.20 shows four examples of the MVS events. The P_t pulse shape took on many varying shapes while MVS events were occurring.

In all cases to date, MVS events were encountered after the cavity had passed the thermal breakdown field, as monitored by P_t pulse.

MVS events also appear to be associated with field emission. Evidence for this statement lies in the conditions under which the MVS events occurred. MVS events were always preceded by normal processing events (as shown in Figure 3.19). Remember that, in addition, MVS events always occurred with the cavity experiencing thermal breakdown. As the fields were further increased (through optimization of the HPP

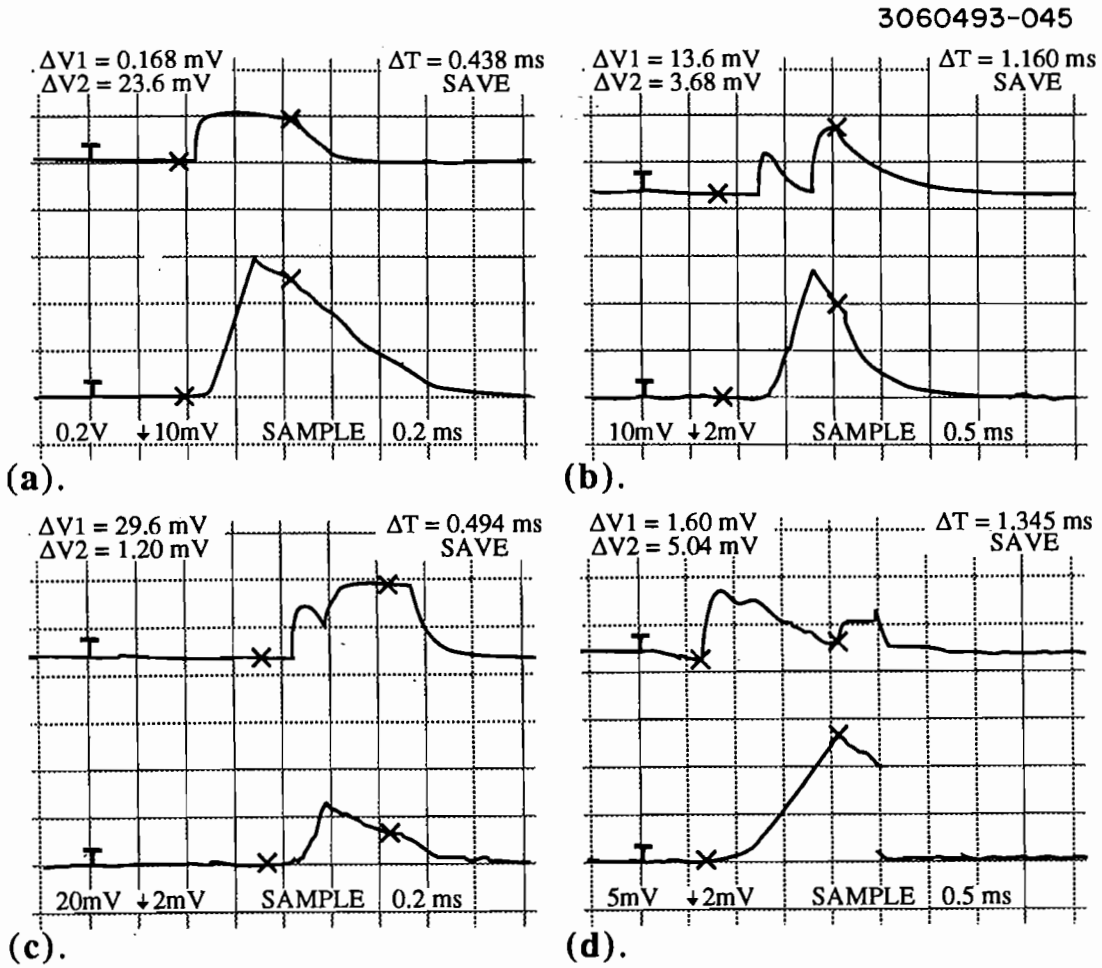

Figure 3.20. Some examples of oscilloscope traces showing MVS events encountered during HPP processing of nine-cell cavities. In part (a), the top trace is incident power on the cavity, and the bottom trace is the transmitted power. In parts (b)-(d) the top trace is reflected power from the cavity. The reflected power traces show that the MVS event stops the cavity from completing its fill.

parameters), the P_t pulse shape would change from the signature of thermal breakdown (see Figures 3.18(d)-(f)), to that of the MVS events (as shown in Figure 3.20). MVS events generally occur for many consecutive RF pulses (remember that HPP occurs at a repetition rate of about 1 Hz). After several RF pulses, the P_t pulse would generally return to its reproducible breakdown pulse shape.

Investigation of the reflected power traces shown in Figure 3.20 further show that the MVS events are initiated before the cavity fields maximize, at which time the fields begin to decay, though on a much longer time scale than either thermal breakdown, or processing events. In addition, Figure 3.20(d) shows that on occasion an MVS event includes the signature of a processing event, though clearly the MVS event had been initiated prior to the processing event. The multiple pulse nature of the events seems to indicate that the mechanism which initiates the MVS event operates on a longer time scale than the pulse period.

MVS events always occurred at relatively high input power ($\geq$ 20 kW), which could indicate that they are caused by processing of various parts of the HPP test stand, such as the input coupler or windows. Once the MVS events were encountered, they were dependent on the field (always occuring at the same field level) in the cavity, independent of the input power. This indicates that the MVS events are related to cavity phenomena. Nonetheless the possibility remains that they are due to some other portion of the test apparatus.

The number of pulses required for the MVS events to subside increase as the electric fields in the cavity are increased. In the best tests of the nine-cell cavities, a limit was eventually reached where no further gains could be made, because the MVS events prevented any further increase of the processing field.

Based on the limitation of nine-cell processing due to the MVS events, we believe that further gains in processing could have been made with more RF power than the 200 kW which was available to the HPP experiments. This will be further discussed in the chapter discussing the thermal breakdown limitations of HPP processing.

3.6. Bypassing the H_{peak} Limit: 2-cell Cavity W3C2-1

As described in the last section, the experience with thermal breakdown limitation in the S3C cavities led us to the conclusion that the magnetic fields were the primary limitation to the effectiveness of HPP processing. (Again, this will be more fully examined in the next chapter.) With this in mind, we determined that it would be worth investigating a cavity with a lower ratio of H_{peak}/E_{peak}. This ratio is determined by the cavity geometry, and can be obtained by the previously mentioned programs URMEL[5] and SUPERFISH[4]. The S3C cavities used for the single-cell and nine-cell experiments described above have H_{peak}/E_{peak} ratios of 23 Oe/(MV/m) and 20 Oe/(MV/m), respectively. After some investigation, we decided to fabricate a two-cell cavity using the geometry of the S-band cavities used by the SRF group at the University of Wuppertal. Interatom GmbH graciously agreed to press the half cells for this cavity. Final trimming and electron beam welding was performed at Cornell. The larger rounding of the equator region reduces the magnetic field to electric field ratio of this two-cell cavity (designated W3C2-1) to H_{peak}/E_{peak} = 14.2 Oe/(MV/m). A diagram of cavity W3C2-1 was shown in Figure 2.2.

Based on the reduced H_{peak}/E_{peak} ratio and the observed magnetic field break-down levels (H_{bd} = 1250-1300 Oe) from the S3C cavities, we predicted that the cavity would reach 90-95 MV/m prior to thermal breakdown limitation. The cavity performance exceeded this prediction. The results of the best experiment with cavity W3C2-1 are shown in Figure 3.21. This cavity experiment extended over two cool downs, with a room temperature cycle, but no vacuum break between.

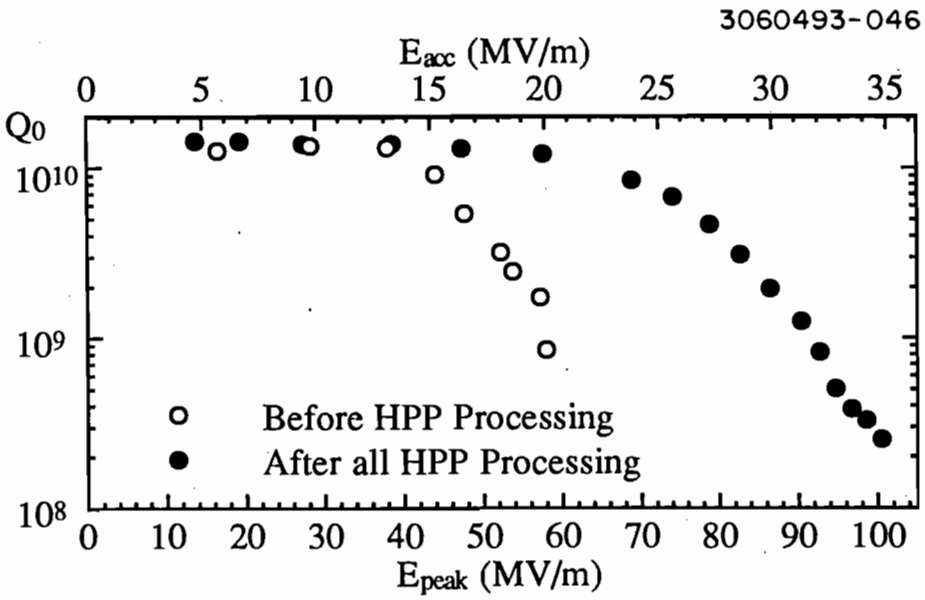

Figure 3.21. Q_0 vs. E_{peak} plots for the best experiment of the two-cell cavity.

On initial rise of power, the cavity performance was similar to that of pre-HPP single cell cavities. FE related Q_0 degradation was measurable at a peak field of E_{peak} = 25 MV/m, though low power processing with P_{inc} = 10 W increased the threshold to E_{peak} = 35 MV/m. The second plot in Figure 3.21 is the best CW measurement from the second day of testing the cavity. This CW measurement followed processing with incident power up to 130 kW, and fields as high as E_{peak} = 103 MV/m, a room temperature cycling, and processing with power up to 100 kW, and fields as high as E_{peak} = 113 MV/m. As can be seen, the improvement is phenomenal. The maximum attained CW field was E_{peak} = 100.6 MV/m, limited by thermal breakdown (H_{peak} = 1430 Oe). This peak electric field is 20 MV/m higher than any accelerating cavity has every been operated CW. Accelerating gradient at E_{peak} = 100.6 MV/m was E_{acc} = 34.8 MV/m.

The Q_0 of the cavity remained above 5 x 10^9 for peak fields as high as 75 MV/m (E_{acc} = 26 MV/m). The experiment was repeated, reaching E_{peak} = 85 MV/m, where it was limited by a superfluid helium leak.

The results of this cavity test clearly verify the hypothesis that the limitation in the S3C cavities was thermal (and thus magnetic field related) in nature, and show that without the thermal limitation, much higher peak electric fields may be processed. All results of cavity W3C2-1 are included in the scatter plots of Figures 3.9 through 3.11. These figures show that the achieved gains in E_{max}, E_x, and E_{fe} follow the same pattern as the single cell and nine cell S3C cavities.

3.7. Comparison of HPP with Low Power CW Processing

Comparison of the phenomena of HPP processing and low power CW processing shows qualitatively similar behavior. This is most clearly seen in Figures 3.14 and 3.15. Low power RF processing is characterized by abrupt improvements in cavity performance (as shown in Figure 3.15), following which the cavity Q_0 vs E_{peak} curve exhibits improved performance. During HPP, the processing events cannot be as easily observed with regard to Q_0 vs E_{peak} behavior. Similar behavior is seen, however, by plotting pre-HPP cavity performance, HPP E_{peak} and Q_0 values, and post-HPP cavity performance, as shown in Figure 3.14.

In addition to the qualitative similarity in Q_0 vs E_{peak} behavior, microscopic investigation of RF surfaces which had been processed by either HPP or CW processing shows the same type of features. The surface features, and their significance, will discussed in detail in Chapter 4.

Based on these observations, we conclude that the mechanism of HPP processing is not inherently different from the mechanism of low power RF processing. Despite the similarities, it is informative to discuss

the significant differences in the conditions of HPP processing (compared to low power CW processing) that led to the improved results.

1. Available Power. The key to HPP processing is forcing the peak fields during processing to higher values. The Q_0 of the cavity rapidly decreases with increasing E_{peak}, thus dissipating more power. It is necessary to have a large source of available power in order to reach the necessary processing fields (empirically found to be 50% or more higher than the desired operational field level).

2. Ability to Match Power Into the Cavity. It is clear from the Figures 3.14 and 3.16 that the Q_0 value for the cavity decreases by as much as four orders of magnitude from its low field value during HPP processing. The input coupler of the HPP experimental apparatus was designed to vary smoothly (with no vacuum break) between 10^5 and 10^{10}, thus the cavity can be unity coupled, even when the cavity Q_0 is driven as low as 1×10^5. The ability to achieve unity coupling allows *all* available power to be coupled into the cavity for processing purposes.

The relatively low Q_{ext} (compared to normal Q_0 values) also contributes to the HPP results, in that the loaded Q also is reduced, which correspondingly decreases the characteristic fill time from hundreds of milliseconds (for a unity coupled cavity with $Q_0 = 10^9$-10^{10}) to tens or hundreds of microseconds. The decreased fill rate is significant for two reasons. First, in non-quench conditions, the cavity is able to fill significantly within the relatively short (hundreds of microsecond) RF pulse length. Secondly, in quench conditions, as described above, the cavity fill may overshoot the CW quench field level in the time that the quench requires to initiate. Decreasing the fill time (increasing the fill rate) of the

cavity allows for more overshoot of the quench field. This will be discussed in detail in the Chapter 6.

3.8. Durability of HPP Processing

Throughout the three year HPP experimental program, various events, both planned and unplanned, have occurred which have tested the durability or sustainability of a cavity which has been processed through the HPP technique. We present here the results of these experiments and accidents.

3.8.1. Temperature Cycling

The simplest phenomena encountered, with regard to durability of HPP processing, is a temperature cycling of the cavity (to room temperature and then cooled back down and re-tested) with no break of the cavity vacuum system. We found that temperature cycling does not significantly affect the overall loading of the cavity. This is clearly shown by investigating the Q_0 vs. E_{peak} (or E_{acc}) curves before and after the temperature cycle. Figure 3.22(a)-(c) shows an example of before and after temperature cycling for a single-cell, two-cell, and nine-cell cavity, respectively.

The local FE behavior of the cavity does however change. Figure 3.23, parts (a) and (b) shows temperature maps (See the chapter on thermometry for a complete discussion of the thermometry system) before and after a room temperature cycle. The maps were taken at approximately the same peak electric field ($E_{peak} \approx 45$ MV/m). The temperature map clearly shows a change in the temperature profile of the cavity for the same electric field, indicating that new emission sites have been created, while possibly old sites are gone. This phenomena supports a model in which contaminants adsorbed on the inner cavity surface play an important role in emission. Upon warming to room temperature the

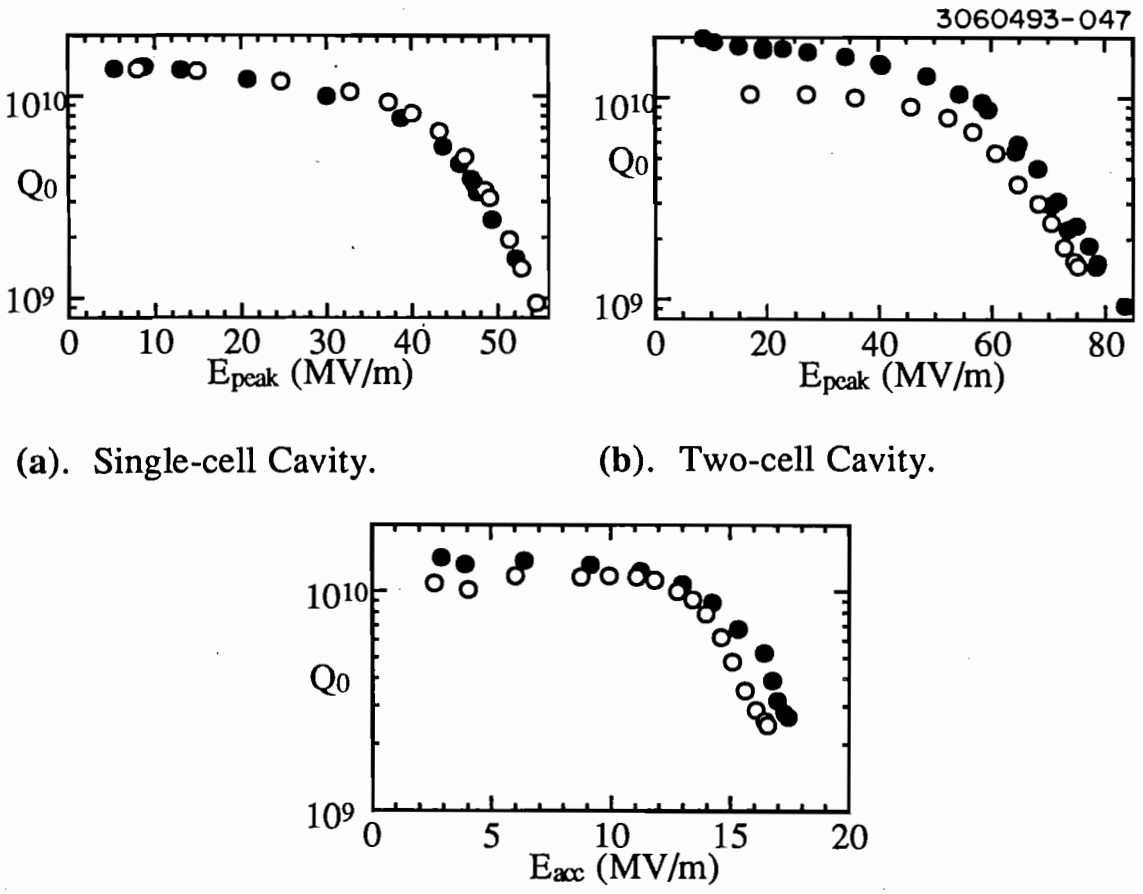

(a). Single-cell Cavity.

(b). Two-cell Cavity.

(c). Nine-cell Cavity.

Figure 3.22. Q_0 vs. E_{peak} (or E_{acc} for the nine-cell) curves showing the change in cavity loading following a temperature cycle without vacuum break. In each plot, the open symbols are for before the temperature cycle, and the solid symbols after. As shown, the loading can increase or decrease slightly, but the changes are not significant.

adsorbed contaminants could dislodge from the surface, and upon re-cooling to liquid helium temperatures re-adsorb in a new location, possibly inducing emission at this new site.[64]

In addition, we have found that cavities which were processed with all available power on an initial cool down, and stopped progressing,

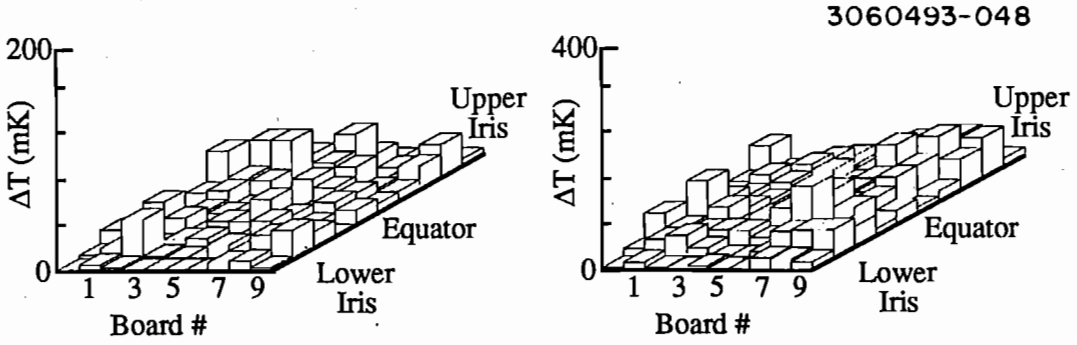

(a). Before temperature cycle, E_{peak} = 45 MV/m.

(b). After temperature cycle, E_{peak} = 45 MV/m.

Figure 3.23. Temperature maps showing change in localized emission behavior in a single-cell cavity following a temperature cycle without vacuum break. Note the larger scale in (b).

could sometimes be processed to higher fields in a second cool down. Figure 3.24 is an updated version of Figure 3.22(c), now including the results following HPP during the second cool down. We see that following the room temperature cycle, the cavity (a nine cell cavity)

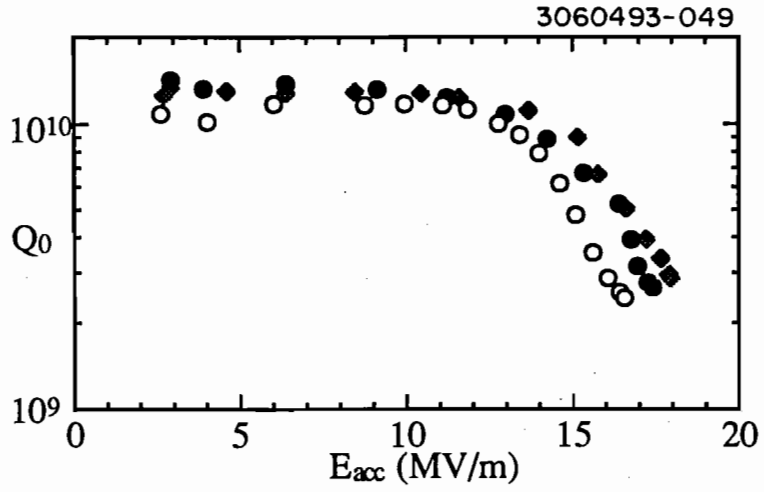

Figure 3.24. Updated from Figure 3.22(c), Q_0 vs. E_{acc} showing the change in FE loading in a nine-cell cavity following a temperature cycle without vacuum break, and also following further HPP processing.

reached an accelerating gradient of E_{acc} = 18 MV/m, whereas at the end of the first cool down, accelerating gradients were limited to E_{acc} = 17 MV/m. This can be explained by changes in the localized emission sites to a more easily processable type due to the temperature cycle.

3.8.2. Temperature Cycling with Exposure to Filtered Air

HPP processing is foreseen as a possible method of cavity preparation for large scale accelerator facilities. In order to show the applicability to this function, it is necessary to learn what care is required for a cavity following processing to maintain the HPP induced benefits. To this end, we allowed a processed nine cell cavity (low field Q_0 = 1 x 10^{10}, Q_0 > 10^{10} for E_{acc} = 14 MV/m, maximum E_{acc} = 18 MV/m) and cycled it to room temperature. While at room temperature, the cavity was exposed to filtered air (0.3 micron HEPA filter) for 24 hours, and then re-evacuated. The cavity was then re-cooled to liquid helium temperature, and the FE behavior was measured. Figure 3.25 shows the Q_0 vs. E_{acc} plots before and after this exposure. Again, no significant increase in FE loading was

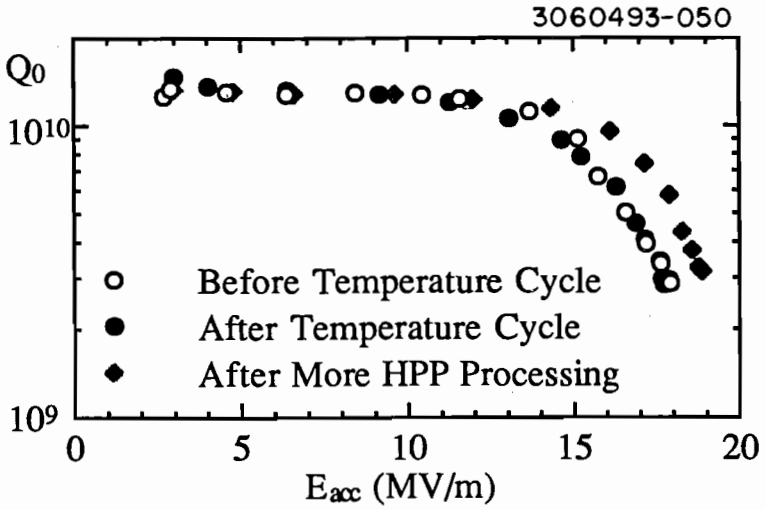

Figure 3.25. Q_0 vs. E_{acc} showing the change in FE loading in a nine-cell cavity following a temperature cycle with exposure to filtered air, and also following further HPP processing.

observed, and in fact, following further HPP processing, the cavity reached higher fields (see the third plot in Figure 3.25), than prior to the exposure test.

This is consistent with the findings of RF processing studies performed on low frequency, heavy ion accelerator cavities at Argonne National Laboratory[65], as well as low power processing of 1.5 GHz cavities at Cornell LNS[49].

3.8.3. Recovery from Vacuum Accidents

Vacuum accidents are an ever present danger in accelerator systems, and the contamination due to such an accident can cause significant degradation of the performance of an accelerator cavity. In this light, we present the results of three exposures of nine cell cavities to unfiltered air, two accidental, one intentional.[66] It has been well established previously that air, especially unfiltered is a source of field emitters.[38],[49],[64]

The circumstances of the first accident were: The cavity had been cooled to 4.2 K, and, at this temperature, was exposed to the roughing vacuum pumps used to pump down the helium bath in order to reduce the temperature to 1.4 K. No measurements had been made on the cavity prior to this accident. Following re-evacuation of the cavity, the experiment was begun. The Q_0 vs. E_{acc} plots are shown in Figure 3.26. The initial rise of power was characterized by very heavy FE, some of which was processable with low power. The second curve in Figure 3.26 is the reproducible Q_0 vs. E_{acc}, following all possible low power processing. The cavity was then HPP processed with power as high as 90 kW, and fields as high as E_{peak} = 58 MV/m. The HPP processing was not only successful in reducing the FE loading, but it also seemingly improved the low field Q_0 value, possibly through RF removal of resistive contaminants on

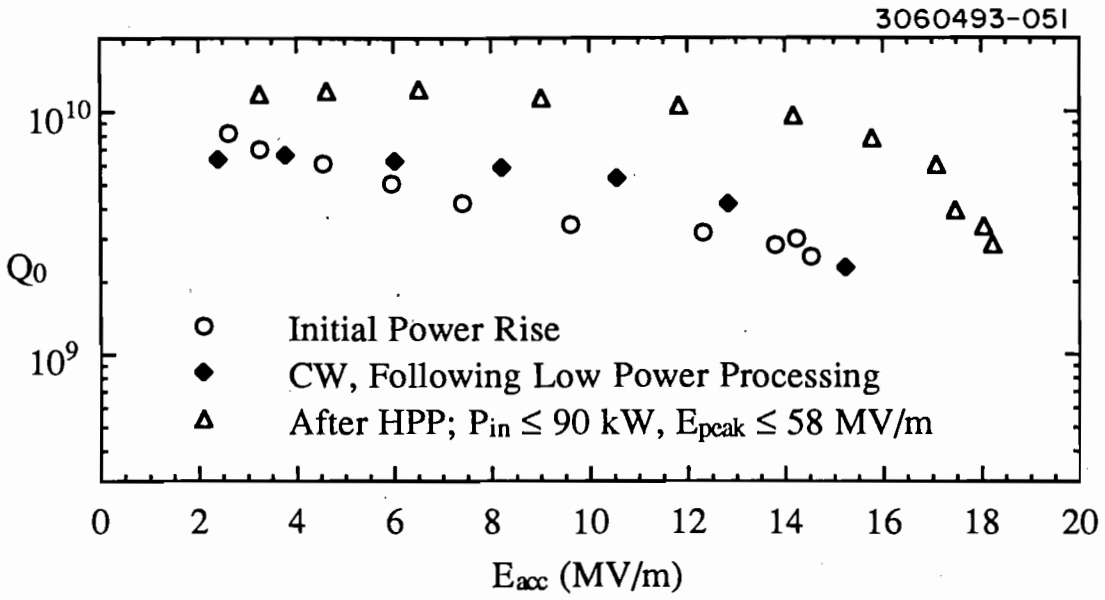

Figure 3.26. Q_0 vs. E_{acc} curves describing the behavior of a nine-cell cavity following the first vacuum accident.

the cavity surface. The Q_0 vs. E_{acc} curve following HPP processing is also shown in Figure 3.26.

The second accident occurred on the same cavity, following the experiment just described. After the cavity was warmed to room temperature, it was accidentally exposed to unfiltered atmosphere. Again, the cavity was re-evacuated, and cooled down for experimentation. The plots for this experiment are shown in Figure 3.27. Similar to the previous test, the initial power rise was characterized by very heavy FE, with significant low power processing. The cavity was then HPP processed, with incident power as high as 100 kW, and fields up to E_{peak} = 57 MV/m. The resulting low power measurement is shown in Figure 3.27. HPP processing was successful in regaining approximately 14 MV/m in accelerating gradient.

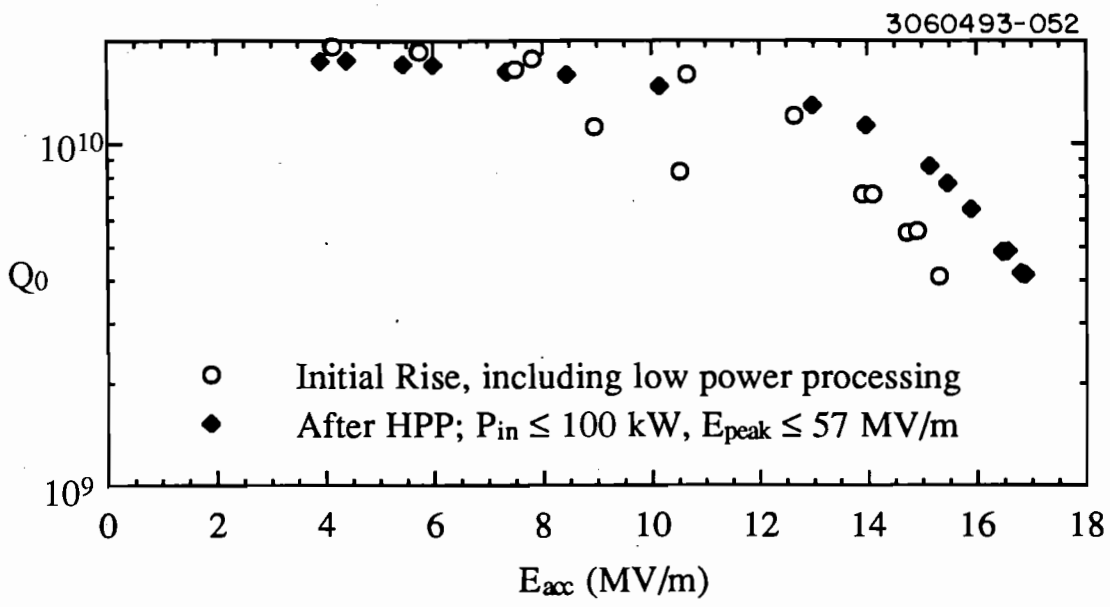

Figure 3.27. Q_0 vs. E_{acc} curves describing the behavior of a nine-cell cavity following the second vacuum accident.

The final event to be reported was an intentional test of a vacuum accident. Again, the same cavity was involved. Following the above described test, the cavity was cycled to room temperature, re-cooled, and re-tested. Then, while the cavity was at liquid helium temperature, the cavity interior was exposed to unfiltered atmosphere. The cavity was then remeasured, showing heavy field emission, as well as a low field Q_0 degradation. Following a room temperature cycle, the cavity was HPP processed, with peak power up to 105 kW, and fields up to E_{peak} = 42 MV/m. Again, partial recovery was made via HPP processing. All Q_0 vs. E_{acc} curves for this experiment are shown in Figure 3.28.

Based on these results, we conclude that HPP processed cavities can be damaged by vacuum accidents, however the performance may be regained through low power and HPP RF processing.

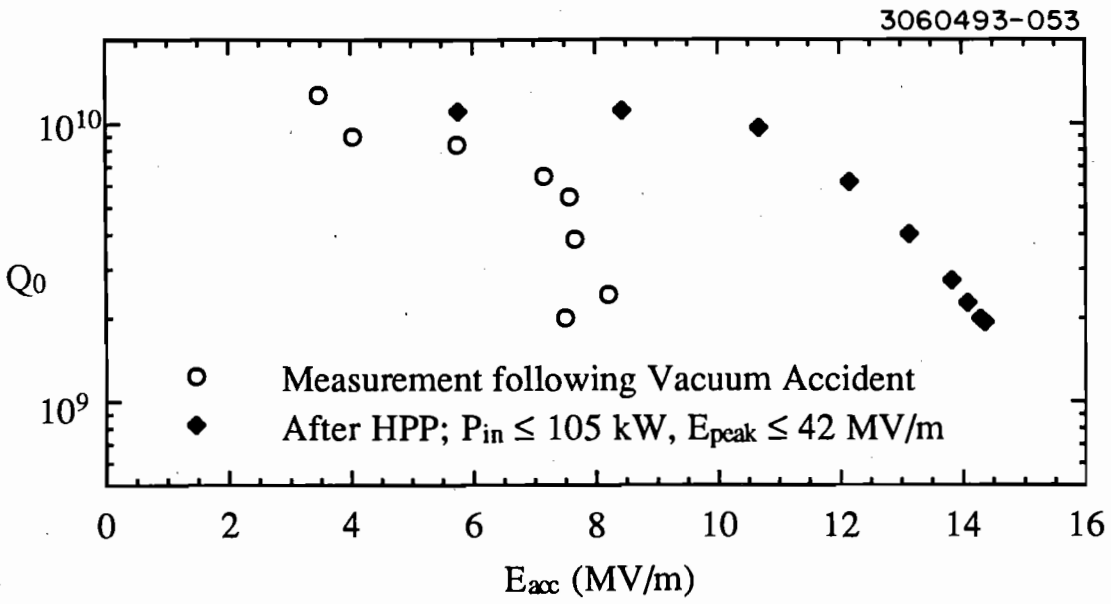

Figure 3.28. Q_0 vs. E_{acc} curves describing the behavior of a nine-cell cavity following the third (intentional) vacuum accident.

3.9. The Need for Gentle Processing

In the earliest tests of HPP processing, the technique was applied rather bluntly. Specifically, in single cell cavities, processing was immediately attempted with incident power of 40-50 kW, and little attention paid to the Q_{ext} of the input coupler. Comparison of Q_0 vs. E_{peak} curves before and after processing indicate reduction of FE loading, however the attainable field is only 1-2 MV/m higher than prior to processing, limited by a thermal breakdown. In each of these cases, the thermal breakdown field was anomalously low for the material purity of the cavities involved, thus making us suspicious as to the occurrence of the quench following high power processing. We now believe that these thermal breakdowns were caused by excessively violent processing events, which created thermal hot spots in the cavity.

Visual evidence was found in one of these cavities. Figure 3.29 shows SEM photographs of a crater region, and a nearby spherical particle composed of indium. While no thermometry was available on this cavity, it is likely that the quench was initiated at these sites.

In subsequent tests, we have learned to avoid creation of quenches due to HPP processing. The manner in which the damage is avoided can be termed "gentle processing," where we start at relatively small incident power, with high Q_{ext}. The Q_{ext} is gradually decreased until the maximum field is reached for this input power. Then the power is increased, and the cycle is repeated. Since adopting this "gentle" manner of processing, we have not created any anomalously low thermal breakdowns in subsequent experiments.

The physical size of the crater region shown in Figure 3.29 also lends credence to the idea that processing need be more gradual. Crater regions are a common feature in cavities which have been successfully processed without creation of thermal breakdown phenomena. In non-breakdown cavities, however, the craters have sizes on the order of a few microns, while the crater region shown in Figure 3.29(a) and 3.29(b) is approximately 400 microns in diameter. The larger size supports the theory that this processing event was more violent than those of later cavities. The craters in the RF surface, and their significance to the processing phenomena, are extensively discussed in Chapter 4 of this dissertation.

3.10. Conclusions

Pulsed high peak power RF processing has been shown to be an effective means of reducing field emission loading in 3 GHz niobium accelerating cavities. Attainable and usable accelerating gradients can be

(a).

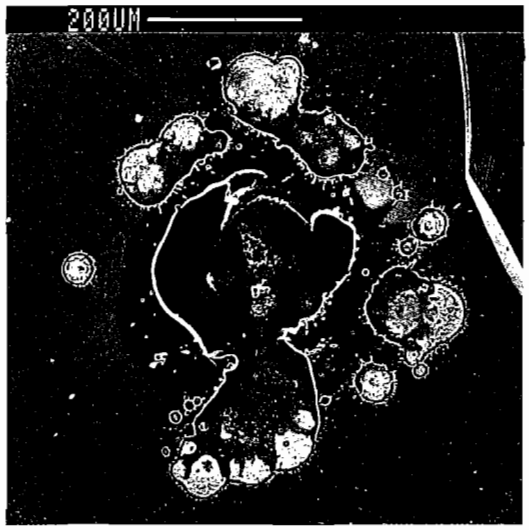

(b).

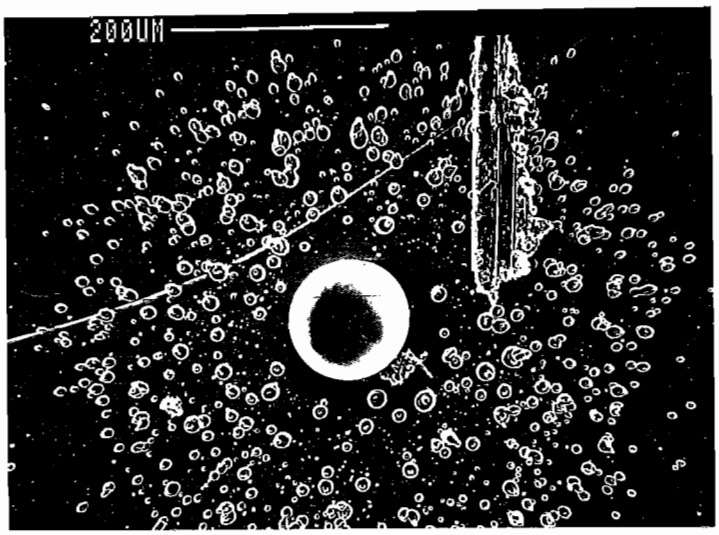

(c).

Figure 3.29. SEM photographs of the damage region found near the iris in one of the early cavities tested with HPP processing. Part (a) shows a crater region (upper feature), and an indium particle and field (lower feature). Parts (b) and (c) are enlargements of the crater and indium field, respectively.

increased up to 50% above what is attainable with the power available (hundreds of watts) for a typical low power RF measurement apparatus.

Processing success is directly related to the magnitude of peak electric fields reached during HPP processing. Thermal effects, specifically quench or thermal break-down, limit the maximum peak electric field achieved during HPP processing. A special two cell cavity with a lower magnetic field to electric field ratio (and thus higher electric field quench level, since quench is determined by magnetic fields) was tested, and through HPP processing reached a CW peak electric field of 100.6 MV/m and accelerating gradient 34.6 MV/m, the highest peak electric field and accelerating gradient ever sustained in a superconducting accelerating cavity.

The effects of high power processing are durable upon cycling to room temperature and re-cooling. In addition, exposure to filtered air does not negate the gains achieved through HPP processing. Even with exposure to unfiltered air, the cavity performance has been largely recovered through HPP processing. Based on these results, HPP processing is a promising technique for the construction of large scale accelerating structures.

CHAPTER 4: MICROSCOPIC INVESTIGATION OF HPP PROCESSED RF SURFACES

4.1. Introduction

Surface investigation studies of the cavities in the HPP program was initiated with the goal of finding physical evidence of processing on the RF surface. We were encouraged by the findings of the Mushroom cavity project[24] at Cornell, in which a specially designed, non-accelerating cavity was examined in a Scanning Electron Microscope (SEM) following RF cold tests. Multiple phenomena were encountered in the high electric field regions of the cavity, indicating a possible link to field emission activity.

In order to better establish the link between surface features and RF processing, the thermometry information was included in the analysis, as will be further discussed below.

SEM investigation of the cavities involves dissection of the single cell cavities in order to facilitate investigation of the RF surface. Since the investigation involves destruction of the cavity, it is the final step performed on a test cavity, and generally is only performed if there is reason to believe interesting phenomena will be detected.

Ultimately it is desirable to gather microscopic information on field emission sites. DC field emission studies[39] have shown that these are micron or sub-micron features, for example, superficial particles. Even with guidance from thermometry, where the resolution is of the order of a few square millimeters, location of such minuscule features after dissection of a cavity presents a significant challenge. Fortunately, as this study shows, if the emission site processes, or undergoes significant change during cavity operation, then the additional features associated with the processing event make it substantially easier to locate the site. Some of these features are

several hundred microns in diameter. Most of this work has accordingly focused on trying to locate field emission sites after processing. In a few cases, it is believed that emission sites have been found before processing. One example of a thermal breakdown site is also presented.

4.2. General Results of Thermometry

The general experimental procedure was outlined in detail in Chapter 2. In all tests, the procedure was to take a series of temperature maps of the cavity at varying electric field levels. Field emission induced temperature rise is measured by the thermometers. The maps are then analyzed for emitter location, F-N properties and the effect of RF processing with or without HPP. The thermometry data was analyzed with the analysis programs previously developed at Cornell University, for use in the 1.5 GHz experimental program.[54]

Figure 4.1 shows four typical temperature maps. These maps show a good example of a change in heating behavior due to HPP processing. In Figure 4.1(a) emission related heating can be seen at E_{peak} = 32 MV/m on board #8, near the upper iris region. (Upper refers to geometrical orientation of the cavity during RF cold testing.) Figure 4.1(b) shows the result at the same field of one HPP session on this emission site. (HPP parameters were: incident power P_{inc} = 2 kW, and pulse length t_{RF} = 630 μsec) During HPP the peak surface electric field reached was 49 MV/m. As can be seen in map 4.1(b), the heating is reduced in comparison to the rest of the cavity. The reduction in local temperature signals following HPP processing was observed regularly in many tests on similar cavities. At a higher CW field (34 MV/m) emission related heating at the same site grows again. The emitter is still quite strong. Further HPP has a dramatic effect on the

emission. (HPP parameters were: P_{inc} = 3.5 kW, t_{RF} = 630 μsec.) The maximum field reached during the second HPP session was 54 MV/m.

These results support our interpretation that the benefits of HPP are achieved through weakening and/or destruction of individual emission sites.

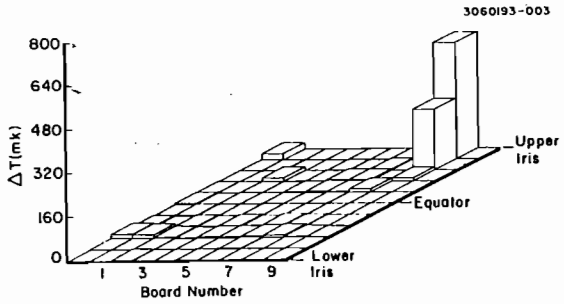

(a). Initial Rise; E_{peak} = 31.7 MV/m.

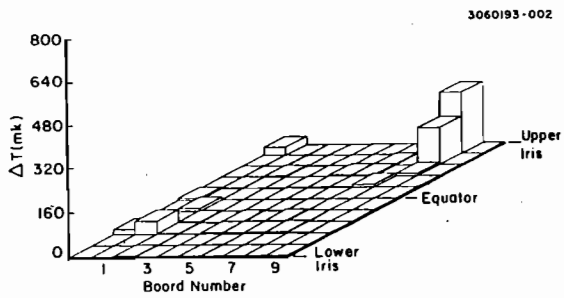

(b). After HPP; E_{peak} = 32.3 MV/m.
HPP :P_{inc} = 2 kW, $E_{peak} \leq$ 49 MV/m.

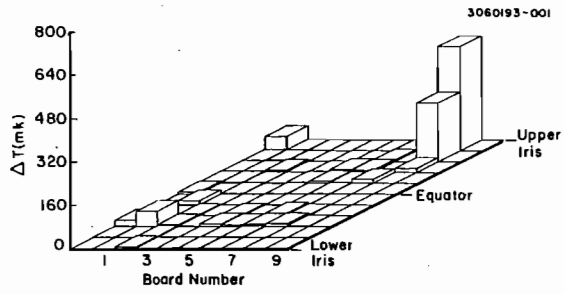

(c).After HPP; E_{peak} = 33.6 MV/m.

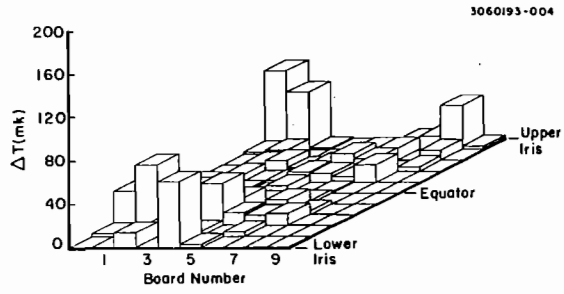

(d). 2nd HPP; E_{peak} = 36.3 MV/m.
HPP: P_{inc} = 3.5 kW, $E_{peak} \leq$ 54 MV/m

Figure 4.1. Examples of temperature map detection of changes in emission related heating due to HPP processing. Note the reduced scale in part (d), compared to parts (a)-(c).

Although it is not the primary purpose of this study, The thermometry system, on several occasions also showed heating unrelated to FE sources. Examples will be discussed further below where it relates to SEM investigations.

4.3. Simulated Thermometry via Electron Trajectory Calculations

Given the temperature maps produced by the thermometry system, the next step was to characterize emission at these sites based on the thermometry response. The field enhancement β and emitter area A are characteristics of the enhanced Fowler-Nordheim theory of field emission, as discussed in Section 1.3.1. As stated there, no definite physical significance can be attributed to β or A, but they are still useful quantities for characterizing the nature of emitters.

Values for β can be extracted by two methods. The first is to plot the temperature rise (ΔT) in "Fowler-Nordheim" form, that is $\ln(\Delta T/E^2)$ vs. $1/E$, where E is local electric field at the emission site. If the thermometer behavior is field emission dominated, the plot will be a straight line, with the slope of the plot proportional to $-1/\beta$, and the intercept at $1/E = 0$ proportional to $\ln(A)$. The tool for this method is the program TEMPER, which is part of the previously mentioned package of thermometry analysis programs.

The second method of obtaining β is to match the simulated temperature rise of an entire azimuth of thermometers to the experimentally obtained response. This is done for several different electric field levels. This method also allows a determination of A. β and A are varied until an optimum fit is found over the largest possible range of electric field values.

In general, the two methods produce very similar values for β, but only the second method is capable of yielding A.

The tools for this step are two packages of computer programs, **MULTIP** and **POWER**, developed at Cornell LNS[63] for simulation of FE phenomena. **MULTIP** computes electron trajectories by solving the relativistic equations of motion for an emitted electron. Typical trajectories were shown in Figure 1.3. **POWER** takes the output of **MULTIP**, and then computes various phenomena associated with emission, e.g. emission current, power deposition on the surface, predicted thermometer response, and others. The input parameters of each of these programs, e.g. local enhancement β, emitter area A, and emitter location, can be tailored to suit the field emission to be simulated.

Some examples of matched β and A will be discussed below with respect to the SEM sites associated with processing events. In addition, more examples of β and A will be discussed in the next chapter, along with analysis of their significance to the processing phenomena.

The Q_0 vs. E_{peak} measurements of cavity performance can also be used to derive β by plotting the dissipated power in the cavity in a F-N style: $\ln(P_{diss}/E^2)$ vs. $1/E$. This procedure is valid if the cavity is dominated by a single field emission site. Similar to the thermometry based F-N plot, if the cavity is field emission dominated, the curve will be a straight line with slope proportional to $-1/\beta$.

4.4. Correlation of SEM, Thermometry and Simulations for Processed Emission Sites

In this section we present several examples of correlations between heating due to field emission detected by thermometry, a change in field

emission from processing and associated microscopic features. In each case the F-N properties of the emission sites are also derived.

In order to correlate the SEM findings to the thermometry, two complementary approaches were used: 1) Experimental temperature maps were examined, looking for potential emission sites as well as changes in emission as a result of RF processing or HPP. If emission heating, with subsequent change due to processing was found, then simulations were carried out to pin-point the location of an emitter which could explain the temperature map *before* the change. After completion of the RF test, the cavity was examined in the SEM, specifically in the location indicated by the thermometry change, searching for any features which could be the result of a full or partial processing event. 2) General SEM scans were performed on nearly all of the cavities, looking for interesting phenomena. If anything was found, then simulated temperature signals were produced using an emitter at the determined location. The simulations were compared with the measured temperature maps, to see if any correlated temperature rises or changes were present at the predicted locations.

We were quite successful in regularly finding correlations with the first approach. The second approach was not as fruitful, but with good reasons. 1) The temperature of the cavity is not monitored at all times that the RF field is on. Apart from the purpose of acquiring a temperature map, RF field is applied for several functions, primarily measurement of power levels for determination of the Q of the cavity. Emission related heating could be transient, and thus missed by the thermometry system when it is not activated. 2) The site may not be in good alignment with thermometer boards. As mentioned in Chapter 2, the active area of the thermometers covers less than 5% of the cavity surface. 3) In the case of HPP

processing, the CW fields may not be extended high enough prior to processing to cause a measurable temperature increase. 4) The thermometers near the phenomena can be faulty.

4.4.1. The Smoking Gun: 1 Thermometry Event, 1 RF Surface Feature

Several sites were found which have both a significant thermometry signal, a change in signal after processing, and an associated surface feature. One example stands out above the rest, as the clearest processing event. This site was found in cavity 1-5, which was RF tested specifically with the goal of limiting the run to one or two processing events, and then stopping for examination, rather than pushing the cavity gradient as high as possible (as was done in other cavity tests). This site may also be used as an excellent example of the procedure of matching the β and A based on temperature response at several field levels. Four complete temperature maps associated with this run were shown in Figure 4.1. Figures 4.1(a)-(c) show very clearly that one emission site dominated the pre-HPP behavior of this cavity. Following the second HPP session, the dominant emitter was substantially reduced. The cavity still had several heating sites.

Figure 4.2 shows three sets of longitudinal temperature plots, as well as the associated simulations with the optimized β and A values, for the board which was best aligned with the emission site.

The scatter plots in Figure 4.2(a) are from the first low power rise of the cavity, with E_{peak} = 27.7, 30.1, and 31.7 MV/m ($E_{emitter}$ = 23.7, 26.4, and 27.1 MV/m, respectively, at the emission site). The line plots in Figure 4.2(a) show the simulation for this emitter, with β = 200 and A = 3.2 x 10^{-10} cm^2, and the emission site is located at S_0 = -3.66 cm. The simulation program predicts emission power of 1.38 W at the highest field, whereas the experimental value from total RF dissipation was determined to be 2.9 W.

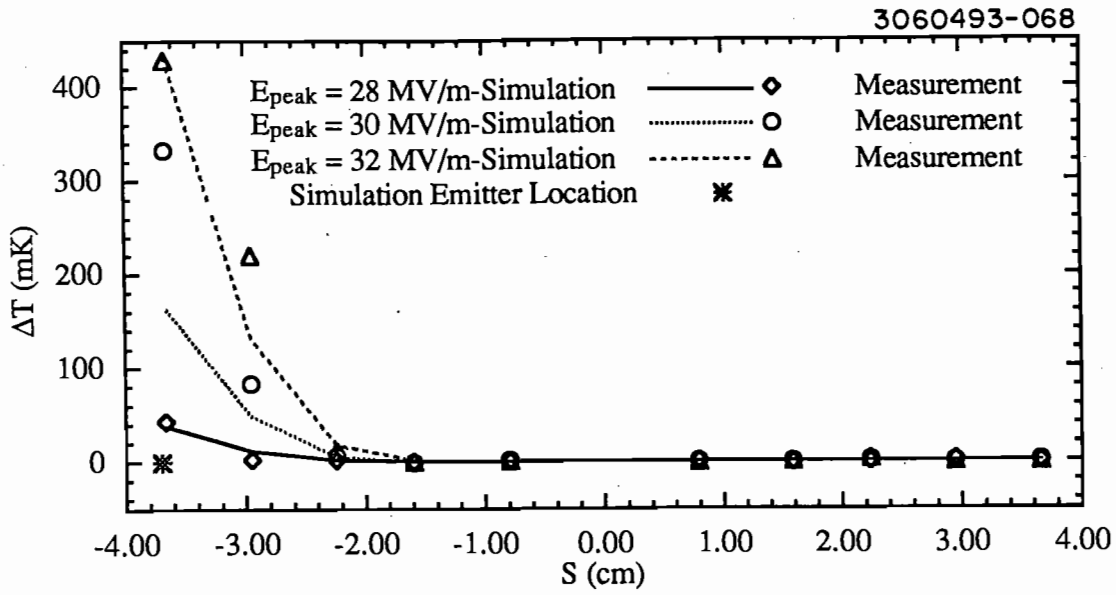

Figure 4.2.(a) Comparison of simulated and measured ΔT vs. S plots for initial low power CW rise of cavity 1-5. Simulation assumes $\beta = 200$ and $A = 3.2 \times 10^{-9}$ cm^2.

This discrepancy is most likely caused by a slight misalignment of the emitter and the thermometer board (see Appendix E for a more complete discussion of errors in correlation of thermometry and SEM examinations). If the simulation is repeated with an area of $A = 6.86 \times 10^{-10}$ cm^2, the powers agree, and the temperature of the iris resistor is predicted to be 915 mK, instead of the 425 mK measured. Based on the FWHM of the thermometer response for a point heat source, the temperature shortfall can be explained by a 3 degree misalignment between the emitter and the thermometer board. For convenience in making the comparisons between data and simulations, we choose to present the simulation which agrees with temperature rather than with power, with the understanding that the emitter area value can be different. This is also the case for Figures 4.2(b) and 4.2(c).

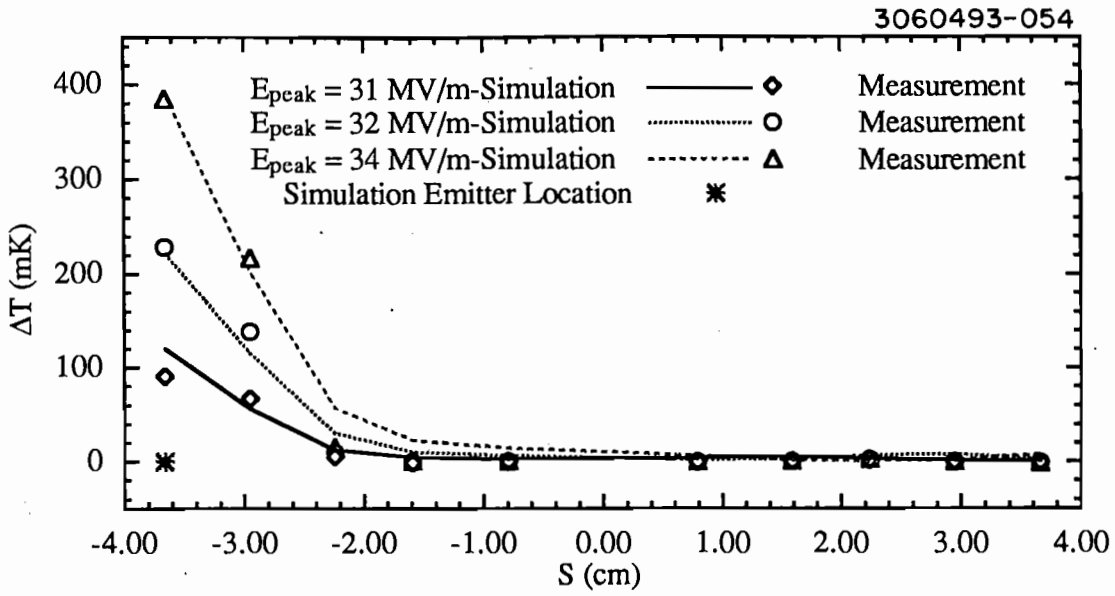

Figure 4.2.(b) Comparison of simulated and measured ΔT vs. S plots for second low power CW rise of cavity 1-5, following HPP with P_{inc} = 2 kW, t_{RF} = 630 μsec, and $E_{peak} \leq$ 49 MV/m. Simulation assumes β = 210 and A = 7.0 x 10^{-10} cm^2.

The scatter plots in Figure 4.2(b) are from the second low power test, with E_{peak} = 30.9, 32.3, and 33.6 MV/m. This cw power rise followed HPP processing with incident power P_{inc} = 2 kW, and $E_{peak} \leq$ 49 MV/m. The associated simulation is shown in the line plots of Figure 4.2(b), with β = 210 and A = 7.0 x 10^{-11} cm^2. As can be seen, this processing session reduced the heating slightly. Comparison of the temperature maps in Figures 4.1(a) and 4.1(b) show that in the initial rise at E_{peak} = 31.7 MV/m, the peak temperature was 425 mK, whereas in the second CW power rise at E_{peak} = 32.3 MV/m, the peak temperature was 230 mK, a reduction in loading of approximately one half. This is also reflected in the dissipated power related to field emission, which dropped from 2.96 W at E_{peak} = 31.7 MV/m to 1.6 W at E_{peak} = 32.3 MV/m.

The scatter plots in Figure 4.2(c) are from the final low power test, with E_{peak} = 33.6, 34.3, and 36.4 MV/m. The associated simulation is shown in the line plots of Figure 4.2(c), with β = 300 and A = 1.0 x 10^{-13} cm^2. This CW power rise followed HPP processing with incident power P_{inc} = 3.5 kW, and $E_{peak} \leq$ 54 MV/m. The processing was much more successful than with 2 kW, as heating from this site is reduced by a factor of 10. This is clear in Figure 4.1(d). Note the reduction of scale as compared with Figures 4.1(a)-(c). However, heating from this site is still not totally eliminated.

SEM examination of this cavity following dissection produced a starburst/crater/debris site nearly exactly in the predicted spot. Figure 4.3 shows the SEM photographs of the site found in cavity 1-5.

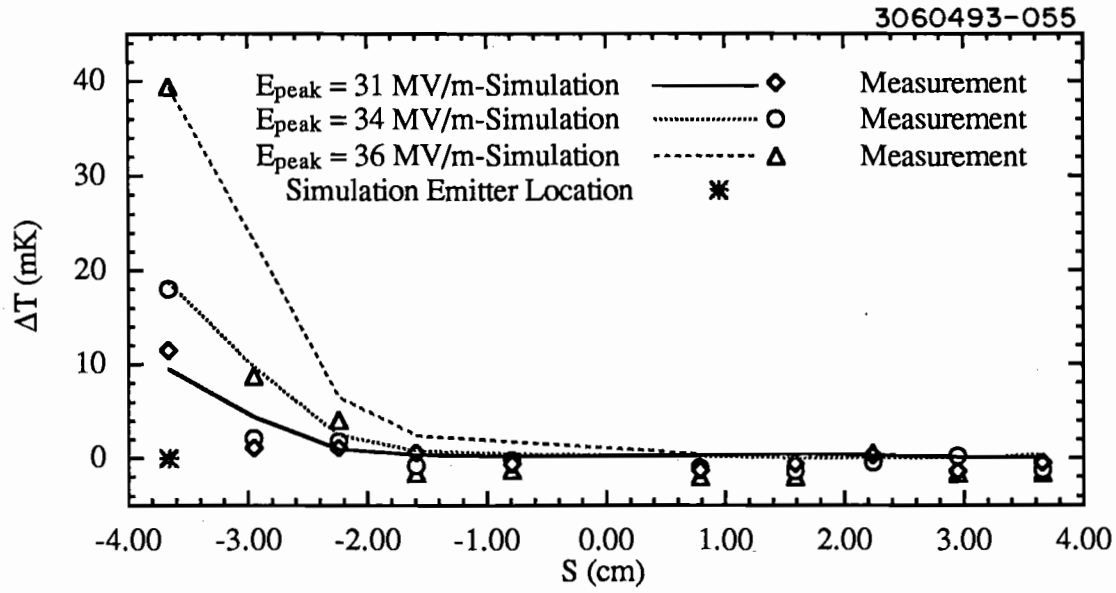

Figure 4..2(c) Comparison of simulated and measured ΔT vs. S plots for third low power CW rise of cavity 1-5, following HPP with P_{inc} = 3.5 kW, t_{RF} = 630 µsec, and $E_{peak} \leq$ 54 MV/m. Simulation assumes β = 300 and A = 1.0 x 10^{-13} cm^2.

No other significant phenomena were found within a several cm range radially, or several millimeter range azimuthally, strengthening the conclusion that the starburst and craters shown in Figure 4.3 are the direct result of the processing event. The crystalline-appearing sites which surround the starburst in all parts of Figure 4.3 are surface geometric features called "etch pits," found over the entire surface of the cavity. Etch pits appear frequently in cavities which are chemically etched following high temperature vacuum baking. As the pits appear throughout the cavity, they are judged to have no discernible effect on field emission behavior.

The nature of the starburst and crater regions (as shown in Figure 4.3) are discussed more fully in the section 4.6 and in Chapter 5, along with some interpretations. Briefly, when the field emission from a superficial contaminant site becomes sufficiently intense, a micro-discharge or RF spark is initiated. It is believed that the starburst is the residue of the discharge activity. At the core of the spark, the heating is sufficiently intense to initiate melting and cratering. Foreign elements from the original emission site are often left behind as debris. Our studies with parameters of HPP show that in order to process a field emission site it is necessary to raise the local field emission current high enough, by raising the electric field high enough, to initiate the discharge.

As noted above, the site of Figure 4.3 was not completely destroyed, as there is heating still (though greatly reduced) after the HPP processing. A possible explanation for this can be seen in the SEM photographs of Figure 4.3. Figure 4.3(d) is an higher magnification picture of the region to the immediate right of the starburst shown in full in Figure 4.3(c). The debris in this picture was analyzed via X-ray spectra to reveal titanium, calcium, carbon, and oxygen. This debris does not appear to have become

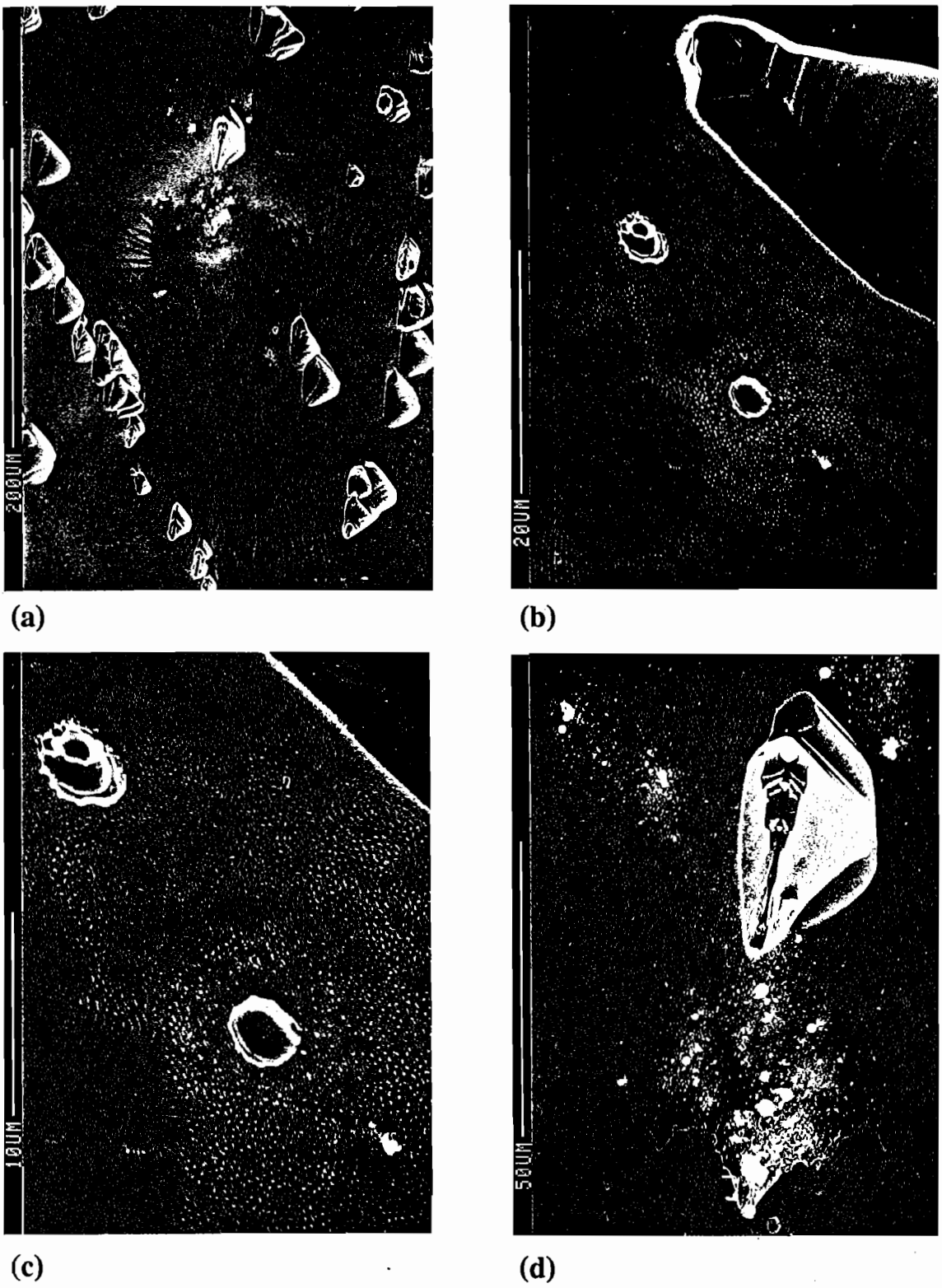

Figure 4.3. SEM photographs of starburst/crater region found in cavity 1-5.

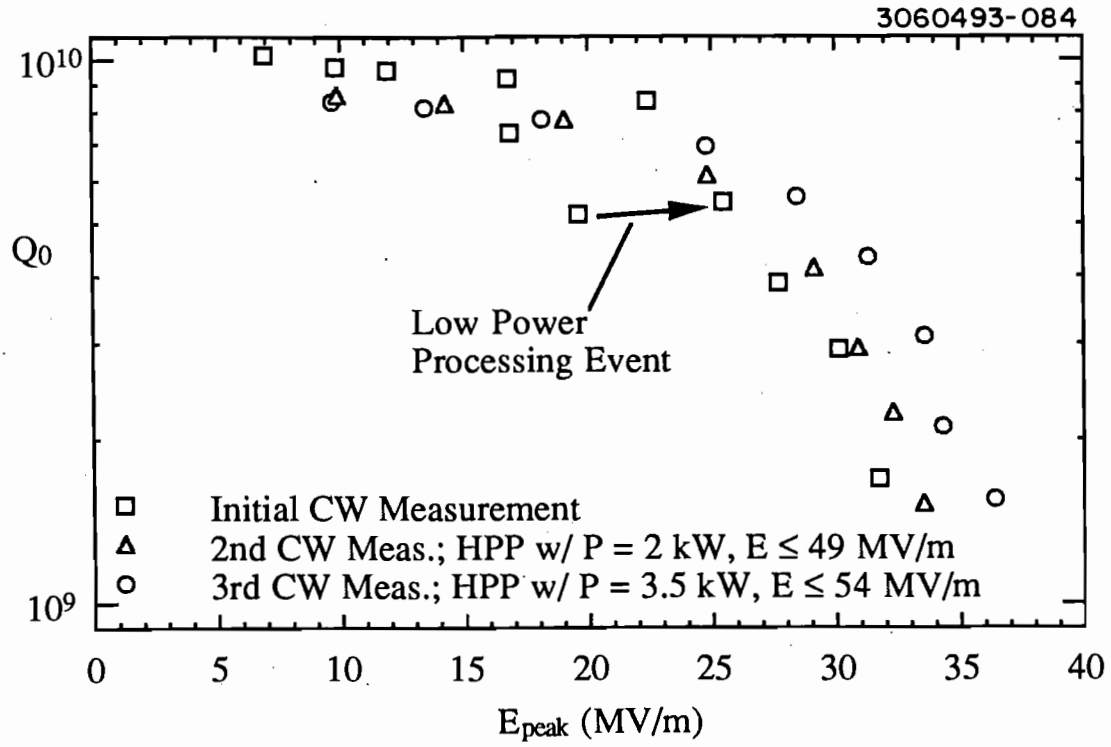

Figure 4.4. Low power, CW Q_0 vs. E_{peak} measurements for cavity 1-5, showing gains due to pulsed HPP RF processing.

molten, possibly indicating a contaminant based emission region which has not been processed.

Figure 4.4 shows the Q_0 vs. E_{peak} plots from the three CW power rises of this experiment. As can be seen, a processing event took place in the initial rise of the cavity, indicated by the arrow. The temperature maps shown in Figure 4.5 indicate that this event occurred at the same site as the HPP site. However there is not enough data at lower fields to allow a meaningful analysis for β and A.

The F-N plots for the emission related power derived from Figure 4.4 are shown in Figure 4.6. This procedure yields β values of 226 and 210, respectively for the first two power rises, essentially equal to the β values

of 200 and 210 from Figures 4.2(a) and 4.2(b) of from the temp map analysis. However, there is a clear trend towards a decreased intercept (proportional to ln[A]).

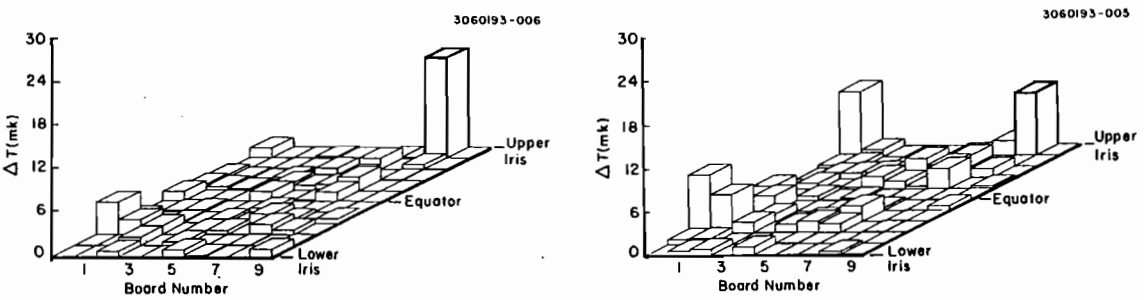

(a) Before low power event; E_{peak} = 20 MV/m.

(b) Following low power event; E_{peak} = 25 MV/m.

Figure 4.5. Temperature maps showing cavity 1-5 before and after the low power processing event which occurred in the initial cw measurements. Note that the location of the hot spot is at the top of Board 8, as it was at higher fields.

4.4.2. The Supporting Cast

Several more sites have been found with features similar to the site shown in Figures 4.1-4.6. These best examples of correlation between thermometry and microscopy are shown in Figures 4.7 through 4.9. All of the starbursts shown in Figures 4.7-4.9 are associated with cavity 1-7. The figures are each structured in the following manner: The scatter plots show the measured temperature signal for the board aligned with the starburst, with longitudinal plots shown before and after HPP processing. The line plots in each of Figures 4.7 through 4.9 are the simulated longitudinal plots

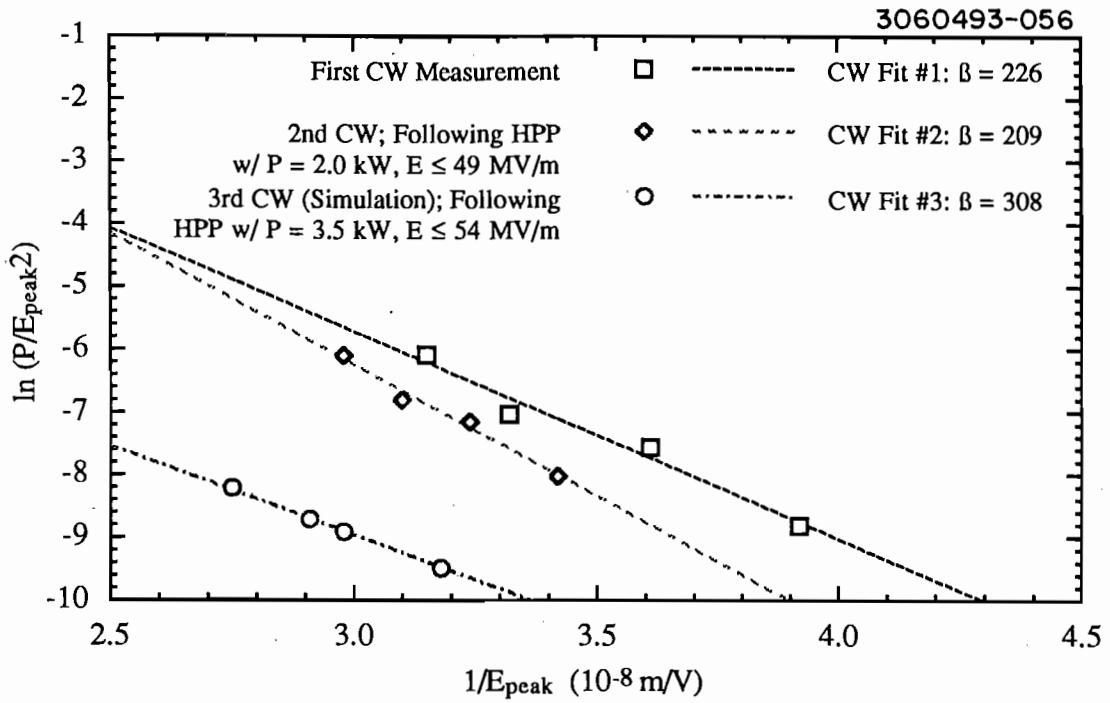

Figure 4.6. Fowler-Nordheim type power plots for the first two CW measurements of Cavity 1-5. The plot for the third CW measurement is a simulated plot based on the analyzed behavior of the processed emission site following the second HPP RF processing.

for before and after processing. Values of β and A for the simulated longitudinal plots were obtained by varying the parameters until the best agreement with the measured temperature plots was achieved. SEM photographs of the particular sites are included as part (b) of the Figures. In each case a starburst with a central molten crater was found. Unfortunately, no SEM photograph of the starburst for Figure 4.9 was taken, although it was recorded that there was a starburst present.

Special note should be made of the confidence we have that we have the correct site for the temperature change, primarily for cavity 1-7 which had 37 starbursts, some rather close together. In all cases where we claim a

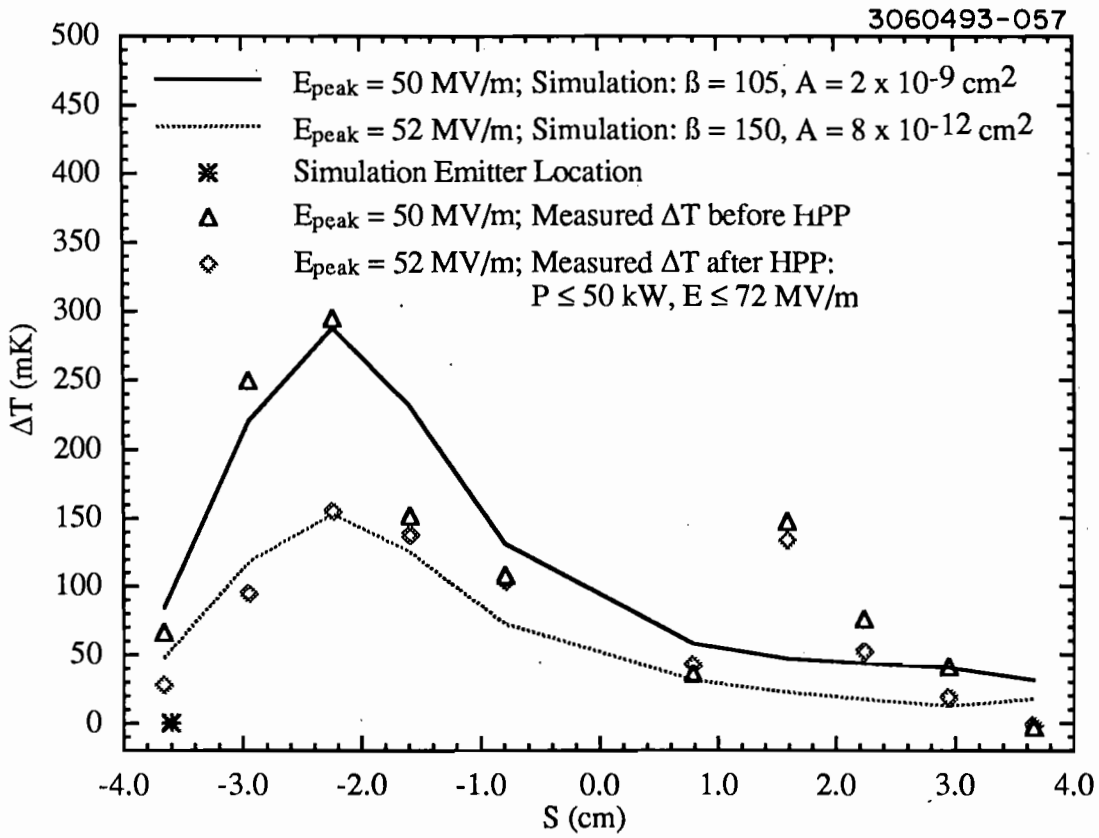

(a) Measured and simulated temperature rises before and after HPP.

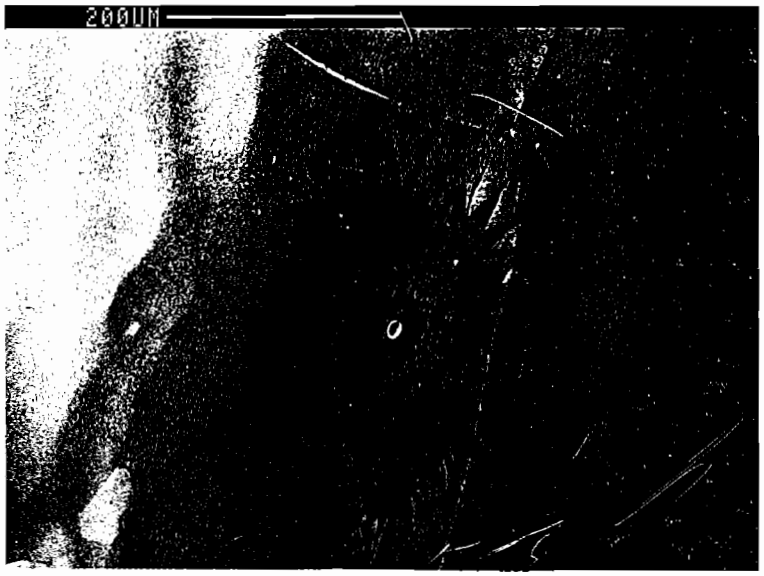

(b) SEM photograph of the site associated with the temperature signals shown in part (a).

Figure 4.7. An example of an SEM located surface site associated with HPP RF processing of field emission.

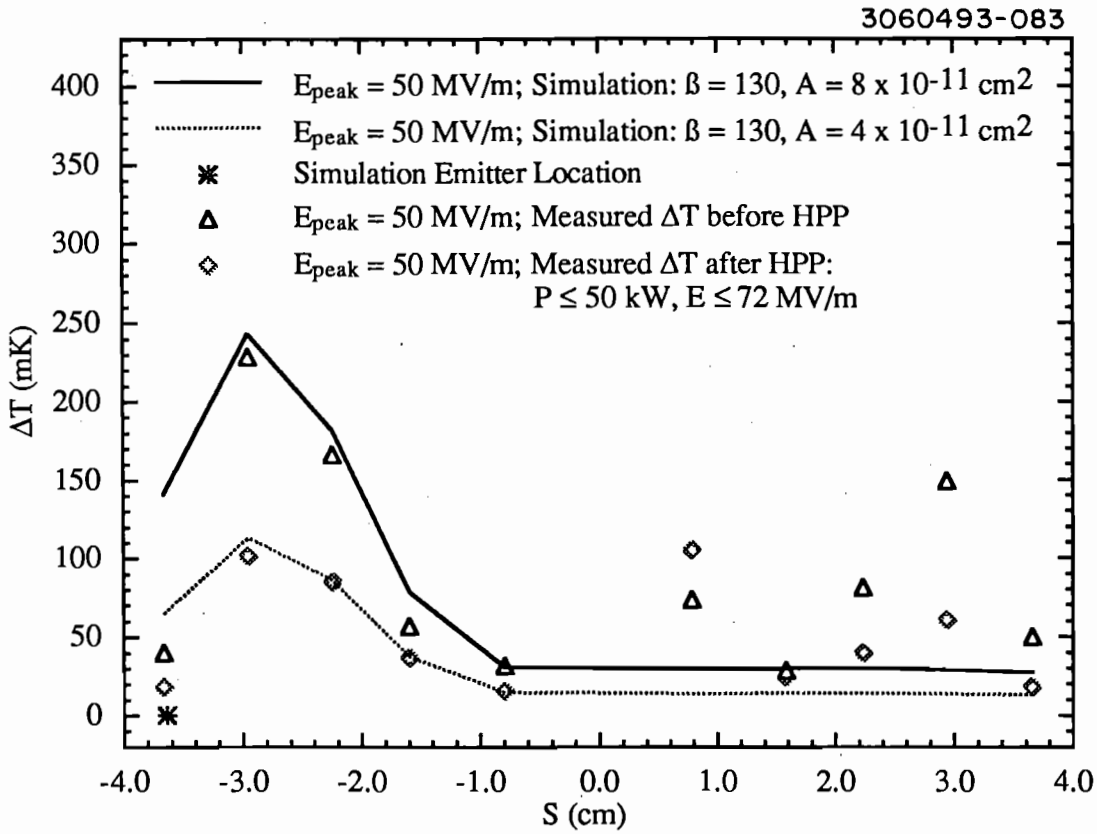

(a) Measured and simulated temperature rises before and after HPP.

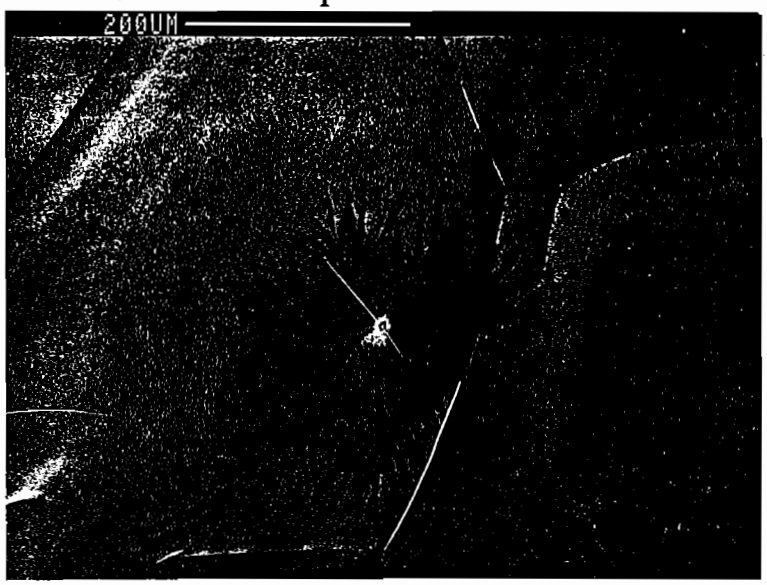

(b) SEM photograph of the site associated with the temperature signals shown in part (a).

Figure 4.8. An example of an SEM located surface site associated with HPP RF processing of field emission.

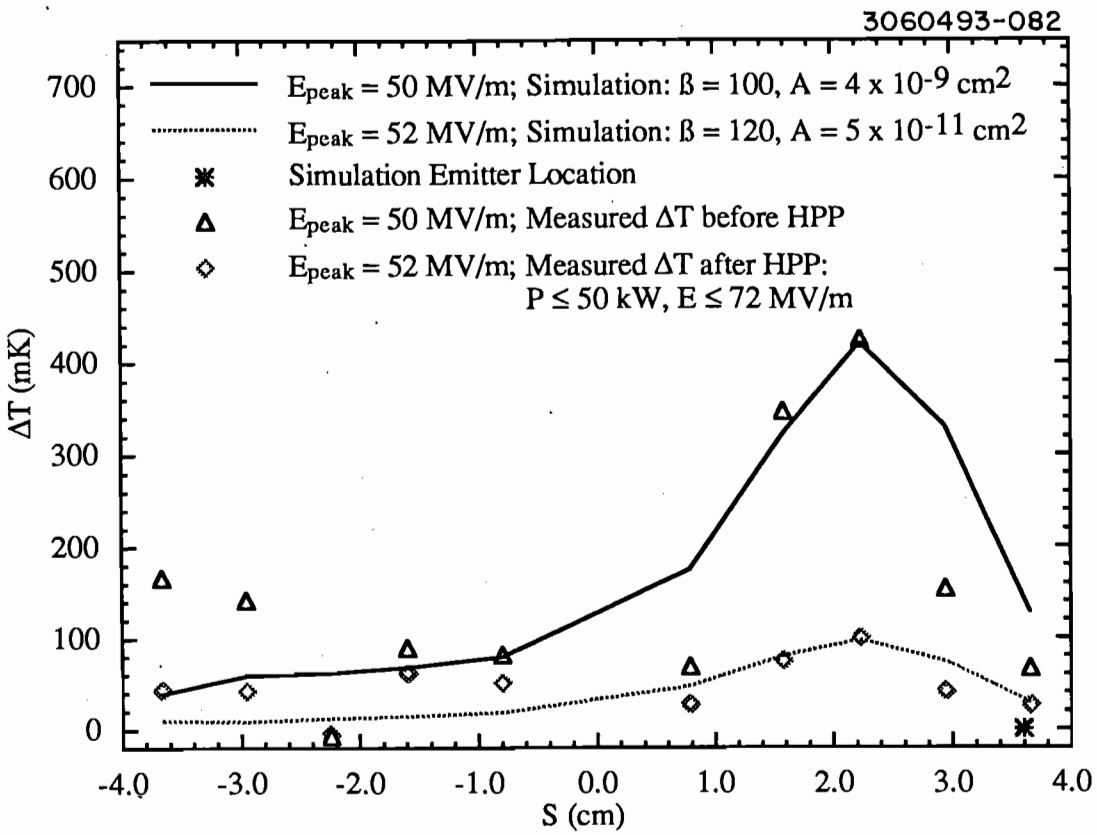

Figure 4.9. A final example of measured and simulated temperature rise before and after all HPP processing on an SEM located surface site. No SEM photograph was taken.

starburst is the result of an identifiable thermometry change, the nearest starburst is at least 1 mm away in the radial direction. This distance is far enough to significantly distinguish the thermometry signal along the thermometer board.

The next example comes from the attempt to study emission, processing and microscopic features from RF processing, but without HPP. Cavity 1-4 was tested with only low power, to try to determine if any difference could be found between RF processing with low power CW and pulsed HPP processing. The Q_0 vs. E_{peak} plot for the RF cold test of 1-4 is shown in Figure 4.10. As is shown in Figure 4.10, a significant processing event

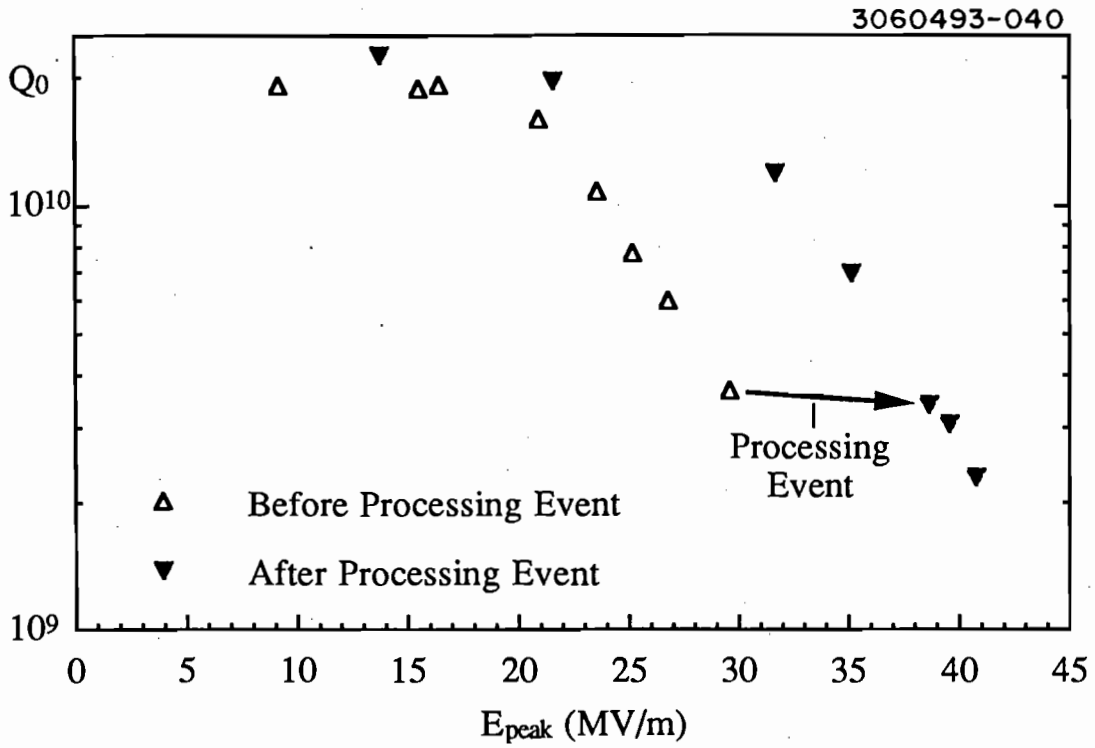

Figure 4.10. CW Q_0 vs. E_{peak} measurements for cavity 1-4, showing low power RF processing event. Also shown as Figure 3.15.

was encountered, where with an increase in incident power (from 1.8 W to 3.4 W) the peak field jumped from 29.6 MV/m to 38.7 MV/m. Clearly the field emission behavior is much improved as seen from Figure 4.10.

The temperature map just prior to the processing event is shown in Figure 4.11(a), with E_{peak} = 29.6 MV/m. One azimuth (Board 6) dominates the heating behavior. Following processing, the heating was greatly diminished, as can be seen in Figure 4.11(b), taken at E_{peak} = 31.7 MV/m.

Upon dissection and investigation in the SEM, two starburst/crater sites were located (both in the lower cup), one of which was in the vicinity of Board 6, the other near Board 2. Clearly the temperature maps captured the processed event near Board 6. Signals near Board 2 are too close to the noise level to say anything definitive. SEM photographs of the site of Board

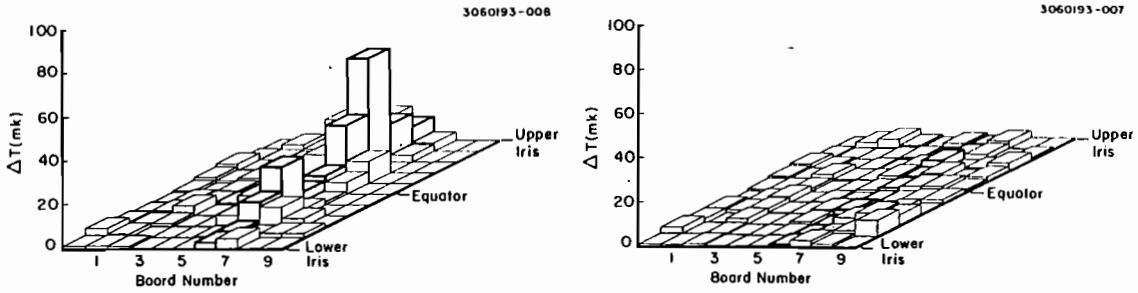

(a). Before low power event; E_{peak} = 29.6 MV/m.

(b). Following low power event; E_{peak} = 31.7 MV/m.

Figure 4.11. Temperature maps showing cavity 1-4 before and after the low power processing event which occurred in the initial cw measurements.

6 are shown in Figures 4.12(a) and 4.12(b). EDX analysis of particulate matter in the crater region revealed copper as the only contaminant element. SEM photographs of the site near Board 2 are shown in Figures 4.13(a) and 4.13(b). Again EDX analysis revealed particulate matter to be copper.

Unfortunately, for this event, efforts to reproduce the thermometer response with the simulation have been only partially successful. The difficulties can be attributed to the azimuthal misalignment of the thermometer board with the actual emission site, as mentioned previously. Comparison of measured power dissipation with simulated emitter dissipation indicates a predicted peak measured temperature of approximately 1 K, whereas the peak measured temperature rise was only 50 mK. The discrepancy in measured and simulated thermometer response indicates a very large misalignment between emission azimuth and the nearest thermometer

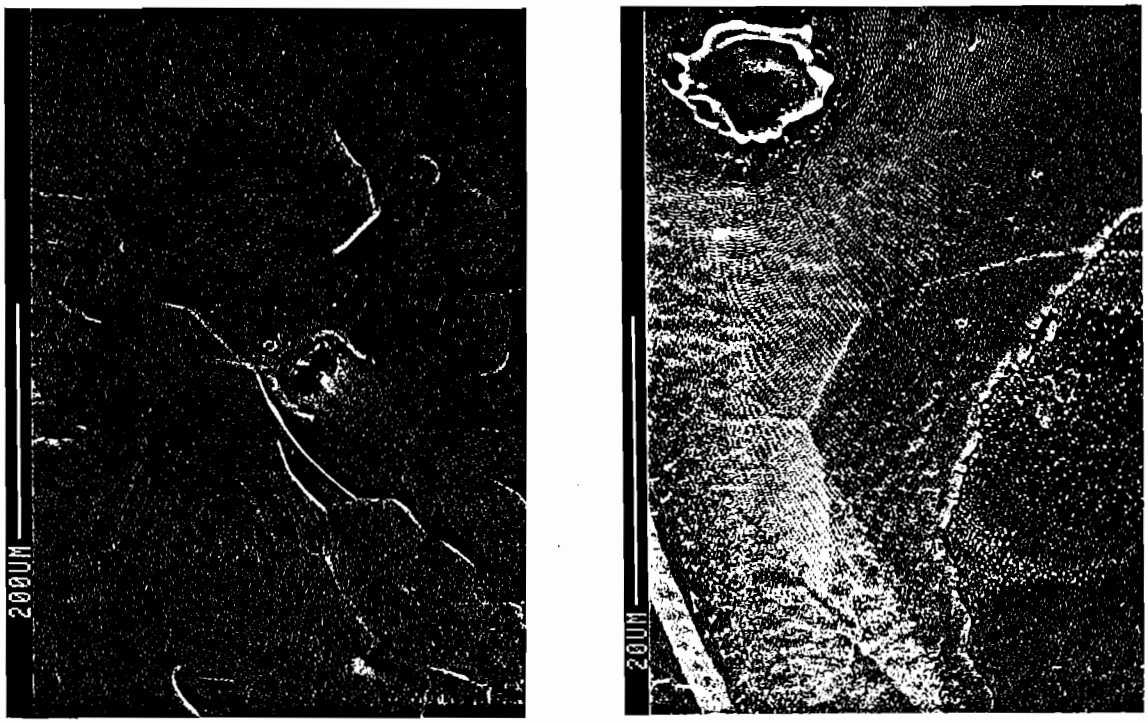

(a) (b)

Figure 4.12. SEM photographs of site found near Board 6 in Cavity 1-4.

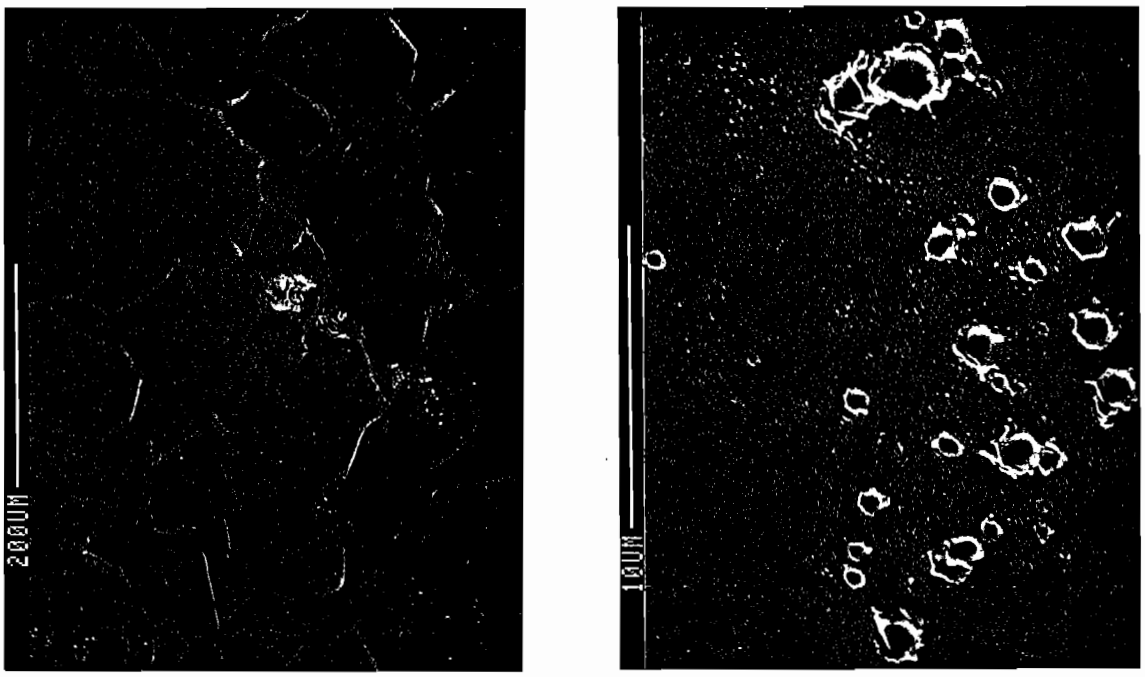

(a) (b)

Figure 4.13. SEM photographs of site found near Board 2 in Cavity 1-4.

board. Indeed, we find that the azimuthal coordinate of the SEM located site places it between thermometer Boards 6 and 5, approximately 12 degrees from Board 6 (24 degrees from Board 5). From the FWHM of thermometer response. it is reasonable to expect the signal to drop from 1 K to 50 mK in 0.6 cm. Lending further support to this argument, Board 5 does show some signs (tens of milliKelvins) of the heating before the processing event, as shown in Figure 4.11(a). Again, because of the variation in sensitivity of the individual thermometers, the detail shape of the heating profile is altered when the signal is attenuated by such a large factor from the distance to the heating source.

In this case, β can be estimated from the total cavity power dissipation, since this cavity was initially dominated by a single field emitter. Plotting $\ln(P_{diss}/E^2)$ vs. $1/E$ produces a nominal value of $\beta = 410$

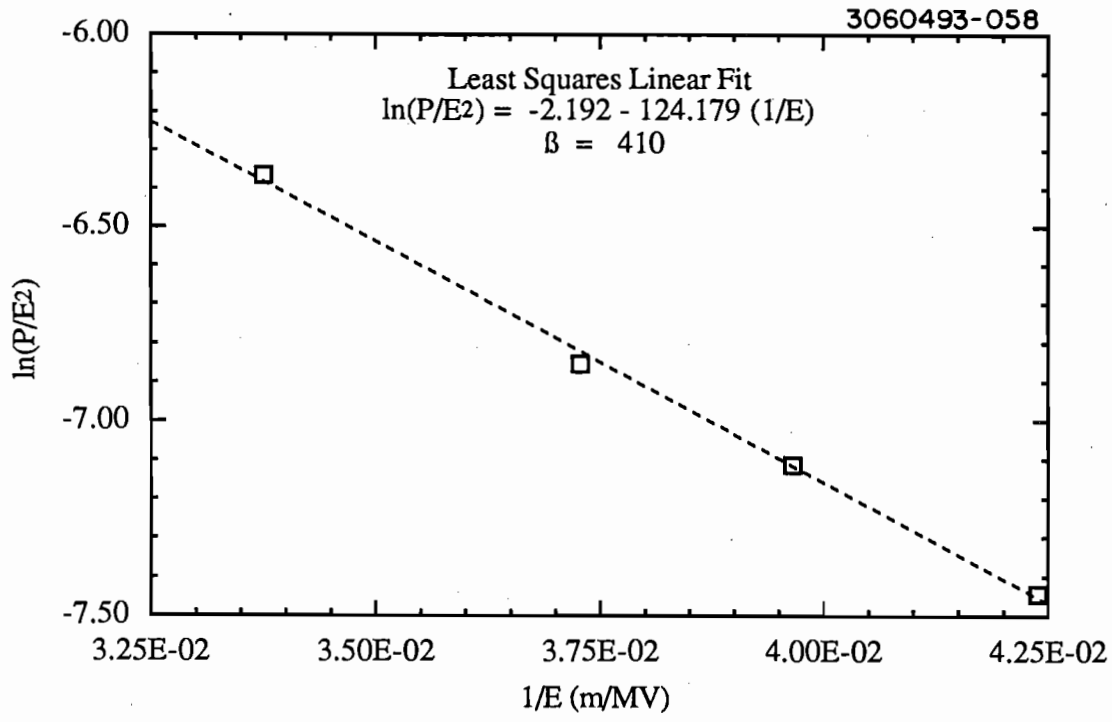

Figure 4.14. Fowler-Nordheim plot of dissipated power in cavity 1-4 before processing event.

for the data prior to the processing event. The indicated plot is shown in Figure 4.14. The small thermometry response makes extraction of a meaningful value of β from the thermometry data impossible.

It must be noted that despite the misalignment difficulty, we remain confident that the SEM site is associated with the processing event, since the signal on Boards 6 and 5 were so drastically altered following the event, and since this feature was the only significant feature located in the vicinity of Board 6 in the cavity.

Table 4-1 presents a summary of the features of sites described in this section.

TABLE 4-1: SUMMARY OF SEM SITES DISCUSSED IN SECTION 4.4.2.

Figure	Cavity	Maximum E_{peak}	Contaminants	Comments
4.1-4.6	1-5	54 MV/m - pulsed	C,O,Ti,Ca	Best HPP site
4.7	1-7	72 MV/m - pulsed	In	
4.8	1-7	72 MV/m - pulsed	In	
4.9	1-7	72 MV/m - pulsed	In	No photograph
4.12	1-4	18 MV/m - CW	Cu	Low Power Only - local E ≈ 12 MV/m at site
4.13	1-4	18 MV/m - CW	Cu	Low Power Processing no good thermometry

4.5. General Results of SEM Investigations

As already shown in Section 4.4, the most common manifestation of RF processing is the feature we have named a *starburst*. Several examples of starbursts were shown in section 4.4. Another strong example of a starburst is shown in Figure 4.15. Generally a starburst consists of a darkened (in terms of its appearance in the SEM) burst-like region of approximately 200 micron diameter. At the center of the darkened region we usually find a crater or formerly molten region of a few microns in size.

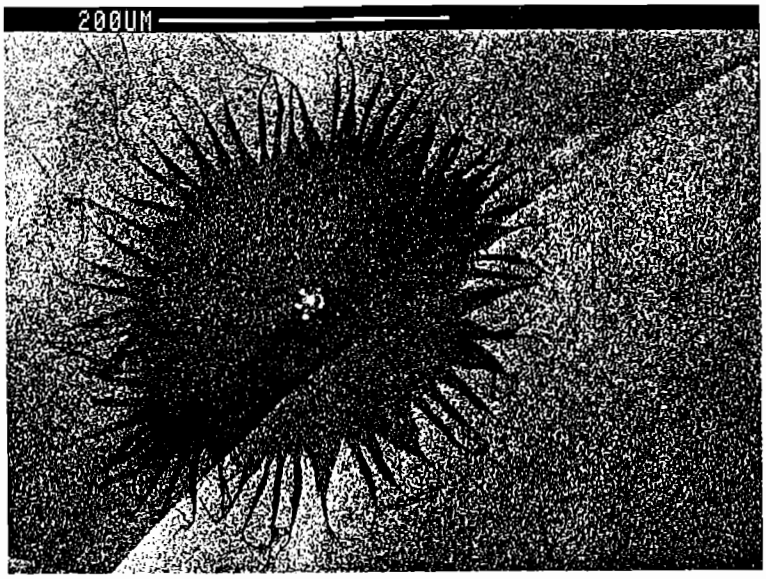

(a) Overall view of a typical starburst.

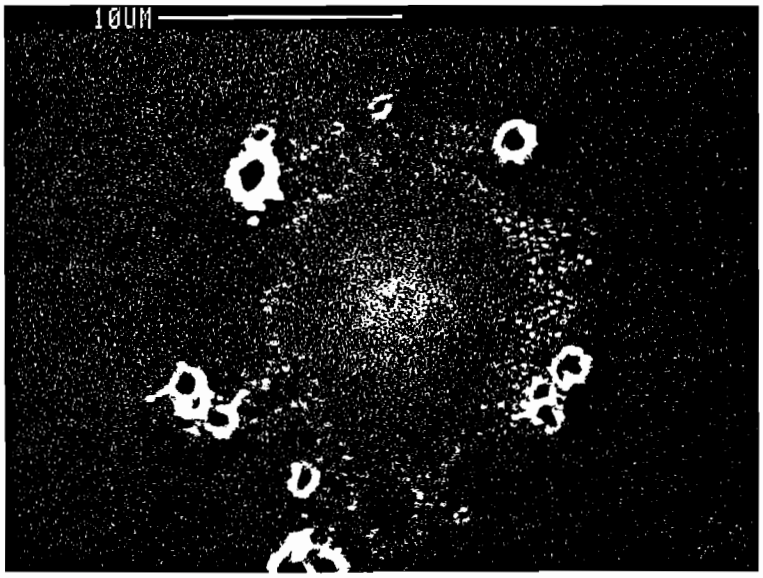

(b) Expanded view of the starburst center.

Figure 4.15. SEM photographs of a starburst in an S3C cavity following HPP Processing.

An example of a central area is shown in Figure 4.15(b). In many starburst examples we find micron size contaminant particles. Often the molten crater region also shows traces of foreign elements.

TABLE 4-2: EXPERIMENTAL HISTORY OF S3C CAVITIES EXAMINED IN SEM

Cavity	Maximum E_{peak}	Top Starbursts	Bottom Starbursts	Top Other	Bottom Other
1-1	49 MV/m	0	1	0	1
1-7	72	14	23	2	10
1-4	41	0	2	0	0
1-2	68	1	14	0	0
1-8	65	1	0	12	2
1-5	54	1	0	9	0
Totals	---	17	40	23	13

In all we have found 57 starburst/crater sites after dissecting 6 S3C-1 cell cavities. Table 4-2 gives the maximum surface electric field applied in each cavity test before dissection, and the distribution of starburst/crater sites for the cavities. The number of starburst/crater sites is plotted against maximum peak electric field in the cavity in Figure 4.16. Clearly the number of sites increases with increasing electric field, although the highest

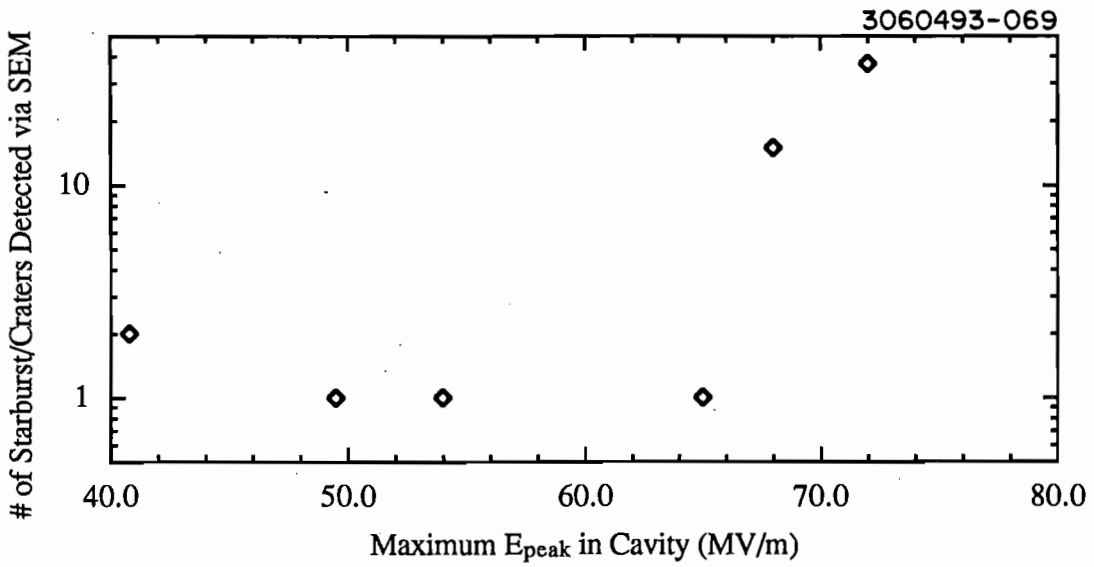

Figure 4.16. Number of starbursts found in S3C cavities plotted against peak electric field reached in the cavity.

number (37 sites in cavity 1-7) is most likely artificially high, as will be discussed below.

The starbursts are usually located in towards the iris of the cavity. This is consistent with the findings of number of starbursts a function of peak electric field, since the surface electric fields are highest in the iris region. Figure 4.17 shows a histogram of the locations of all starbursts found

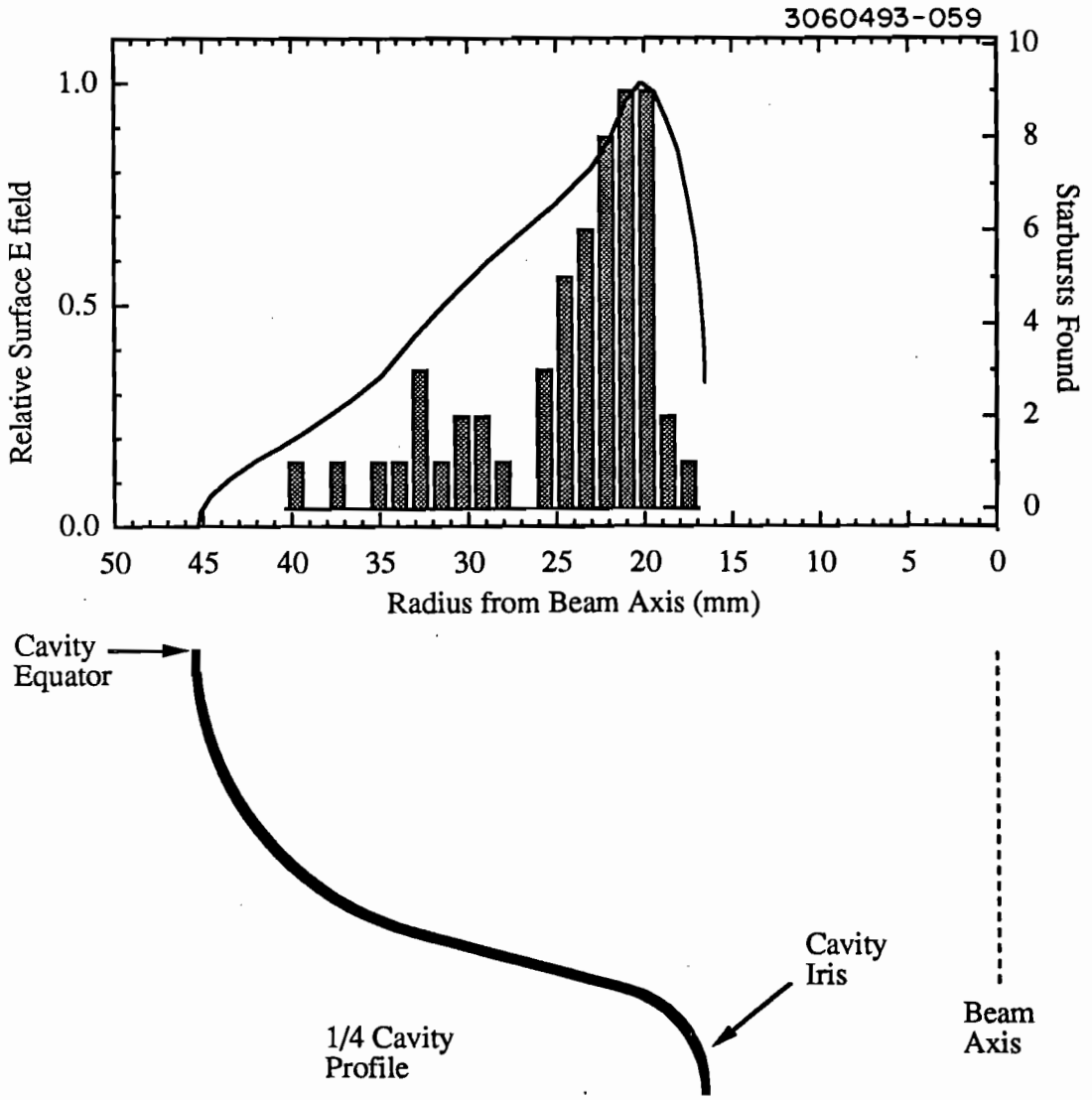

Figure 4.17. Correlation of starburst location in cavity with local electric field. The 1/4 cavity profile is aligned properly with the plots shown above it.

in all S3C cavities which have been examined. Also plotted on this graph is the relative strength of electric field along the surface of the cavity. Below these graphs is a diagram of an S3C cavity, aligned in the proper position. This clearly shows the higher density of sites in the iris area.

Table 4-2 is a tabulation of all types of sites found in all cavities dissected to date, with differentiation made for top and bottom half cell. Top and bottom refer to the orientation of the cavity on the test stand during RF cold tests. As can be seen, the first four cavities examined showed a markedly higher number of sites on the bottom half cells. This could support a model where the contaminants which cause emission are more likely to adsorb or settle on the lower surface than on the upper surface. The last two cavities have not continued the dominance of lower half cell sites, however, each of these cavities had only one starburst/crater site.

The EDX system associated with the SEM allows for x-ray analysis to determine elemental composition of phenomena located with the SEM. Many of the starburst/crater regions contained foreign elements. Table 4-3 lists foreign elements, and their frequency of appearance, which have been found in starburst/crater regions in all S3C cavities examined to date. Obviously, the high frequency of starburst/crater contamination supports the contaminant based models of emission.

In the second cavity (1-7, maximum E_{peak} = 72 MV/m), which had thirty seven total starburst sites, more than half contained indium. This was a surprise since each RF cold test is preceded by chemical etching of the cavity. We found that the BCP (Buffered Chemical Polish: comprised of HF, HNO_3, H_3PO_4) used in the chemical etch of the cavity was ineffective in removing indium in time scales used in cavity etching. Subsequently a thirty minute soak in nitric acid was added to the

TABLE 4-3: CONTAMINANT ELEMENTS FOUND IN SEM CAVITIES; EITHER STARBURST OR OTHER PHENOMENA

Element	Starbursts	Other Phenomena
Indium	19	8
Copper	4	16
Iron	11	2
Chromium	2	0
Titanium	2	4
Silver	0	5
Rubidium	0	5
Aluminum	0	4
Calcium	1	1
Zinc	0	2
Silicon	1	1
Tin	0	2
Oxygen	1	12
Carbon	1	12
No Foreign Elements	21	--
Totals	63	74

preparation procedure when a cavity was used multiple times. The resulting reduction in starbursts containing indium led us to the conclusion that the indium contamination was nearly exclusively a result of the process of removing indium from the flanges of the cavity, prior to preparation for reuse. As a result of routinely following the nitric acid soak practice, no further indium contamination has been encountered.

Because of this indium contamination, we believe that the large number of sites in cavity 1-7 is higher than one would normally expect at 72 MV/m. Similarly, the two copper sites found in cavity 1-4 likely would not have been encountered had that test included a nitric acid soak.

Since the elimination of the indium contamination source, the total number of starburst sites has significantly dropped as well. This is clearly seen in Table 2, where cavities 1-2, 1-8, and 1-5 were tested after inclusion of the Nitric Acid soak in the cavity preparation sequence. Figure 4.18 shows the same starburst frequency distribution as shown in Figure 4.17, but with some element composition included. The data also show no correlation between axial location of starburst and the type of contaminants found in the starburst.

Cavity 1-2, the other cavity with a large number (15) of starburst/crater phenomena was tested without thermometry, as the thermometry apparatus did not fit this cavity due to a difference in beam tube geometry. This cavity did not show any indium contaminated sites.

With the exception of the indium contamination discussed above, the sources of the contamination have not been conclusively determined.

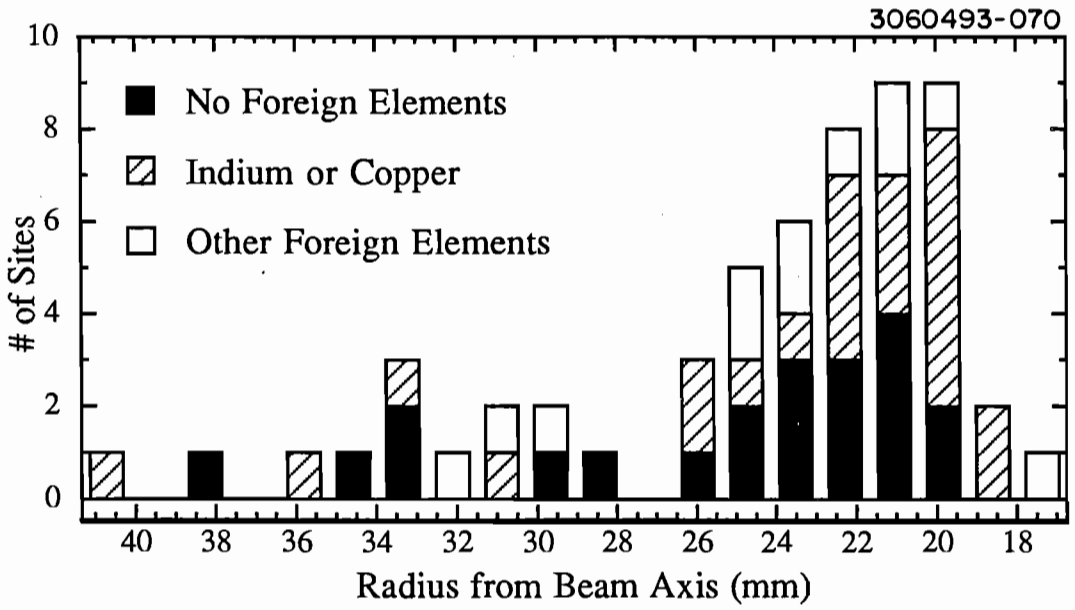

Figure 4.18. Histogram plot of location of starbursts found in all S3C cavities, with differentiation made for elemental contaminants.

Several possible sources are immediately apparent, however. Carbon and oxygen containing contaminations are likely due to airborne dust particles, in spite of assembly in a class 100 clean room environment. RF probes, both input and monitoring, are made of copper. Titanium is used in the ion sputtering vacuum pumps which maintain the UHV in the cavity test apparatus, making the pump system a possible source of the titanium contaminants. Iron and aluminum could come from the fabrication processes. Stainless steel tools are used in many of the assembly and disassembly procedures. These tools are possible sources of such elements as iron, chromium, and nickel. In addition, there exists the possibility that contaminants are intrinsically a part of the bulk niobium used to fabricate the cavity. These contaminants would then be exposed as the surface was removed through etching.

4.6. Discussion of Starburst Features and Processing

There is plenty of evidence in the literature[24],[37]-[41],[67] to show that superficial micron size contaminant particles can give rise to enhanced field emission, often referred to as pre-breakdown field emission. Studies of arcing and breakdown induced by a high DC voltage applied across a narrow vacuum gap show many of the molten craters and crater features that we have found[34],[35],[44],[47]. It is particularly interesting to note the similarity in the features of the individual craters and the phenomenon of multiple craters. A DC high voltage arc in a Nb vacuum gap recently also showed[67] an 80 micron diameter starburst with familiar central craters of molten Nb. After the arc, a substantial decrease in the field emission current was also observed.

The first evidence of starbursts/molten craters in a SC Nb RF cavity was found in the high electric field region of the Mushroom cavity, as mentioned above. Our studies reported here have, for the first time, correlated the pre-breakdown field emission current site, the processing at the emission site, and the identification of a starburst/crater/debris item at the same location. This evidence will be further examined in the next chapter, when we develop a working model for RF processing.

4.7. Correlation of SEM, Thermometry and Simulations for Features Other than Processed Emission Sites

4.7.1. Thermal Breakdown Sites

SEM investigation of S3C cavities produced several microscopic features, which were not of the starburst/crater type, and which could be linked with heating in the cavity from measured temperature signals. A striking case of this was found in cavity 1-8. The test of this cavity was dominated by a thermal breakdown, which was well located by the thermometry apparatus. The Q_0 vs. E_{peak} plots for the low power cw RF tests are shown in Figure 4.19. Figures 4.20(a)-(e) show the thermometry maps of the cavity at the highest field reached in each of the low power rises, E_{peak} = 43.0, 43.2, 43.2, 43.2, and 44.2 MV/m, respectively. As can be seen, in all cases the cavity was dominated by heating in the upper regions of board number eight. X-ray production was present in each of these tests, indicating field emission, however the emission loading was not severe, indicated by the relatively flat Q_0 vs. E_{peak} curves shown in Figure 4.19.

HPP processing was partially successful in reducing the emission loading in this cavity. The change in field emission behavior can be seen in the change in the relative response of the thermometers along board eight

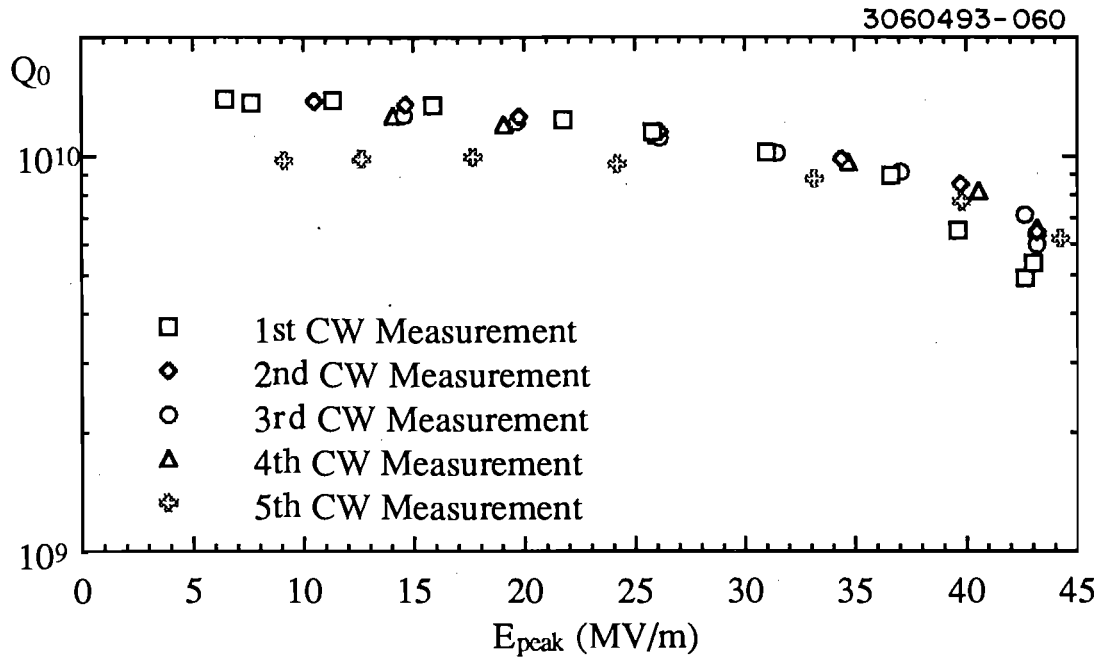

Figure 4.19. CW Q_0 vs. E_{peak} measurements for cavity 1-8.

(see Figure 4.20) changed as HPP processing was attempted on the cavity. The characteristics of the HPP sessions are shown in Table 4-4.

Despite the reduction in FE loading, HPP did not significantly affect the dominant heating site (resistor number 2). The heating observed in this region appears to consist both of purely resistive (ΔT proportional to E_{peak}^2), and exponential components. Figures 4.21(a) and 4.21(b) show the

TABLE 4-4: PARAMETERS OF ALL HPP SESSIONS OF CAVITY 1-8

HPP	Incident Power	Pulse length	Maximum E_{peak}
1	1, 2 kW	975 µsec	56.2 MV/m
2	5	945	58.2
3	10	700	60.6
4	40	500	65.5

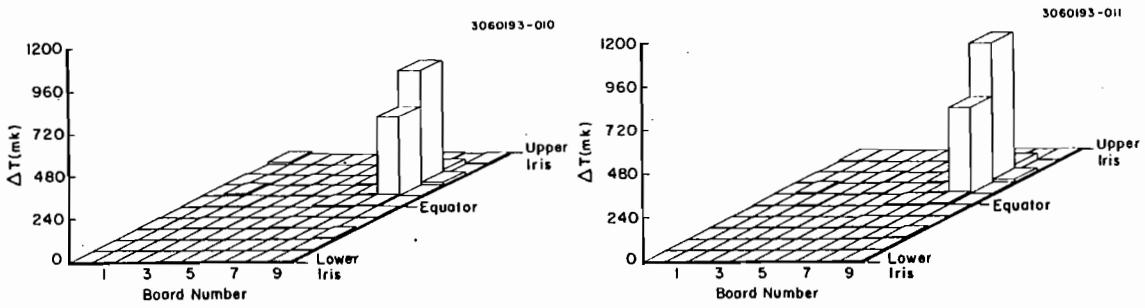

(a) Initial Rise; E_{peak} = 43.0 MV/m. **(b)** After 1 HPP; E_{peak} = 43.2 MV/m.

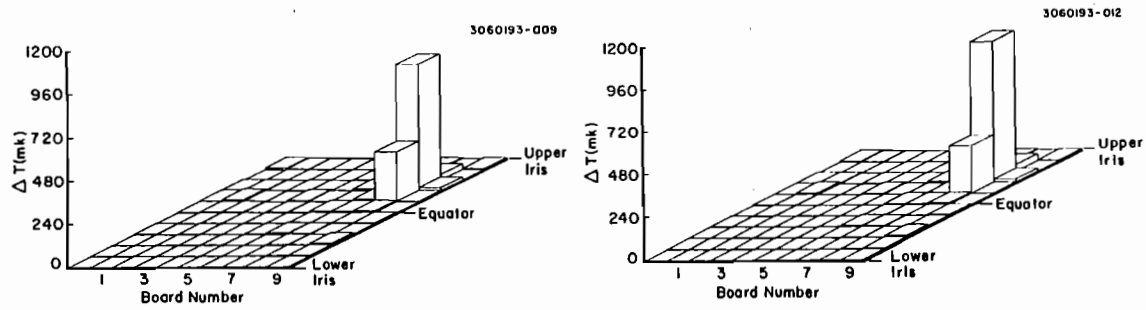

(c) After 2 HPP; E_{peak} = 43.2 MV/m. **(d)** After 3 HPP; E_{peak} = 43.2 MV/m.

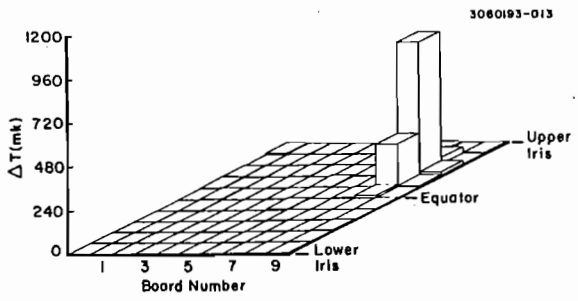

(e) Following 4th HPP; E_{peak} = 44.2 MV/m.

Figure 4.20. Temperature maps at the highest field reached for each of the low power CW measurements of cavity 1-8. HPP parameters are shown in Table 4.

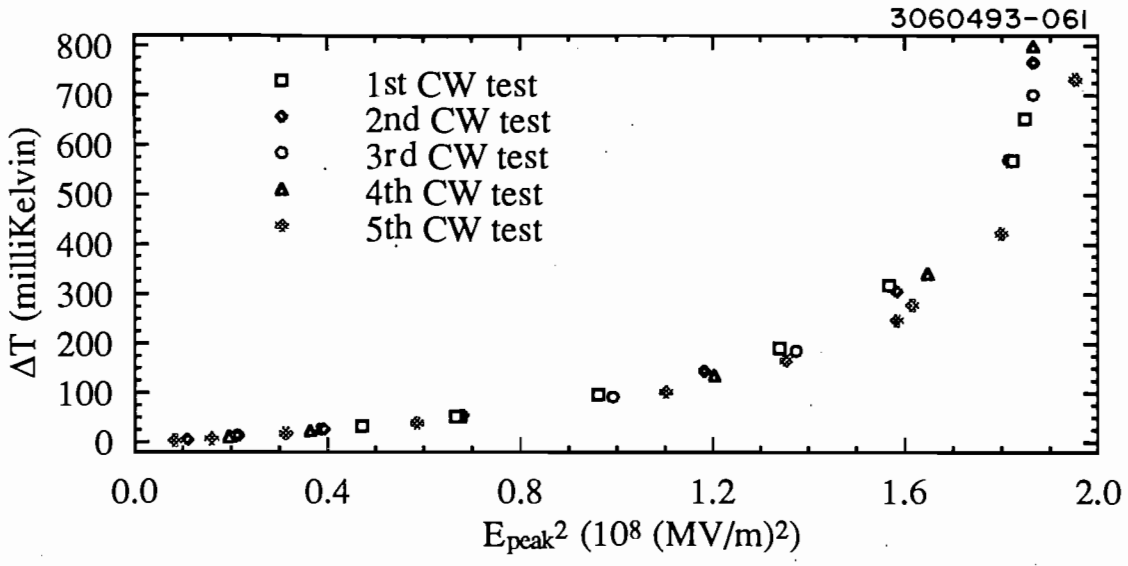

(a) Board 8, Resistor 2.

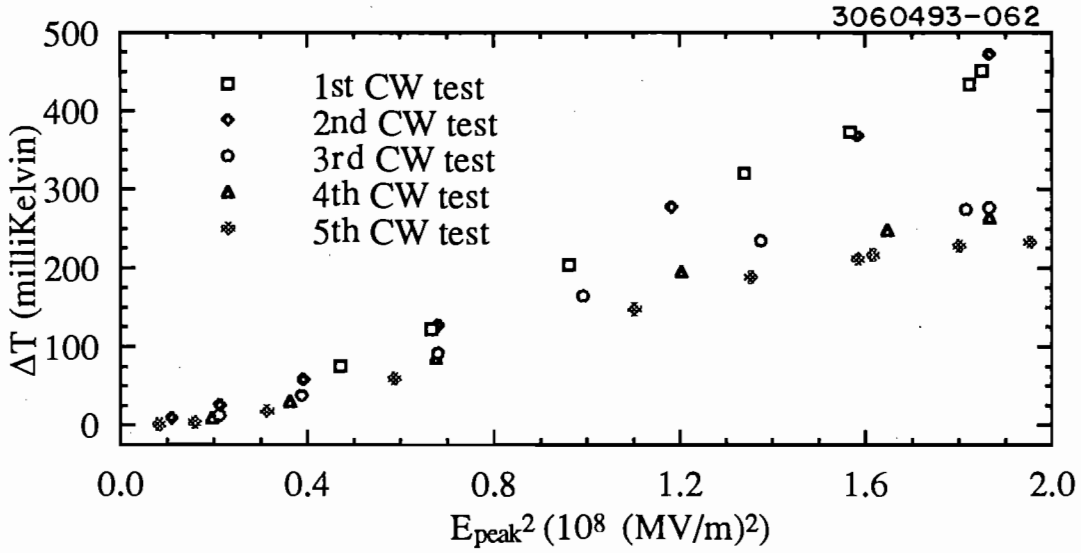

(b) Board 8, Resistor 3.

Figure 4.21. Evolution in ΔT vs. E_{peak}^2 behavior of the two "hot spot" resistors on Board 8 in cavity 1-8. HPP parameters for this experiment are listed in Table 4.

evolution in ΔT vs. E_{peak}^2 behavior for thermometers 2 and 3 respectively. It was not possible to model the temperature behavior via a simple emission or defect model.

Dissection and SEM investigation of this cavity revealed a cluster of sites. Figure 4.22 shows a map of the region spanned by thermometer boards 7-9, with the pertinent sites marked at their proper locations, and differentiation in plot symbol based on the general nature of the SEM site. The most striking of these sites are those we have termed "cheerios", shown in Figures 4.23(a)-(f). In all the cheerios, EDX analysis revealed the particles to be copper. The largest grouping of the cheerios is near the two resistors which showed the greatest temperature signals, indicating that they were responsible for at least part of the heating in this region. As can be seen in the lower magnification pictures of Figure 4.23 (parts (b) and (e)), the entire region around the cheerios was covered with small particles. EDX analysis of the spread out regions again revealed a large copper signal.

The remainder of the SEM sites in the map of Figure 24 are shown in Figures 26(a)-26(m). Of particular note are Figures 26(a)-26(e). Based on trajectory calculations, a field emitter at any of these sites could be responsible for heating at thermometers 3 and 4 on Board 8.

4.7.2. Candidates for Non-Processed Emission Sites

Several sites have been located among the dissected cavities which can be plausibly associated with field emission heating which was *not* processed. In most cases, however, no other site was detected nearby to explain the measured temperature signal. As with the starburst sites, multiple heating sources had to be dealt with on several of the boards investigated here. They were treated via a superposition principle described in Appendix E.

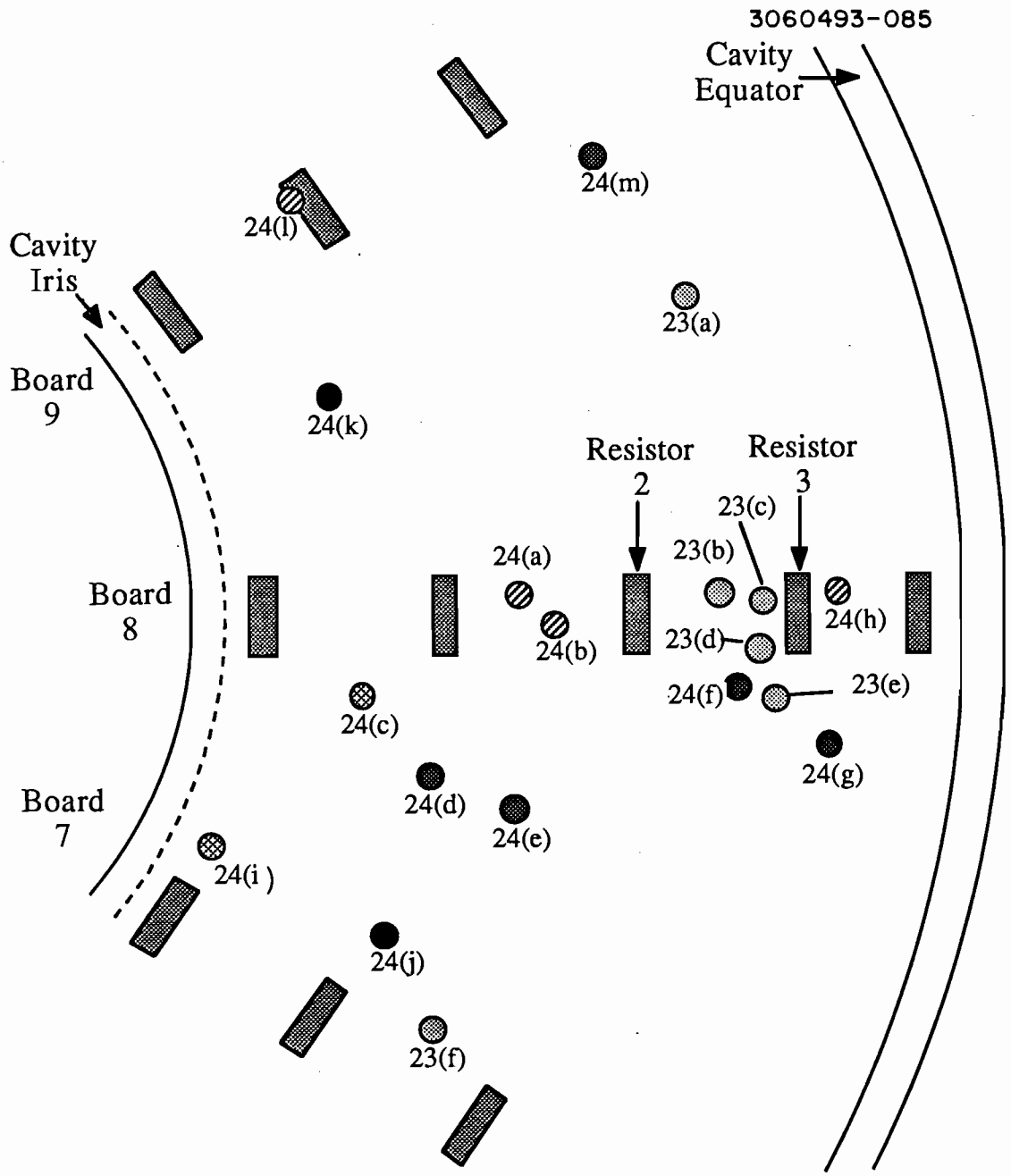

Figure 4.22. Map of SEM located phenomena in cavity 1-8. Similar plot symbols refer to similar phenomena. For photos, see the indicated portions of Figures 4.23 and 4.24. The thermal breakdown in this cavity was initiated in the region of Board 8, Resistors 2 and 3 (indicated above).

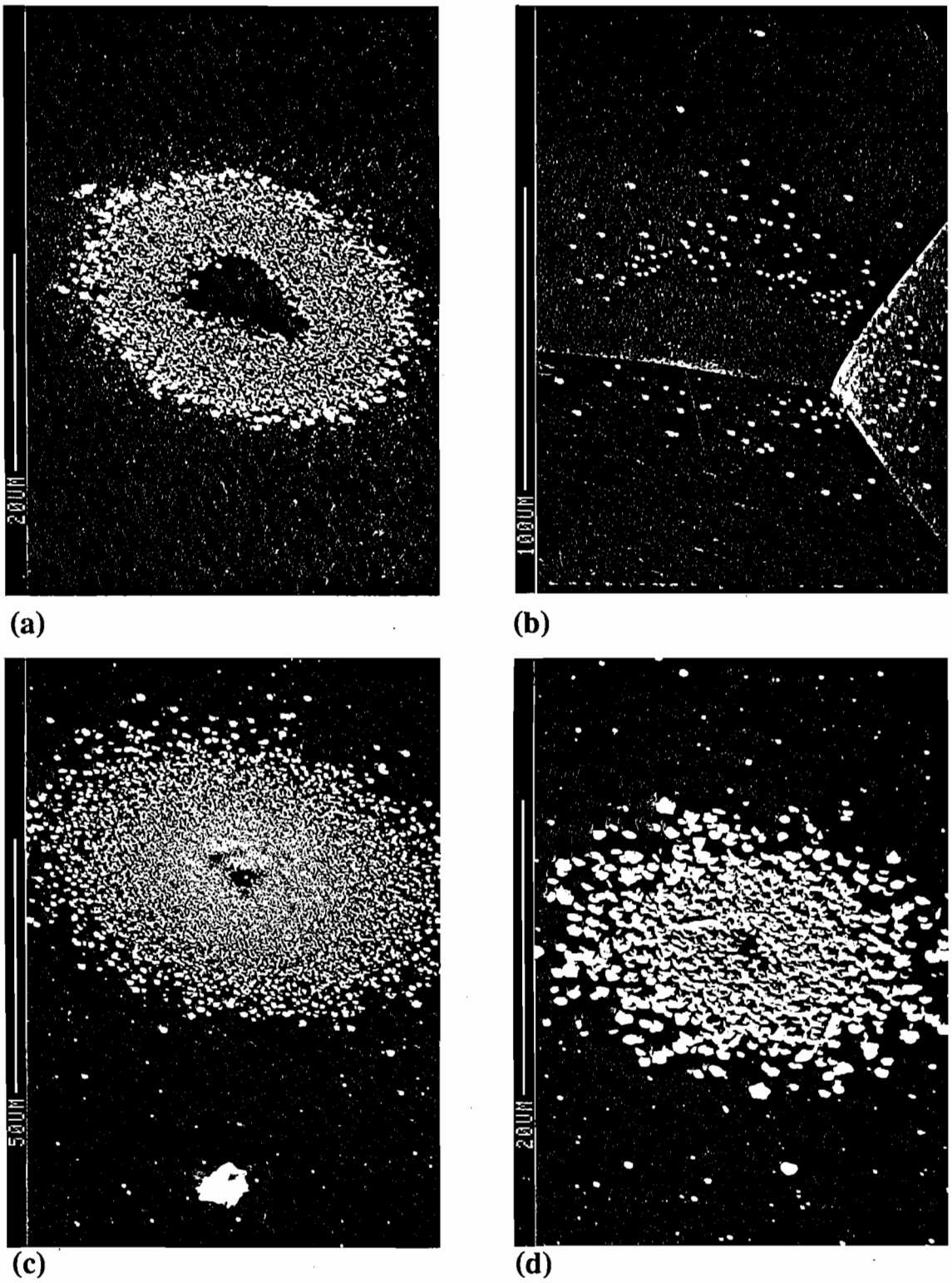

Figure 4.23. SEM photographs of the "cheerio" sites found near Board 7-9 in Cavity 1-8.

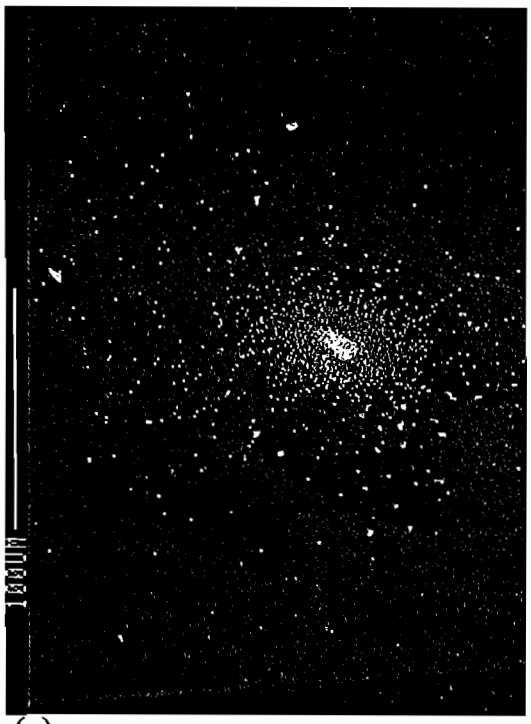

(e)

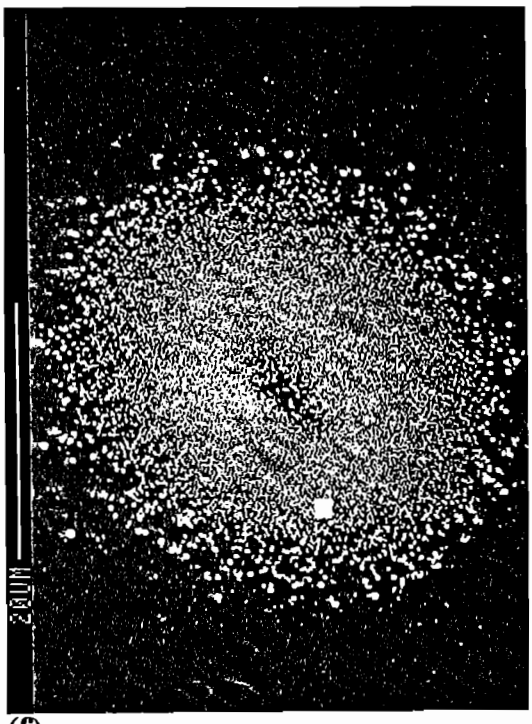

(f)

Figure 4.23 (continued).

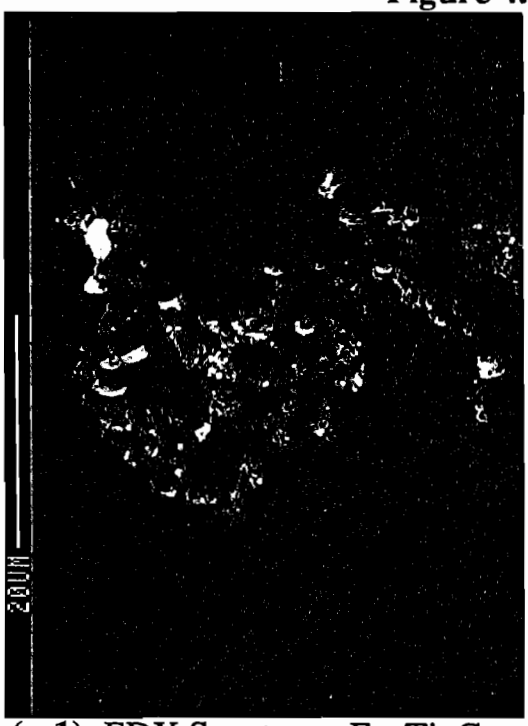

(a-1) EDX Spectrum: Fe, Ti, C.

(a-2) Higher mag. of (a-1).

Figure 4.24. SEM photographs of other sites found near Board 7-9 in Cavity 1-8.

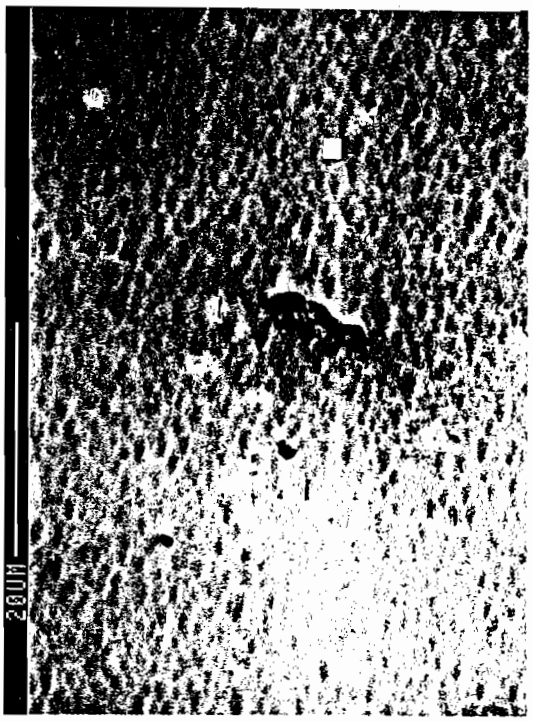

(b) EDX Spectrum: Ti, C.

(c) EDX Spectrum: Indeterminate.

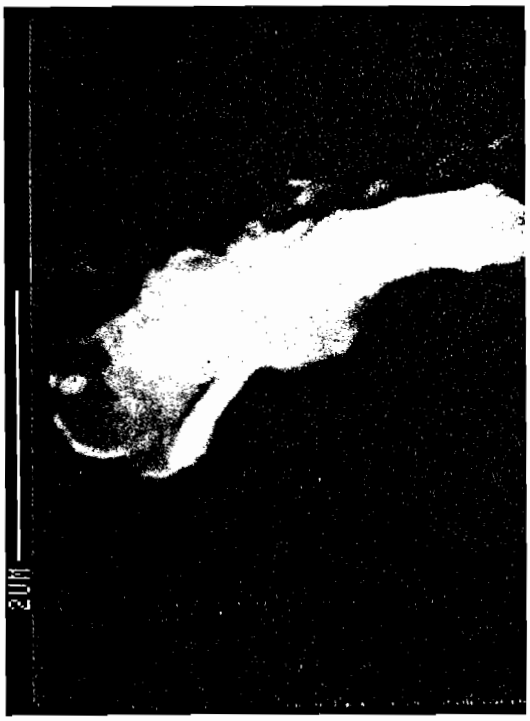

(d) EDX Spectrum: C, O, Al.

(e) EDX Spectrum: C.

Figure 4.24 (continued).

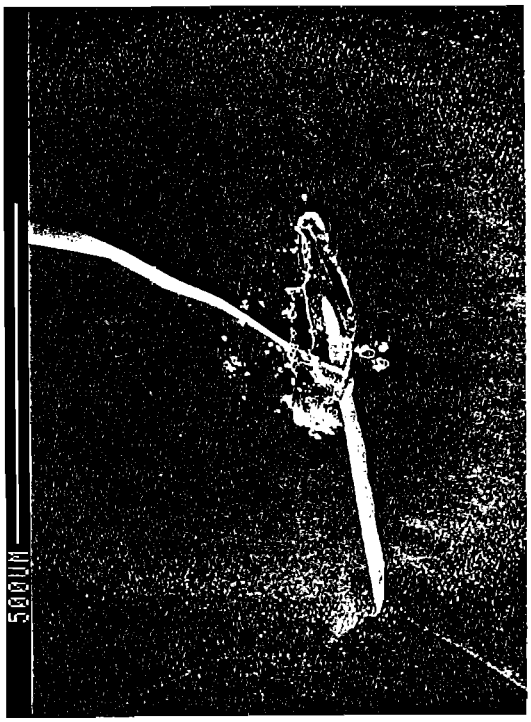

(f) EDX Spectrum: Cu.

(g) EDX Spectrum: Indeterminate.

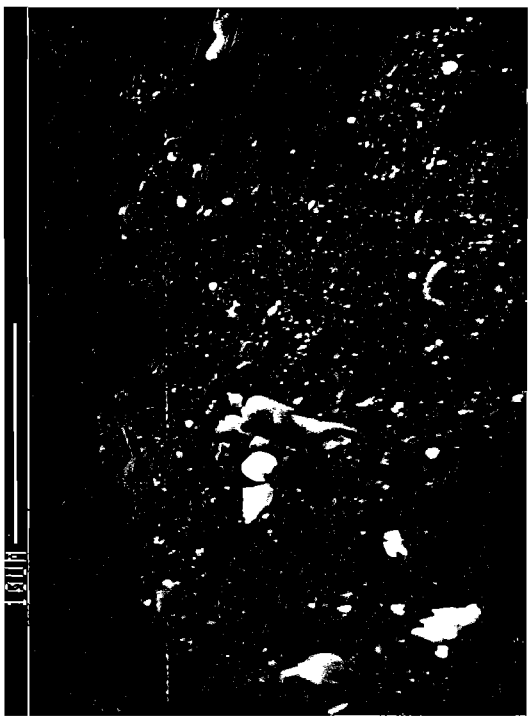

(h) EDX Spectrum: Fe, O, C, Cr, Ni.

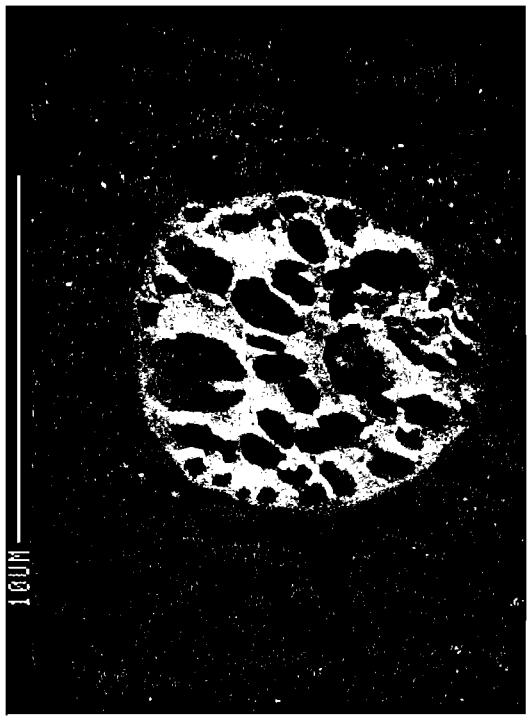

(i) EDX Spectrum: O.

Figure 4.24 (continued).

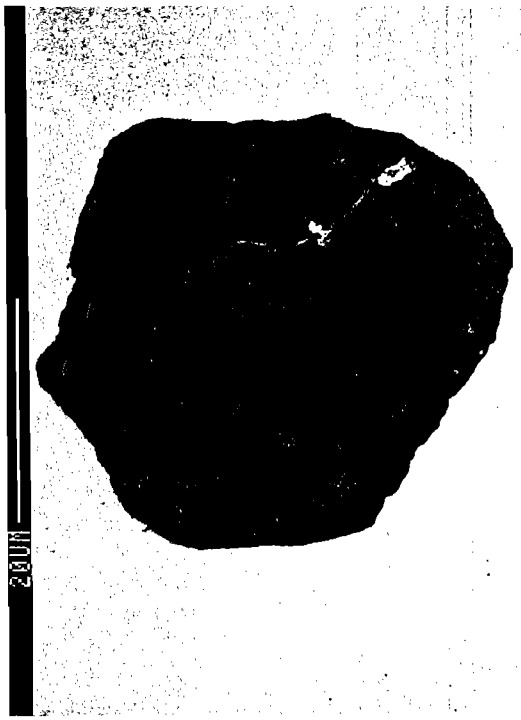

(j) EDX Spectrum: C,O.

(k) EDX Spectrum: C, O.

(l) EDX Spectrum: Ti, C, O.

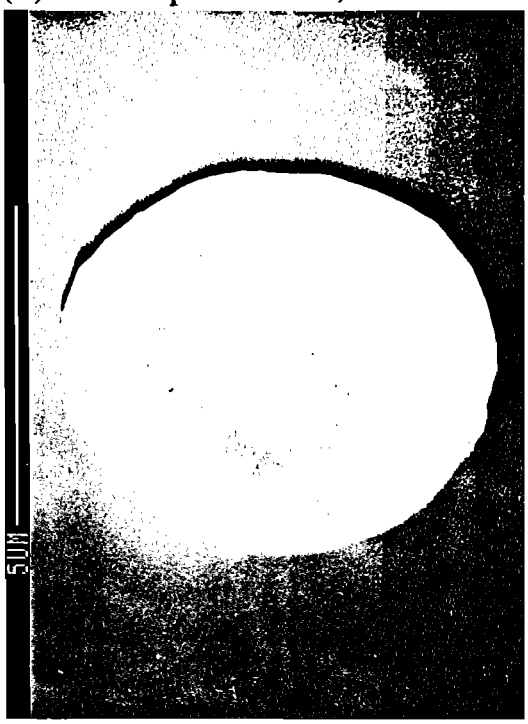

(m) EDX Spectrum: Cu, Ag, C.

Figure 4.24 (continued).

Figure 4.25 details the case for a particle found in cavity 1-5. The scatter plots in Figure 4.25(a) show the evolution of the temperature signal along board number 1 with changing electric field in the final low power rise for this cavity. The line plots of Figure 4.25(a) show a simulation (β = 90, A = 1.2 x 10^{-5} cm^2, S_0 = -3.75 cm) based on an emitter located at the site of the particle (near the upper iris), which is shown in Figure 4.25(b). The EDX spectrum indicated that the particle included titanium, carbon, oxygen, and possibly sodium, indium, aluminum, and silicon.

Figure 4.26 also comes from cavity 1-5, but with a group of sites rather than a single site. These sites were grouped together (axially within 0.5 mm, radially within 5 mm) at the upper iris near board 7. The simulations based on this location indicate that a significant signal will appear on board number 2, diametrically opposite to board 7. Figure 4.26(a) shows the measured temperature responses (scatter plots) and simulation predictions (line plots) for several electric fields for boards 7 and 2. Figure 4.26(a) also shows the simulated trajectories. The diagram of simulated trajectories is situated such that the top and bottom temperature plots correspond to the top and bottom of the cavity as shown. The four most distinct sites detected in the SEM are shown in Figure 4.26(b). EDX spectrum analysis revealed such elements as calcium, iron, titanium, aluminum, carbon, oxygen, and silicon.

Figure 4.27(b) is an indium particle which was found in cavity 1-7, near board 9. Note that this particle is molten only over a small region, as appears from the spherical shaped portion. Heating of this type is unlikely to arise from the resistive heating (H^2) or dielectric heating (E^2). It is more plausible to suggest that the heating here was from local field emission current emanating from near the spherical segment. The scatter plots in

Figure 4.27(a) show the evolution of the temperature response of Board 9 over several electric field values during the last cw power rise. The line plots in Figure 4.27(a) show the predicted temperature rise for an emission site located at the site of the indium flake (S_0 = 2.2 cm), with β = 350, and A = 1.91 x 10^{-11} cm^2.

Table 4-5 presents a summary of the features of the sites described in this section.

TABLE 4-5: SUMMARY OF SITES DESCRIBED IN SECTION 4.7.

Figure	Cavity	Contaminants	Comments
4.23	1-8	Cu	Cheerios found near thermal breakdown region
4.24	1-8	Fe,Ti,C,Ca,Al, Cu,Cr,Ni,Ag	Other sites found near thermal breakdown region
4.25	1-5	Ti,C,O,Na,In, Al,Si	Possible emission site near iris.
4.26	1-5	Ca,Fe,Ti,Al,C, O,Si	Group of possible emission sites near iris
4.27	1-7	In	Indium flake, with partial molten region. Possible emission site.

4.8. Conclusions

A primary goal of this investigation was to show a link between processed field emitters (as measured by thermometry) and surface features (as detected in the SEM). Field emission was detected by thermometry, successful processing was confirmed by thermometry, and finally, a starburst/ crater/debris site was located by SEM.

The effort to correlate SEM findings with thermometry data from cold RF tests has lead to direct evidence that the starburst phenomena in SRF cavities are a by-product of RF processing of field emission.

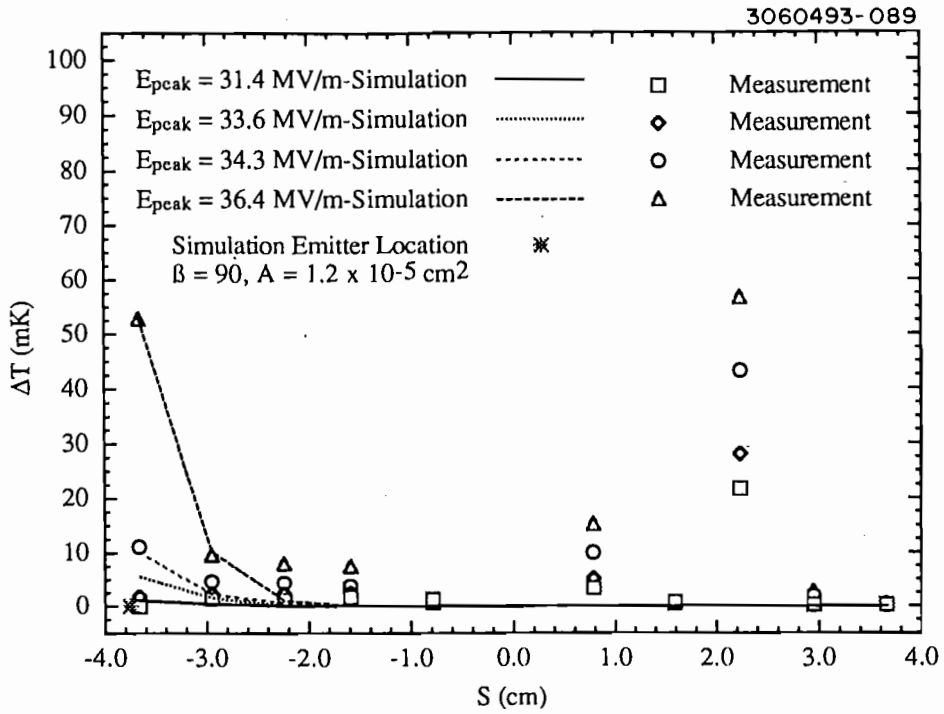

(a Measured and simulated temperature rises on an unprocessed emission site.

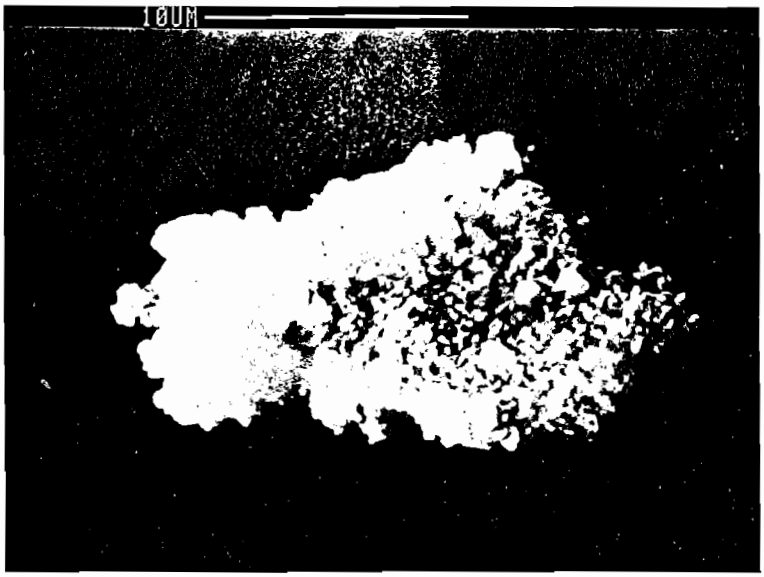

(b) SEM photograph of the site associated with the temperature signals shown in part (a).

Figure 4.25. An example of an SEM located surface site associated with a field emission site which was not processable through HPP.

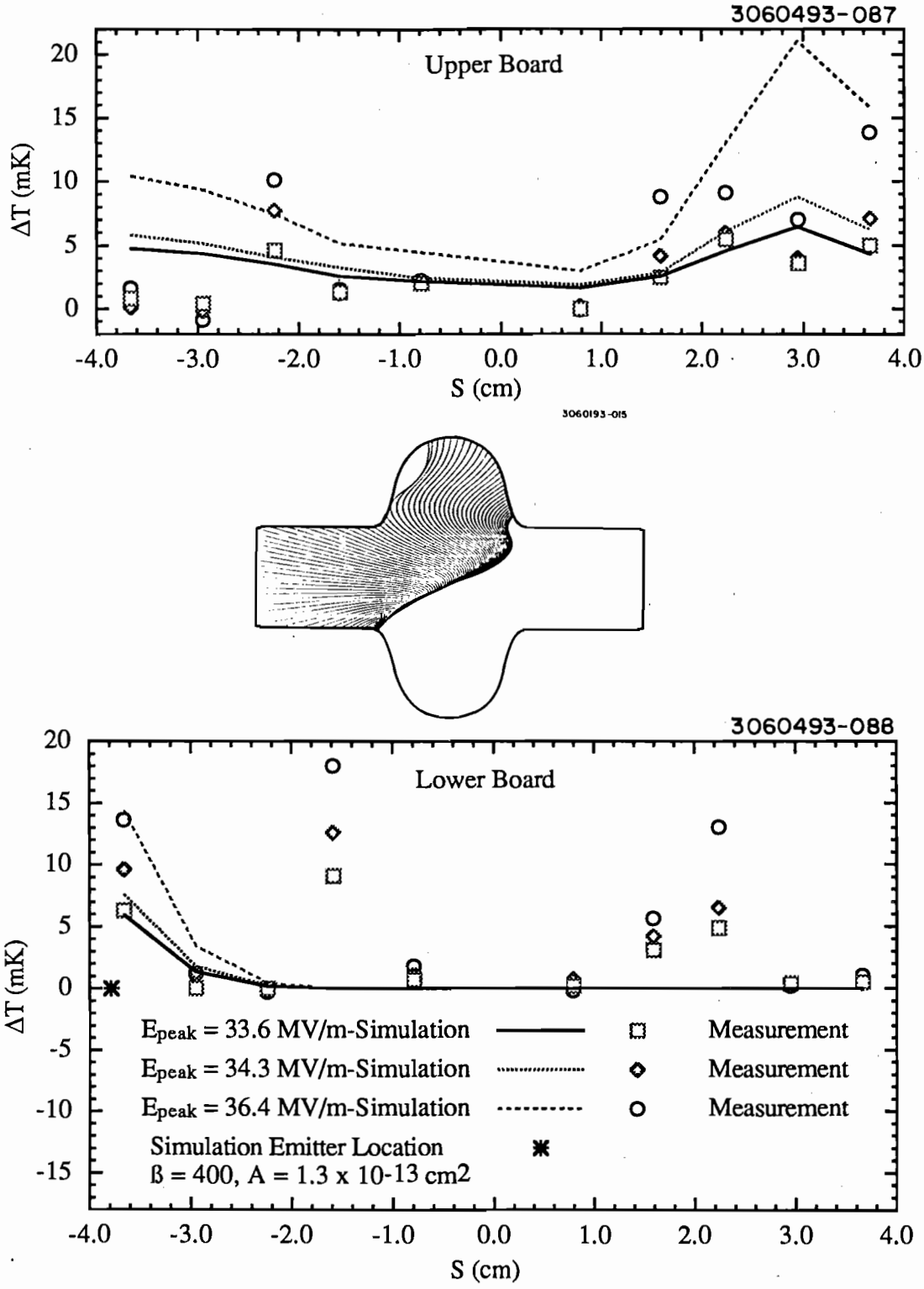

Figure 4.26.(a) Simulated and measured temperature rises, along with predicted emission trajectories for group of sites found in cavity 1-5.

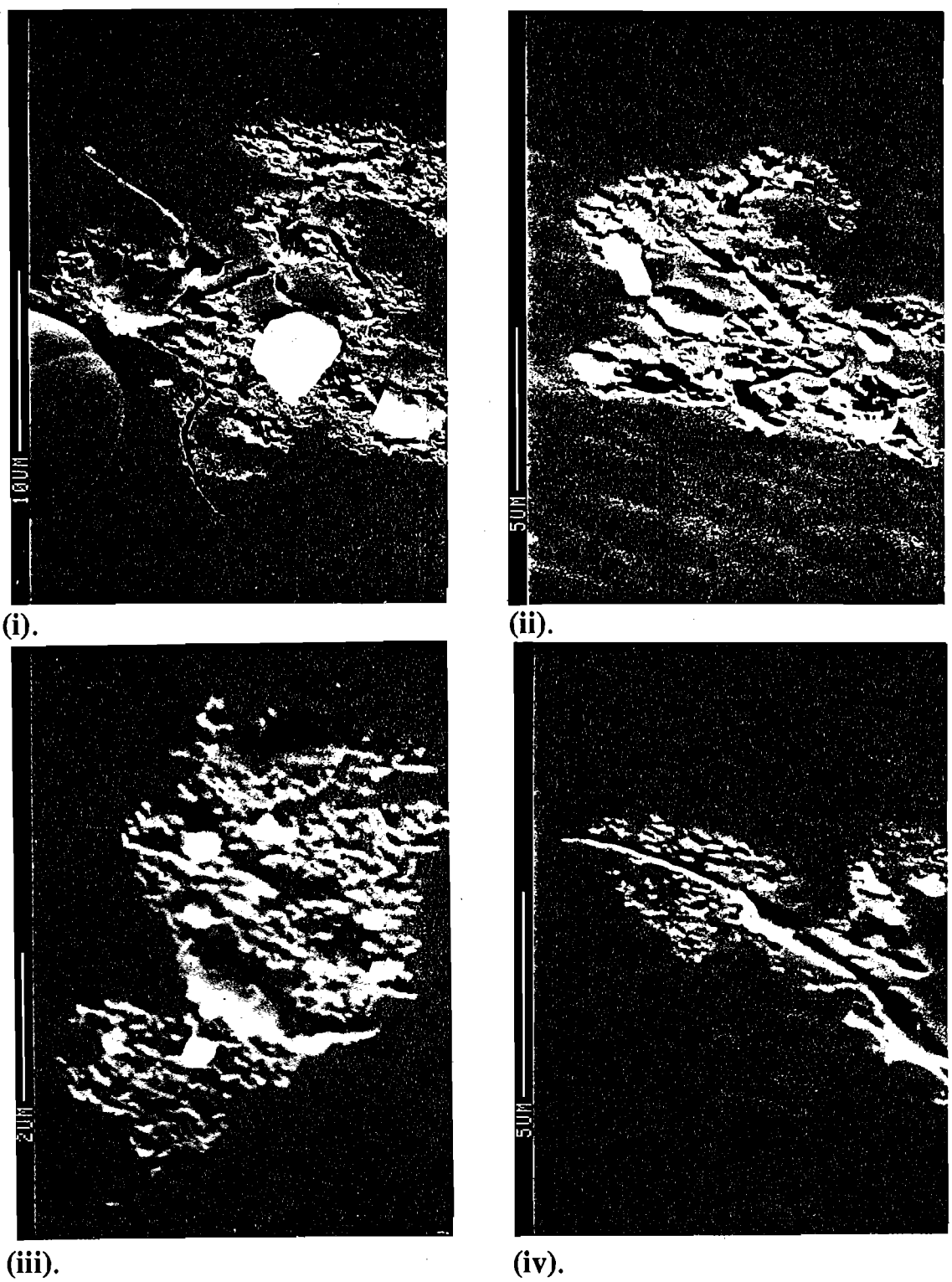

(i). (ii).

(iii). (iv).

Figure 4.26.(b) SEM photographs of the sites found near the Iris of Board 6 in cavity 1-5.

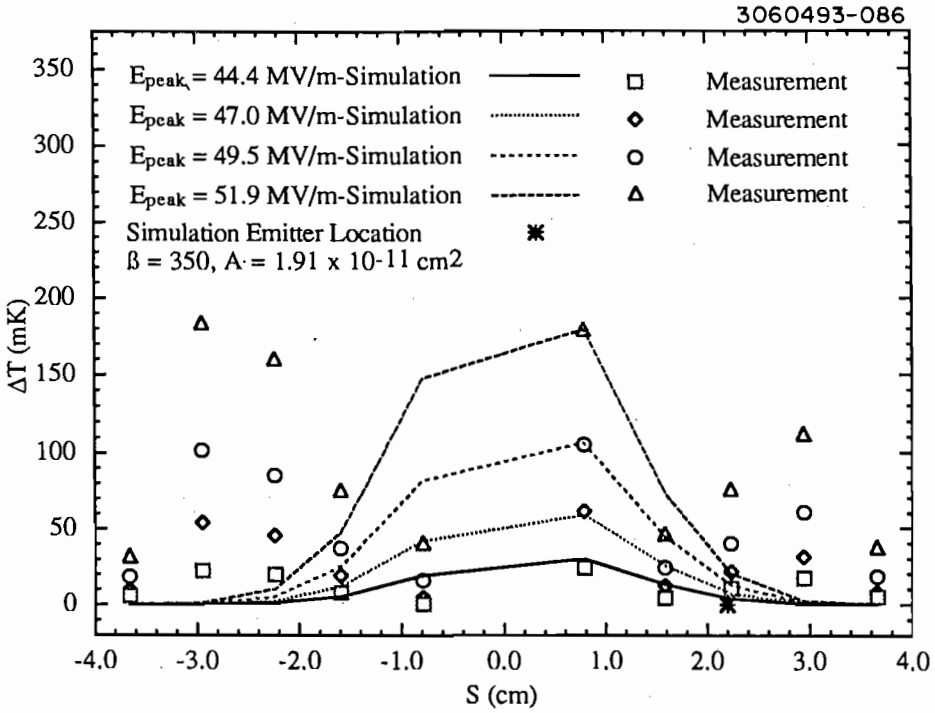

(a) Measured and simulated temperature rises on an unprocessed emission site.

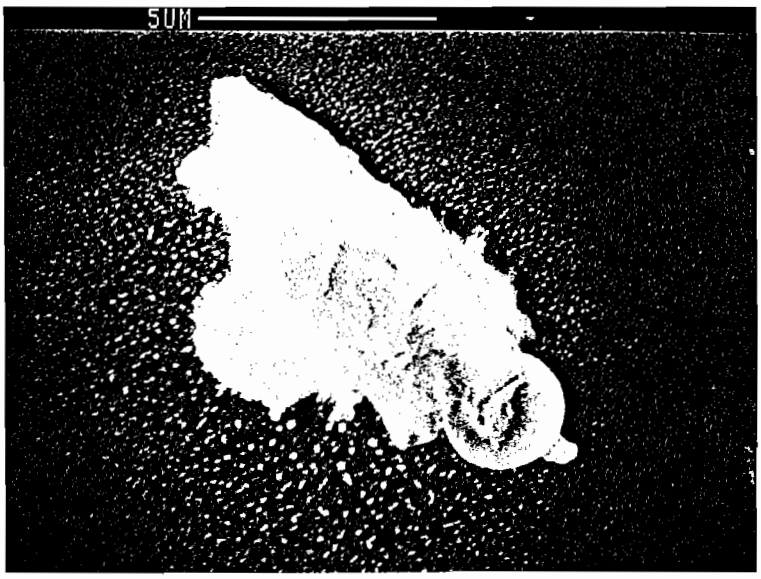

(b) SEM photograph of the site associated with the temperature signals shown in part (a).

Figure 4.27. A final example of an SEM located surface site associated with a field emission site which was not processed through HPP. EDX analysis showed the material to be indium.

In addition, x-ray analysis has shown a large correlation between foreign material contaminants and emission sites, based on the residue found in crater regions. This supports the hypothesis that superficial contaminant particles are good candidates for field emission.

We have presented several cases of contaminant sites which can be put forward as plausible sources of field emission, based on agreement with measured and simulated thermometry responses. One example of a cluster of defects that led to thermal breakdown was discovered.

CHAPTER 5: THERMOMETRY IN HPP PROCESSED CAVITIES

5.1. Introduction

In the last chapter, we confined our examination of thermometry information to identification and characterization of features found on the RF surface. In this chapter, we examine the thermometry data to improve our understanding of the mechanism of RF processing. Furthermore, we now expand the analysis to include all experiments with thermometry, rather than just those which preceded the dissection and SEM examination of a cavity.

We close this chapter by presenting a "model" of RF processing, based upon the experimental evidence, from this work and others.

5.1.1. Fowler-Nordheim Characteristics

We examine the thermometry with respect to the enhanced Fowler-Nordheim model, which was described in Chapter 1. The parameters of note are the enhancement β, and the area, A. The methods for extracting these quantities from experimental measurements were described in Chapter 4.

5.2. Correlations Between F-N Characteristics and "Processability"

From Chapter 1, recall that the current density j in the enhanced F-N model is given by equation 5-1:

$$j = C \frac{1}{\phi} (\beta E)^2 \exp\left(-B \frac{\phi^{\frac{3}{2}}}{\beta E}\right) \tag{5-1}$$

and the total current is given by equation 5-2:

$$I = C \frac{A}{\phi} (\beta E)^2 \exp\left(-B \frac{\phi^{\frac{3}{2}}}{\beta E}\right) \tag{5-2}$$

We examine the effect of RF processing on both the parameters β and A, as well as the current density and total current. It is important to remember that no clear physical meaning can as yet be ascribed to either β or A. This point will be re-emphasized below. The goal of this analysis is to find any correlation between the F-N characteristics and the "processability" of an emission site.

5.2.1. Processing Results at Individual Emission Sites

When we examine the change in F-N characteristics of emission sites which show clear improvement due to HPP processing, a distinct pattern becomes apparent: the overriding effect from successful processing is a reduction in A, while β is either unchanged, or (surprisingly) increased. Figure 5.1 shows several examples of the changes in β and A, as the site processes. One series includes a temperature cycle to room temperature, where the emission worsened following the cycle, but through further processing the emitter was eventually destroyed.

The increases in β are counterintuitive because in the past we have always viewed high β values as associated with strong field emitters. It is therefore worthy of some discussion. According to the enhanced F-N model, an increase in β results in an increase in the current density. If the enhanced F-N model is correct, then processing is successful because the reduction in emitter area is a larger effect than increase in current density. It is more likely, however that these results point out inadequacies in the enhanced F-N model, as we are using it. Possible shortcomings are many. Parameters other than β and A could be changing, for example the metal work function ϕ. Equations 5-1 and 5-2 treat the entire emission site as a single emitter, whereas SEM investigation has clearly shown that emission sites are often composed of multiple sources.

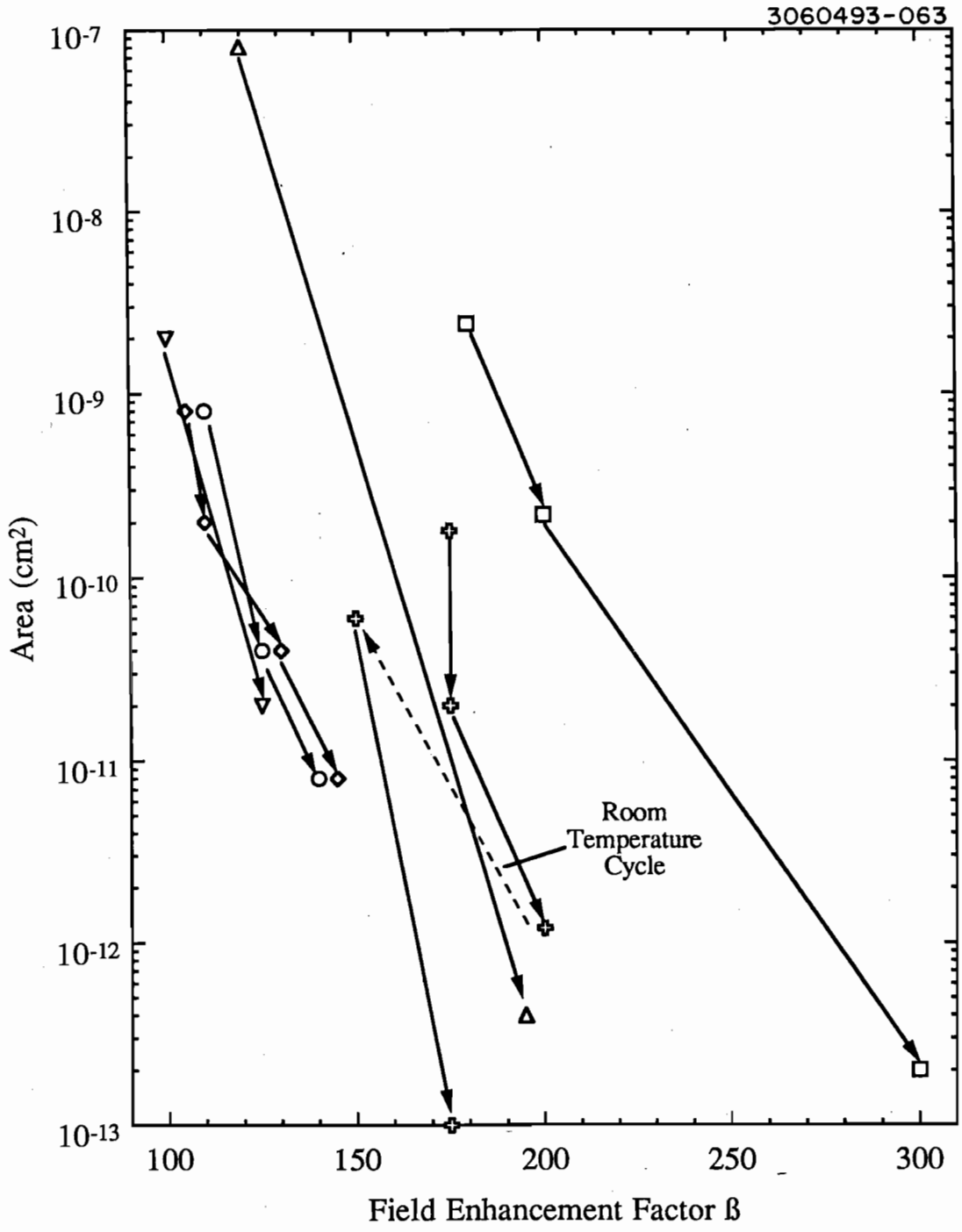

Figure 5.1. Evolution of β and A values as individual emission sites process.

The method of extracting the β and A values from measurements is total current driven. By matching the thermometry measurements over a series of electric field values we actually match the total current out of the emission site, irrespective of the current density or area. In this light, it is perhaps better to describe β and A not as measures of field enhancement and emitter area, but rather as measures of the rate of change of emission current with respect to field, and the emission current intensity, respectively.

5.2.2. "Processability " of an Emission Site

It is desirable to determine not only the change of F-N characteristics as a result of HPP processing, but also to determine when a site will process, based on its F-N characteristics. During HPP processing, we have no means of tracking the emission current from individual sites, and therefore no means of extracting β and A values. We can, however, obtain an estimate of processing conditions by extrapolating the current density (equation 5-1), and total current (equation 5-2), by using the β and A from the CW measurements preceding the HPP processing, together with the measured fields during the HPP processing.

Success in processing has been shown in the last section to be reduction in total current out of an emitter. We can then define processing success in terms of a quantity ζ, the ratio of current before processing to current after processing, with both currents measured at the same CW field. The more that ζ deviates from unity, the more successful the processing. In Figure 5.2, we plot ζ as a function of emitter current during HPP processing. A clear pattern is apparent, showing that the larger the current which can be drawn out of an emitter, the larger the gain in performance that can be obtained. Furthermore, we see that a minimum total current of

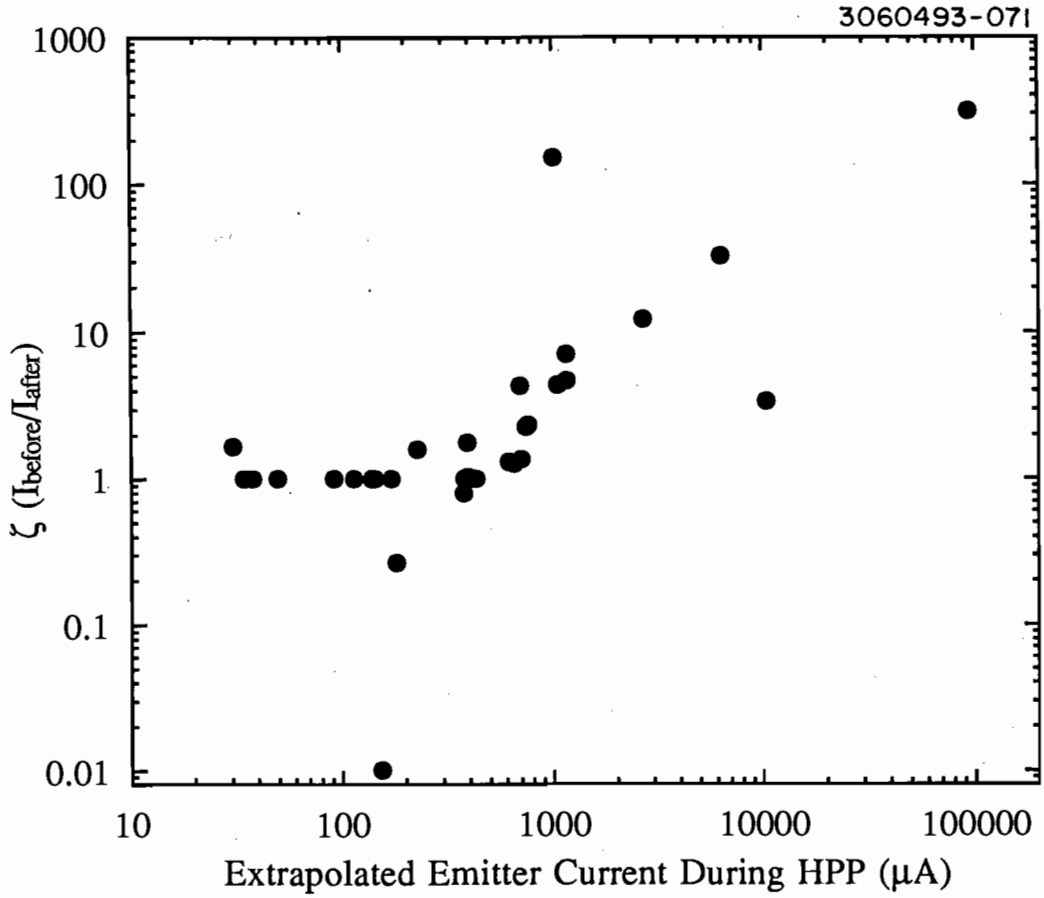

Figure 5.2. Emitter current reduction ratio (ζ), plotted as a function of extrapolated total current during High Power Processing.

approximately 1 mA is necessary for any processing to occur. Simulations of emitters with **MULTIP** and **POWER** indicate that a total current of 1 mA will result in an emission related power dissipation of 100 to 1000 W (in a single-cell cavity with peak fields ranging from 50 to 70 MV/m, typical processing values), corresponding to Q_0 values of 10^8 to 10^7. Since 1 mA is a minimum current for processing success, the associated Q values are in reasonably good agreement with those obtained in the analysis of Chapter 3. This analysis will be carried further in the next chapter, on thermal limitations.

The correlation between current and processability is entirely consistent with the overall results of HPP processing (see section 3.3), where we have shown that success in processing is directly proportional to the maximum electric field attained during processing. The high electric fields are necessary to extract enough current out of the emitter to induce processing to occur.

Calculations have previously shown[67] that melting of the niobium surface is dependent upon the current density, regardless of the emitter area. Figure 5.3 shows ζ as a function of emitter current density during HPP. If the processability of a site depends on the onset of melting, then the data

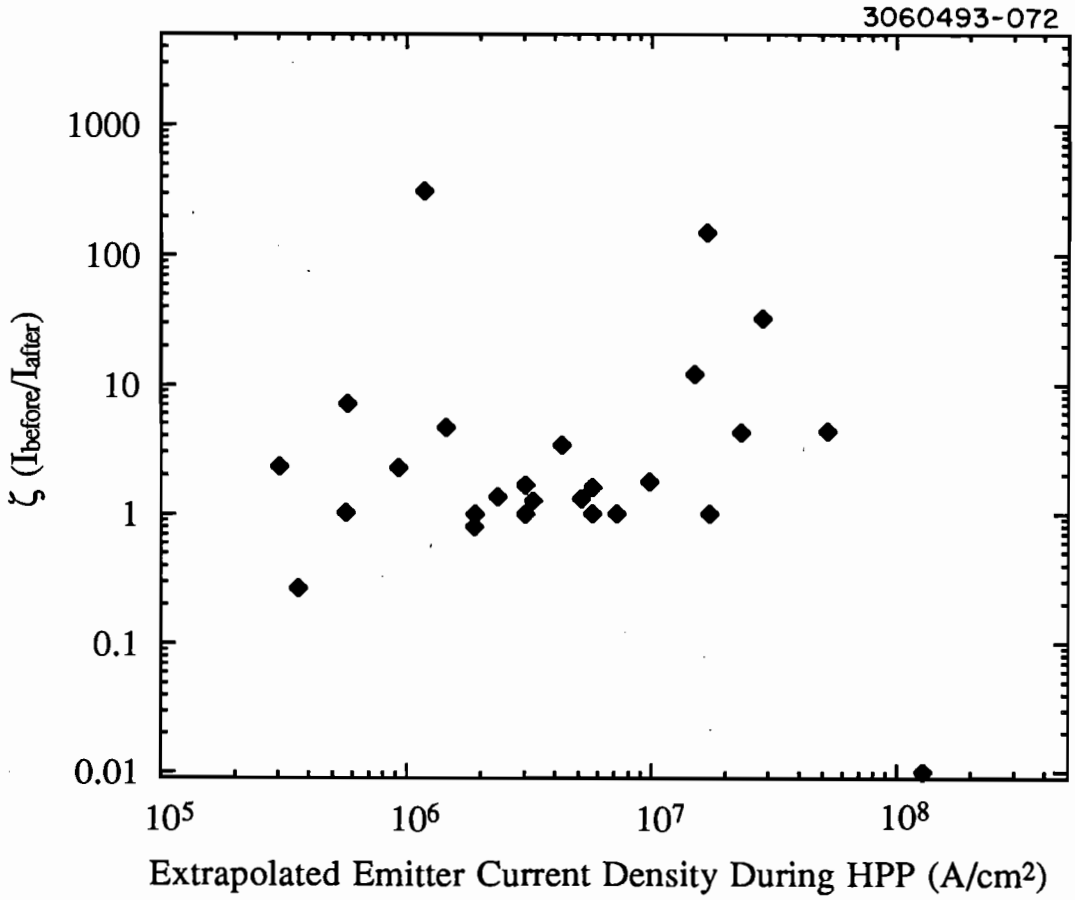

Figure 5.3. Emitter current reduction ratio (ζ), plotted as a function of extrapolated current density during High Power Processing.

plotted in Figure 5.3 clearly does not agree with this calculation, otherwise its appearance would be similar to that of Figure 5.2.

5.3. Complete Model of RF Processing

With the available evidence of this project now presented, we are in a position to offer a plausible model for the mechanism of RF processing. As we present each part of the model, we refer to the experimental evidence which supports it.

5.3.1. Prior to Processing

Stable field emitters (before RF processing) are qualitatively well described by the enhanced Fowler-Nordheim model for field emission, as evidenced by the accuracy with which thermometry measurements can be well represented by simulations based on this model.[33],[49],[51],[55] Typical β values are 100-200, and typical A values vary from 10^{-8} cm^2 to 10^{-10} cm^2. In addition, the measured power dissipation follows an exponential increase with field which is also predicted by this model.

Mechanisms for the field enhancement are not well understood. Geometrical enhancements can be calculated relatively simply.[34],[35] The geometric effects have been effectively ruled out, however, as structures with β values of 100 or greater have never been detected on emitting surfaces.[33],[38] Contaminant based enhancement is supported by the frequent detection of contaminant materials in processed emitters, both in HPP cavities, and the Mushroom cavities.[31] DC studies,[39] which directly associate emission sites with surface contaminations further support a strong correlation between field enhancement and surface contamination.

Contamination sites are often multiply grouped within a small enough area such that they are treated as essentially one site. SEM studies

confirm the multiple nature of many sites in both the Mushroom and HPP cavities. This multiple nature very likely introduces complications in attempting to model the behavior of the emitter as a single site based on Fowler-Nordheim theory.

5.3.2. What is Processing?

Processing occurs when the emitter current reaches a magnitude such that the dissipated power due to Joule heating (I^2R) cannot be conducted away before melting or vaporization occurs. We conclude that the high current is necessary based on the correlation between processing success and magnitude of electric field reached. Calculations have shown that if the current density in Niobium reaches 10^9 A/cm^2, the melting temperature can be exceeded in nanoseconds. Similar values of the time to reach the melting temperature have been calculated and measured[34]-[36],[47],[48] in DC conditions. Such a short time is necessary in order for the material to be thermally isolated in a temporal sense. This is especially important in RF conditions, where the emitter is active for at most half of an RF cycle.

It is clear by the physical evidence left in the cavity following processing events that melting and/or vaporization occurs. Craters and other molten phenomena have been detected in both RF and DC emission studies,[43]-[45],[67] superconducting and normal conducting. The HPP study clearly established the link between crater/starburst sites and specific processing events (described in Section 4.4). SEM investigations of HPP cavities and Mushroom cavities have shown that the Niobium, or surface contaminants, or both can become molten during processing.

The processing event is likely an explosive event, resulting in the creation of a plasma. The physical nature of the craters found in all studies (HPP, Mushroom, DC) indicates an explosive nature, with "splash" type

features at the edges of the craters. Calculations[34]-[36] indicate that an explosive event with creation of a plasma is a plausible method of crater formation. High speed photography of vacuum breakdown events in DC studies has clearly shown the explosive nature of these events.

Further evidence for the explosive nature, and creation of a plasma, of the processing event comes from the starburst phenomenon. The radius of the starbursts in the HPP and Mushroom cavities was shown to be approximately proportional to the inverse of the cavity resonance frequency. Furthermore, the size of the starbursts is equal to one half RF period times a velocity of approximately 6 x 10^5 m/s, which is a reasonable expansion rate for the electron cloud associated with thermionic emission from an expanding plasma, based on DC sparking models.[35]

5.3.3. When Will an Emitter Process?

As stated in the last section, calculations have been performed indicating the need for current densities on the order of 10^9 A/cm^2 in order to exceed the melting point with a few RF cycles.[67] This is in good agreement with measurement and calculation in DC experiments. The analysis of thermometry data from the HPP studies indicate that approximately 1 mA of current must be extracted from the emitter in order for processing to be successful. No such correlation could be made with current density, based on the HPP experiments. This likely points out limitations in the enhanced F-N model of field emission in predicting current density.

It is again informative to consider the difference in HPP processing, as compared with low power RF processing, which make it more effective in emission reduction. The current out of the emitter is highly dependent on the electric field. The electric field is in turn limited by the available power and the mechanisms which dissipate the available power. In HPP process-

ing, the rapid increase in power dissipation with increase in electric field is overcome, thus allowing for higher fields, and the correspondingly higher emission currents. It has been clearly shown that the high emission currents make processing successful.

5.3.4. Results of Processing

The dominant outcome of successful RF processing is a decrease in the current emitted at a given electric field. The thermometry data of the HPP program indicate that this is due primarily to reduction of the F-N characteristic area A.

SEM investigations indicate that processing results from the vaporization or melting of surface contaminants.

The thermometry findings of reduction of A and increase of β lend support to a model in which β is material (contaminant) induced. Consider a contaminant site of several particles. Ostensibly, all particles would have similar values of β in this picture, and the β of the emission site would be an aggregate of all components. If some of the particles are processed away, then the emitting area would decrease, but since all remaining particles were still the same, β would not change significantly. This would indicate the possibility of β decrease as well as increase, but β decrease has not been measured to date. SEM investigations have shown many instances where contaminant materials have been partially removed due to processing, which would support a model of this nature.

Finally, the nature of RF processing can be contrasted with that of helium processing. Helium processing was found to reduce emission by reducing the enhancement factor β. The mechanism of helium processing is not well understood, but based on this result, would appear to be fundamentally different than RF processing.

CHAPTER 6: THERMAL LIMITATIONS TO THE HPP EXPERIMENTS

6.1. Evidence for the Thermal Nature to the HPP Limitation

In Chapter 3, we touched upon the exploration of the limitations on HPP processing. In this chapter we will further investigate the aspects of the limitations which can be attributed to thermal breakdown. First, we state again the evidence which leads us to believe that the limitations are, in fact, thermal in nature.

It is easiest to correlate HPP limits with thermal breakdown in cavities where the breakdown was attainable under CW conditions. In these cavities, the rate of increase of HPP peak fields decreased greatly (see section 3.4.2. for details) at fields slightly exceeding the CW thermal breakdown field, indicating a connection to the thermal breakdown limitation.

The most apparent change in the HPP behavior is a change in the shape of the transmitted power curve (as monitored on an oscilloscope, see Figure 3.18 for an excellent example of the change when passing the thermal breakdown threshold). Prior to the change, the P_t pulse decays as expected, exponentially with characteristic time τ, given by $\tau = Q_L/\omega. \approx Q_{ext}/\omega.$. During HPP, Q_{ext} is typically 10^6 to 10^7, which translates to $\tau = 50$ to 500 μsec. Above the breakdown field, the decay time decreases to the order of μsec, approximately what is expected for a 3 GHz normal conducting cavity.

Finally, temperature maps were occasionally obtained during HPP processing, under what we assume to be breakdown conditions. The thermal nature of the breakdown event is further confirmed by the temperature maps, an example of which is shown in Figure 6.1, where nearly the entire cavity is registering temperature signals on the order of a few Kelvin.

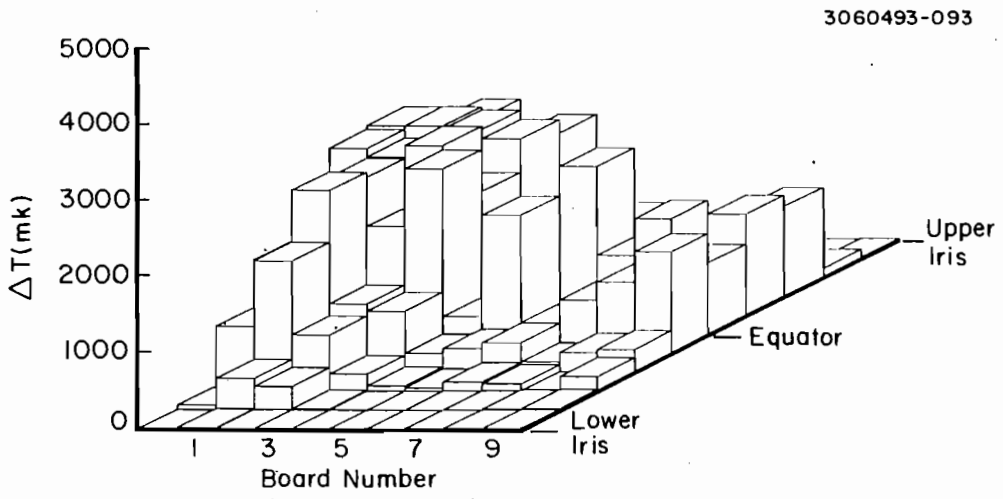

Figure 6.1. Temperature map of a cavity taken during breakdown events during HPP processing.

6.1.1. Possible Breakdown Mechanisms

With the determination that the limitations were a thermal breakdown, the question remained as what was the origin of the thermal breakdown. The possibilities are defects, Global Thermal Instability (GTI), or field emission, all of which were discussed in Chapter 1.

GTI can be eliminated as a mechanism, based on the initiation time of the breakdown. Experimental measurements indicate that the HPP breakdown events are initiated in times on the order of tens of microseconds, or faster. Numerical simulations of GTI (to be discussed in Section 6.2.1) indicate that a GTI induced breakdown cannot initiate faster than several hundreds of microseconds. This prediction has also been verified analytically.[68] This result clearly eliminates GTI as the mechanism observed in HPP.

With regard to defect or field emission breakdown, no distinction can be made on the basis of initiation time. The basis for distinction between the two types is the constancy of the field level at which breakdown is

encountered. The field for a defect induced breakdown remains constant for the duration of the experiment. The emission induced breakdown field can be increased, if the field emission is altered, e.g. through processing. We believe, in fact, that we have encountered both types of breakdown.

6.1.2. Aspects of HPP Measurements to be Modelled

In order to better understand the limitations and capabilities of HPP processing, we modelled the thermal limitations. With the model, we were able to predict the following three aspects of the HPP thermal breakdown phenomena:

1) Relationship Between CW Breakdown Field and Achieved E_{HPP}: Achieved peak electric fields during HPP processing routinely have surpassed CW breakdown fields by as much as 20 MV/m (corresponding to 460 Oe in magnetic field), or up to 40% higher than the CW breakdown field. The model predicts the overshoot based on processing parameters, such as input power, coupling, breakdown level, etc.

2) Timing of Breakdown Occurrence: The model also predicts the initiation time of the breakdown, as measured experimentally.

3) Observed Transmitted Power Pulse Shape During HPP Processing: We have extensive data on observed pulse shapes during breakdown events, such as presented in Figure 3.16(e)-(f). The model reproduces these shapes.

Of course, all of these aspects are interrelated and accurate modelling of one is consistent with the others.

6.2. Thermal Modelling 1: Theoretical Conduction in an Ideal System

Extensive modelling of steady state thermal processes in niobium cavities has been performed over the last ten to fifteen years.[69] This

modeling has been necessary due to the frequent problem of thermal breakdown limitation to SRF cavities, as was initially described in Chapter 1.

Useful results have been obtained by studying a cylindrically symmetric system (allowing for simplification to a two-dimensional problem) of a niobium disk, with a liquid helium bath at one circular surface, and constant magnetic fields at the opposite surface. For numerical solution, the disk is assumed to consist of stacks of cylindrical rings. Defects may be placed at the center of the RF surface, to study the heat conduction away from the defect. A diagram of the physical set-up of this model is shown in Figure 6.2. The model incorporates the non-linear thermal conductivity and heat capacity of niobium, as well as the Kapitza resistance[70] at the niobium liquid helium interface.

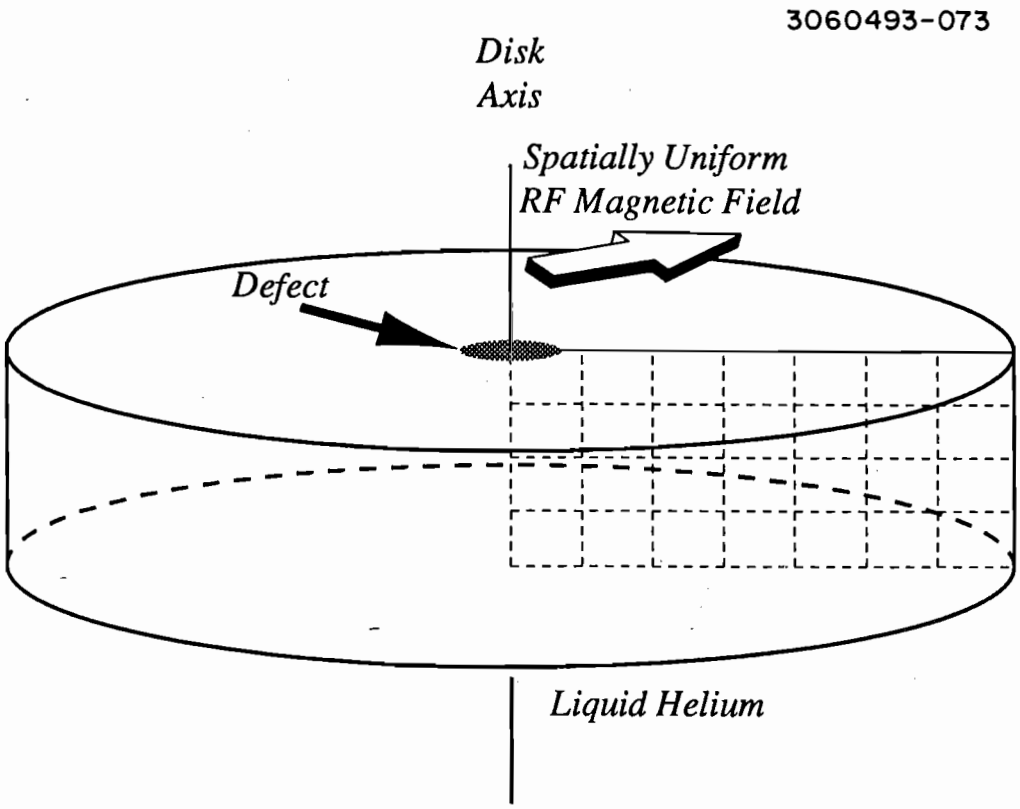

Figure 6.2. Diagram of the model used for investigation of thermal processes in superconducting niobium.

The problem was originally solved for steady state (simulating CW) conditions with the **HEAT** program series.[71] Further enhancement of this model was obtained with the inclusion of a variable mesh.[69] The output of Program **HEAT** is the steady state temperature distribution of the disk, RF dissipated power, and power transfer to the helium bath.

More recently, this model has been extended to transient problems, through the program **Transient_HEAT**.[72] The physical model for **Transient_HEAT** is identical to that of **HEAT**, shown in Figure 6.2, however, instead of solving for steady state solutions, **Transient_HEAT** iterates forward in time, producing time dependent temperature distributions and power flow through the disk.

6.2.1. Comparison of Predictions with Measurements

The steady state programs have successfully predicted[69], CW behavior, specifically breakdown fields as a function of operating prarameters, e.g. niobium purity (based on *RRR*), bath temperature, and RF frequency. The steady state programs also predict the occurrence of GTI phenomena. The GTI phenomena is the thermal runaway process which occurs in the absence of any localized surface defect. A further description of GTI, modelling and measurement is given in Appendix F. The steady state programs have no means of predicting HPP phenomena.

Program **Transient_HEAT** was used as an initial step in modelling the HPP breakdown phenomena. In steady state conditions, **Transient_HEAT** simulations agree with those of **HEAT**. In addition, breakdown fields agree with those predicted by the steady state program. The agreement can be seen in Appendix F, the description of GTI Breakdown.

Transient_HEAT was used to investigate the initiation time of GTI induced breakdown, as discussed previously, and through this modelling (as

discussed in Section 6.1), we were able to rule out GTI as a possible mechanism for HPP breakdown. While the entire cavity does show heating (as predicted by GTI), the initiation time is too short (tens of microseconds) for GTI. The breakdown event must initiate at some nucleation site (possibly a small defect), and then grow outward from there.

In modelling defect-related breakdown, **Transient_HEAT** was able to predict the field level at which breakdown is intiated, and the rate at which the normal conducting region of the cavity grows.

6.3. Thermal Modelling 2: Modelling the Response of SRF Cavities to Pulsed RF Excitation

6.3.1. The Model

With the results of **Transient_HEAT**, as described above, we developed the following model for cavity behavior under HPP conditions. A cavity which is filling due to an external source fills as a function of time according to equation 6-1 (previously developed as equation 3-2):

$$E_{peak}(t) = E_{EQM}\left(1 - \exp\left(-\frac{\omega t}{2Q_L}\right)\right) \tag{6-1}$$

where ω is the angular frequency, and the equlibrium field (E_{EQM}) is given by:

$$E_{EQM} = k_E\sqrt{U_{EQM}} = k_E\sqrt{\frac{P_{diss}Q_0}{\omega}} \tag{6-2}$$

where Q_0 is the unloaded quality factor of the cavity and P_{diss} is the dissipated power in the cavity. Equation 6-1 is only valid if the cavity behavior is unchanging during the fill. To further expand, we need to model the possible loading sources in the cavity.

The loaded quality factor of the cavity (Q_L) is defined as:

$$\frac{1}{Q_L} = \frac{P_{total}}{\omega U} = \frac{1}{\omega U} \sum_{\substack{\text{all loss} \\ \text{mechanisms}}} P_i \tag{6-3}$$

where U is now the instantaneous stored energy in the cavity. We allow for four different loss mechanisms: superconducting wall losses, input coupler losses, field emission losses, and normal conducting wall losses. We assume that transmitted power out of the monitor probe is negligible. The power into each of the non-negligible mechanisms is defined respectively by equations 6-4a through 6-4d. The superconducting wall loss power is given by:

$$P_0 = \frac{\omega U}{Q_{00}} \tag{6-4a}$$

where Q_{00} is the low field unloaded quality factor of the cavity. Coupler losses are given by:

$$P_e = \frac{\omega U}{Q_{ext}} \tag{6-4b}$$

where Q_{ext} is the quality factor of the input coupler. The field emission loading is given by:

$$P_{FE} = a(E_{peak})^2 \exp\left(-\frac{b}{E_{peak}}\right) \tag{6-4c}$$

The field emission loading is in a form consistent with Fowler-Nordheim theory. The constants a and b were extracted from CW measurements on the cavities. Finally the normal conducting losses are given by:

$$P_{nc} = \frac{1}{2} R_{nc} (H_{peak})^2 \pi (r_{nc})^2 \tag{6-4d}$$

where R_{nc} is the normal conducting surface resistance, and r_{nc} is the radius of the normal conducting surface region.

We assume the cavity has a single breakdown initiation region, which activates at a given magnetic field (H_{BD}). When H_{BD} is surpassed, a circular normal conducting region begins to grow on the RF surface of the cavity, with the radius of the normal conducting (r_{nc}) region growing at velocity v_{nc}, which is given by the relationship:

$$v_{nc} = A + B\left(H_{peak} - H_{BD}\right)^2 \tag{6-5}$$

This velocity fitting function was obtained by determining the growth rate of the normal conducting region as a function of magnetic field with **Transient_HEAT.**

While the cavity is filling (H_{peak} increasing), we use equation 6-5 for v_{nc}. When the cavity fields begin to decrease, we can no longer use this form, as the thermal relaxation time is such that it is possible to maintain the growth of the normal conducting region. The thermal relaxation time can be estimated using the thermal conductivity, heat capacitance, and characteristic distance over which temperatures must equalize. Using tabulated values of conductivity and capacitance at 10 Kelvin, we find that hundreds of microseconds are necessary for temperatures to equalize over a distance of millimeters. For computational simplicity in this model, we take v_{nc} to be a constant 75% of its maximum value during cavity field decay due to breakdown.

The value of 75% was obtained empirically by fitting several transmitted pulses. A more exact determination of v_{nc} as the cavity fields

decay would require solution of the heat flow equations with initial conditions determined by the temperature distribution at the time of the cavity breakdown. **Transient_HEAT** has potential to solve this particular problem, with some modification. It is worth noting that the only significant facet of the model predicted results which the change in v_{nc} function affects is the P_t pulse shape. The maximum field achieved and the initiation time to breakdown are not affected.

A and B (in equation 6-5) are constants which may be adjusted to accurately model any particular cavity. In practice it was found that values of A = 5.0 m/s and B = 5.0 x 10^{-3} m/s $(Oe)^{-2}$ were accurate within 10-20% for nearly all cavities modelled. Corresponding maximum normal conducting region expansion velocities were generally found to be a few hundred to a few thousand meters per second.

Given these loading mechanisms, the unloaded quality factor of the cavity can be defined as:

$$\frac{1}{Q_0} = \frac{1}{Q_{00}} + \frac{1}{\omega U}(P_{FE} + P_{nc}) \tag{6-6}$$

and the corresponding input coupling coefficient is given by:

$$\beta = \frac{Q_0}{Q_{ext}} \tag{6-7}$$

The procedure of the simulation is then to diffentiate equation 6-1, and iterate forward in time, taking into account changes in the cavity behavior, specifically in field emission (equation 6-4c) or breakdown (equation 6-4d), and incorporating these changes into Q_L and coupling coefficient β.

In order to make the input parameters the same as those controlled during HPP processing, we combine equations 6-1, 6-2, 6-7, along with the relationship between incident and dissipated power:

$$P_{diss} = \frac{4\beta}{(1+\beta)^2} P_{inc} \tag{6-8}$$

to get the following expression for E_{peak} as a function of time:

$$E_{peak}(t) = k_E \sqrt{\frac{P_{inc} Q_{ext}}{\omega}} \frac{2\beta}{(1+\beta)} \left(1 - \exp\left(-\frac{\omega t}{2Q_L}\right)\right) \tag{6-9}$$

This equation is then differentiated, and iterated forward in time, to obtain the HPP behavior ($E_{peak}(t)$, $P_t(t)$, $P_{diss}(t)$, etc.) of an SRF cavity. Note that time dependence can enter into this equation directly through t, or indirectly through changes in either β or Q_L.

6.3.2. The Program: ***FEBD***

The model described in the last section was implemented with the program **FEBD**, written in LabVIEW™, on a Macintosh IIsi. The Lab-VIEW-Mac II environment was chosen for its convenience in graphical presentation, as well as ease in accessing experimental data, which was measured and stored with the same system. The display screen for **FEBD**, with a typical calculation, is shown in Figure 6-3.

Output includes electric fields as a function of time, transmitted power as a function of time, dissipated, reflected, and approximate field emission dissipated power as functions of time, NC radius and growth velocities as functions of time, and the maximum field, and maximum NC growth velocity during the pulse.

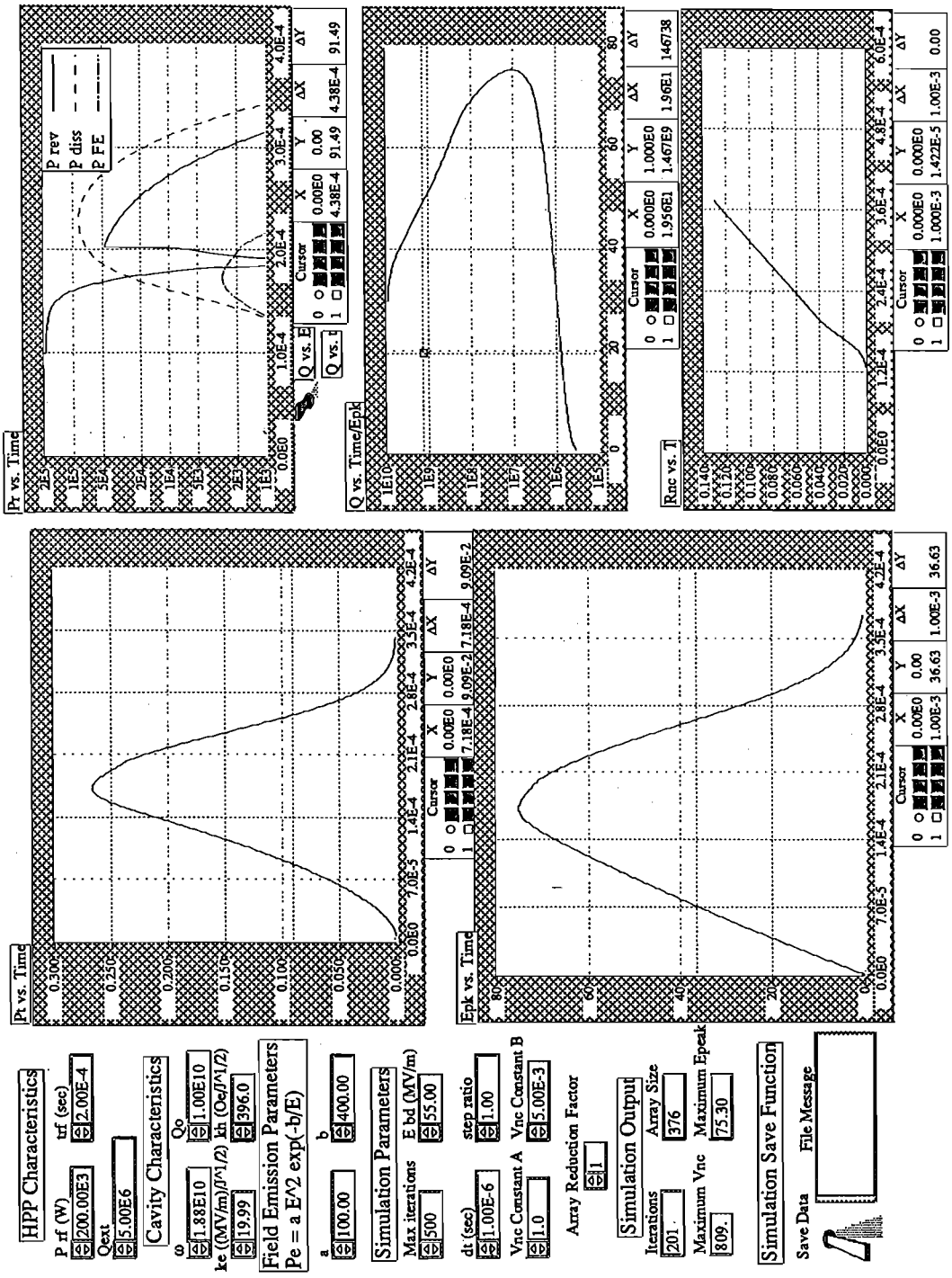

Figure 6.3. Display screen for program **FEBD.**

During HPP experiments, the transmitted power was monitored on an oscilloscope. Maximum electric field during the pulse was obtained via the calibration of the transmitted power. Often photographs were taken of the pulse shape, as shown in Figures 3.18-3.20.

We will compare the attained fields, time to breakdown event, and shape of P_t pulse from experiment to **FEBD** simulation.

6.3.3. Comparison of Predictions with Measurements

The most striking result of program **FEBD** is that nearly all of the HPP experiments can be accurately modelled with only slight variations in A and B, the parameters used to obtain the expansion velocity of the normal conducting region. In the successful cases, the program self-consistently models achieved fields as a function of HPP parameters (power pulse length, input coupling) for the entire experiment with a constant set of parameters (A, B, E_{BD}, etc.).

Figure 6.4 shows an example of the comparison between predicted field with **FEBD**, and measured field during HPP. This is the same experimental data as shown in Figure 3.13. Note how much more accurately the field is predicted with **FEBD** than it was with simple use of equation 3-3, as shown in Figure 3.13. It is the inclusion of transient thermal effects which improves the predictive capabilities. The plot shown in Figure 6.4 is for a single cell cavity, and the indicated agreement between prediction and measurements is typical. Figure 6.5 shows the same sort of plot for a nine-cell cavity. Again, the agreement between measured field and **FEBD** predicted field is remarkable.

Additional support for the model can be seen in comparison of pulse shapes. Figure 6.6(a) shows an oscilloscope trace of the transmitted power for two-cell cavity W3C2-1, while experiencing thermal breakdown during

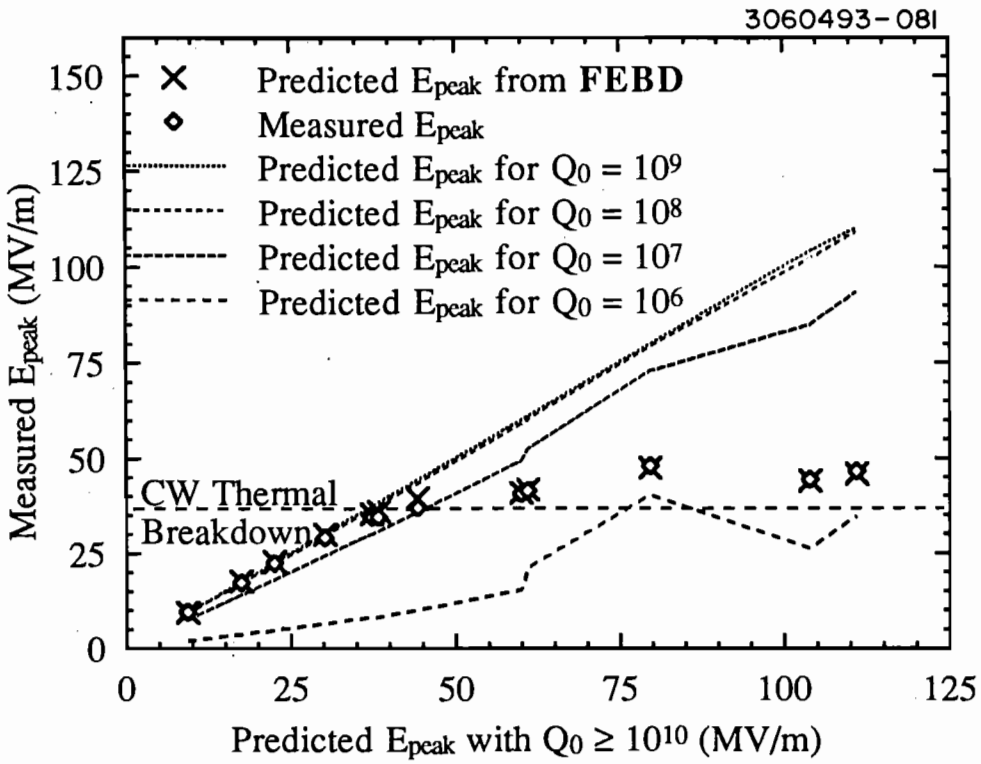

Figure 6.4. Comparison between measured electric field during HPP and predicted field with **FEBD**. The same data was plotted in Figure 3.13.

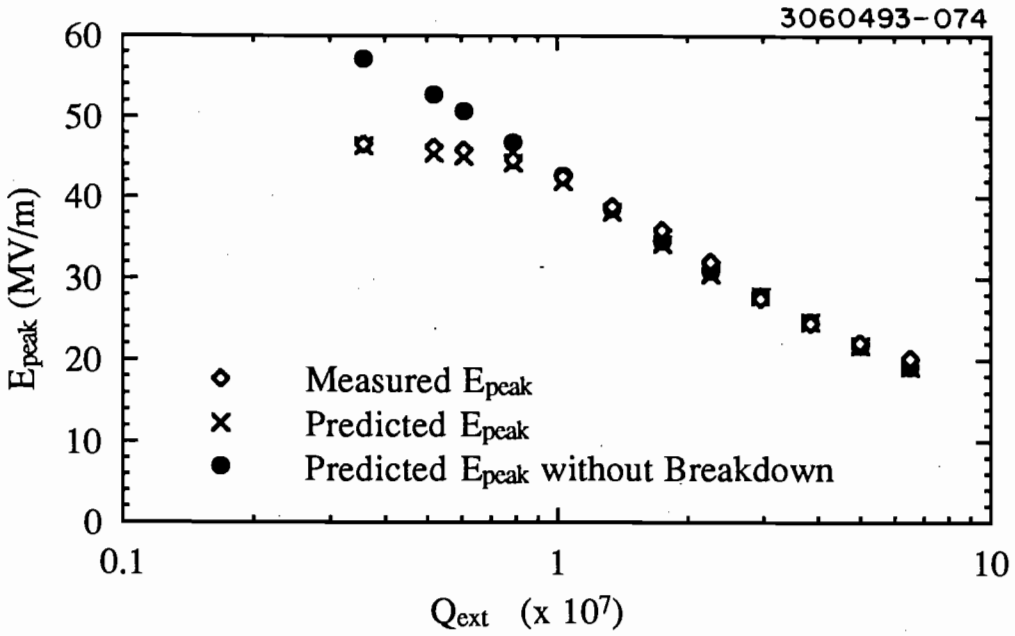

Figure 6.5. A second comparison between measured electric field during HPP and predicted field with **FEBD**, this time for a nine-cell cavity.

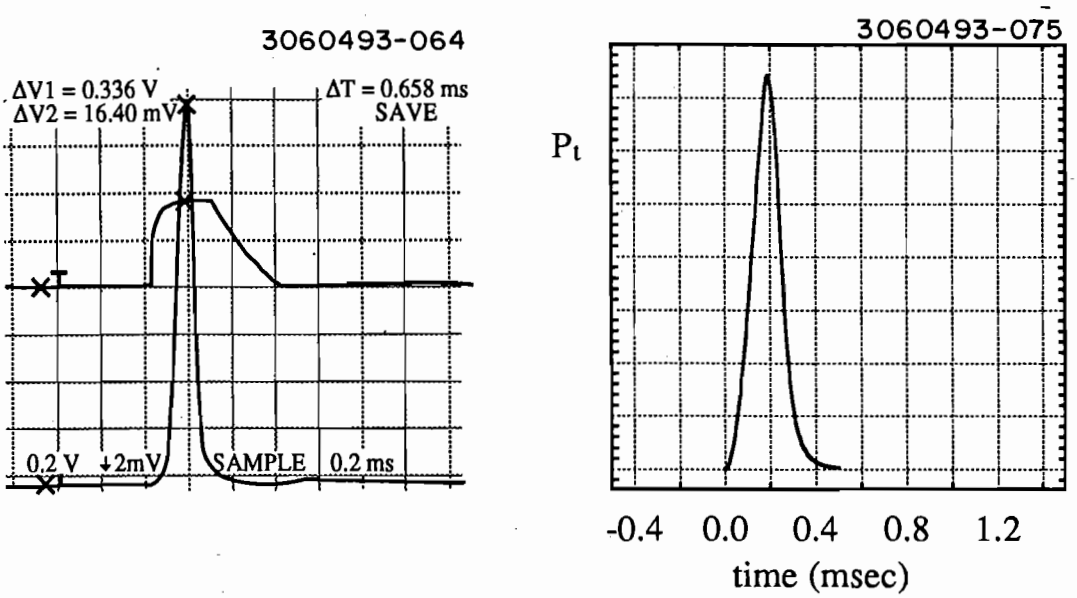

Figure 6.6. Measured and simulated P_t pulses for two-cell cavity W3C2-1 during HPP processing.

HPP processing. The maximum attained peak field in this plot is 100.5 MV/m. HPP parameters were P_{RF} = 48 kW, t_{RF} = 280 μsec, and input Q_{ext} = 4.88 x 10^6. CW measurements showed the breakdown field was approximately 90 MV/m prior to HPP. Figure 6.6(b) shows a simulation of the same conditions via **FEBD**. The pertinent parameters input to FEBD were: P_{RF} = 45 kW, t_{RF} = 280 μsec, input Q_{ext} = 5.0 x 10^6, F-N parameters a = 100 and b = 570 (obtained from the CW measurements preceding HPP), E_{BD} = 90 MV/m, and v_{nc} parameters A = 5.0 m/s and B = 1 x 10^{-2} m/s(Oe)$^{-2}$. The maximum electric field in the simulation was 102.3 MV/m. The agreement in pulse shapes is also very good.

A second example of this is shown in Figure 6.7 and 6.8. Figure 6.7 shows the measured tansmitted power pulses at field levels just above and below the thermal breakdown transition from a test of a nine-cell cavity. The HPP parameters for these traces were P_{RF} = 8.5 kW and t_{RF} = 1.00 msec. As can be seen, with Q_{ext} ≐ 3.45 x 10^7, the measured E_{peak} was 35

MV/m, and the decay appears to be a roughly constant exponential. When Q_{ext} was decreased to 3.15 x 10^7, the field increased to E_{peak} = 36 MV/m, and the decay is interrupted by a breakdown type phenomena, approximately 100 μsec after the RF pulse ended.

FEBD was run with P_{RF} and t_{RF} as listed above, with the results shown in Figure 6.8. The agreement is very nearly perfect. The simulation used A = 1.0 m/s, B = 5.0 x 10^{-3} m/s(Oe)$^{-2}$, and assumed that the breakdown field was E_{peak} = 30 MV/m. Unfortunately, this cavity would not reach E_{peak} = 30 MV/m under CW conditions due to field emission, so the breakdown field value could not be confirmed. Nonetheless, the agreement is remarkable. With Q_{ext} = 3.7 x 10^7, predicted E_{peak} = 35 MV/m, and the decay shows no breakdown. When Q_{ext} is reduced to 3.35 x 10^7, E_{peak} rises to 36 MV/m, and the pulse shows breakdown, with nearly the same features as measured (Figure 6.7).

The predictions and consistency of **FEBD** maintain this performance as long as the breakdown mechanism is clearly defect related, or constant in field. All nine-cell experiments were modelled to within 5% on attained electric field (when MVS events were not occurring-See section 6.3.4.) Seven of eight of the single-cell HPP experiments could successfully be modelled. The two-cell experiments could not, as will be discussed below.

In the case of field emission type breakdowns, where the breakdown initiation field is changing, individual events can be accurately modelled (as shown in Figure 6.6), however to model the entire experiment selfconsistently the breakdown parameters (E_{BD}, A, and B) must be changed. This is most likely due to the changing nature of the breakdown in field emission type breakdowns. This was the case with two-cell cavity W3C2-1. The

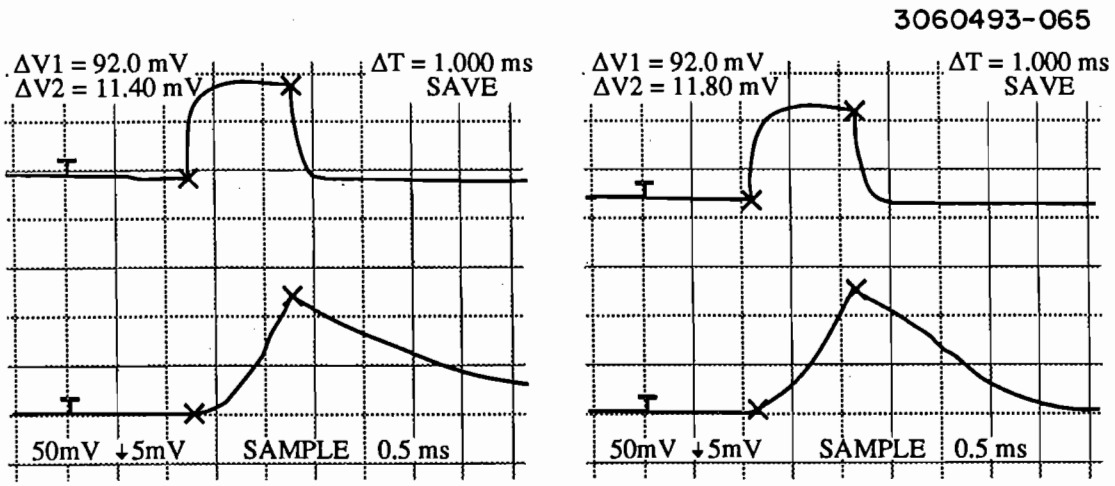

Figure 6.7. Transmitted power pulses (lower trace) for a nine-cell cavity at fields just below and above the thermal breakdown transition. A description of the conditions can be found in the text.

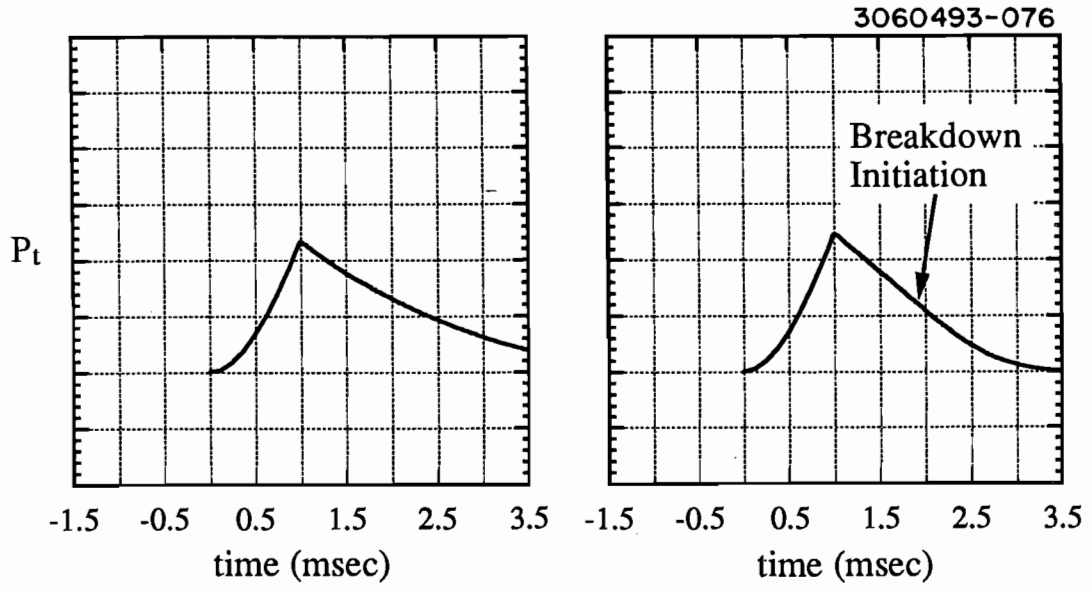

Figure 6.8. **FEBD** simulation of the measured transmitted power pulses shown in Figure 6.7.

CW measurements of the cavity were initially limited by a thermal breakdown at E_{peak} = 92 MV/m. Following all HPP processing, the thermal breakdown threshold had been increased to E = 100.6 MV/m. As indicated above, **FEBD** can accurately model individual events but not the overall experiment.

Use of the FE loading term in the model (equation 6-4c) also allows for estimation of power coupled into field emission during HPP processing. The FE loading term includes two constants, a and b, which can be estimated for a cavity by fitting its CW power dissipation to a Fowler-Nordheim form. The HPP power into field emission is then obtained by using the values of a and b from the CW run before the HPP processing session being modelled.

6.3.4. Analysis of Nine-cell Limitations

Since most results of nine-cell cavities were similar to single-cell cavities, it is to be expected that **FEBD** should successfully predict the measured nine-cell behavior. The program turns out to be very successful (see Figure 6.5), until the MVS events are encountered, as described in Section 3.5.2. A clear case of this is shown in Figure 6.9, where measured and predicted fields coincide through the thermal breakdown limit, up until the MVS threshold is reached. This result is not surprising, as MVS events were clearly shown (section 3.5.2) to be inherently different from "normal" thermal breakdown events.

Therefore, as we predicted in Chapter 3, **FEBD** confirms that thermal events can not be the limiting mechanism in HPP processing of nine-cell cavities. This result implies that if the MVS events are in fact field emission related, then more available power might have proved successful in processing to higher fields.

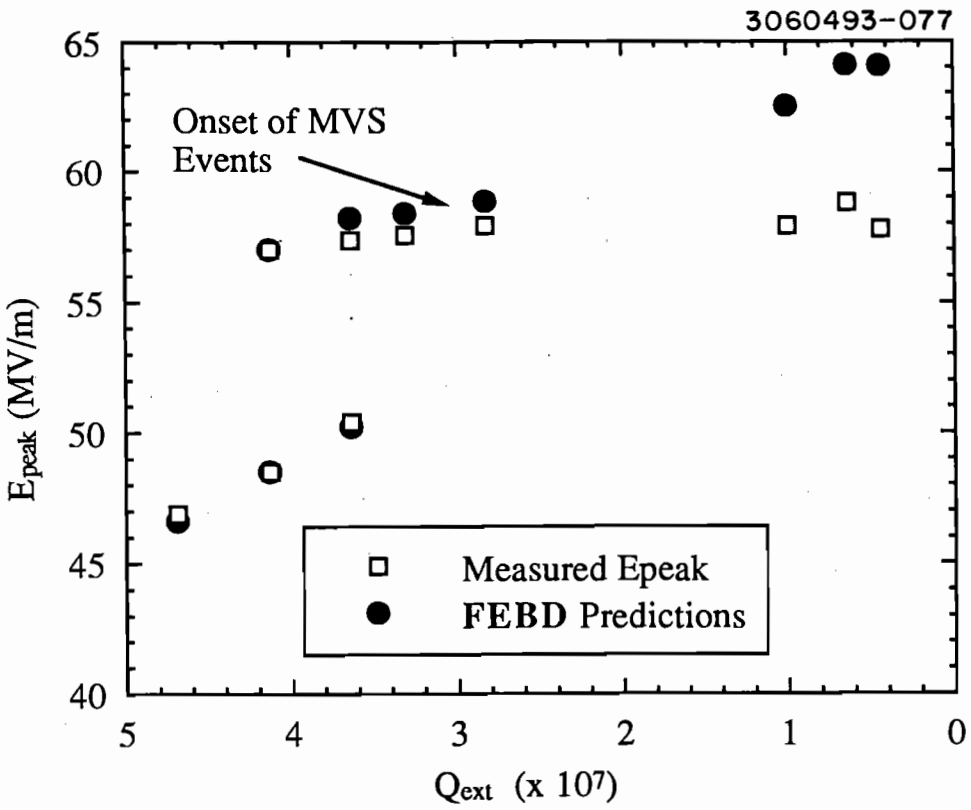

Figure 6.9. Comparison of measured and predicted E_{peak} during HPP on a nine-cell cavity. Note the agreement until MVS events are encountered.

Another significant result is obtained by examining to what end the power is being used during the HPP processing. Let us examine the dissipated power during HPP on a nine-cell cavity, with incident power P_{inc} = 200 kW. Figure 6.10 is a plot of the dissipated power in the cavity, and in each cavity loss mechanism, as a function of time. Clearly the dominant power dissipation mechanism is the thermal breakdown, responsible for 95% of the power being dissipated in the cavity. We find that of the 200 kW available, less than 5 kW are actually being coupled into field emission. The implications of this result and possible methods of avoiding it are discussed below in Section 6.3.6.

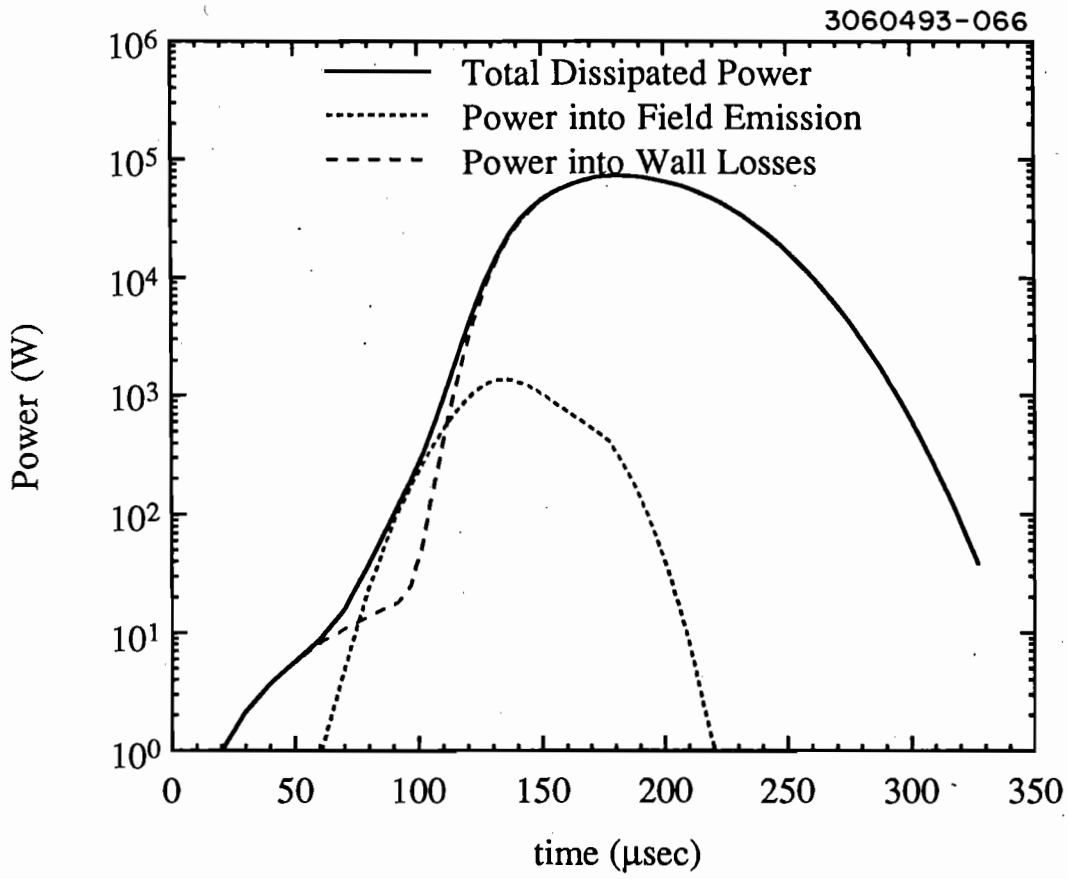

Figure 6.10. Dissipated power into all loss mechanisms plotted as a function of time during HPP on a nine-cell cavity. Incident power was 200 kW. Note the dominance of normal conducting wall losses.

6.3.5. Further Predictions of ***FEBD***

Further interesting results are gained by further examination of single cell results. In all single cell experiments, the maximum power used during HPP processing was 50 kW. In all of these experiments, the CW performance stopped improving at or below this level, therefore increased power was never attempted. Investigation of powers up to 200 kW with **FEBD** indicate that based on this model, and the thermal limitations encountered, the additional power will increase achieved fields to near E_{peak}

= 90 MV/m, which corresponds to a surface magnetic field of H_{peak} = 2070 Oe, which is higher than ever achieved with a superconducting cavity, even under pulsed conditions. This investigation could also allow for exploration of the superheating limit (see section 1.1.2.), which has important bearing on the ultimate limits of SRF technology.

6.3.6. The Importance of Avoiding Thermal Limitations When Possible

The results of Chapter 3 clearly showed that FE processing success is determined by attained electric field. From this chapter, we can add that maximizing electric field in turn maximizes the power being coupled into field emission (equation 6-4c). The results of **FEBD** clearly show, however, that in the 3 GHz cavities, the available power was being wasted in thermal breakdown processes. In section 6.3.4, we showed that in a nine-cell experiment where we couple nearly all of 200 kW into the cavity, only a maximum of 5 kW of this power was being coupled into field emission, and thus into processing. Similarly, single-cell cavities were subjected to as much as 50 kW incident power, yet this analysis indicates that a maximum of a few kilowatts were dissipated in FE. Finally, the same behavior is apparent in the two-cell cavity, which while subjected to as much as 100 kW incident power, dissipated only 1 to 2 kW in FE.

Interestingly, the power coupled into field emission is in reasonable agreement with the power levels required for significant field emission processing, as described in Section 5.2.2. We found that success in processing required a few hundred to a few thousand watts of power. Thus we see that if we can avoid the thermal breakdown phenomena, significantly more power would be available for processing.

There are two primary methods of removing the thermal breakdown limitation: 1) use of a different cavity geometry to reduce the ratio of

magnetic fields to electric fields, 2) use of lower RF frequency, and 3) improvement of thermal conductivity (or improved *RRR*).

Use of a different cavity shape was clearly shown to be successful in the case of cavity W3C2-1. With its reduced H_{peak}/E_{peak} ratio, this cavity was processed to peak electric fields as high as 100 MV/m without thermal breakdown, and as high as 113 MV/m with thermal breakdown. The results were an effectively emission free surface up to E_{peak} = 65 MV/m, and maximum E_{peak} = 100 MV/m, the highest CW field ever reached in an SRF accelerating cavity.

Use of a lower frequency would reduce the thermal breakdown problem in two ways. 1) The reduced RF frequency of the cavity gives a lower BCS surface resistance (See Chapter 1), thus lowering the overall dissipated power in the cavity. 2) The surface area of a cavity varies as the inverse square of the RF frequency. **FEBD** has shown that in order for thermal breakdown to occur, the normal conducting region must grow to roughly 5% of the entire RF surface, therefore the larger RF surface of lower frequency cavities requires a longer time to reach a breakdown condition. (**Transient_HEAT** results indicate that the expansion velocity of normal conducting regions is roughly constant for frequencies between 1 and 3 GHz.) The disadvantages of lower RF frequencies are the increased physical size of all equipment, and the need for increased power, which varies with the inverse cube of the frequency. Several experimental programs have now been started to explore the lower frequency option to reduce thermal limitations to HPP.[73],[74]

Increase in *RRR* would also reduce the thermal breakdown problem in two ways. 1) The increased thermal conductivity of the bulk material would increase the field at which the breakdown is initiated. 2) Higher

thermal conductivity would also decrease the expansion velocity of the normal conducting region, since the dissipated heat would be conducted away without as much temperature rise, as with lower *RRR* material. Higher purity cavities are currently being investigated at many laboratories. In addition, two single-cell cavities with *RRR* = 700 are presently awaiting testing with the HPP apparatus.

CHAPTER 7: CONCLUSIONS AND REMARKS

7.1. Effectiveness of HPP Processing

The HPP experiments were initiated with the primary intention of investigating high power RF processing as a means of reducing field emission loading in superconducting cavities. Based on the results described in Chapter 3 of this dissertation, HPP Processing is a viable means of reducing field emission in SRF cavities. Attainable peak fields and accelerating gradients were increased up to 100% compared to before high power processing. A solid statistical data set was obtained showing the effectiveness of HPP in single-cell, two-cell, and nine-cell cavities.

Processed surfaces have been shown to be durable, in that the effects of processing are not lost when the cavity is exposed to filtered air. Furthermore, HPP processing has been shown to be an effective method of regaining cavity performance following exposure to unfiltered air (e.g. vacuum accidents), a known cause of field emission.

The strongest example of the capabilities of HPP processing was the achievement of the highest CW surface electric field ever sustained in a superconducting accelerating cavity, 100 MV/m in the two-cell cavity W3C2-1. Prior to HPP, the cavity was limited to a peak electric field of 60 MV/m. During processing, surface fields reached 113 MV/m. The final accelerating gradient was 34 MV/m, also a record for an SRF cavity.

7.2. Determining Characteristics of HPP Processing

Achieved peak field during HPP processing is the best predictor of the success of processing. In Chapter 3, plots of maximum CW field and CW field emission thresholds following processing clearly show the correlation between processing field and subsequent CW performance.

The major difference in HPP processing as compared with CW processing is the available power, and the ability to couple all of this power into the cavity. Analysis of processing phenomena showed that the Q of the cavity drops as much as four orders of magnitude during processing. In order to use the available power, the input coupler must be able to couple the power into the cavity under these extreme conditions.

Thermal breakdown was the primary limitation to the HPP experiments. Several methods of avoiding this limit were suggested, including improved thermal conductivity, lower RF frequency, and reduced magnetic field to electric field ratio by altering cavity geometry. It was with the last method, reduced magnetic field, that the record performance of two-cell cavity W3C2-1 was achieved.

In spite of the thermal breakdown limit, we found that the CW thermal breakdown field could be surpassed by as much as 20 MV/m (40%), or 460 Oe under pulsed conditions. Under pulsed conditions, single-cell cavities reached a new record surface magnetic field of 1650 Oe.

The ability of cavities to exceed CW breakdown fields under pulsed conditions was explained with a simple model of a propagating normal conducting region on the superconducting surface, as described in Chapter 6. This model also predicts that under pulsed conditions with all available power, single-cell cavities may challenge the theoretical superheating critical magnetic field of niobium (2300 Oe).

7.3. Advances in Understanding the Mechanism of RF Processing

Correlations between thermometry and RF surface features located in the Scanning Electron Microscope indicate that the mechanism of RF processing involves an explosive emission process. Similar to DC

explosive emission experiments, RF processing involves an explosive event brought on by intense field emission current. The RF processing event leaves a crater as evidence of its occurrence. The net effect of the event is reduced emission current from the emitter. Investigations also showed that the RF processing mechanism is the same in HPP processing and in rare, low power RF processing events.

Analysis of the thermometry data indicates that processing success is directly related to the ability to induce the emitter to produce sufficient current (approximately 1 mA) for the explosive event to occur. This is consistent with the correlation between processing success and magnitude of field reached during processing. The increasing electric field is necessary to induce higher currents from the emitters for processing.

Analysis of RF processed cavities in the SEM also solidified the link between RF surface contaminations and field emission. Contaminant materials were found in more than half of the crater regions created by HPP processing events. The contaminant elements included indium, copper, iron, chromium, carbon, and titanium. Many of these contaminants can be traced to stages of cavity preparation, indicating possible gains in cavity performance with further improvement of techniques.

7.4. Looking Ahead: Further Work, Different Frequencies

The most tangible motivation for the HPP experiments is the proposed TESLA[1] (TeV Superconducting Linear Accelerator), a 1 TeV center of mass electron positron linear collider. Design studies[1] indicate that accelerating gradients of at least 20 MV/m are necessary to make this project economically feasible. The results of the HPP experiments indicate that high power RF processing is a very promising technique for producing

this gradient. The studies of durability of processed surfaces and vacuum accident recovery further demonstrate the usefulness of high power processing for a project such as TESLA.

Investigation of the limitations of the HPP experiments have clearly shown the need to avoid thermal processes as much as possible in future work. These results, along with other economic and power considerations have led to the present design choice of 1.3 GHz as the operating frequency of TESLA.[1] Initial high power processing experiments have begun on 1.3 GHz cavities. Initial tests already show promising results.[74]

APPENDIX A: USEFUL TERMS AND EQUATIONS

A.1. Definition of Mathematical Symbols and Relationships

In the description of the HPP experimental program, we use a large number of symbols. Table A-1 defines all terms associated with the HPP experimental program. Table A-2 develops several useful equations. We will return to these definitions many times. Derivations of many of the equations and relationships may be found in the previously mentioned M.S. Thesis[61], or any of several books on microwave measurements.[75],[76]

TABLE A-1. DEFINITION OF SYMBOLS FOR THE HPP EXPERIMENTAL PROGRAM

Independent or Measured Variables

Symbol	Definition	Units
ν	Resonant RF frequency of the cavity	Hz
U	Energy stored in the RF fields of the cavity	J
P_{inc}	Incident power on the cavity at the input coupler	W
P_{ref}	Reflected power from the cavity at the input coupler	W
P_{diss}	Power dissipated the cavity	W
P_t	Power transmitted to RF monitor probe	W
P_e	Power emitted to input coupler when $P_{inc} = 0$ (Primarily used when P_{inc} is modulated)	W
P_{RF}	Incident power on cavity during HPP processing	W
t_{RF}	RF pulse length during HPP processing	s
f_{rep}	Repetition rate of HPP processing pulses	s^{-1}
E_{peak}	Peak surface electric field in the cavity	MV/m
H_{peak}	Peak surface magnetic field in the cavity	Oe
E_{acc}	Accelerating gradient in the cavity	MV/m

TABLE A-2. DERIVED QUANTITIES

Symbol	Definition	Units	Equation
ω	Angular frequency of the cavity	s^{-1}	
	$\omega = 2\pi\nu$		(A-1)
Q_0	Unloaded quality factor of the cavity	none	
	$Q_0 = \frac{\omega U}{P_{diss}}$		(A-2)
Q_{ext}	Quality factor of the input coupler	none	
	$Q_{ext} = \frac{\omega U}{P_e} = \frac{P_{diss}}{P_e} Q_0$		(A-3)
Q_t	Quality factor of monitor probe	none	
	$Q_t = \frac{\omega U}{P_t} = \frac{P_{diss}}{P_t} Q_0$		(A-4)
β	Input coupling factor	none	
	$\beta = \frac{Q_0}{Q_{ext}} = \frac{P_e}{P_{diss}}$		(A-5)
β_t	Input coupling factor	none	
	$\beta_t = \frac{Q_0}{Q_t} = \frac{P_t}{P_{diss}}$		(A-6)
Q_L	Loaded quality factor of the cavity	none	
	$\frac{1}{Q_L} = \frac{P_{total}}{\omega U} = \frac{1}{\omega U}(P_{diss} + P_e + P_t)$		
	$\frac{1}{Q_L} = \left(\frac{1}{Q_0} + \frac{1}{Q_{ext}} + \frac{1}{Q_t}\right) = \frac{1}{Q_0}(1 + \beta + \beta_t)$		
	$Q_L = \frac{Q_0}{1+\beta+\beta_t} \approx \frac{Q_0}{1+\beta}$ *for* $\beta_t \ll 1$		(A-7)

TABLE A-2. DERIVED QUANTITIES (CONTINUED)

Symbol	Definition	Units	Equation
k_e	Ratio of peak surface electric field to square root of cavity stored energy	MV/m/(J$^{1/2}$)	
	$k_e = \frac{E_{peak}}{\sqrt{U}}$		(A-8)
k_h	Ratio of peak surface magnetic field to square root of cavity stored energy	Oe/(J$^{1/2}$)	
	$k_h = \frac{H_{peak}}{\sqrt{U}}$		(A-9)
τ	Time constant of the cavity	s	
	$\tau = \frac{Q_L}{\omega}$		(A-10)

TABLE A-3. OTHER USEFUL RELATIONSHIPS

Relationship (all assuming $\beta_t \ll 1$)	Equation
Dissipated Power Related to Incident Power, Given Input Coupling	
$P_{diss} = \frac{4\beta}{(1+\beta)^2} P_{inc}$	(A-11)
Reflected Power Related to Incident Power, Given Input Coupling	
$P_{ref} = \left(\frac{1-\beta}{1+\beta}\right)^2 P_{inc}$	(A-12)
Input Coupling β as a Function of Incident and Reflected Power	
$\beta = \frac{1 \mp \rho}{1 \pm \rho}$ where $\rho = \sqrt{\frac{P_{ref}}{P_{inc}}}$	(A-13)
Emitted Power Related to Incident Power, Given Input Coupling, Under Modulated Conditions	
$P_e = \beta P_{diss} = \frac{4\beta^2}{(1+\beta)^2} P_{inc}$	(A-14)

TABLE A-3. OTHER USEFUL RELATIONSHIPS (CONTINUED)

Relationship (all assuming $\beta_t \ll 1$)	Equation
Input Coupling β as a Function of Incident and Emitted Power, Under Modulated Conditions	$$\beta = \frac{1}{2\sqrt{\frac{P_{inc}}{P_e}} - 1}$$ (A-15)
Transmitted Power Related to Incident Power, Given Input and Transmitted Coupling Factors	$$P_t = \beta_t P_{diss} = \frac{4\beta\beta_t}{(1+\beta)^2} P_{inc}$$ (A-16)
Transient Peak Electric Field during Cavity Fill	$$E_{peak}(t) = E_{EQM}\left(1 - \exp\left(\frac{-t}{2\tau}\right)\right)$$ (A-17)
Steady State (Equilibrium) Peak Electric Field, Given Input Power and Coupling	$$E_{EQM} = k_e\sqrt{U_{EQM}} = k_e\sqrt{\frac{P_{diss}Q_0}{\omega}} = k_e\frac{2\beta}{1+\beta}\sqrt{\frac{P_{RF}Q_{ext}}{\omega}}$$ (A-18)
Transient Stored Energy during Cavity Fill	$$U(t) = U_{EQM}\left(1 - \exp\left(\frac{-t}{2\tau}\right)\right)^2$$ (A-19)
Decay of Cavity Stored Energy, when $P_{inc} = 0$	$$U_{decay}(t) = U_{(t=0)}\exp\left(\frac{-t}{\tau}\right) = U_{(t=0)}\exp\left(\frac{-\omega t}{Q_L}\right)$$ (A-20)

APPENDIX B: HISTORY OF HPP EXPERIMENTS

Cavity S3C1-1

Date	4.2K Q_0	max Q_0	Max. CW Field E_{peak} (MV/m)	Q_0	Limit. Mech.	HPP Processing max P_{RF} (kW)	max E_{peak} (MV/m)
	5 mins BCP						
08/01/89	6.4e7	7.6e8	NA	NA			
		1.2e9	22.7	4.2e8			
	Low power processed Multipacting, quit due to lack of Helium						
08/02/89	7.9e7	1.1e9	24.0	3.9e8	FE	30	49
			26.4	6.4e8	BD		
	Cut open for SEM examination						

Cavity S3C1-2

Date	4.2K Q_0	max Q_0	Max. CW Field E_{peak} (MV/m)	Q_0	Limit. Mech.	HPP Processing max P_{RF} (kW)	max E_{peak} (MV/m)
	Yttrification, 5 mins BCP						
06/26/89	8.1e7	7.6e8			He		
06/27/89	9.4e7	1.6e9	9.3	8.5e8	'heating' phenomena		
	Methanol rinse						
07/18/89	6.4e7	1.0e9	19.8	2.1e8	FE ,He		
07/19/89	8.0e7	9.7e8	19.5	2.0e8	FE	40	34
			20.1	8.0e8	BD		
	10 mins BCP						
02/16/90	NA	3.0e8	NA	NA	bad Q, no further testing		
	10 mins BCP						
04/19/90	6.6e7	7.5e8	27.8	6.7e8	Q-short beam tubes		
	2 mins BCP						
04/30/90	6.6e7	2.7e9	28.1	3.6e8	FE	no HPP	
	spool pieces to lengthen beam tubes; no x-rays						
	1 min BCP, 2 hours UHV 900 C						

Cavity S3C1-2 (continued)

Date	4.2K Q_0	max Q_0	Max. CW Field E_{peak} (MV/m)	Q_0	Limit. Mech.	HPP Processing max P_{RF} (kW)	max E_{peak} (MV/m)
05/29/90	7.8e7	2.6e10	28.2	9.1e9	X-ray	3	47
		2.5e10	32.4	8.7e9	X-ray	10	57
		2.1e10	38.6	5.6e9	FE	50	62
		2.1e10	43.7	2.9e9	FE		
	room temp cycle, no vacuum break						
06/01/90	7.4e7	2.5e10	48.4	1.5e9	FE	40	62
		1.6e10	50.2	1.6e9	BD	40 w/He	40
		7.27e9	33.7	4.5e8	HPP w/He damage		
	1 hr HNO3, 2 mins 1:1:2 BCP						
05/29/91	7.50e7	7.5e9	44.1	1.5e9	FE	15	59
		7.5e9	49.7	1.2e9	BD	30	59
		7.8e9	50.2	1.5e9	BD		
	cut open for SEM examination						

Cavity S3C1-3

Date	4.2K Q_0	max Q_0	Max. CW Field E_{peak} (MV/m)	Q_0	Limit. Mech.	HPP Processing max P_{RF} (kW)	max E_{peak} (MV/m)
	8 mins BCP						
11/16/89	NA	3.5e9			FE-Amp probs, no HPP		
11/17/89	NA	2.6e9	22.6	3.2e8	FE		
	welds ground, 10 mins BCP						
12/04/89	NA	9.8e9	32.9	3.5e8	FE		
12/15/89	NA	8.0e8			post UV,bad vac		
	2 mins BCP						
01/08/90	NA	6.0e9	37.0	1.9e8	FE		
02/06/90	9.0e7	1.00e10	28.4	1.8e9	15W Q damage		

Cavity S3C1-3 (continued)

Date	4.2K Q_0	max Q_0	Max. CW Field E_{peak} (MV/m)	Q_0	Limit. Mech.	HPP Processing max P_{RF} (kW)	max E_{peak} (MV/m)
02/07/90	NA	1.50e9	27.5	4.6e8	FE	3	35
		1.20e9	27.5	5.2e8	BD	10	42
		1.10e9	27.0	8.4e8	BD		
	10 mins BCP						
03/26/90	8.0e7	7.1e10	55.3	2.2e9	FE		
	room temp cycle						
03/28/90	9.5e6			Q damaged			
	10 mins BCP						
04/10/90	6.0e7	1.3e9		didn't raise, to save Q			
	acid accident, cavity destroyed						

Cavity S3C1-4

Date	4.2K Q_0	max Q_0	Max. CW Field E_{peak} (MV/m)	Q_0	Limit. Mech.	HPP Processing max P_{RF} (kW)	max E_{peak} (MV/m)
	8 mins BCP						
11/27/89	NA	1.3e10	26.2	6.5e9	FE - switch		
		4.0e9	23.3	7.9e8	Q dam.	no HPP	
	10 mins BCP						
12/29/89	NA	4.3e9	18.3	4.2e8	bad vac	no HPP	
	2 mins BCP						
01/22/90	NA	9.6e9	34.0	1.6e9	FE 1	no HPP	
	rinsed with methanol						
03/16/90	4.5e7	NA	NA	NA	bad Q, HPP at 4.2K		
	5 mins BCP						
04/04/90	7.7e7	1.3e10	10.0	1.0e10	Dingle-Berry BD		
	1 hour nitric acid, 5 mins BCP						
04/13/90	7.0e7	2.0e10	29.6	3.7e9	low Q-no HPP		

Cavity S3C1-4 (continued)

Date	4.2K Q_0	max Q_0	Max. CW Field E_{peak} (MV/m)	Q_0	Limit. Mech.	HPP Processing max P_{RF} (kW)	max E_{peak} (MV/m)
	3 mins BCP						
04/23/90	8.0e7	3.4e9	22.1	8.5e8	X-rays	10	13
			24.2	1.1e9	X-rays	12	30
			31.9	6.8e8	X-rays	15	56
		2.6e9	35.6	5.2e8	FE		
	5 mins BCP						
05/02/90	2.1e7	NA	NA	NA	bad Q, no further testing		
	1 min BCP, 2 hours 900 C, room air leak, 45 s BCP, vac leak, 45 s BCP, 2 min 1:1:2 BCP						
05/01/91	7.9e7	1.9e10	40.8	2.3e9	low power test only		
	cut open for SEM examination						

Cavity S3C1-5

Date	4.2K Q_0	max Q_0	Max. CW Field E_{peak} (MV/m)	Q_0	Limit. Mech.	HPP Processing max P_{RF} (kW)	max E_{peak} (MV/m)
	10 mins BCP						
05/08/90	8.0e7	4.5e9	15.7	4.0e8	Dingleberry BD		
	10 mins BCP						
05/21/90	4.0e7	NA	NA	NA	lowQ	no HPP	
	1 min BCP, 2 hours 900 C						
07/11/90	7.8e7	4.1e9	36.8	8.9e8	FE	2.5	35
		3.4e9	35.2	1.7e9	FE	10	46
		3.6e9	36.6	2.2e9	BD	45	56
		3.5e9	35.0	2.6e9	BD	45	56
		3.4e9	37.3	2.7e9	BD		
	1 min BCP, 4 hours 1400 C with Ti, 10 mins outside BCP						
11/27/90	6.98e7	3.90e9	35.5	2.8e9	BD		
	room temp cycle, no vacuum break; 1st test of Temp Map System						

Cavity S3C1-5 (continued)

Date	4.2K Q_0	max Q_0	Max. CW Field E_{peak} (MV/m)	Q_0	Limit. Mech.	HPP Processing max P_{RF} (kW)	max E_{peak} (MV/m)
12/15/90	7.60e7	6.60e9	34.8	5.4e9	bad Q_0 from iron rods		
	30 mins nitric acid, 2 mins BCP						
05/04/92	7.50e7	1.0e10	31.7	1.7e9	FE	1.8	49
		8.7e9	33.6	1.5e9	FE	3	54
		8.4e9	36.4	1.5e9	FE		
	one major processing event; cut open for SEM examination						

Cavity S3C1-6

Date	4.2K Q_0	max Q_0	Max. CW Field E_{peak} (MV/m)	Q_0	Limit. Mech.	HPP Processing max P_{RF} (kW)	max E_{peak} (MV/m)
	12 mins BCP						
05/08/90	7.0e7	7.8e8	27.0	3.1e8	bad Q- no HPP		
	1 min BCP, 2 hours 900 C, 1 min BCP, 4 hours 1400 C with Ti, 10 mins outside BCP						
10/23/90	1.0e8	3.6e9	22.7	4.2e8	FE	10	47
		5.7e9	32.3	3.5e8	FE	30	57
		4.4e9	35.5	1.0e9	BD		
	30 mins LCP						
11/01/90	5.8e7	5.5e9	46.0	5.8e8	FE	10	57
		5.5e9	46.5	9.6e8	BD	35	67
		3.8e9	45.7	5.4e9	BD	35	68
			FE switch at 41 MV/m				
		3.3e9	46.5	6.4e8	BD		
			switch was irreversible				
	1 hr nitric; 2 x 45sec 1:1:1 BCP; 2 x 45sec 1:1:2 BCP						
11/18/91	7.0e7	3.9e10	58.8	1.4e9	BD	10	66.0
		2.5e10	58.3	1.3e9	BD		
	1 hr nitric; 2 x 60sec 1:1:2 BCP						
12/12/91	7.8e7	3.3e10	55.5	1.1e9	GTI; no FE		

Cavity S3C1-7

Date	4.2K Q_0	max Q_0	Max. CW Field E_{peak} (MV/m)	Q_0	Limit. Mech.	HPP Processing max P_{RF} (kW)	max E_{peak} (MV/m)
12/12/91	7.8e7	3.3e10	55.5	1.1e9	BD		
	Yttrification, 8 min 1:1:1 BCP prior to equator weld, 4 mins 1:1:2 BCP after weld						
01/13/91	7.7e7	8.4e9	54.3	1.7e9	BD-GTI	No HPP	
	1 min 1:1:2 BCP						
01/28/91	7.4e7	7.2e9	54.8	1.6e9	FE	10	NA
		5.7e9	52.9	1.5e9	FE	80	NA
		4.3e9	54.1	1.3e9	BD		
	Limited, bad Pt signal- all HPP E's uncertain						
	2 mins 1:1:2 BCP						
02/13/91	7.8e7	1.5e10	40.1	2.3e9	FE	3	56
		1.4e10	47.3	2.4e9	FE	25	70
		1.4e10	51.8	2.0e9	FEBD	25	70
		1.4e10	54.6	9.4e8	BD		
	room temp cycle, no vacuum break						
02/25/91	7.5e7	1.3e10	52.2	1.6e9	BD	6	60
		1.4e10	48.2	3.1e9	FE	30	67
		1.3e10	53.5	1.2e9	BD		
	4 mins 1:1:2 BCP						
03/19/91	7.4e7	1.4e10	43.5	2.4e9	FE	'switch'	
		1.2e10	31.9	1.9e9	FE-2	10	61
		1.4e10	44.2	2.1e9	FE	18	69
		1.1e10	50.3	1.6e9	BD		
	room temp cycle, no vacuum break						
03/27/91	7.0e7	1.4e10	49.6	1.1e9	FE	15	68
		1.4e10	51.0	1.3e9	BD	30	70
		1.4e10	52.7	1.3e9	BD	30	72
		1.3e10	51.9	1.6e9	BD		
	cut open for SEM examination						

Cavity S3C1-8

Date	4.2K Q_0	max Q_0	Max. CW Field E_{peak} (MV/m)	Q_0	Limit. Mech.	HPP Processing max P_{RF} (kW)	max E_{peak} (MV/m)
	Yttrification, 8 min 1:1:1 BCP prior to equator weld, 4 mins 1:1:2 BCP after weld						
02/06/91	7.8e7	7.4e9	35.4	5.6e9	BD	no HPP	
	4 mins 1:1:2 BCP, vacuum leak; 4 mins 1:1:2 BCP, vacuum leak						
02/08/92	6.0e7	1.4e10	43.0	5.4e9	BD	2	55
		1.4e10	43.2	6.5e9	BD	3	58
		1.3e10	43.2	6.0e9	BD	5	61
		1.3e10	43.2	6.6e9	BD	25	65
		1.0e10	44.2	6.2e9	BD		
	cut open for SEM examination						

Cavity S3C1-9

Date	4.2K Q_0	max Q_0	Max. CW Field E_{peak} (MV/m)	Q_0	Limit. Mech.	HPP Processing max P_{RF} (kW)	max E_{peak} (MV/m)
	Russian high RRR Nb, 8 min 1:1:1 BCP prior to equator weld, 4 mins 1:1:2 BCP after weld						
03/12/92	8.0e7	1.7e10	34.0	8.4e8	BD		
	30 mins Nitric; 3 mins 1:1:2 BCP						
04/07/92	7.3e7	2.0e10	47.7	7.6e9	BD @Eq weld overlap		

Cavity S3C9-1

Date	4.2K Q_0	max Q_0	Max. CW Field E_{acc} (MV/m)	Q_0	Limit. Mech.	HPP Processing max P_{RF} (kW)	max E_{peak} (MV/m)
	10 mins BCP						
07/03/90	4.60e7				bad Q		
	45 mins Nitric acid on flanges, 2 hours 700 C						

Cavity S3C9-1 (Continued)

Date	4.2K Q_0	max Q_0	Max. CW Field E_{acc} (MV/m)	Q_0	Limit. Mech.	HPP Processing max P_{RF} (kW)	max E_{peak} (MV/m)
07/18/90	8.0e7	8.0e8	6.15	2.0e8	low Q	40	30
		8.0e8	6.25	5.0e8	low Q		
	8 mins 1:1:2 BCP, 2 hrs 900 C						
08/29/90	8.7e7	1.6e10	9.62	1.5e9	FE	10	33
		8.2e9	11.6	4.3e9	FE	20	41
		7.2e9	12.7	5.1e9	FE	40	47
		6.2e9	10.7	5.8e9	He		
08/30/90	7.9e7	7.7e9	14.8	5.8e9	BD	90	45
		7.21e9	14.4	3.2e9	FE		
	Exposure to clean Air, Methanol Rinse						
10/03/90	7.8e7	7.3e9	7.21	5.1e8	FE	10	18
		8.8e9	7.11	4.9e8	FE	20	35
		1.2e10	8.80	1.6e9	FE	40	20
		8.6e9	8.99	1.0e9	WG Vacuum Bad		
Sent to Wuppertal for HT with Titanium protection, followed by low power test. Returned- tuned; 1 hr nitric; 2 x 1 min 1:1:2 BCP; 2hrs cont. flow water-accident; tuned; 1 min 1:1:2 BCP 2 hrs cont. flow water rinse; mount							
07/02/91	7.4e7	2.1e10	14.7	2.3e9	FE	25	58
		2.2e10	17.3	3.3e9	FE	40	61
		1.5e10	20.0	4.3e9	He		
07/03/91	7.4e7	2.1e10	20.2	4.2e9	FE	15	62
		2.2e10	20.0	4.2e9	FE-WG window damaged		
	1 hr nitric; 2 mins 1:1:2 BCP; 2 hrs water						
07/23/91	7.0e7	6.6e9	11.8	1.6e9	FE	40	43
		5.4e9	13.8	3.3e9	FE	80	50
		5.0e9	17.3	3.0e9	FE	80	52
		4.9e9	17.8	3.1e9	FE	130	53
		4.6e9	17.8	3.1e9	FE	140	57
		4.6e9	18.9	3.4e9	FE		
	1 hr nitric; 2 mins 1:1:2 BCP; 2 hrs 900 C- leak						
	1 hr nitric; tune; 2 hrs water rinse						

Cavity S3C9-1 (Continued)

Date	4.2K Q_0	max Q_0	Max. CW Field E_{acc} (MV/m)	Q_0	Limit. Mech.	HPP Processing max P_{RF} (kW)	max E_{peak} (MV/m)
09/04/91	7.5e7	7.9e9	15.1	2.3e9	FE	5	37
		6.3e9	16.4	4.3e9	BD	50	47
		5.1e9	15.1	4.0e9	BD		
	1 hr nitric; 3 x 45 sec 1:1:2 BCP; 3 hrs water; tune						
09/18/91	7.5e7	1.2e10	12.4	6.4e9	FE-switch no HPP yet		
		1.2e10	11.1	1.1e9	FE	6	41
		1.5e10	15.3	2.1e9	FE	12	54
		1.2e10	15.8	2.4e9	FE	35	57
09/19/91	7.5e7	1.2e10	16.7	2.5e9	FE	50	58
		1.2e10	16.6	2.5e9	FE		
	room temp cycle; no vacuum break						
10/10/91	7.5e7	1.4e10	17.4	2.7e9	FE	65	57
		1.3e10	17.9	2.9e9	FE	95	58
		1.3e10	17.1	2.6e9	FE	150	59
		1.2e10	17.6	2.7e9	FE		
	room temp cycle; cavity bled with filtered air						
10/21/91	7.5e7	1.4e10	17.7	2.8e9	FE	65	59
		1.3e10	18.9	3.2e9	FE	145	58
		1.3e10	18.1	3.0e9	FE		

Cavity S3C9-5

Date	4.2K Q_0	max Q_0	Max. CW Field E_{acc} (MV/m)	Q_0	Limit. Mech.	HPP Processing max P_{RF} (kW)	max E_{peak} (MV/m)
	Yttrification, 8 min 1:1:1 BCP prior to equator weld, 2 mins 1:1:2 BCP after weld						
02/28/92	7.5e7	1.00e9			bad Q		
	30 mins nitric; 12 mins 1:1:2 BCP; 2 hrs 900 C						
03/17/92	7.5e7	4.6e9	6.76	8.2e8	FE	21	24
		3.6e9	8.33	5.7e8	FE	50	30
		4.50e9	9.84	1.3e9	FE-HPP behavior strange		
	30 mins nitric; 10 mins 1:1:2 BCP; 2 hrs 900 C						

Cavity S3C9-5 (Continued)

Date	4.2K Q_0	max Q_0	Max. CW Field E_{acc} (MV/m)	Q_0	Limit. Mech.	HPP Processing max P_{RF} (kW)	max E_{peak} (MV/m)
04/16/92	7.3e7	5.4e9	6.31	3.3e8	FE	10	25
		6.10e9	8.35	3.1e8	FE	NA	NA
		6.30e9	12.6	1.9e9	FE	95	48
		6.50e9	13.3	3.2e9	FE		
	room temp cycle; no vac break						
04/24/92	7.4e7	6.4e9	14.8	2.6e9	HPP	100	NA
	Pt measurement problems						
	Pt probs fixed; 30 mins Nitric; 2 x 90 sec 1:1:2 BCP; no heat; slight vac accident!						
05/13/92	8.0e7	8.1e9	15.2	2.3e9	FE	90	58
		1.2e10	18.2	2.8e9	FE		
	room temp cycle; another vacuum accident						
05/21/92	8.3e7	1.9e10	15.3	4.6e9	FE	100	57
		1.8e10	16.9	4.2e9	FE		
	room temp cycle; no vacuum break						
09/03/92	8.e7	2.0e10	16.4	4.5e9	FE		
	Intentional Vacuum Accident						
09/21/92	7.0e7	1.1e10	8.0	2.0e9	FE	105	42
		1.0e10	14.4	2.0e9			

Cavity W3C2-1

Date	4.2K Q_0	max Q_0	Max. CW Field E_{acc} (MV/m)	Q_0	Limit. Mech.	HPP Processing max P_{RF} (kW)	max E_{peak} (MV/m)
	Yttrification, 8 min 1:1:1 BCP prior to equator weld, 2.5 mins 1:1:2 BCP after weld						
12/03/91	8.4e7	2.0e10	54.0	1.14e10	BD		
	1 hr nitric; 4 min 1:1:2 BCP						
12/08/91	7.8e7	2.0e9	25.1	4.6e8	BD; Q virus		

Cavity W3C2-1 (Continued)

Date	4.2K Q_0	max Q_0	Max. CW Field E_{peak} (MV/m)	Q_0	Limit. Mech.	HPP Processing max P_{RF} (kW)	max E_{peak} (MV/m)
	30 mins nitric; 6 mins 1:1:2 BCP; 2 hrs 900 C						
01/13/92	7.4e7	1.2e10	58.1	2.0e9	FE	5	87
		1.2e10	73.4	1.4e9	FE	50	99
		1.2e10	75.6	1.4e9	FE	130	103
		1.0e10	75.2	1.5e9	FE, Power		
	new 200W TWT; room temp cycle, no vacuum break						
01/28/92	7.7e7	2.0e10	92.8	3.0e8	BD	20	108
		1.3e10	94.8	2.4e8	BD	65	113
		1.4e10	100.6	2.5e8	BD	100	112
		1.4e10	99.8	3.4e8	BD		
	30 mins nitric; 2.5 mins 1:1:2 BCP						
02/18/92	7.5e7	6.0e9	81.5	2.5e9	Power	6	104
		5.6e9	84.4	1.8e9	Power	25	106
		4.9e9	81.6	2.3e9	Test limited by He leak		

APPENDIX C: MULTI-CELL CAVITIES: FIELD FLATNESS AND TUNING

Multi-cell cavities present an extra complication for testing which is not present in single-cell cavities. The individual cells of a multi-cell cavity couple together to form a series of coupled oscillators. The analysis of this problem has been covered in depth in several of the references,[8],[78],[79] and therefore we do not delve deeply into it here. We will limit our description to the practical considerations which must be observed with regards to the measurement of the behavior of a multi-cell cavity.

As in the case of single-cell cavities, we are interested in attaining the highest possible accelerating gradient in the cavity. In a multi-cell cavity, a simple analysis, shows that an n-cell cavity (n identical cells) will split each mode of an equivalent single cell cavity into n modes. A description of this phenomena can be found in References 8 and 79. It is found that the highest accelerating gradient is obtained by operating in the "π" mode (assuming a standing wave structure), where the electric field in adjacent cells of the cavity is oppositely directed. The cell length is chosen such that the particle traverses one cell in one half RF period, thus always experiencing an accelerating force. It is further found that within the π mode, the highest accelerating gradient through the entire cavity is obtained when the peak electric field is the same in each cell, which is termed "Field Flatness."

Measurement of the field flatness is done through what is called a "bead-pull" measurement. In this measurement, the cavity is excited in its π mode, and a small metal bead is pulled along the axis of the cavity. Perturbation theory may be invoked to show that for a small metal bead, the frequency shift is proportional to square of the electric field at the position of the bead. The frequency shift in the π mode is measured as the bead

traverses the cavity, and then the relative strengths of the electric field may be computed from the frequency shift.

Bead pulls were routinely performed before and after all nine-cell RF tests, to insure that the cavity performance was being accurately measured. If the field distribution is not flat, then the relationships used to determine cavity performance during the test (specifically the ratios of stored energy to peak surface fields) must be re-calibrated.

If the field distribution is not flat, then the relative frequency shifts may be used to determine the necessary adjustments to the individual cells of the cavity. The mathematics of this procedure are developed in Reference 79, and computer programs have been developed to implement this theory. On a practical level, we have found that even nine-cell cavities can be tuned to within 10% (in peak electric field) without the computer programs.

Tuning of the cavity to restore field flatness is performed through deformation of the individual cells. If the relative field in a cell is too low, then the cell is lengthened (along the beam axis). If the field is too high, the cell is shortened.

Finally, we briefly discuss the reason for the different shaped end cells of a multi-cell cavity, which was mentioned in section 2.2.1. All interior cells interact with neighbor cells at both irises (see Figure 2.2), whereas the end cells interact with a neighbor cell at one iris, and with the beam tube at the other iris. The end cell geometry is adjusted slightly to compensate for the different boundaries of the end cell, in order to produce a field flat cavity. The mathematical treatment of this phenomena can be found in Reference 79.

APPENDIX D: RESIDUAL RESISTIVITY RATIO (*RRR*) AND ITS MEASUREMENT

The Residual Resistivity Ratio (*RRR*) of niobium is the ratio of the room temperature resistivity to the normal conducting resistivity at $T = 4.2$ K. The *RRR* is a good measure of the impurities in the niobium, as at cryogenic temperatures impurities are the dominant scattering mechanism for the electrons in the normal conducting state. These impurities are a dominant limitation on the thermal conductivity in the superconducting state. An excellent investigation of the thermal characteristics of niobium is available in the Ph.D. dissertation of K. Krafft.[81]

Table D-1[82] lists the theoretical effect that various common impurities will have on the *RRR* of niobium, at a contamimation level of 1 weight part per million.

The thermal conductivity of niobium in the superconducting state at $T = 4.2$ K varies approximately linearly with the *RRR*.[81] The thermal breakdown magnetic field for niobium has been shown both computationally and experimentally[83] to be proportional to the square root of *RRR*.

Commercially available niobium has improved over the last ten to fifteen years[82],[84] from so-called reactor grade niobium, with $RRR \leq 30$, to electron beam melted samples with *RRR* in excess of 250. In addition,

TABLE D-1. THE EFFECT OF COMMON IMPURITIES ON THE *RRR* OF NIOBIUM

Element	RRR for 1 weight ppm
O	5000
N	3900
C	4100
H	1550
Ta	550,000

sources in Russia have recently made available small quantities of niobium with *RRR* in excess of 500.

The *RRR* of a sample of niobium is obtained locally by measuring the resistivity of a small niobium sample, first at room temperature, and then at 4.2 K. At cryogenic temperatures, the sample is forced into the normal conducting state by placing it inside a coil which produces a DC magnetic field. The magnetic field is increased through the critical field, and then the 4.2 K resistivity is obtained by extrapolation of the resistivity versus magnetic field curve to zero applied field. Voltage measurements are made with a low frequency alternating current, in order to avoid the systematic error introduced by contact voltages.

APPENDIX E: ERROR ANALYSIS IN CORRELATION OF RESULTS FROM SEM, THERMOMETRY, AND SIMULATIONS

In this Appendix, we discuss several sources of errors referred to in Chapter 4: (a) the uncertainty in determining the location of features in the SEM, (b) the relative uncertainty between the positioning of the thermometers with respect to the SEM locations, and (c) the effect of small errors or variations on predicted thermometry results (d) the variation in thermometer sensitivities.

The thermometer positions, S values, and SEM X-coordinate positions are shown with a typical S3C cavity in Figure E.1. The inside S coordinate is the distance along the cavity's inner surface from the cavity equator. The outside S coordinate is the distance along the cavity outer wall from the equator (S=0). In the simulations the location of the emitter is defined in terms of the inside S coordinate. The simulations also give the temperature rise at the outside S coordinate which also corresponds to the nominal center of the thermometers.

The SEM X-coordinate is a finely graduated measuring system: each increment in the X-coordinate is equivalent to radial increment of 100 microns. The beam axis, i.e. the axis of cylindrical symmetry (**z** direction), and the radial axis are shown in Figure E.1. The azimuthal coordinate is spanned by the different thermometer boards, placed every 36 degrees.

The locations of centers of thermometers with respect to the SEM X-coordinate system were obtained as follows: A previously examined (and dissected) cavity was marked externally with a scribe at thermometer positions; these marks were then translated to the inside of the cavity by pinching the cavity with a point micrometer at the thermometer center location.

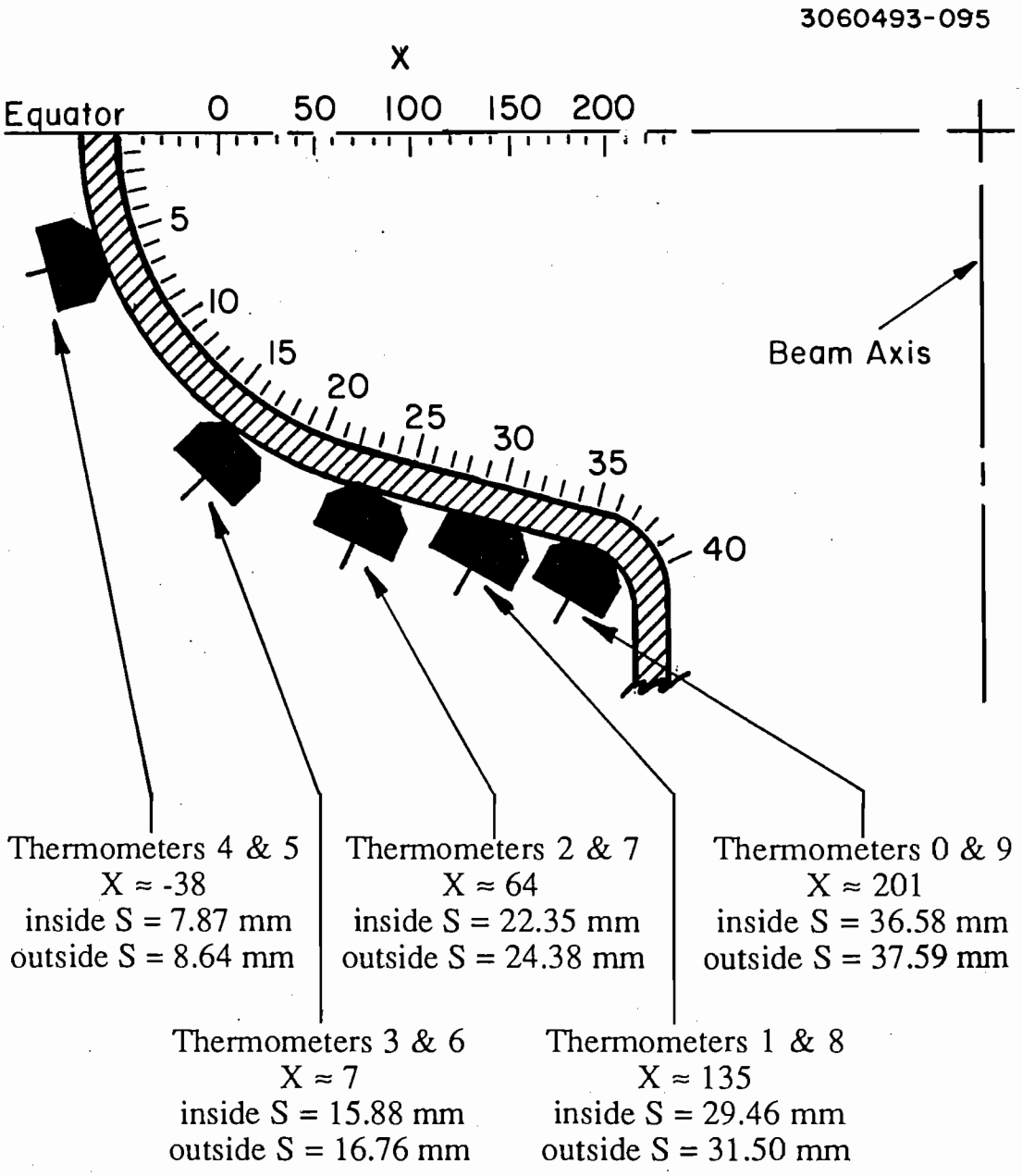

Figure E.1. Geometric correlations between thermometer positions, *S* value on cavity surface, and SEM *X* coordinate. *S* is marked in millimeters.

Finally, this marked half cell was examined in the SEM, and SEM *X*-coordinate positions were determined for each thermometer position. Uncertainty in the position of the marks on this particular half cell with respect to true thermometer position is empirically estimated to be less than 1 mm.

There is another uncertainty in obtaining the "*S*" value for each of the thermometers: The *S* values were obtained by simply measuring position with a flexible ruler. The measured values were then checked against a calculated value, based on cavity shape and thermometer board configuration. Uncertainty in the *S* positions of the thermometers is estimated to be less then 1 mm.

Uncertainty in the measured *S* value as determined by *X*-coordinate is likely less than 500 microns. This accuracy is limited by the resolution of the *X* coordinates, and reproducibility of holder/cavity positioning. Each of the error estimates listed above was obtained by repeating the mounting/dismounting process (of the half-cell in its holder) several times, and measuring the variation in values. Similarly the *S* values of the thermometers were measured several times.

Errors in the quantities discussed above would manifest themselves in a disagreement between the shape of a predicted and measured longitudinal temperature plot. Figure E.2 shows the variation in predicted longitudinal temperature plot with changes only in S_0, the position of the emission site. S_0 changes from -3.70 cm to -3.50 cm in Figure E.2. As can be seen, the shape of the plot changes markedly when the location of a hypothetical emitter changes by approximately 0.04 cm. This is comparable to the typical uncertainty in S_0 value for SEM-located phenomena. Thus, following a processing event, a multiple correlation between position of surface features, trajectory calculations, and a measured change in thermometry

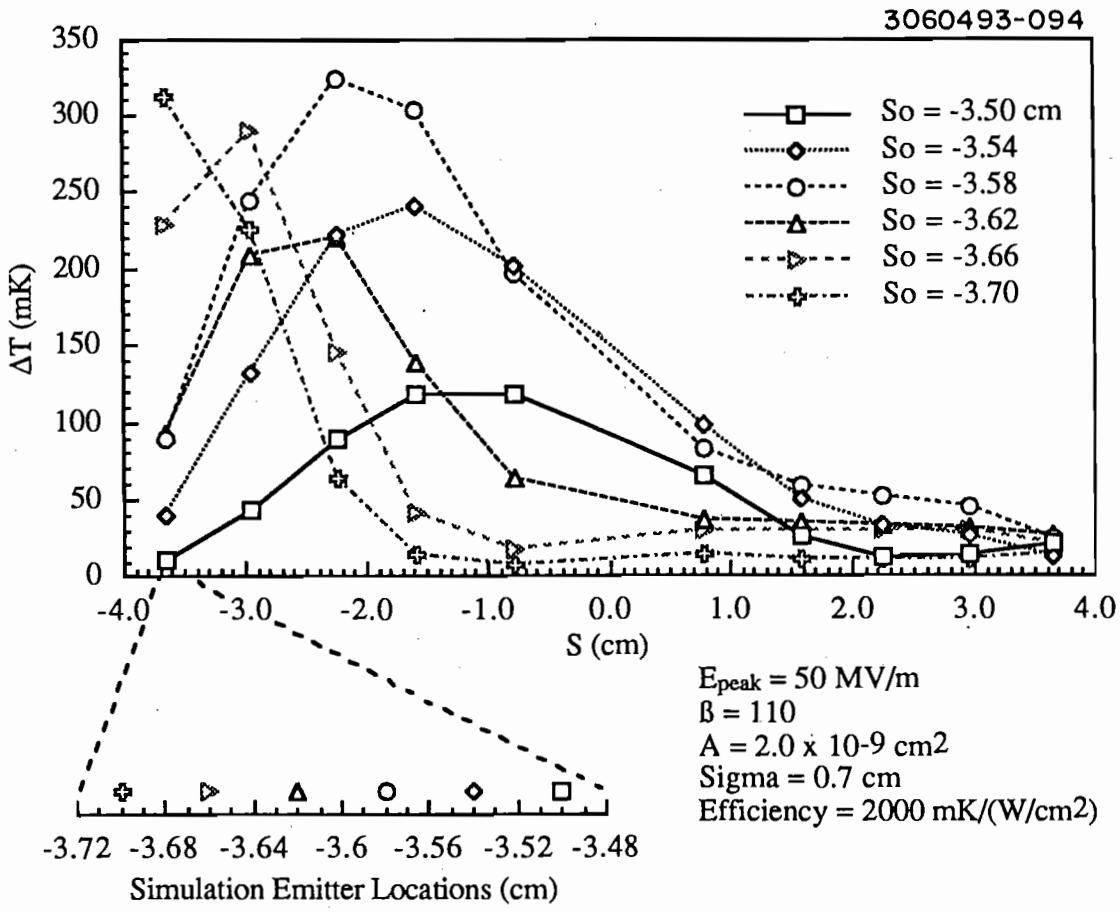

Figure E.2. Variation in the predicted temperature distribution along a single azimuth with change in emitter location.

behavior is good indication of a strong link between processing and the surface feature.

Uncertainty of position can manifest itself in one further area: azimuthal alignment of the thermometer boards. The azimuthal alignment is determined by making an axially aligned mark on the cavity along both sides of Board 0. Following dissection of the cavity, the half cell to be examined (in the SEM) was mounted in a holder such that a reference mark on the holder was equidistant azimuthally from each of the marks which bounded Board 0. The reference mark on the holder was then taken as the

azimuthal coordinate of Board 0, and all subsequent azimuthal coordinates were measured relative to the reference mark.

As mentioned above, the temperature boards are spaced at 36 degree intervals around the cavity; this corresponds to distance separations between adjacent boards of approximately 1.14 cm at the iris resistors, and 2.85 cm at equator resistors. The marks which outlined Board 0 were separated by approximately 0.75 cm, the width of the thermometer mounting. The errors in azimuthal alignment are estimated at largest 10 degrees (approximately half of the distance separating the marks indicating Board 0, again estimated by repeated trials), corresponding to 0.32 cm at the iris, and 0.79 cm at the equator. For material with the characteristics of the niobium used in the S3C cavities ($RRR \approx 400$), the temperature signal will have a full width half maximum (FWHM) of approximately 0.64 cm (as modeled by heat conduction simulations such as **HEAT**[71]). Based on this spread of temperature signal, a misalignment of 10 degrees could reduce the expected signal on the board closest to the heating source by a factor of 0.4 at the iris and a factor of 0.08 at the equator. This misalignment would not, however, be enough to confuse with temperature signals from the adjacent boards. In order to produce a measurable signal ($\geq$ 10 mK) on an adjacent board, the "hot" area would have to be at least 1 K at the iris or at least 15 K at the equator.

As stated, however, a misalignment of an emitter with thermometer boards would be enough to reduce the temperature rise measured on the thermometers of the nearest board. Figure E.3 shows an axial view of the cavity with thermometer positions indicated. The nature of the fields in the fundamental mode of an accelerating cavity dictate that emitted electrons will follows trajectories with no azimuthal velocity component. For

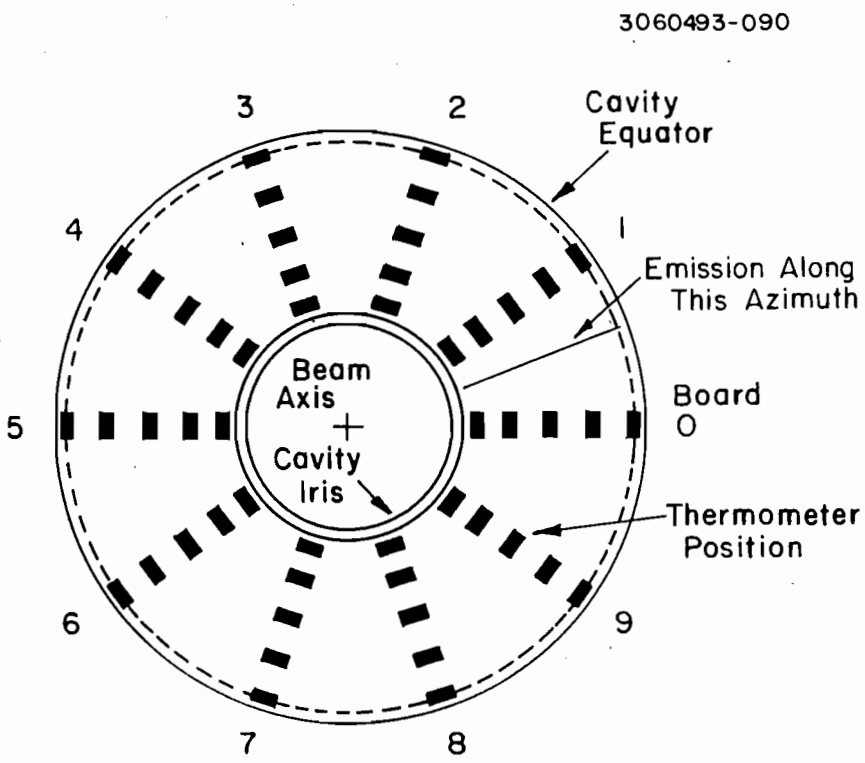

Figure E.3. Axial view of an S3C cavity, showing a misaligned field emission site.

illustrative purposes, an emission site is shown in Figure E.3 equidistant between two of the thermometer boards. As can be seen, the heating source is located significantly further from the thermometers in the equator region of the cavity than in the iris region. The effect of a azimuthal misalignment would be to reduce the temperature signal more in the equator thermometers than in the iris regions. This problem appeared in the case of cavity 1-4, as mentioned in section 4.4.

The problem of misalignment of boards with heating sources has also manifested itself in analysis of thermal breakdown location. In a test of single cell cavity 1-9, no field emission was observed (through thermometry or x-ray detection) and no heating of any other type was observed up to a peak electric field of 47 MV/m (corresponding to peak surface magnetic

field of 1080 Oe), where a thermal breakdown or quench occurred. This was unusual because a thermal breakdown is normally preceded by heating (proportional to the square of cavity fields) at the breakdown site. Multiple maps were obtained while the cavity was quenching, with occasional captures of a quench phenomena. From these maps it was determined that the breakdown site was located nearly equidistant between two of the thermometer boards, explaining why the smaller, pre breakdown signals were not detected. (This site was later determined to be the overlap in the equator weld.)

A final source of error in correlation of thermometry and field emission heating simulation comes from non-uniform response of individual thermometers. Variation in efficiencies of individual thermometers was found to be approximately 20% by Müller and Kneisel[77]. The efficiencies can be affected by several factors: varying thermal contact from thermometer to the cavity wall and variations in construction of individual thermometers. Variation in thermal contact arise from fluctuations in spring pressure or thickness of apiezon grease which is used to "glue" the thermometer to the niobium surface. Variations in construction come from the amount of carbon exposed during grinding, for example. Finally, in all experiments using the thermometry system, a certain number of the thermometers (usually 2 to 5 thermometers out of 100) were shorted out or broken, yielding zero response.

All of these effects influence the ability to make a successful comparison between simulation and measured temperature response. Complicating matters further, in many cases, an individual thermometer board could be responding to multiple heating sites. When multiple heat sources appeared to be acting, a superposition principle was assumed. Each of the

individual heat sources was assumed to produce the temperature response as it would were it the only source on the given azimuth. The signals from each source were then added to give the complete signal measured on the board.

APPENDIX F: GLOBAL THERMAL INSTABILITY

Global Thermal Instability (GTI) is a thermal breakdown phenomenon of SRF cavities. It has been previously predicted,[69],[80] but never conclusively identified until the HPP experiments.

GTI is initiated, because even in the absence of any point defects in the RF surface of a superconducting cavity, the surface dissipates power, due to the non-zero surface resistance, R_s, as was shown in equation 1-8, repeated as F-1

$$R_s = A\,\frac{\omega^2}{T}\exp\left(-\frac{\Delta(0)}{k_B T}\right) + R_0 \qquad \text{(F-1)}$$

GTI occurs when the power dissipated in the RF surface becomes enough to overwhelm the capability of the niobium to conduct away the heat. The temperature begins to rise, and the exponentially growing BCS portion of the surface resistance (the first term in equation F-1) causes a thermal runaway process, resulting in thermal breakdown.

GTI was identified multiple times in HPP cavities, through thermometry measurements at fields near the thermal breakdown level. Temperature maps of cavities approaching a thermal breakdown have historically shown a well-defined "hot spot," as shown in Figure F.1(a). In GTI, the heating is not limited to such a local area, but rather is measured throughout the equator region of the cavity, as shown in Figure F.1(b). The equator region is the high magnetic field region, where power dissipation due to surface currents is greatest.

In two of the instances when GTI was identified, the cavity was free of competing loss mechanisms, and was therefore easily identified and characterized. In addition, we can compare the measured behavior of the

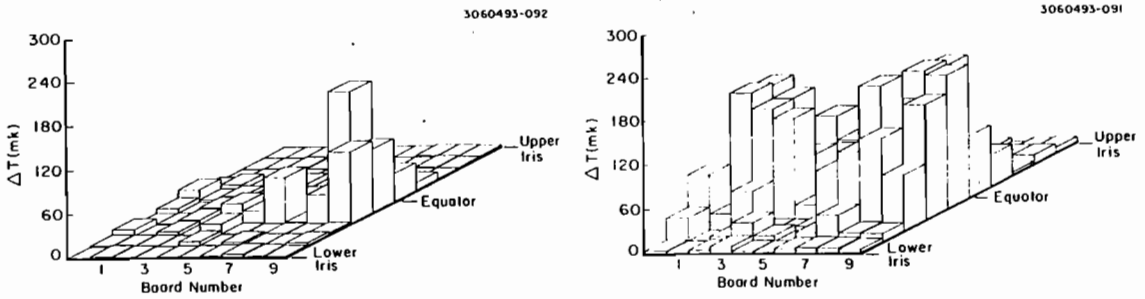

(a) Defect Breakdown (b) GTI Breakdown

Figure F.1. Comparison of temperature maps showing cavity heating at fields just below thermal breakdown, for (a) a defect region, and (b) GTI.

cavities with the predictions of the thermal conduction programs, **HEAT** and **Transient_HEAT**.

Figures F.2 contains Q_0 vs. E_{peak} plots which shows the comparisons of measured and predicted behavior for the first of the cavity tests in question. The predicted Q_0 vs. E_{peak} curves (solid lines) are equivalent for either **HEAT** or **Transient_HEAT**. This is not a surprising result, as the Q_0 vs. E_{peak} curves are measured under CW (steady state) conditions. **HEAT** and **Transient_HEAT** share the same physical model (described in chapter 6), therefore we expect **Transient_HEAT** to agree with **HEAT** in steady state conditions.

The experimental measurements were obtained with a bath temperature of 1.4 K. The agreement between measured and predicted Q_0 vs. E_{peak} for T_{bath} = 1.4 K is not good, as shown in Figure F.2. A probable reason for this discrepancy is that the thermal model assumes that the helium bath

temperature is unchanging, while experimental measurements showed that the bath temperature changed significantly when breakdown was imminent. Comparison of the measured results with the predicted plot for T_{bath} = 1.8 K, in fact, show nearly the same breakdown field. The temperature measurements during cold RF tests do not eliminate the possibility of a 400 mK temperature rise, immediately prior to breakdown. The measured Q_0 vs. E_{peak} plot is then equivalent to portions of both of the predicted plots, moving to higher bath temperatures as the fields (and thus the dissipation) increase until breakdown finally occurs.

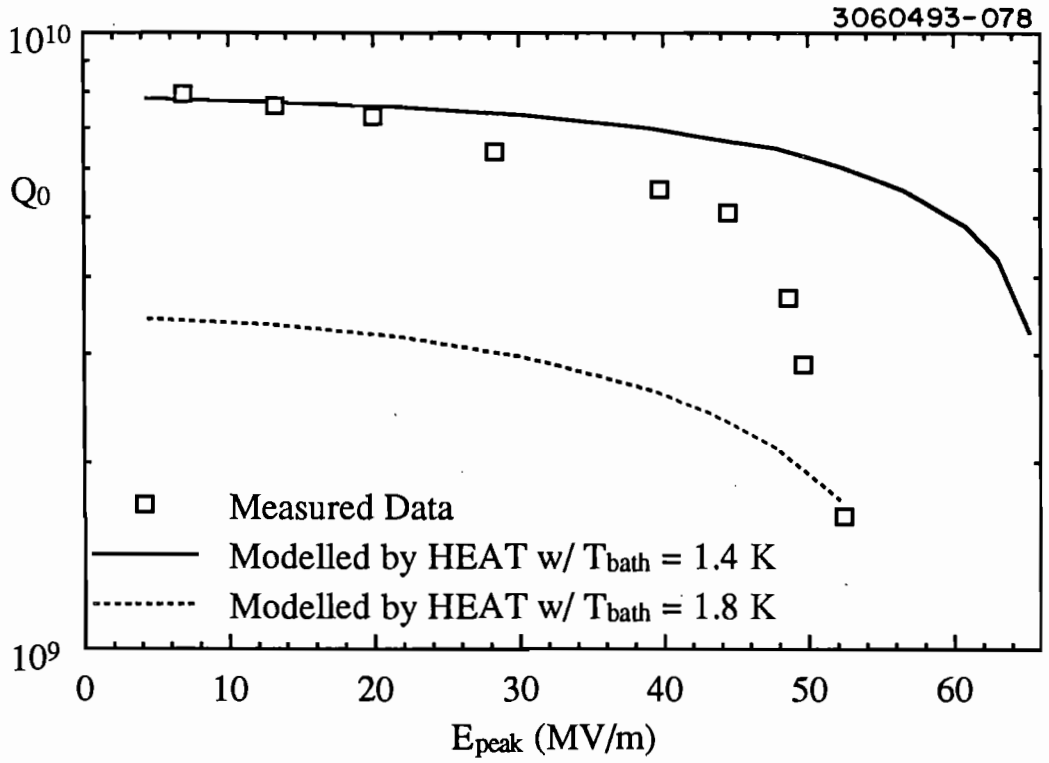

Figure F.2. Measured and predicted Q_0 vs. E_{peak} curves for the first cavity test which showed GTI, with no competing losses.

APPENDIX G: ERROR ANALYSIS IN LOW POWER CW MEASUREMENTS, OR WHY WE MEASURE WITH B ≈ 1

In chapter 2, we alluded to the fact that it is desirable to perform low power, CW measurements on SRF cavities with the input coupling β approximately equal to 1. There are two reasons for this choice: The first reason is that $\beta = 1$, or unity coupling, insures that all available power is being coupled into the cavity (See equation A-11: $P_{diss} = P_{inc}$, when $\beta = 1$). This is very important when trying to extend the fields as high as possible. The second reason for measurement at unity coupling is to minimize error propagation in the measurements. We illustrate this point here with the computation for the coupling factor β, but the analysis is equivalent for any of the quantities derived from the measured variables.

β can be determined by measuring the incident power and emitted power in modulated conditions, as shown in Figure 2.12, or the incident and reflected power, either modulated or CW. The coupling is determined by either equation A-15 or A-13, repeated here as G-1 and G-2:

$$\beta_e = \frac{1}{2\sqrt{\frac{P_{inc}}{P_e} - 1}} \tag{G-1}$$

$$\beta_r = \frac{1 \mp \rho}{1 \pm \rho} \text{ where } \rho = \sqrt{\frac{P_{ref}}{P_{inc}}} \tag{G-2}$$

We differentiate each equation with respect to both power measurements, and assume a triangular relationship between the average errors, given by equation G-3:

$$A = A(x,y) \text{ then } \langle \Delta A \rangle \approx \sqrt{\left(\frac{\partial A}{\partial x}\langle \Delta x \rangle\right)^2 + \left(\frac{\partial A}{\partial x}\langle \Delta x \rangle\right)^2} \tag{G-3}$$

Then, based on this, we can get an estimate of the percentage error in β, as determined by either method:

$$\frac{\langle \Delta\beta_e \rangle}{\beta_e} \approx \left(\frac{1+\beta_e}{2}\right)\sqrt{\left(\frac{\langle \Delta P_{inc} \rangle}{P_{inc}}\right)^2 + \left(\frac{\langle \Delta P_e \rangle}{P_e}\right)^2} \tag{G-4}$$

$$\frac{\langle \Delta\beta_r \rangle}{\beta_r} \approx \left(\frac{1-\beta_r{}^2}{4\beta_r}\right)\sqrt{\left(\frac{\langle \Delta P_{inc} \rangle}{P_{inc}}\right)^2 + \left(\frac{\langle \Delta P_{ref} \rangle}{P_{ref}}\right)^2} \tag{G-5}$$

In Figure G.1, we plot the projected average percentage error in computed β as a function of actual β, assuming that the average error in each of the power measurements is 5%. Also plotted is the Reflected power ratio, ρ. Clearly, the error propagation becomes unacceptable for any measurement in which β differs from unity by more than an order of magnitude.

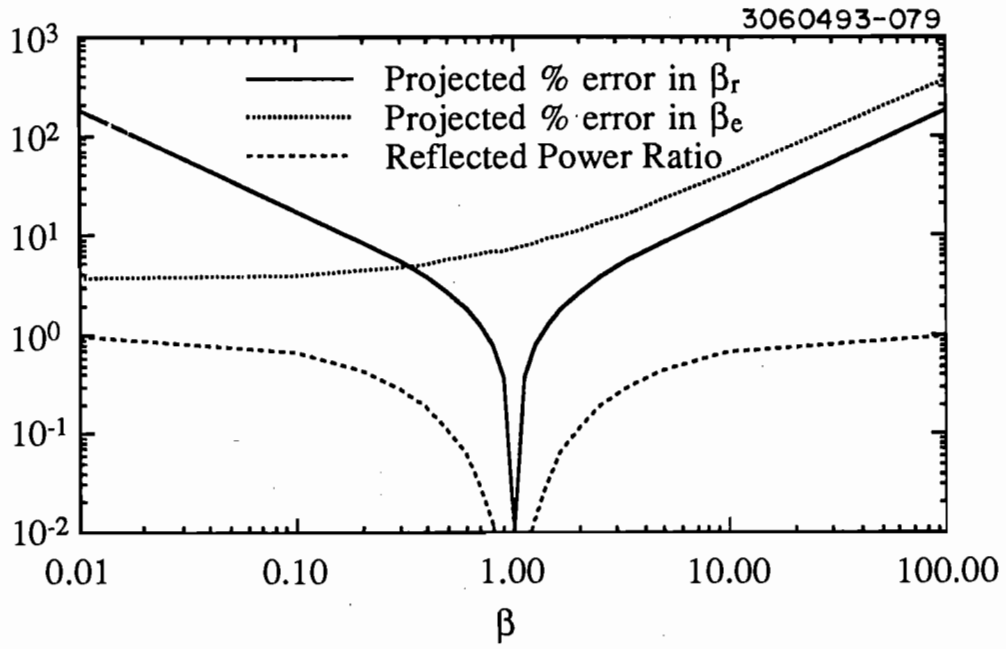

Figure G-1. Plots of projected percentage error in computed value of β as a function of true β, assuming a 5% average error in all power measurements.

APPENDIX H: HIGH POWER RF KLYSTRON CIRCUIT

The klystron circuit for the HPP program was developed prior to the author's joining the project. A diagram of the Klystron circuit is shown in Figure H.1. The RF input to the Klystron circuit is provided by the low power circuit described in the chapter 2. The place of breaking the low power circuit for feeding of the Klystron circuit is shown in Figure 2.3. Phase locking of the RF frequency was found to be necessary for optimal results during HPP processing. The lock was obtained in the same manner as for the low power circuit, since the low power circuit was used to feed the klystron circuit.

Table H-1 lists the parameters of the HPP klystron circuit. It is worth mentioning that in order to reach the highest output power to the cavity (200 kW), the RF pulse length must be shortened to $t_{RF} \approx$ 200-300 μsec, and the pulse repetition rate reduced to $f_{rep} \approx 0.5$ Hz.

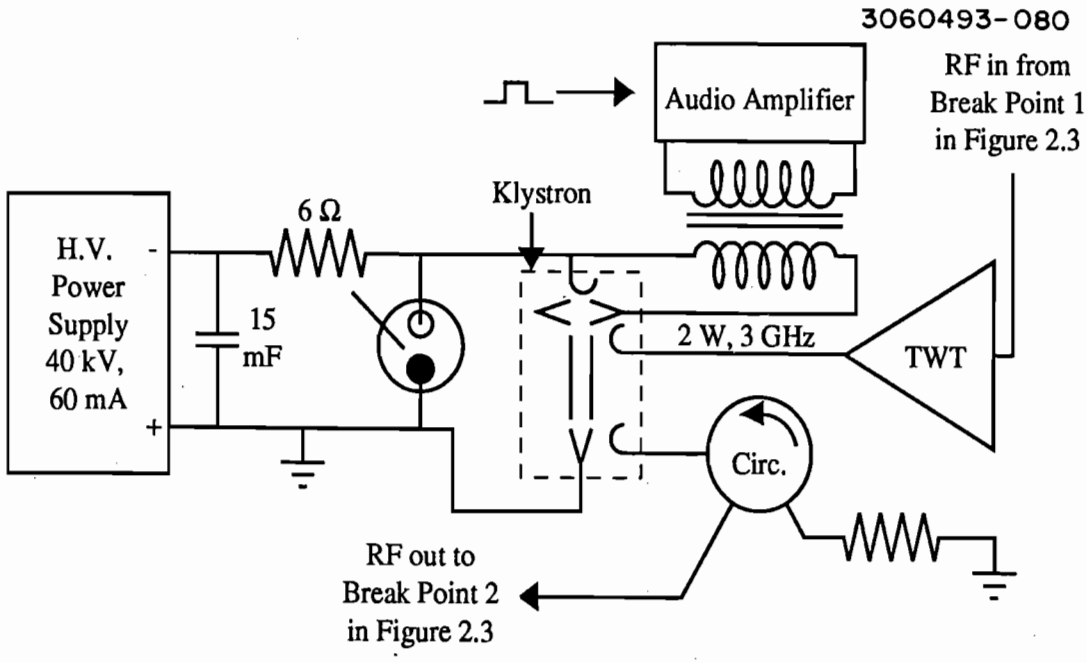

Figure H.1. The Klystron circuit used in the HPP experiments.

TABLE H-1. HPP KLYSTRON CIRCUIT PARAMETERS

Parameter	Description	Value
f_{rep}	Repetition frequency	0.5-1.6 Hz
t_{RF}	Output RF pulse length	50 μsec - 2 msec
P_{RF}	Output RF power	≤ 200 kW
ν_{RF}	Central klystron frequency	3 GHz
	3 dB Bandwidth	90 MHz

REFERENCES

1 *Proceedings of the 1st TESLA (TeV Superconducting Linear Accelerator) Workshop*, Cornell University, Ithaca, NY, **CLNS 90-1029** (1990).

2 *Proceedings of International Workshop on Next-Generation Linear Colliders,* , **SLAC-Report- 335** (1988).

3 *Proceedings of the Capri Workshop on Linear Colliders*, L. Palumbo, S. Tazzari, and V.G. Vaccaro eds., INFN Frascatti (1989).

4 K. Halbach and R.F. Holsinger, *Part. Acc.* **7**, 213 (1976); and Los Alamos Accelerator Code Group, **LA-UR-87-126**, Los Alamos National Laboratory, Los Almos, New Mexico (1987).

5 T. Weiland, *Nuc. Instr. Meth.*, **216**, 329 (1983).

6 U. Van Rienen and T. Weiland, **DESY-86-004** (1986).

7 R. Klatt, et al., *Proceedings of the 1986 Linear Accelerator Conference*, **SLAC-Report-303**, 276 (1986).

8 H. Piel, *Proceedings of the CERN Accelerator School 1988,* S. Turner ed., DESY, Hamburg, West Germany, **CERN 89-04,** 149 (1988).

9 *Proceedings of the Workshop on RF Superconductivity*, M. Kuntze ed., KfK Karlsruhe, Karlsruhe, West Germany, **KfK-Report 3019** (1980).

10 *Proceedings of the 2nd Workshop on RF Superconductivity*, H. Lengeler ed., CERN, Geneva, Switzerland (1984).

11 *Proceedings of the 3rd Workshop on RF Superconductivity*, K. Shepard ed., Argonne National Laboratory, Argonne, IL, USA, **ANL-PHYS-88-1** (1988).

12 *Proceedings of the 4th Workshop on RF Superconductivity*, Y. Kojima ed., KEK, Tsukuba, Japan, **KEK-Report 89-21** (1989).

13 *Proceedings of the 5th Workshop on RF Superconductivity*, D. Proch ed., DESY, Hamburg, Germany, **DESY M-92-01** (1992).

14 J. Bardeen, L.N. Cooper, and J.R. Schrieffer, *Phys. Rev.* **108**, 1175 (1957).

15 D.C. Mattis and J. Bardeen, *Phys. Rev.* **111**, 412 (1958).

16 A.A. Abrikosov, L.P. Gorkov, and I.M. Khalatnikov, *Sov. Phys. JETP* **8**, 182 (1959).

17 H. London, *Nature* **133**, 497 (1934).

18 J.P. Turneaure, Ph.D. Dissertation, Stanford University (1967).

19 J. Halbritter, *Z. Phys.* **238**, 466 (1970).

20 J. Halbritter, ibid. ref. 10, 427 (1984).

21 F. Palmer, ibid. ref. 11, 309 (1988).

22 M.A. Allen, et al., *IEEE Trans. Nuc. Sci*, **NS-18**, 188 (1971).

23 J. Matricon and D. St. James, *Phys. Lett.* **24A**, 241 (1967).

24 D. Moffat, et.al, ibid. ref 12; also **CLNS 89-934** (1989).

25 J.R. Delayen, et al., ibid. ref. 13, 376 (1992).

26 H. Padamsee, *J. Less Common Metals*, **139**, 167 (1988).

27 H. Padamsee, *IEEE Trans. Mag.*, **Mag-21**, 1007 (1985).

28 Q.S. Shu, et al., ibid ref. 12, 539 (1989).

29 R.W. Röth, *Proceedings of the 2nd European Particle Accelerator Conference*, EPAC, Nice, 1097 (1990).

30 B. Bonin and R.W. Röth, ibid. ref. 13, 210 (1992).

31 D. Moffat, et al., *Proceedings of the 1991 Particle Accelerator Conference*, **IEEE Cat. No. 91CH3038-7**, (1991).

32 R.H. Fowler and L. Nordheim, *Proc. Roy. Soc. Lond.*, **A119**, 173 (1928).

33 H.A. Schwettman, et al., *J. Appl. Phys.*, **45**, 914 (1974).

34 G.N. Fursey, *IEEE Trans. Elec. Insul.*, **EI-20**, 659 (1985).

35 E.A. Litvinov, ibid ref. 34, 683 (1985).

36 V.I. Rakhovsky, *IEEE Trans. Plas. Sci.*, **PS-15**, 481 (1987).

37 R.V. Latham, *IEEE Trans. Elec. Insul.*, **EI-18**, 194 (1983).

38 Ph. Niedermann, Ph.D. Dissertation No. 2197, U. of Geneva (1986).

39 Ph. Niedermann and O. Fischer, *IEEE Trans. Elec. Insul.*, **EI-24**, 905 (1989).

40 R.V. Latham, ibid ref. 37, 9 (1983).

41 R.V. Latham, et al., ibid ref. 39, 897 (1989).

42 S. Bajic, et al., ibid ref. 39, 891 (1989).

43 G.A. Mesyats, ibid ref. 37, 218 (1983).

44 B. Jüttner, ibid ref. 36, 474 (1987).

45 B. Jüttner, *J. Phys. D.: Appl. Phys.*, **14**, 1265 (1981).

46 S.N. Nazarov, et al., *IEEE Trans. Plas. Sci.*, **PS-18**, 682 (1990).

47 G.A. Mesyats, ibid ref. 39, 883 (1989).

48 G.K. Kartsev, et al., *Sov. Phys. Dok.*, **15**, 475 (1970).

49 H. Padamsee, et al., ibid ref. 12, 207 (1989).

50 Q.S. Shu, et al., *Proceedings of the 1989 Particle Accelerator Conference*, **IEEE Cat. No. 89CH2669-0**, 491 (1989).

51 W. Weingarten, ibid ref. 10, 551 (1984).

52 H. Heinrichs, ibid ref. 10, 141 (1984).

53 P. Kneisel, *IEEE Trans. Mag.*, **Mag-23**, 1417 (1987).

54 H. Padamsee, et al., *Proceedings of the 1987 Particle Accelerator Conference*, **IEEE Cat. No. 87CH2387-9**, 1824 (1987).

55 Ph. Bernard, et al., *Proceedings of the 11th International Conference on High Energy Accelerators*, CERN, 878 (1980).

56 I.E. Campisi, *IEEE Trans. Mag.*, **Mag-25**, 134 (1985).

57 I.E. Campisi and Z.D. Farkas, **SLAC/AP-16** (1984).

58 K. Shepard, Argonne National Laboratory, priv. comm.

59 G. Loew and J.W. Wang, *Proceedings of the XIIIth International Symposium on Discharges and Electrical Insulation in Vacuum*, Paris, France, also **SLAC-PUB-4647** (1988).

60 G. Loew, et al., *Proceedings of the XIVth International Symposium on Discharges and Electrical Insulation in Vacuum*, Sante Fe, New Mexico, also **SLAC-PUB-5320** (1990).

61 J. Graber, M.S. Thesis, Cornell University (1990).

62 Q.S. Shu et al., *Nuc. Instr. Meth.*, **A278**, 329 (1989)

63 Cornell Report **SRF/D-910124-24**, W.H. Hartung ed., (1989).

64 Q.S. Shu, et al., *IEEE Trans. Mag.*, **Mag-25**, 1868 (1985).

65 K. Shepard, Argonne National Laboratory, priv. comm.

66 P. Schmüser, et al., **SRF-921117-10** (1992).

67 D. Moffat, ibid ref. 13, 245 (1992).

68 H. Safa, Saclay, priv. comm.

69 G. Müller, ibid ref. 11, 331 (1988)

70 K. Mittag, Cryogenics, **13**, 94 (1973).

71 H. Padamsee, **CERN/EF/RF 82-5** (1982).

72 X. Cao, ibid ref. 13, 727 (1992).

73 A. Mosnier, Saclay, priv. comm.

74 C. Crawford, Fermilab, priv. comm.

75 E.L. Ginzton, *Microwave Measurements*, McGraw-Hill, New York (1957).

76 *Microwave Transmission Circuits*, G.L. Ragan ed., M.I.T. Radiation Laboratory Series, Volume 9, Boston Technical Publishers, Inc., Lexington, MA (1964).

77 G. Müller and P. Kneisel, Cornell Report, **SRF-851201** (1985).

78 T.I. Smith, Stanford, **HEPL-Report-437** (1966).

79 P. Schmüser, Cornell Report, **SRF-920925-10** (1992).

80 P. Fernandes and R. Parodi, **Cryogenics**, August 1984, 433 (1984).

81 K. Krafft, Ph.D. Dissertation, Cornell University (1983).

82 H. Padamsee, ibid ref. 10, 339(1984).

83 H. Padamsee, IEEE Trans. Mag., **Mag-21**, 149 (1985).

84 H. Padamsee, invited talk at the 1986 Applied Superconductivity Conference, (1986).